

2017-01-01

# Modeling The Effects Of Manufacturing Geometric Imperfections In The Buckling Analysis Of Three-Dimensional Structures

Juan Carlos Salcido

University of Texas at El Paso, [jcsalcido@miners.utep.edu](mailto:jcsalcido@miners.utep.edu)

Follow this and additional works at: [https://digitalcommons.utep.edu/open\\_etd](https://digitalcommons.utep.edu/open_etd)



Part of the [Civil Engineering Commons](#), and the [Mechanical Engineering Commons](#)

---

## Recommended Citation

Salcido, Juan Carlos, "Modeling The Effects Of Manufacturing Geometric Imperfections In The Buckling Analysis Of Three-Dimensional Structures" (2017). *Open Access Theses & Dissertations*. 548.

[https://digitalcommons.utep.edu/open\\_etd/548](https://digitalcommons.utep.edu/open_etd/548)

This is brought to you for free and open access by DigitalCommons@UTEP. It has been accepted for inclusion in Open Access Theses & Dissertations by an authorized administrator of DigitalCommons@UTEP. For more information, please contact [lweber@utep.edu](mailto:lweber@utep.edu).

MODELING THE EFFECTS OF MANUFACTURING GEOMETRIC  
IMPERFECTIONS IN THE BUCKLING ANALYSIS OF  
THREE-DIMENSIONAL STRUCTURES

JUAN CARLOS SALCIDO

Doctoral Program in Civil Engineering

APPROVED:

---

Carlos Ferregut, Ph.D., Chair

---

Cesar Carrasco, Ph.D.

---

Stephen W. Stafford, Ph.D.

---

Imad Abdallah, Ph.D.

---

Charles Ambler, Ph.D.  
Dean of the Graduate School

Copyright ©

by

Juan Carlos Salcido

2017

## Dedication

*To God for always providing me with the strength,  
perseverance, and means to complete this work.*

*Likewise, I dedicate the hard work and accomplishment of my  
dissertation to my caring family and many friends.*

*A special feeling of gratitude to my loving mother, Graciela Talamantes, whose words of  
encouragement and constant love have sustained me during this process;*

*To my only brother, Roberto Salcido, who never left my side and for his continuous support  
which inspired me throughout the achievement of this dissertation; and  
finally, to the memory of my caring **grandmother** who always provided me  
with words of encouragement during my life.*

MODELING THE EFFECTS OF MANUFACTURING GEOMETRIC  
IMPERFECTIONS IN THE BUCKLING ANALYSIS OF  
THREE-DIMENSIONAL STRUCTURES

by

JUAN CARLOS SALCIDO, MECEE

DISSERTATION

Presented to the Faculty of the Graduate School of  
The University of Texas at El Paso  
in Partial Fulfillment  
of the Requirements  
for the Degree of

DOCTOR OF PHILOSOPHY

Department of Civil Engineering  
THE UNIVERSITY OF TEXAS AT EL PASO

December 2017

## **Acknowledgements**

I offer the deepest gratitude to my professor, graduate research supervisor, and committee chairman Dr. Carlos Ferregut, for his excellent guidance, assistance, patience, and instruction during the development of my dissertation, providing me with an excellent atmosphere to conduct research. I am very thankful to him for his mentorship and direction that allowed me to reach my objective to become a Ph.D.

I would like to thank my dissertation co-chair, Dr. Cesar Carrasco, for his continuous assistance during my graduate career. It was his constant advice and assistance during the development of the research that allowed me to complete this dissertation.

I also want to thank Dr. Stephen W. Stafford and Dr. Imad Abdallah for their participation and assistance during the development of this dissertation and for being part of my dissertation committee. I am very grateful for their immense support that helped me to overcome many challenges during the development of this research.

Furthermore, I would have never been able to complete my dissertation without the assistance of many other institutions and people. Special thanks to Geometrica® for providing me with the sample materials subject to testing during this research and for its partial financial support to complete my doctoral studies. Also, I would like to thank the Center for Transportation Infrastructure Systems (CTIS) staff for their help and support in the experimental research developed in this research. Likewise, my gratefulness to all the faculty and staff of the Civil Engineering Department for their continuous support.

This material is based upon work supported by the National Science Foundation (NSF) under Grant No. #1060113. Any opinions, findings, and conclusions or recommendations expressed in this material are those of the author(s) and do not necessarily reflect the views of the National Science Foundation.

Finally, I would like to recognize my partner and friend, Alfonso A. Garcia, for his help, support, and inspiration during this process.

## **Abstract**

Reticulated three-dimensional structures follow design practices based on the common assumption that joints are either rigid, or pinned. However, the actual non-linear behavior of the jointing system interaction is required to be incorporated into the analysis of the structure to accurately predict its buckling stability. Besides, currently, there is a concern on how manufacturing imperfections of these jointing systems affect the global behavior of three-dimensional structures. This dissertation incorporates and captures the effect that manufacturing geometric imperfections in the fir-tree jointing system produce in the non-linear buckling behavior of three-dimensional structures.

To understand the effect that initial manufacturing imperfections of the joints have in the buckling behavior and critical capacity of three-dimensional structures, experiments were conducted on small-scale structures to capture the actual buckling behavior of three-dimensional structures built using the Geometrica® 6Sd-00 fir-tree connection. Then, two finite element models identical in geometry and loading conditions to the tested structures were developed. One model was created using rigid joint connections while the other model was developed using the semi-rigid behavior of the Geometrica® 6Sd-00 fir-tree jointing system. These models were created to analytically: (1) assess how the rigidity of this jointing system influences the buckling behavior of three-dimensional structures and (2) predict the actual buckling behavior of three-dimensional structures built with these joints. The comparison of analytical to experimental results indicated that the finite element model that includes the semi-rigid properties of the fir-tree connections better predicted the experimentally observed buckling behavior of the tested structures than the model that uses completely rigid connections

After the accuracy of the results obtained from the finite element model that uses the semi-rigid properties of the fir-tree jointing system were verified, finite element models of a 30-foot span three-dimensional structure were developed using this semi-rigid modeling technique under two different conditions: (1) incorporating the as-designed behavior of the jointing system and (2) using the manufactured imperfect as-built behavior of the jointing system. The semi-rigid properties of the fir-tree jointing system were obtained and utilized from a parallel research conducted at the same time as this study. The comparison of finite element simulation results of the as-designed vs. as-built three-dimensional structures modeled during this study demonstrated that manufacturing geometric imperfections in the jointing system do not have a remarkable effect on the buckling behavior and capacity of such structures.

## Table of Contents

|   |     |
|---|-----|
| Acknowledgements .....  | v   |
| Abstract .....  | vii |
| Table of Contents .....   | ix  |
| List of Figures .....   | xiv |
| List of Tables .....  | xxi |
| Chapter 1: Introduction .....                                       | 1   |
| 1.1 Introduction to Three-Dimensional Structures.....               | 1   |
| 1.2 Progress of Three-Dimensional Structures .....                  | 2   |
| 1.3 Problem Statement .....   | 7   |
| 1.4 Scope of the Research .....                                     | 8   |
| 1.5 Objectives.....   | 12  |
| 1.6 Significance of the Study to the Engineering Profession.....    | 14  |
| Chapter 2: Literature Review .....                                  | 15  |
| 2.1 Structural Stability of Three-Dimensional Structures.....       | 15  |
| 2.1.1 Buckling Loads of Three-Dimensional Structures.....           | 17  |
| 2.1.2 Geometric Imperfections of Three-Dimensional Structures ..... | 18  |
| 2.2 Buckling Modes of Three-Dimensional Structures.....             | 20  |
| 2.2.1 Local or Nodal Buckling .....                                 | 20  |
| 2.2.2 Rotated Node Buckling .....                                   | 21  |

|  |    |
|--|----|
| 2.2.3 General or Overall Buckling .....  | 22 |
| 2.2.4 Member Buckling.....   | 24 |
| 2.3 Classical Buckling Theories Based on Continuum Shell Analysis.....                 | 25 |
| 2.4 FEA of Three-Dimensional Structures with Different Jointing System Rigidities..... | 27 |
| 2.4.1 Buckling of Rigidly Jointed Three-Dimensional Structures .....                   | 27 |
| 2.4.2 Buckling of Semi-Rigid Jointed Three-Dimensional Structures.....                 | 30 |
| 2.5 Experimental Studies to Characterize Buckling Stability of 3D Structures .....     | 40 |
| 2.6 Review of the Fir-Tree Jointing System .....                                       | 47 |
| 2.6.1 Description of the Fir-Tree Jointing System .....                                | 47 |
| 2.6.2 Fir-Tree Jointing System: Previous Analytical and Experimental Studies .....     | 49 |
| 2.6.3 Geometrica 6Sd-00 Fir-Tree Jointing System: Concurrent Numerical Study .....     | 54 |
| 2.7 Summary of Literature Review .....   | 58 |
| Chapter 3: Modeling of 3D Structures and Laboratory Test Verification .....            | 60 |
| 3.1 Laboratory Tests of Bench-Scale 3D Structures.....                                 | 62 |
| 3.1.1 Laboratory Facilities, Equipment, and Instrumentation.....                       | 62 |
| 3.1.2 Geometry .....   | 64 |
| 3.1.3 Construction .....   | 66 |
| 3.1.4 Test Procedures .....  | 67 |
| 3.1.5 Test Results .....   | 70 |
| 3.2 Finite Element Simulation: Bench-Scale Structures .....                            | 73 |

|  |     |
|--|-----|
| 3.2.1 Geometry .....   | 73  |
| 3.2.2 Material Properties .....  | 74  |
| 3.2.3 Boundary and Loading Conditions .....  | 77  |
| 3.2.4 Jointing System Modeling.....  | 78  |
| 3.2.4.1 Modeling of the Rigid Jointing System.....                                   | 78  |
| 3.2.4.2 Modeling of the Semi-Rigid Jointing System .....                             | 79  |
| 3.2.5 Selected Finite Element Simulation Results .....                               | 82  |
| 3.3 Laboratory vs. Analytical Results: Comparative Analysis .....                    | 82  |
| Chapter 4: Finite Element Modeling of a Large Span Three-Dimensional Structure ..... | 86  |
| 4.1 Geometry.....  | 87  |
| 4.2 Material Properties .....  | 89  |
| 4.3 Boundary and Loading Conditions .....  | 92  |
| 4.4 Jointing System Modeling .....   | 95  |
| 4.4.1 Modeling of the Semi-Rigid Jointing System .....                               | 97  |
| 4.5 Selected Finite Element Simulation Results .....                                 | 99  |
| 4.5.1 Applied Load-Displacement and Applied Load-Rotation .....                      | 101 |
| 4.5.2 Applied Load-Interaction Index .....   | 101 |
| Chapter 5: Finite Element Simulation Results: As-Designed Structures.....            | 105 |
| 5.1 Applied Load-Displacement .....  | 106 |
| 5.2 Applied Load-Rotation.....   | 108 |

|  |     |
|--|-----|
| 5.3 Applied Load-Interaction Index .....   | 110 |
| Chapter 6: Finite Element Simulation Results: As-Built Structures.....           | 114 |
| 6.1 Applied Load-Displacement: b-090 3D Structures Model Set .....               | 116 |
| 6.2 Applied Load-Rotation: b-090 3D Structures Model Set .....                   | 120 |
| 6.3 Applied Load-Interaction Index: b-090 3D Structures Model Set.....           | 124 |
| Chapter 7: Finite Element Simulation Results: Comparative Analysis .....         | 133 |
| 7.1 As-Designed vs. As-Built 3D Structures: Applied Load-Displacement.....       | 134 |
| 7.2 As-Designed vs. As-Built 3D Structures: Applied Load-Rotation .....          | 138 |
| 7.3 As-Designed vs. As-Built 3D Structures: Applied Load-Interaction Index ..... | 142 |
| 7.4 Conclusion of Comparisons .....  | 149 |
| Chapter 8: Summary, Conclusions, and Recommendations.....                        | 150 |
| 8.1 Summary .....  | 150 |
| 8.2 Conclusions .....  | 152 |
| 8.3 Contribution of the Study.....   | 154 |
| 8.4 Future Work Recommendations .....  | 155 |
| References .....   | 156 |
| Appendix A.....  | 163 |
| Finite Element Simulation Results: As-Designed 3D Structures.....                | 163 |
| d-090 3D structure.....  | 164 |
| Appendix B .....   | 167 |

|   |     |
|---|-----|
| Finite Element Simulation Results: b-090 3D Structures Model Set..... | 167 |
| b-AA 090 3D Structure .....   | 168 |
| b-AB 090 3D Structure .....   | 174 |
| b-AC 090 3D Structure .....   | 180 |
| b-BA 090 3D Structure .....   | 186 |
| b-BB 090 3D Structure.....  | 192 |
| b-BC 090 3D Structure.....  | 198 |
| b-CA 090 3D Structure .....   | 204 |
| b-CB 090 3D Structure.....  | 210 |
| b-CC 090 3D Structure.....  | 216 |
| b-RD 090 3D Structure .....   | 222 |
| Curriculum Vitae .....  | 226 |

## List of Figures

|  |    |
|--|----|
| <b>Figure 1.1</b> Single Layer Frame (Photo courtesy of Geometrica® 2015) .....  | 3  |
| <b>Figure 1.2</b> Double Layer Frame (Photo courtesy of Geometrica® 2015) .....  | 3  |
| <b>Figure 1.3</b> Dome Located in Marchwood England (Photo courtesy of Geometrica® 2015) .....                                     | 4  |
| <b>Figure 1.4</b> Double Layer Barrel Vaulted Storage Located in Samalayuca, Mexico (Photo<br>courtesy of Geometrica® 2015) .....  | 5  |
| <b>Figure 1.5</b> Hypar Shape 3D Stucture, Chapultepec Aviary Located in Mexico City (Photo<br>courtesy of Geometrica® 2015) ..... | 5  |
| <b>Figure 1.6</b> Millennium Dome Located in London, UK (Jin 2004) .....   | 6  |
| <b>Figure 1.7</b> Geometrica® 6-Sierra Delta (6Sd-00) Jointing System (After Garcia 2017) .....                                    | 9  |
| <b>Figure 1.8</b> Geometrica® 6Sd-00 Jointing System Contact Surfaces (After Garcia 2017) .....                                    | 10 |
| <b>Figure 1.9</b> Geometrica® 6Sd-00 Jointing System Axial and In-Plane Stiffness .....  | 11 |
| <b>Figure 2.1</b> Manifestations of Buckling .....   | 16 |
| <b>Figure 2.2</b> Buckling Loads in Three-Dimensional Structures (Kato et al. 1998) .....  | 18 |
| <b>Figure 2.3</b> Node Deviation Geometric Imperfection (After Garcia 2017) .....  | 19 |
| <b>Figure 2.4</b> Member Curvature Geometric Imperfection (After Garcia 2017) .....  | 19 |
| <b>Figure 2.5</b> Local or Nodal Buckling (Kato et al. 2005) .....   | 21 |
| <b>Figure 2.6</b> Rotated Node Buckling (Kato et al. 2005) .....   | 21 |
| <b>Figure 2.7</b> General or Overall Buckling (Kato et al. 2005) .....   | 22 |
| <b>Figure 2.8</b> Symmetric and Anti-symmetric Buckling in 3D Structures (Kato et al. 2005) .....                                  | 23 |
| <b>Figure 2.9</b> Band Shape Buckling (Kato et al. 2005) .....   | 23 |
| <b>Figure 2.10</b> Member Buckling (Kato et al. 2005) .....  | 24 |
| <b>Figure 2.11</b> Members and End Connections Modeled by Amiri and Davodi (2002) .....  | 30 |

|  |    |
|--|----|
| <b>Figure 2.12</b> ORTZ Jointing System (López et al. 2007a) .....                             | 31 |
| <b>Figure 2.13</b> Members and Connections Modeled by López et al. (2007a; 2007c) .....        | 32 |
| <b>Figure 2.14</b> Bolt-Ball Jointing System (Fan et al. 2012a) .....                          | 32 |
| <b>Figure 2.15</b> Finite Element Model Developed by Fan et al. (After 2010b) .....            | 33 |
| <b>Figure 2.16</b> Bolted Connections (Hwang et al.2009).....                                  | 33 |
| <b>Figure 2.17</b> Moment-Rotation Curves of Jointing System (Hwang et al.2009) .....          | 34 |
| <b>Figure 2.18</b> Load- Displacement of Axial Loading Tests (Hwang et al.2009).....           | 35 |
| <b>Figure 2.19</b> Finite Element Model Developed by Hwang et al.(2009).....                   | 35 |
| <b>Figure 2.20</b> Socket Jointing System (Fan et al. 2012a) .....                             | 36 |
| <b>Figure 2.21</b> Simplification of the Bending-Rotation Curves by Fan et al. (2011).....     | 37 |
| <b>Figure 2.22</b> Finite Element Model Developed by Ma et al. (2013b) .....                   | 38 |
| <b>Figure 2.23</b> Welded Hollow Spherical Joint (After Han et al. 2016) .....                 | 39 |
| <b>Figure 2.24.</b> Model of Aluminum Space Frame Dome Developed by Wright (1969) .....        | 40 |
| <b>Figure 2.25</b> Implosion Stability Failure of Space Frame Dome (Wright 1969) .....         | 41 |
| <b>Figure 2.26</b> Dimpled Stability Failure of Space Frame Dome (Wright 1969) .....           | 42 |
| <b>Figure 2.27</b> Schematic Dome Test Arrangement Shibata et al. (1993) .....                 | 43 |
| <b>Figure 2.28</b> General Experimental Set Up (López et al. 2007a; c) .....                   | 44 |
| <b>Figure 2.29</b> Experimental and Numerical Results (López et al. 2007a; c) .....            | 45 |
| <b>Figure 2.30</b> Load-Deflection Curves Obtained by Fong et al. (2012) .....                 | 46 |
| <b>Figure 2.31</b> Fir-Tree Extruded Aluminum Connector .....                                  | 48 |
| <b>Figure 2.32</b> Coined Pressed Ends Tubular Element (Geometrica® 2015) .....                | 48 |
| <b>Figure 2.33</b> Fir-Tree Jointing System (After Narayanan 2007).....                        | 49 |
| <b>Figure 2.34</b> Behavior of Fir-Tree Jointing System (Afer Sugizaki and Kohmura 1994) ..... | 50 |

|  |    |
|--|----|
| <b>Figure 2.35</b> Failure Mode of Dome with Fir-Tree Joint (Sugizaki and Kohmura 1994).....                       | 51 |
| <b>Figure 2.36</b> Tension Load-Deformation Curves Obtained Experimentally by Doran (1997) .....                   | 52 |
| <b>Figure 2.37</b> Geometrica® 6Zd-00 Jointing System FEM (Ferregut and Carrasco 1998).....                        | 53 |
| <b>Figure 2.38</b> Load-Displacement Curve of Geometrica® 6Zd-00 Jointing System (Ferregut and Carrasco 1998)..... | 54 |
| <b>Figure 2.39</b> Geometrica® 6Sd-00 Jointing System Axial Semi-Rigid Configuration .....                         | 55 |
| <b>Figure 2.40</b> Geometrica® 6Sd-00 Jointing System In-Plane Bending Semi-Rigid Configuration .....              | 55 |
| <b>Figure 3.1</b> MTS Universal Testing Machine .....  | 63 |
| <b>Figure 3.2</b> Geometry of Bench-Scale Tested Structures.....   | 65 |
| <b>Figure 3.3</b> Construction of Bench-Scale Tested Structures .....  | 66 |
| <b>Figure 3.4</b> MTS Universal Testing Machine and Bench-Scale Structure Configuration .....                      | 67 |
| <b>Figure 3.5</b> Supporting Conditions of Bench-Scale Tested Structures .....                                     | 68 |
| <b>Figure 3.6</b> Laboratory Test of Bench-Scale Structure in Progress .....                                       | 69 |
| <b>Figure 3.7</b> Rotated Nodal Buckling Failure of Tested Bench-Scale Structures.....                             | 71 |
| <b>Figure 3.8</b> Finite Element Model of Bench-Scale Structure .....  | 73 |
| <b>Figure 3.9</b> Coupon Tension Test in Progress .....  | 74 |
| <b>Figure 3.10</b> Bench-Scale Structure Material Properties: Aluminum A6061-T6 .....                              | 75 |
| <b>Figure 3.11</b> Bench-Scale Structure Material Properties: Steel A500 Grade B .....                             | 75 |
| <b>Figure 3.12</b> Boundary and Loading Conditions of Modeled Bench-Scale Structures.....                          | 77 |
| <b>Figure 3.13</b> Rigid Jointing System: FEM of Bench-Scale Structure .....                                       | 78 |
| <b>Figure 3.14</b> Semi-Rigid Jointing System: FEM of Bench-Scale Structure.....                                   | 79 |
| <b>Figure 3.15</b> Axial Semi-Rigid Behavior of the Jointing System: s-104 .....                                   | 80 |

|   |     |
|---|-----|
| <b>Figure 3.16</b> In-Plane Bending Semi-Rigid Behavior of Jointing System: s-104 .....               | 81  |
| <b>Figure 3.17</b> Load-Displacement of Bench Scale Structure: r-104 vs. s-104 vs. Test 1 .....       | 83  |
| <b>Figure 3.18</b> Load-Displacement of Bench Scale Structure: r-104 vs. s-104 vs. Test 2 .....       | 83  |
| <b>Figure 3.19</b> Load-Displacement of Bench Scale Structure: r-104 vs. s-104 vs. Test 3 .....       | 84  |
| <b>Figure 4.1</b> Fir-Tree Jointing System Tubular Element Parameters .....                           | 87  |
| <b>Figure 4.2</b> Three-Dimensional Structure Finite Element Model .....                              | 88  |
| <b>Figure 4.3</b> ASTM Tension Test in Progress .....   | 89  |
| <b>Figure 4.4</b> Stress-Strain Curve of Aluminum A6061-T6.....                                       | 90  |
| <b>Figure 4.5</b> Stress-Strain Curve of Steel A500 Grade B .....                                     | 90  |
| <b>Figure 4.6</b> Three-Dimensional Structure with Simply Supported Boundary Conditions .....         | 92  |
| <b>Figure 4.7</b> Three-Dimensional Structure under Base Snow Load .....                              | 94  |
| <b>Figure 4.8</b> Developed FEM of the Three-Dimensional Structure.....                               | 96  |
| <b>Figure 4.9</b> Typical Axial Stiffness of the Jointing System (After Garcia 2017) .....            | 97  |
| <b>Figure 4.10</b> Typical In-Plane Bending Stiffness of the Jointing System (After Garcia 2017)..... | 98  |
| <b>Figure 4.11</b> Selected Members of the Structure to Study .....                                   | 100 |
| <b>Figure 5.1</b> Applied Load-Displacement of Node 13: d-090 3D Structure.....                       | 106 |
| <b>Figure 5.2</b> Applied Load-Rotation of Node 2: d-090 3D Structure .....                           | 108 |
| <b>Figure 5.3</b> Applied Load-Interaction Index of Beam Element 62: d-090 3D Structure .....         | 110 |
| <b>Figure 5.4</b> Axial Semi-Rigid Behavior: d-090 (After Garcia 2017) .....                          | 112 |
| <b>Figure 5.5</b> In-Plane Bending Semi-Rigid Behavior: d-090 (After Garcia 2017).....                | 113 |
| <b>Figure 6.1</b> Applied Load-Displacement of Node 13: b-090 3D Structures Model Set.....            | 119 |
| <b>Figure 6.2</b> Applied Load-Rotation of Node 2: b-090 3D Structures Model Set.....                 | 123 |
| <b>Figure 6.3</b> Mean Axial Semi-Rigid Behavior: b-090 3D Structures Model Set .....                 | 129 |

|  |     |
|--|-----|
| <b>Figure 6.4</b> Mean In-Plane Bending Semi-Rigid Behavior: b-090 3D Structures Model Set.....        | 130 |
| <b>Figure 6.5</b> Applied Load-Interaction Index of Beam 62: b-090 3D Structures Model Set.....        | 131 |
| <b>Figure 7.1</b> Applied Load-Displacement of Node 13: d-090 vs. b-090 $\mu$ 3D Structures .....      | 135 |
| <b>Figure 7.2</b> Applied Load-Rotation of Node 2: d-090 vs. b-090 $\mu$ 3D Structures .....           | 139 |
| <b>Figure 7.3</b> Applied Load-Interaction Index of Beam 62: d-090 vs. b-090 $\mu$ 3D Structures ..... | 145 |
| <b>Figure 7.4</b> Axial Semi-Rigid Behavior: d-090 vs. b-090 $\mu$ 3D Structures .....                 | 146 |
| <b>Figure 7.5</b> In-Plane Bending Semi-Rigid Behavior: d-090 vs. b-090 $\mu$ 3D Structures .....      | 146 |
| <b>Figure B.1</b> Applied Load-Displacement of Node 13: b-AA 090 3D Structure .....                    | 168 |
| <b>Figure B.2</b> Applied Load-Rotation of Node 2: b-AA 090 3D Structure.....                          | 169 |
| <b>Figure B.3</b> Applied Load-Interaction Index of Beam 62: b-AA 090 3D Structure .....               | 171 |
| <b>Figure B.4</b> Axial Semi-Rigid Behavior: b-AA 090 (After Garcia 2017).....                         | 172 |
| <b>Figure B.5</b> In-Plane Bending Semi-Rigid Behavior: b-AA 090 (After Garcia 2017) .....             | 173 |
| <b>Figure B.6</b> Applied Load-Displacement of Node 13: b-AB 090 3D Structure.....                     | 174 |
| <b>Figure B.7</b> Applied Load-Rotation of Node 2: b-AB 090 3D Structure.....                          | 175 |
| <b>Figure B.8</b> Applied Load-Interaction Index of Beam 62: b-AB 090 3D Structure .....               | 177 |
| <b>Figure B.9</b> Axial Semi-Rigid Behavior: b-AB 090 (After Garcia 2017).....                         | 178 |
| <b>Figure B.10</b> In-Plane Bending Semi-Rigid Behavior: b-AB 090 (After Garcia 2017).....             | 179 |
| <b>Figure B.11</b> Applied Load-Displacement of Node 13: b-AC 090 3D Structure.....                    | 180 |
| <b>Figure B.12</b> Applied Load-Rotation of Node 2: b-AC 090 3D Structure.....                         | 181 |
| <b>Figure B.13</b> Applied Load-Interaction Index of Beam 62: b-AC 090 3D Structure .....              | 183 |
| <b>Figure B.14</b> Axial Semi-Rigid Behavior: b-AC 090 (After Garcia 2017).....                        | 184 |
| <b>Figure B.15</b> In-Plane Bending Semi-Rigid Behavior: b-AC 090 (After Garcia 2017).....             | 185 |
| <b>Figure B.16</b> Applied Load-Displacement of Node 13: b-BA 090 3D Structure.....                    | 186 |

|  |     |
|--|-----|
| <b>Figure B.17</b> Applied Load-Rotation of Node 2: b-BA 090 3D Structure.....             | 187 |
| <b>Figure B.18</b> Applied Load-Interaction Index of Beam 62: b-BA 090 3D Structure .....  | 189 |
| <b>Figure B.19</b> Axial Semi-Rigid Behavior: b-BA 090 (After Garcia 2017).....            | 190 |
| <b>Figure B.20</b> In-Plane Bending Semi-Rigid Behavior: b-BA 090 (After Garcia 2017)..... | 191 |
| <b>Figure B.21</b> Applied Load-Displacement of Node 13: b-BB 090 3D Structure.....        | 192 |
| <b>Figure B.22</b> Applied Load-Rotation of Node 2: b-BB 090 3D Structure .....            | 193 |
| <b>Figure B.23</b> Applied Load-Interaction Index of Beam 62: b-BB 090 3D Structure.....   | 195 |
| <b>Figure B.24</b> Axial Semi-Rigid Behavior: b-BB 090 (After Garcia 2017).....            | 196 |
| <b>Figure B.25</b> In-Plane Bending Semi-Rigid Behavior: b-BB 090 (After Garcia 2017)..... | 197 |
| <b>Figure B.26</b> Applied Load-Displacement of Node 13: b-BC 090 3D Structure.....        | 198 |
| <b>Figure B.27</b> Applied Load-Rotation of Node 2: b-BC 090 3D Structure .....            | 199 |
| <b>Figure B.28</b> Applied Load-Interaction Index of Beam 62: b-BC 090 3D Structure.....   | 201 |
| <b>Figure B.29</b> Axial Semi-Rigid Behavior: b-BC 090 (After Garcia 2017).....            | 202 |
| <b>Figure B.30</b> In-Plane Bending Semi-Rigid Behavior: b-BC 090 (After Garcia 2017)..... | 203 |
| <b>Figure B.31</b> Applied Load-Displacement of Node 13: b-CA 090 3D Structure.....        | 204 |
| <b>Figure B.32</b> Applied Load-Rotation of Node 2: b-CA 090 3D Structure.....             | 205 |
| <b>Figure B.33</b> Applied Load-Interaction Index of Beam 62: b-CA 090 3D Structure .....  | 207 |
| <b>Figure B.34</b> Axial Semi-Rigid Behavior: b-CA 090 (After Garcia 2017).....            | 208 |
| <b>Figure B.35</b> In-Plane Bending Semi-Rigid Behavior: b-CA 090 (After Garcia 2017)..... | 209 |
| <b>Figure B.36</b> Applied Load-Displacement of Node 13: b-CB 090 3D Structure.....        | 210 |
| <b>Figure B.37</b> Applied Load-Rotation of Node 2: b-CB 090 3D Structure .....            | 211 |
| <b>Figure B.38</b> Applied Load-Interaction Index of Beam 62: b-CB 090 3D Structure.....   | 213 |
| <b>Figure B.39</b> Axial Semi-Rigid Behavior: b-CB 090 (After Garcia 2017).....            | 214 |

|  |     |
|--|-----|
| <b>Figure B.40</b> In-Plane Bending Semi-Rigid Behavior: b-CB 090 (After Garcia 2017)..... | 215 |
| <b>Figure B.41</b> Applied Load-Displacement of Node 13: b-CC 090 3D Structure.....        | 216 |
| <b>Figure B.42</b> Applied Load-Rotation of Node 2: b-CC 090 3D Structure .....            | 217 |
| <b>Figure B.43</b> Applied Load-Interaction Index of Beam 62: b-CC 090 3D Structure.....   | 219 |
| <b>Figure B.44</b> Axial Semi-Rigid Behavior: b-CC 090 (After Garcia 2017) .....           | 220 |
| <b>Figure B.45</b> In-Plane Bending Semi-Rigid Behavior: b-CC 090 (After Garcia 2017)..... | 221 |
| <b>Figure B.46</b> Applied Load-Displacement of Node 13: b-RD 090 3D Structure.....        | 222 |
| <b>Figure B.47</b> Applied Load-Rotation of Node 2: b-RD 090 3D Structure.....             | 223 |
| <b>Figure B.48</b> Applied Load-Interaction Index of Beam 62: b-RD 090 3D Structure .....  | 225 |

## List of Tables

|  |     |
|--|-----|
| <b>Table 2.1</b> Joint Classification Based on $\alpha$ and $\beta$ (After Fan et al. 2011) .....                            | 38  |
| <b>Table 2.2</b> As-Designed Jointing System Combinations (After Garcia 2017) .....  | 56  |
| <b>Table 2.3</b> As-Built Jointing System Combinations (After Garcia 2017) .....   | 57  |
| <b>Table 3.1</b> Applied Load-Displacement of Crown Connector of Tested Structures .....                                     | 70  |
| <b>Table 3.2</b> Failure Load-Displacement of Crown Connector of Tested Structures .....                                     | 70  |
| <b>Table 3.3</b> Material Properties of Modeled Bench-Scale Structures .....   | 76  |
| <b>Table 3.4</b> Patran/Nastran Elements used to Model Bench-Scale Structures .....  | 81  |
| <b>Table 4.1</b> Material Properties of Structural Elements .....  | 91  |
| <b>Table 4.2</b> Patran/Nastran Elements to Model Three-Dimensional Structures .....   | 99  |
| <b>Table 6.1</b> Applied Load-Displacement and Statistical Properties of Node 13: b-090 3D<br>Structures Model Set.....      | 117 |
| <b>Table 6.2</b> Applied Load-Rotation and Statistical Properties of Node 2: b-090 3D Structures<br>Model Set.....           | 121 |
| <b>Table 6.3</b> Applied Load-Interaction Index and Statistical Properties of Beam 62: b-090 3D<br>Structures Model Set..... | 125 |
| <b>Table 6.4</b> Force Components and Statistical Properties of Beam 62 at Failure: b-090 3D<br>Structures Model Set.....    | 128 |
| <b>Table 7.1</b> Applied Load-Displacement of Node 13: 090 Comparison.....   | 136 |
| <b>Table 7.2</b> Critical Applied Load-Displacement of Node 13: 090 Comparison.....  | 136 |
| <b>Table 7.3</b> Applied Load-Rotation of Node 2: 090 Comparison .....   | 140 |
| <b>Table 7.4</b> Critical Applied Load-Rotation of Node 2: 090 Comparison .....  | 140 |
| <b>Table 7.5</b> Applied Load-Interaction Index of Beam 62: 090 Comparison.....  | 147 |

|   |     |
|---|-----|
| <b>Table 7.6</b> Applied Load at Failure of Beam 62: 090 Comparison .....                   | 148 |
| <b>Table 7.7</b> Force Components of Beam 62 at Buckling Failure Load: 090 Comparison ..... | 148 |
| <b>Table A.1</b> Applied Load-Displacement of Node 13: d-090 3D Structure .....             | 164 |
| <b>Table A.2</b> Applied Load-Rotation of Node 2: d-090 3D Structure.....                   | 165 |
| <b>Table A.3</b> Applied Load-Interaction Index of Beam 62: d-090 3D Structure .....        | 166 |
| <b>Table B.1</b> Applied Load-Interaction Index of Beam 62: b-AA 090 3D Structure.....      | 170 |
| <b>Table B.2</b> Applied Load-Interaction Index of Beam 62: b-AB 090 3D Structure .....     | 176 |
| <b>Table B.3</b> Applied Load-Interaction Index of Beam 62: b-AC 090 3D Structure .....     | 182 |
| <b>Table B.4</b> Applied Load-Interaction Index of Beam 62: b-BA 090 3D Structure .....     | 188 |
| <b>Table B.5</b> Applied Load-Interaction Index of Beam 62: b-BB 090 3D Structure .....     | 194 |
| <b>Table B.6</b> Applied Load-Interaction Index of Beam 62: b-BC 090 3D Structure .....     | 200 |
| <b>Table B.7</b> Applied Load-Interaction Index of Beam 62: b-CA 090 3D Structure .....     | 206 |
| <b>Table B.8</b> Applied Load-Interaction Index of Beam 62: b-CB 090 3D Structure .....     | 212 |
| <b>Table B.9</b> Applied Load-Interaction Index of Beam 62: b-CC 090 3D Structure .....     | 218 |
| <b>Table B.10</b> Applied Load-Interaction Index of Beam 62: b-RD 090 3D Structure .....    | 224 |

## **Chapter 1: Introduction**

This chapter presents the background and the evolution of three-dimensional structures. It also describes the problem statement, scope of the research, objectives and significance of the study.

### **1.1 Introduction to Three-Dimensional Structures**

Interesting and fairly new structural systems are created when frameworks are brought together to create what is known as Three-Dimensional (3D) structures. A reticulated 3D structure can be defined as a structural system assembled of linear elements arranged for the forces to be transferred in a three-dimensional manner (Lan 2005). Three-dimensional structures are a beautiful form of architectural design. Once regarded as exotic and unconventional, they are now universally accepted as economical and aesthetically pleasing. Three-dimensional structures have become of special interest to engineers and architects because they deliver an extensive solution to provide amazing architectural designs without the constraint to maintain short span distances and as a consequence, allowing designers to create an enormous variety of structural shapes (López et al. 2007b). The usage of lightweight three-dimensional structures is growing around the world. The speed of progress on the development of three-dimensional structures is clearly and rapidly accelerating. During the 1980's many designers, including architects and engineers, contributed to the rapid development and design of reticulated three-dimensional structures (Makowski 1993). During the 90's and 2000's, three-dimensional structures experienced great development, not only expressed in structural forms such as cable structures, deployable and retractable structures, but also expressed in materials used, such as steel, aluminum, concrete, wood, glass, and so on (Salcido et al. 2016). With these developments, numerous three-dimensional structures have been built,

including but not limited to roofs for venues such as sports stadiums/arenas, gymnasiums, cultural centers, auditoriums, shopping malls, and railway stations (Yan et al. 2000).

## **1.2 Progress of Three-Dimensional Structures**

The progress of three-dimensional structures has experienced many modifications, as the available materials used in construction have developed. At the beginning of their history, 3D structures were constructed with continuous forms using stone, and at later times they were built using brickwork. Passing through wood timber during the middle ages until the introduction of iron materials, the evolution of reticulated three-dimensional structures has promoted the design of better and lighter structures. The introduction of steel and aluminum alloys produced an enthusiasm in engineers and architects to surround a great amount of space without the consumption of excessive amount of time of construction, expensive formwork and unnecessary use of construction materials (Makowski 1984).

Furthermore, the development of prefabricated structural elements has drastically reduced the difficulty of design and construction of reticulated three-dimensional structures. These elements are arranged in one, two or multiple layers of intersecting members. **Figure 1.1** and **1.2** show a single and double layer frame arrangement, respectively.

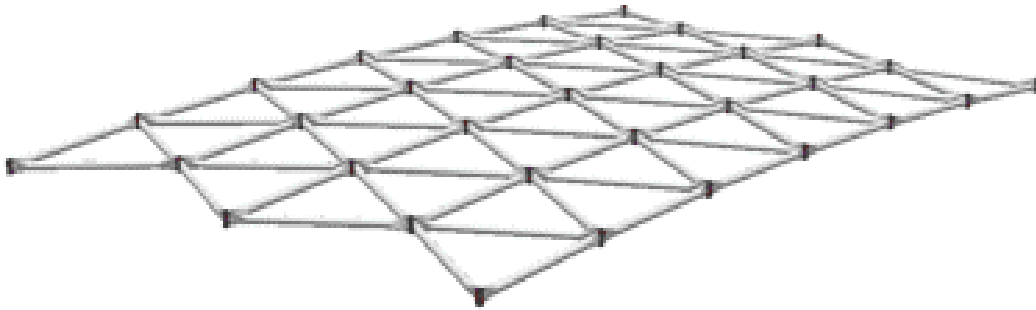


**Figure 1.1** Single Layer Frame (Photo courtesy of Geometrica® 2015)

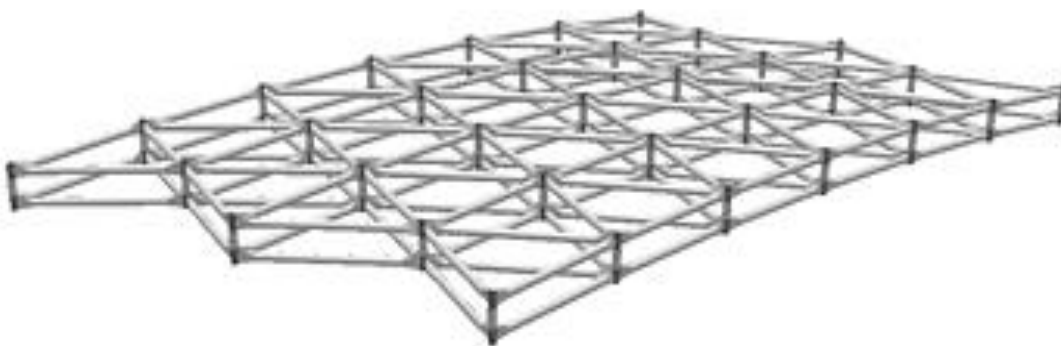


**Figure 1.2** Double Layer Frame (Photo courtesy of Geometrica® 2015)

The straight members are connected to jointing systems in such a way as to avoid the use of any column causing obstruction of the inner space, creating an interrupted long span curved surface with a circular or polygonal base.

There are many types of three-dimensional structural shapes. Domes (**Figure 1.3**), barrels (**Figure 1.4**), and hypars (**Figure 1.5**) are some of the most common of shape forms used to build three-dimensional structures.



**Figure 1.3** Dome Located in Marchwood England (Photo courtesy of Geometrica® 2015)



**Figure 1.4** Double Layer Barrel Vaulted Storage Located in Samalayuca, Mexico (Photo courtesy of Geometrica® 2015)



**Figure 1.5** Hypar Shape 3D Stucture, Chapultepec Aviary Located in Mexico City (Photo courtesy of Geometrica® 2015)

Besides, different approaches have been employed to build three-dimensional structures. One example are the suspended three-dimensional structures, which are composed of a rigid shell and a flexible tensioning system that are widely used in sport gymnasiums, railway stations, airport terminal buildings, conference centers, exhibition halls and some other large-scale public buildings (Nie et al. 2013). **Figure 1.6** shows the Millennium Dome which is supported by a network of cables.



**Figure 1.6** Millennium Dome Located in London, UK (Jin 2004)

One important aspect influencing the rapid development of three-dimensional structures is the development of modern computerized software. Three-dimensional structures are highly statically indeterminate, and their analysis may lead to extremely tedious and time consuming computations (Lan 2005). In the past, the buckling behavior of three-dimensional structures was studied by replacing the complete structure by their continuum equivalents (Wright 1965). However, with the introduction of modern software and computerized models, it is possible to predict the structural stability of complex three-dimensional structures using nonlinear finite

element analysis (Yan et al. 2016). This is important because these types of structures experience, in general, compressive forces acting vertically in the surface of the structure and a lesser horizontal forces (usually tensile) acting around the structure (Mullord 1984). According to Pugnale (2013) structural collapse, in three-dimensional structures, is generally caused by buckling. For this reason, the analysis of the structural stability is essential for the design of three-dimensional structures (Fan et al. 2010a).

### **1.3 Problem Statement**

The buckling behavior of three-dimensional structures is influenced by the effect of three main factors being: (1) the shape of the structure itself; (2) the jointing system semi-rigid behavior; and (3) the existence of geometric imperfections of the elements of the three-dimensional structures due to construction errors (Ma et al. 2013).

In the past, studies have been dedicated to fully understand the effect of joint rigidity and construction geometric imperfections on the buckling behavior of three-dimensional structures. A recent study conducted by Garcia (2017) analyzed how manufacturing geometric imperfections affect the semi-rigid behavior and load capacity of a jointing system used in three-dimensional structures. However, to date, no attention has been directed to incorporate these type of manufacturing geometric imperfections of the joints in the analysis of three-dimensional structures. Therefore, the study of three-dimensional structures including the semi-rigid behavior of manufactured imperfect jointing systems needs to be conducted to understand the effect that these initial imperfections have in the behavior and critical strength/capacity of such structures.

## 1.4 Scope of the Research

This research will characterize and compare the buckling behavior of three-dimensional structures considering the “as-designed” vs. “as-built” semi-rigid behavior of the fir-tree jointing system using Finite Element Analysis (FEA). The specific jointing system to be studied is the Geometrica® 6-Sierra Delta (6Sd-00). This jointing system was chosen because, according to the review of literature (**Chapter 2**), few research works have been conducted to characterize the buckling behavior of three-dimensional structures using the fir-tree jointing system as a model of study. Besides, the fir-tree jointing system imposes important advantages over other connections such as low cost of fabrication, efficient productivity during construction, and a wide variety of structural configurations can be achieved by using this jointing system. The main structural elements of the Geometrica® 6Sd-00 fir tree jointing system are described in the following list and shown in **Figure 1.7**:

- 1) An extruded aluminum connector with serrated keyway (fir-tree) slots;
- 2) Steel tubular elements with their ends pressed to form a coined edge that fits in the connector keyway slots; and
- 3) Aluminum filler shim elements used to fill the non-loaded fir-tree slots of the connector.

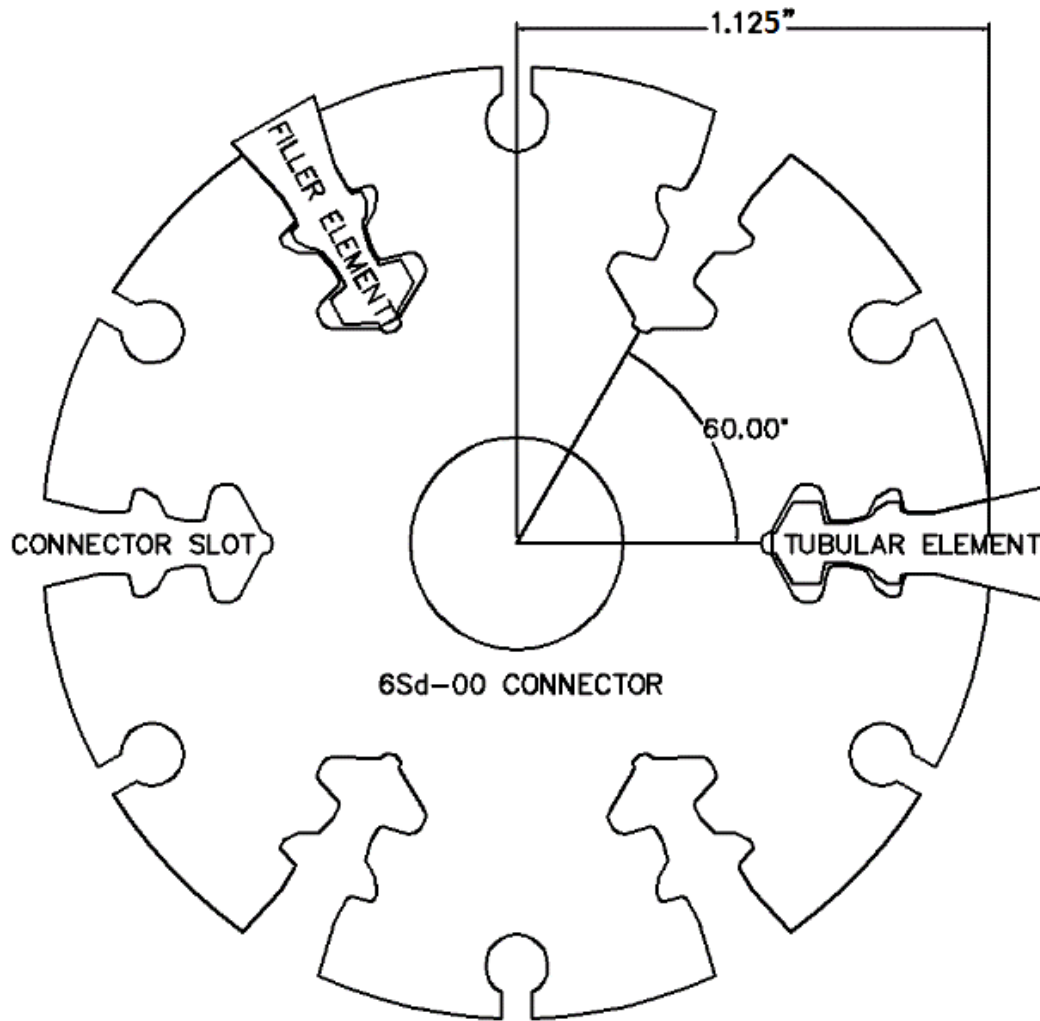


**Figure 1.7** Geometrica® 6-Sierra Delta (6Sd-00) Jointing System (After Garcia 2017)

The term as-designed condition of the jointing system means the idealized perfect condition of how the jointing system is designed and the contact engagement surfaces follow the intended paths of interaction. The as-built condition of the jointing system refers to the imperfect manufactured connection in which the location of contact engagement surfaces do not follow the as-designed path between the connector and beam elements. **Figure 1.8** shows the contacting surfaces of the Geometrica® 6Sd-00 fir tree jointing system.

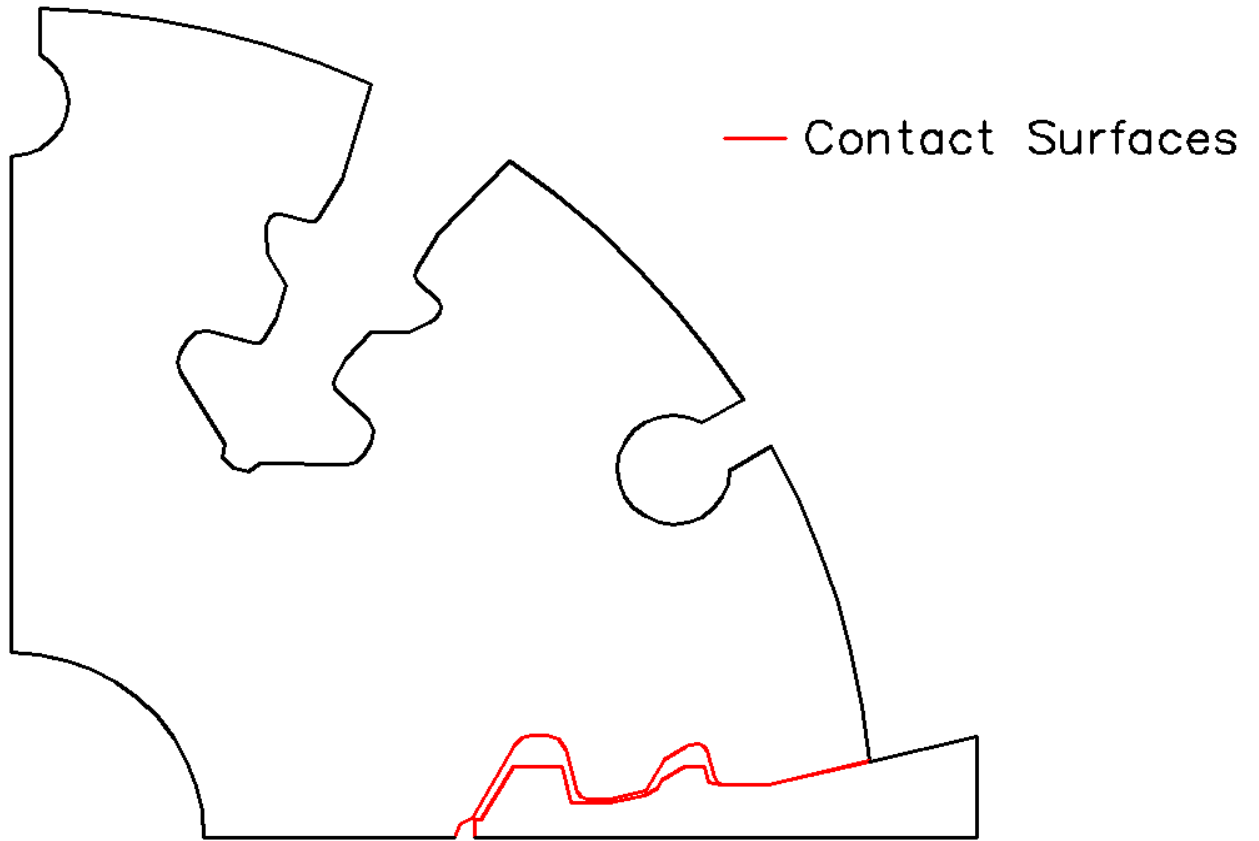


**Figure 1.8** Geometrica® 6Sd-00 Jointing System Contact Surfaces (After Garcia 2017)

Based on the review of literature (**Chapter 2**), the behavior of this type of jointing system is mainly characterized by its axial and in-plane bending stiffness. Thus, during the semi-rigid finite element simulations of three-dimensional structures, the axial tension-compression and in-plane bending stiffness behavior of the jointing system will be considered as shown in **Figure 1.9**.

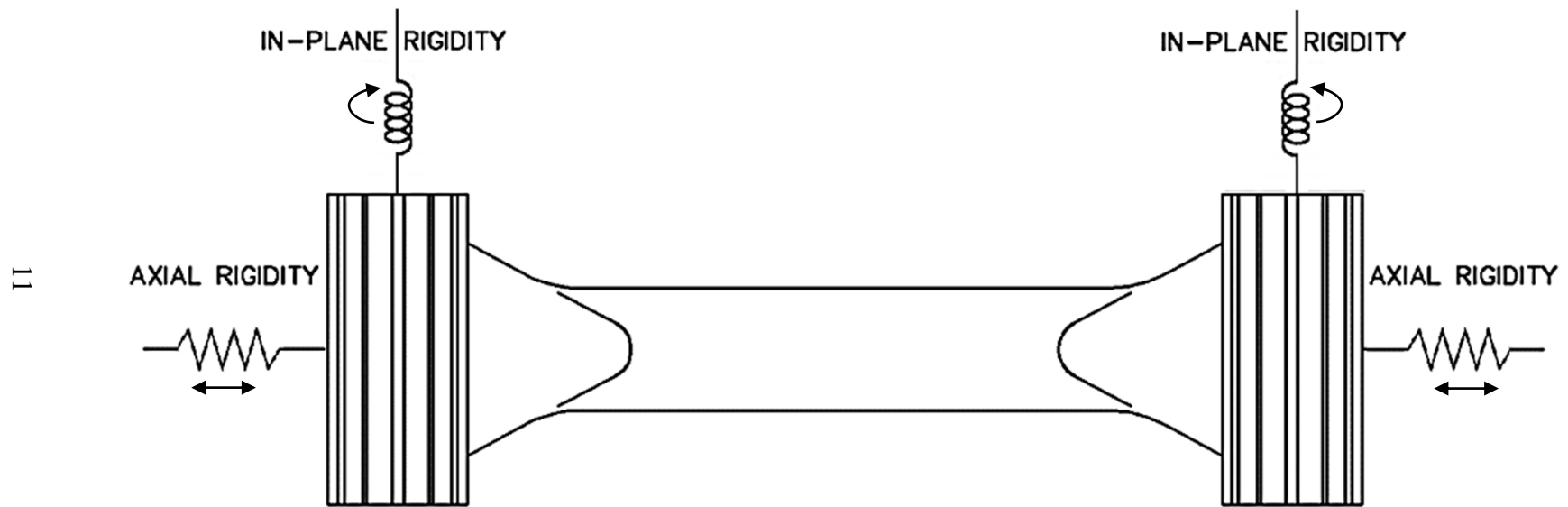


**Figure 1.9** Geometrica® 6Sd-00 Jointing System Axial and In-Plane Stiffness

Furthermore, laboratory tests will be conducted on small-scale models of three-dimensional structures, built using the Geometrica® 6Sd-00 fir-tree jointing system, to capture their actual buckling behavior. The laboratory buckling behavior results of the small-scale structures will enable the verification of results obtained from the Finite Element Models (FEM) of three-dimensional structures that use the semi-rigid behavior of the fir-tree jointing system.

## 1.5 Objectives

The main objective of this dissertation is to quantify how manufacturing geometric imperfections influence the buckling behavior of three-dimensional structures. To achieve this, the results of structures modeled using the as-designed jointing system behavior will be compared with the results of structures modeled using the as-built jointing system behavior. The objective of this research will be accomplished using the following procedure:

- 1) Conduct laboratory tests on small-scale (3.5-feet span) hexagonal shape structures to capture the actual buckling behavior of 3D structures built with the Geometrica® 6Sd-00 fir-tree jointing system. The geometry and size of the structures were chosen based on the dimensions and capability of the equipment available to conduct the laboratory tests. The structures will be tested and the load-deformation behavior of the crown connector of the structure will be collected for comparison purposes with the FEA results (**step 3**);
- 2) Develop two finite element models identical in geometry and loading conditions to the small-scale structures. One model will be developed using rigid joint connections and a second model will be developed including the semi-rigid behavior of the Geometrica® 6Sd-00 fir-tree jointing system. These models will be created to analytically: (1) assess how the rigidity of the Geometrica® 6Sd-00 fir-tree jointing system influences the buckling

behavior of 3D structures and (2) predict the actual buckling behavior of 3D structures built with these joints. The software used for modeling and simulation is Patran/Nastran (MSC 2014);

- 3) Asses the accuracy of results obtained by from the FEM of the small-scale structure that uses the semi-rigid behavior of the Geometrica® 6Sd-00 fir-tree jointing system. This will be accomplished by comparing the small-scale structure FEA results with the results obtained from the laboratory tests;
- 4) Once the accuracy of results obtained from the FEM of the 3D structure that uses the semi-rigid properties of the fir-tree jointing system have been verified, finite element models of a larger span three-dimensional structure will be developed using the same jointing system modeling technique. Two cases will be considered:
  - a. Structures with the as-designed behavior of the jointing system; and
  - b. Structures with the as-built behavior of the jointing system.
- 5) Subsequently, non-linear finite element analyses will be conducted on the previously mentioned 3D structure models to capture their buckling behavior. The buckling behavior of the as-designed vs. the as-built 3D structures will be compared to evaluate how the imperfections in the fir-tree jointing system affect the overall buckling stability of three-dimensional structures.

## **1.6 Significance of the Study to the Engineering Profession**

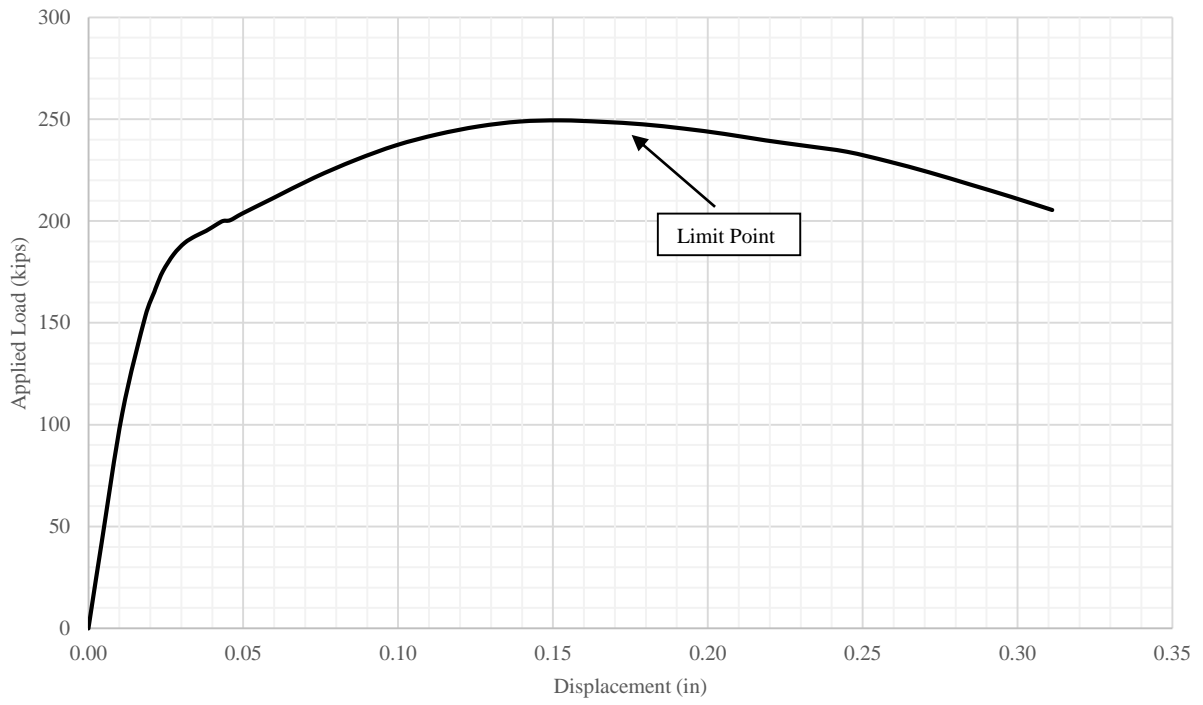
This research contributes to the structural engineering profession by providing a method to consider imperfectly manufactured jointing systems in the buckling analysis of three-dimensional structures. The results of the study will help to assess the effect that the non-linear behavior of the joints containing manufacturing geometric imperfections produce in the buckling behavior and capacity of three-dimensional structures. The results of this study will help structural engineers to more realistically analyze three-dimensional structures.

## Chapter 2: Literature Review

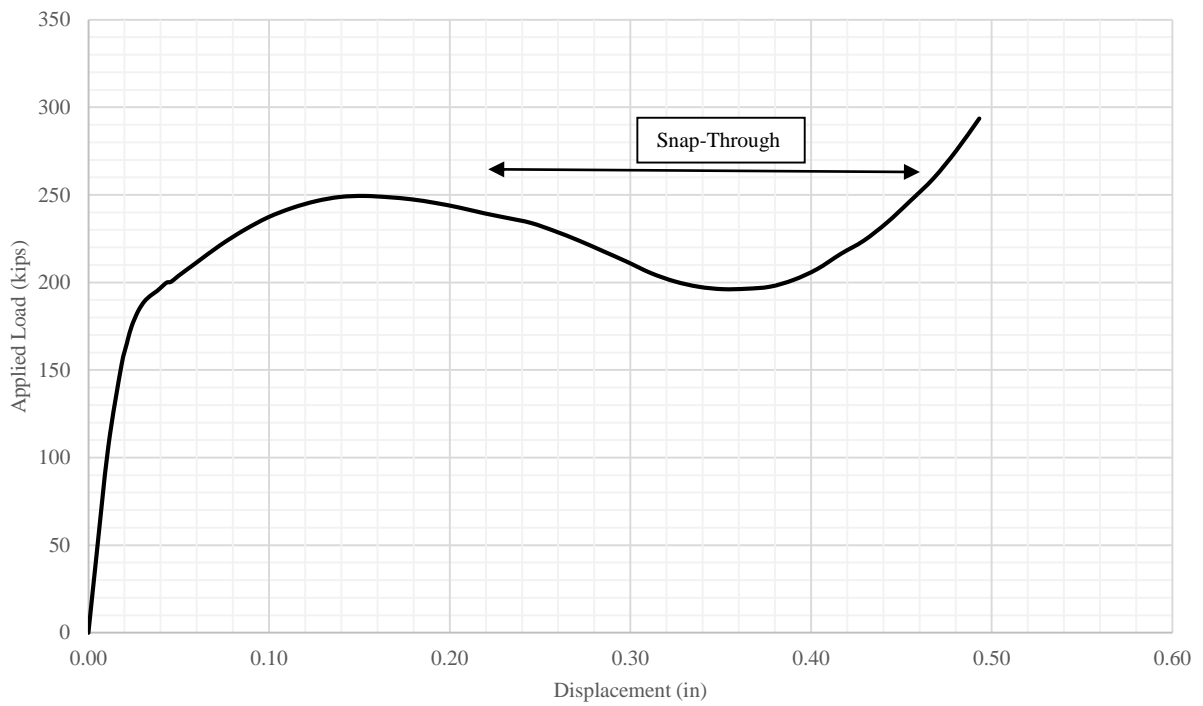
This chapter is a review of literature which describes structural stability and buckling modes of three-dimensional structures. Furthermore, this chapter reviews recent information, from research studies, regarding the determination of buckling behavior and capacity of three-dimensional structures using analytical and experimental approaches.

### 2.1 Structural Stability of Three-Dimensional Structures

The phenomenon of buckling can, in general, be explained as the state in which the load is progressively increased, until a limit point is reached, after which the structure will deform and the deflection will increase without any increase of the load (Ramaswamy et al. 2002). The force corresponding to this behavior is known as critical buckling load. Critical buckling load is an important factor in the design of three-dimensional structures because at this point the structures lose their stiffness (Kato et al. 2005). After the limit point is reached, the structure is forced to seek a new structural equilibrium state referred as “snap-through buckling” (Supple 1984). **Figure 2.1** displays the two manifestations of buckling: (a) limit point, and (b) snap-through.



a) limit point



b) Snap through

**Figure 2.1** Manifestations of Buckling

### 2.1.1 Buckling Loads of Three-Dimensional Structures

Kato et al. (2005) stated that buckling loads are classified based on the type of analysis being conducted on the three-dimensional structures. In a standard classification, buckling loads for these structures can be categorized as: (1) linear buckling load, elastic buckling load, and (3) elastic-plastic buckling load.

Linear buckling load of three-dimensional structures is defined as the critical load corresponding to the loss of stability considering only the effects of axial or in-plane stresses but neglecting any displacement or bending moment effects. In linear buckling analysis of three-dimensional structures, the direction of the applied forces does not change. Furthermore, the deflections, are assumed to be small and stresses of the elements are within the elastic region. Linear critical load is typically denoted in the literature as  $p_{cr}^{lin}$ .

Elastic buckling load is defined as the critical buckling load based on the elastic nonlinear path of the structure considering deflections and bending moments but neglecting the non-linear behavior (strain hardening and ultimate strength) of the material of the elements of the three-dimensional structure. Elastic critical buckling load of three-dimensional structures is denoted as  $p_{cr}^{el}$  (Kato et al. 2005).

Elastic-plastic or elasto-plastic buckling load is defined as the maximum point in the load-deformation equilibrium path/curve considering both the material nonlinear properties and the geometrical nonlinearity of the three-dimensional structure. Elasto-plastic buckling load can also be referred as ultimate strength or collapse load of the structure. Elastic-plastic critical buckling load for three-dimensional structures is denoted as  $p_{cr}^{el-pl}$ . A conceptual relationship between the three types of buckling loads is shown in **Figure 2.2**.

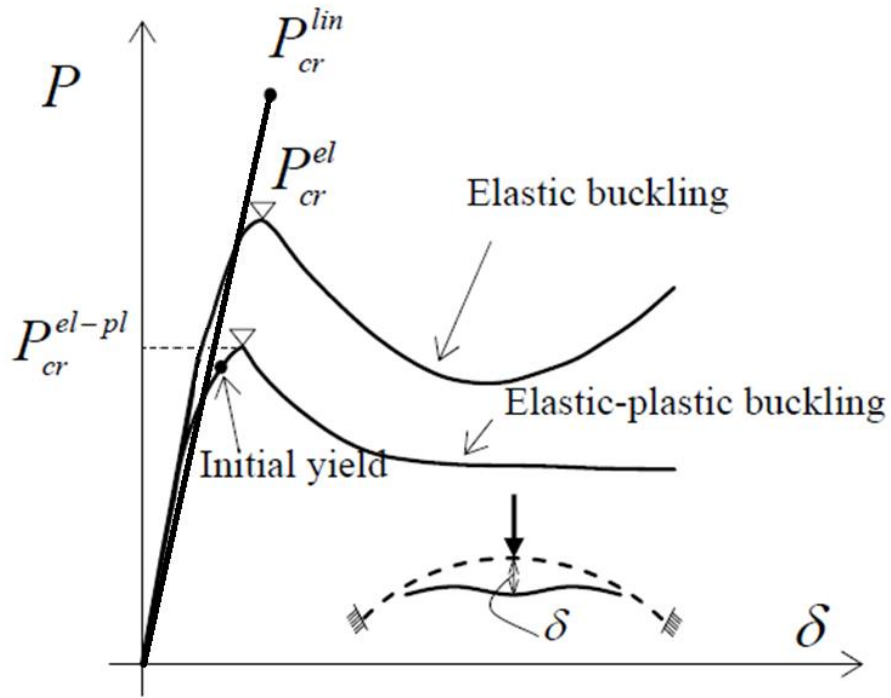


**Figure 2.2** Buckling Loads in Three-Dimensional Structures (Kato et al. 1998)

As observed in **Figure 2.2**, the buckling load and displacements in a linear analysis are greater than the buckling load and displacements in an elastic analysis. Accordingly, in an elastic analysis, the buckling load and displacements are greater than the buckling load and displacements obtained during an elasto-plastic analysis. According to Kato et al. (2005), the  $p_{cr}^{el-pl}$  of three-dimensional structures is lower than  $p_{cr}^{el}$  and  $p_{cr}^{lin}$  because three-dimensional structures look like continuum thin shells and may be sensitive to geometric non-linearities and imperfections which reduce their load bearing capacity.

### 2.1.2 Geometric Imperfections of Three-Dimensional Structures

Geometric imperfections exist in three-dimensional structures due to construction errors (Chen et al. 2016). To have a better understanding of research studies focusing on structural stability in three-dimensional structures, the reader needs to comprehend the different geometric

imperfections that may be present in the construction of three-dimensional structures. Geometric imperfections in three-dimensional structures studied in the past are: (1) node deviation and (2) member imperfections (curvature and length).

Node deviation, as shown in **Figure 2.3**, is a case of geometric imperfection in which one or more nodes (joints) are located in a different position in lieu of their designed location as a result of construction errors (Gidófalvy and Katula 2010).

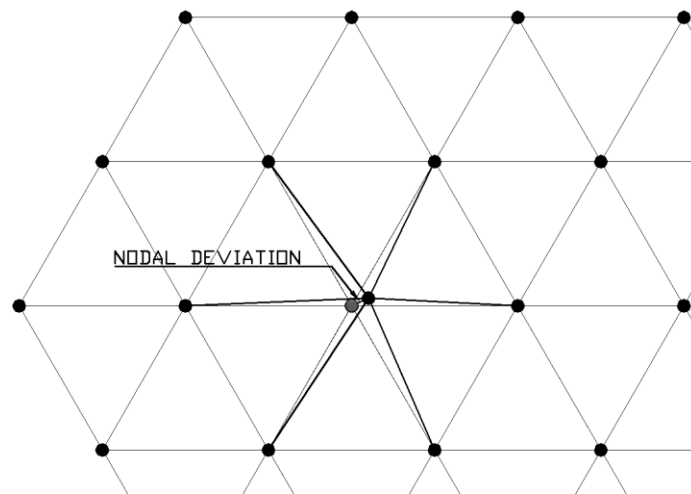


**Figure 2.3** Node Deviation Geometric Imperfection (After Garcia 2017)

Member curvature, is a case of geometric imperfection caused either by production, transportation, and/or installation processes which inevitably curve the shape of members in one way or another (Fan et al. 2012c). **Figure 2.4** shows the member curvature geometric imperfection.

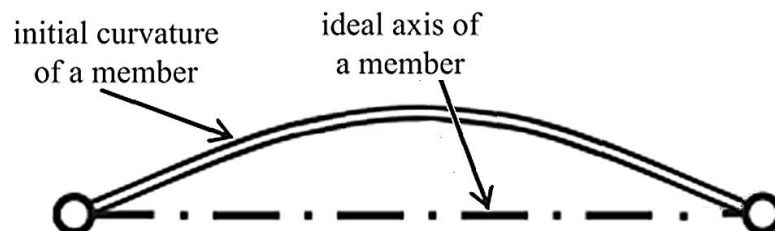


**Figure 2.4** Member Curvature Geometric Imperfection (After Garcia 2017)

Another common type of imperfection in three-dimensional structures is the variation in member length. According to Gidófalvy and Katula (2010), if a member has a shorter or a more elongated length as compared to perfect/designed length member, the structure is more prone to fail at a lower critical load.

The three geometric imperfections described in the previous paragraphs can decrease the buckling capacity and change the buckling mode (**Section 2.2**) of three-dimensional structures as described in the forthcoming sections of this review.

## **2.2 Buckling Modes of Three-Dimensional Structures**

To have a better understanding of current research studies focusing on structural stability in three-dimensional structures, it is important to understand the buckling modes associated to these types of structures. Three-dimensional structures follow four main different types of buckling categorized as: (1) local or joint buckling; (2) rotated node buckling; (3) general or overall buckling of the whole structure; and (4) member buckling (Kato et al. 2005).

### **2.2.1 Local or Nodal Buckling**

Nodal buckling, as shown in **Figure 2.5**, is a case of snap-through (defined in **Section 2.1**) buckling in which only one node snaps with minor displacement of neighborhood nodes/members and it is characterized by strong geometrical nonlinearity (Lan 2005). If the joint system is not completely rigid, three-dimensional structures are very prone to fail by local buckling at a lower critical load as compared to structures with rigid connections (Shibata et al. 1993). Furthermore, nodal buckling hardly occurs in structures under distributed loads. This type of buckling is encountered in three-dimensional structures under a concentrated load (Fitch 1968).

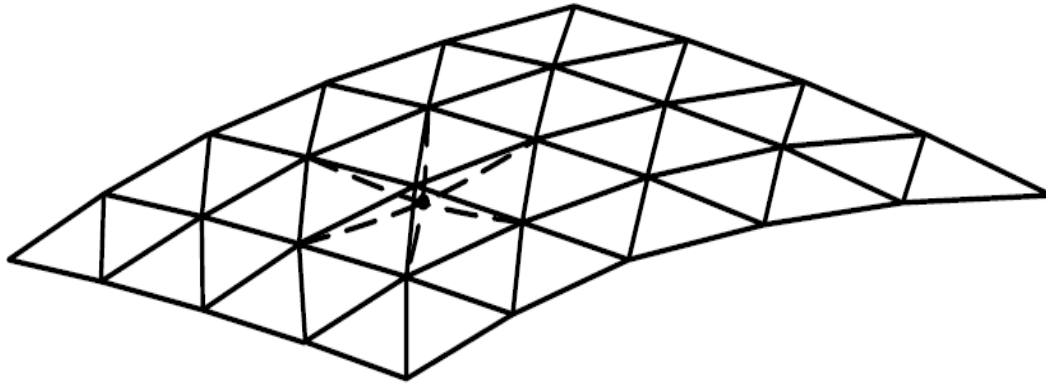


**Figure 2.5** Local or Nodal Buckling (Kato et al. 2005)

### 2.2.2 Rotated Node Buckling

Rotated node buckling is a failure mode in which a node connecting several beam members rotates about the direction normal to the surface of the three-dimensional structure (Kato et al. 2005). According to the research experiments performed by Fülöp and Iványi (2004) on trusses under concentrically and eccentrically loads, this type of buckling is expected to occur in concentric loaded nodes. The results of the study showed that during the collapse/failure of a joint, the node may rotate up to  $6.5^\circ$ . **Figure 2.6** shows rotated node buckling.

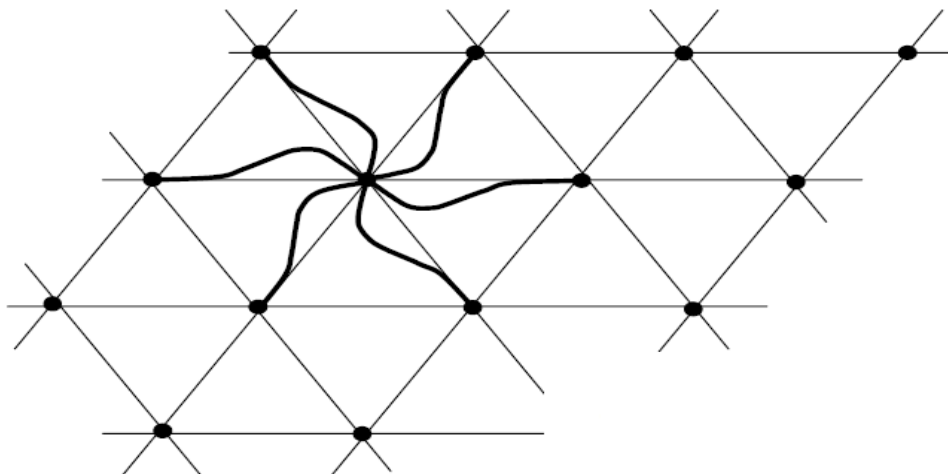


**Figure 2.6** Rotated Node Buckling (Kato et al. 2005)

### 2.2.3 General or Overall Buckling

General or overall buckling, also known as shell-like buckling, occurs when a relatively large area of a three-dimensional structure becomes unstable and many nodes are involved in the failure. This type of failure mode is initiated by local buckling (Lan 2005). During this failure mode, the nodal deformations are developed over a significant region of the three-dimensional structure surface, that at a critical buckling state, leads to a sudden and violent collapse of the structure (Kashani and Croll 1994). **Figure 2.7** shows general or overall buckling in a three-dimensional structure.

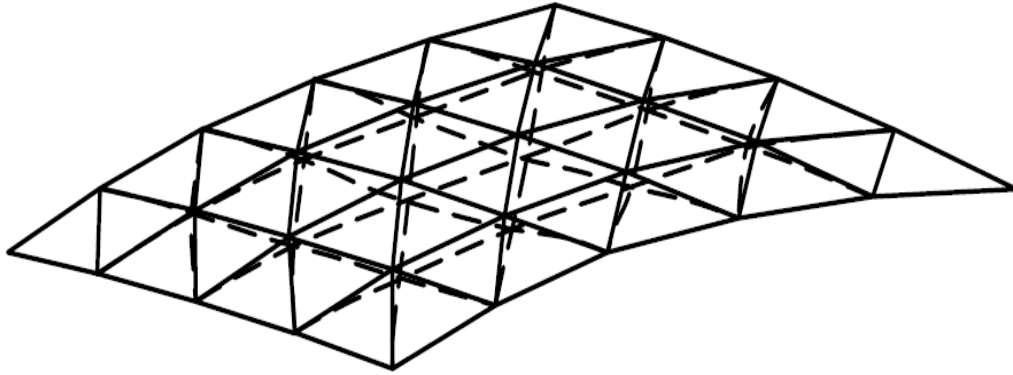
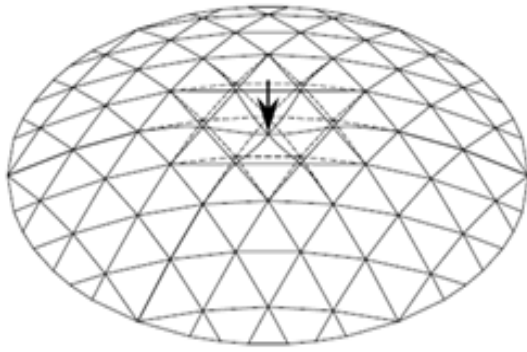
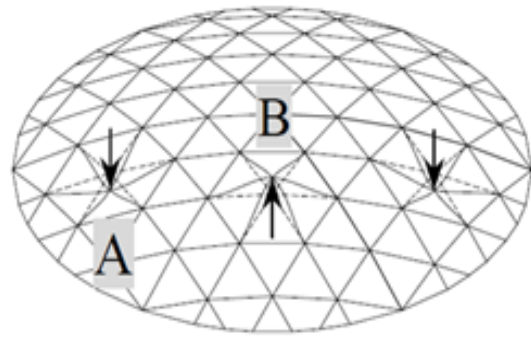


**Figure 2.7** General or Overall Buckling (Kato et al. 2005)

Furthermore, overall buckling can be divided in two categories: (a) symmetric buckling and (b) and anti-symmetric buckling. Symmetric buckling can also be named dimple buckling (nodal buckling of several adjacent nodes), explicitly shown in **Figure 2.8a**. In the case of anti-symmetric bifurcation buckling, some parts of the structure will deform in a certain deformation pattern, but another part will deform in an opposite direction to the former. **Figure 2.8b** shows bifurcation anti-symmetric buckling in a three-dimensional structure (Kato et al. 2005).



a) Symmetric Buckling



b) Anti-Symmetric Buckling

**Figure 2.8** Symmetric and Anti-symmetric Buckling in 3D Structures (Kato et al. 2005)

In addition, Kato et al. (2005) described another common type of overall buckling named band shape buckling. This term of buckling is referred to the excessive deformation of the three-dimensional structure near a boundary, as depicted in **Figure 2.9**. In this deformation mode, several nodes close to the boundaries deform largely leading to a dimple (symmetric) buckling.

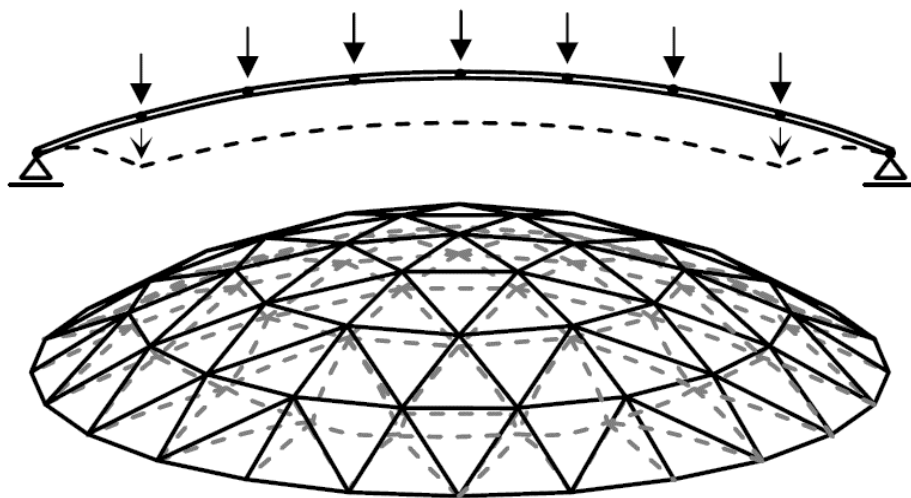


**Figure 2.9** Band Shape Buckling (Kato et al. 2005)

#### 2.2.4 Member Buckling

Member buckling occurs when an individual member within a three-dimensional structure becomes unstable despite the fact that the rest of the structure, including nodes and members, remain unaffected (Lan 2005). When a three-dimensional structure is subjected to vertical loads, the main internal forces of the members are axial forces and bending moments. The magnitude and direction of these forces and moments depend on the stiffness of the members and connections. Thus, if the ratio of bending stresses to axial stresses in the members of the three-dimensional structure increases, the member buckling load decreases (Fan et al. 2012). **Figure 2.10** shows member buckling in a three-dimensional structure.

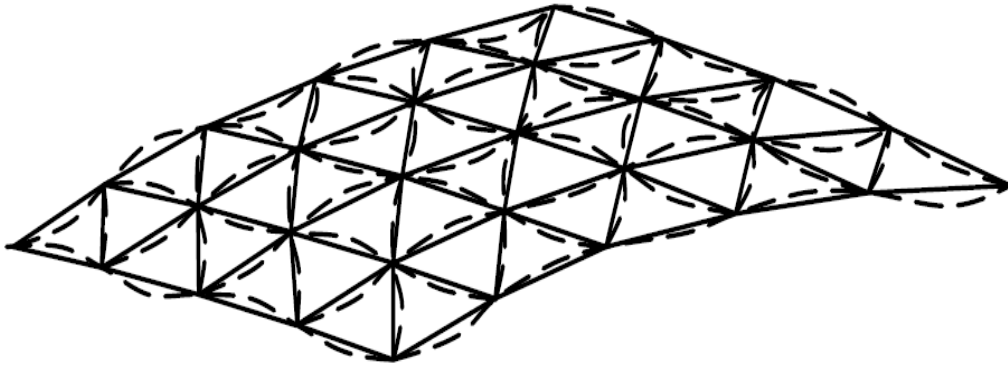


**Figure 2.10** Member Buckling (Kato et al. 2005)

Kato et al. (2005) explained that although there may be a clear distinction among the previously described buckling patterns, the actual behavior of the structure may include one or several buckling patterns combined at the time of failure. Since three-dimensional structures are composed of beam-columns elements and look like continuum shells, there exists a possibility, for instance, that shell-like buckling and member buckling may occur at the same time. For this

reason, in the past, the structural analysis of three-dimensional structures was performed by using their continuum equivalent.

### 2.3 Classical Buckling Theories Based on Continuum Shell Analysis

The theoretical analysis of buckling behavior of three-dimensional structures may be approached by the continuum analogy analysis since almost all structures are constructed from nearly identical units arranged in a regular pattern. In the past, it was generally accepted that the analysis on the basis of the equivalent continuum served as an important tool in the research of the buckling behavior of three-dimensional structures (Lan 2005).

Wright (1965) proposed a method to predict the buckling loads for single layer three-dimensional structures. This method provided an accurate determination of thickness, elastic moduli, and Poisson's ratio for an imaginary continuum that has the same extension, flexural, shearing, and twisting resistance under external loadings as the original three-dimensional structure. He studied a special case of framework having an equilateral triangular pattern with identical bar sizes, leading to an isotropic continuum.

The solution is as follows:

Equivalent Elastic Modulus

$$E' = \frac{AE}{3r_g l} \quad (2.1)$$

Equivalent Thickness

$$t' = 2\sqrt{3r_g} \quad (2.2)$$

Equivalent Poisson's Ratio

$$v' = \frac{1}{3}v \quad (2.3)$$

where  $A$  is the member cross-sectional area,  $E$  is the modulus of elasticity,  $r_g$  is the radius of gyration of the member, and  $l$  is the node spacing or member length, respectively.

Member critical buckling pressure is calculated as follows:

$$q_{cr} = \frac{2\sqrt{3}\pi^2 EI}{al^3} \quad (2.4)$$

where  $q_{cr}$  is a uniform radial critical pressure on a spherical shell of radius  $a$ , and  $I$  is the moment of inertia of the beam element, respectively.

Nodal buckling is calculated as an equivalent distributed load applied to the node, and having a range of critical pressure of:

$$\frac{AEI}{12a^3} \leq q_{cr} \leq \frac{AEI}{6a^3} \quad (2.5)$$

Overall buckling critical pressure is obtained as follows:

$$q_{cr} = 0.4 \frac{E't'^2}{a^2} \quad (2.6)$$

As mentioned earlier, in the past, the structural stability analysis of three-dimensional structures was performed by substituting the structures by their continuum equivalent. Nevertheless, modern computer software has allowed to accurately predict the elasto-plastic buckling behavior and load capacity of three-dimensional structures. Yet, the results of computerized analyses of three-dimensional structures are only as accurate as the assumptions under which they are modeled. **Section 2.4** presents a review of research studies dedicated to

developing models and determine the buckling behavior of three-dimensional structures, using finite element analysis software programs, considering different jointing system rigidities.

## **2.4 FEA of Three-Dimensional Structures with Different Jointing System Rigidities**

Several idealizations, in numerical analyses, assume the structures to have rigid connections. However, the behavior of semi-rigid connections should be considered in the model to obtain more realistic and reliable results (Kartal et al. 2010). The subsequent sections review research studies, regarding the evaluation of the buckling behavior of three-dimensional structures, under the assumption of rigidly jointed connections and, later, under semi-rigid jointed connections. For both assumptions, studies with and without the introduction of geometric imperfections (described in **Section 2.1.2**) are included in the review.

### **2.4.1 Buckling of Rigidly Jointed Three-Dimensional Structures**

A description of studies performed, using FEA software programs, to predict the buckling behavior of three-dimensional structures under the assumption of rigidly jointed connections is presented in this section.

Ogawa and Kuwada (1998) predicted the elasto-plastic buckling mode of rigidly jointed single-layer three-dimensional domes loaded under uniform forces using non-linear FEA. This was conducted first without any geometrical imperfections and next introducing geometrical initial imperfections to the structure. The geometrical initial imperfections considered in the model were node deviations. The results of the study showed that three-dimensional domes without node deviations collapse by general buckling while domes with node deviation collapse by nodal buckling.

Zamanzadeh et al. (2010) conducted a study to investigate the elastic buckling behavior of single layer three-dimensional domes. In the study, the types of buckling of concern were the general buckling, nodal buckling and buckling of a member. To obtain a geometric characteristic of three-dimensional domes, the slenderness factor  $S$ , which represents the openness and slenderness of the dome structure, is calculated as follows:

(2.7)

$$S = \frac{l}{\sqrt{r_g a}}$$

where,  $a$  is the dome radius,  $l$  is the typical member length, and  $r_g$  is the radius of gyration of the member, respectively. The results showed that general buckling is observed for structures with a slenderness factor  $S < 2.5$ . As the slenderness factor  $S$  increases, the dimple buckling (nodal buckling of several adjacent nodes) is observed and, finally, the buckling of a member is recognized.

Fan et al. (2010a) investigated the elasto-plastic stability behavior of rigidly jointed single-layer three-dimensional domes using a non-linear finite element analysis software. During the research, more than 2000 models and non-linear analyses were conducted in three-dimensional structures considering geometric imperfections. The initial geometrical imperfections considered in the study were the deviation of the nodes location from their as designed location. Magnitude lengths of node deviations of  $r = 0$ ,  $r = L/1000$ ,  $r = L/500$ ,  $r = L/300$  ( $r$  is the magnitude length of geometrical imperfections and  $L$  the span of the dome) were considered in the models. Based on the large amount of conducted analyses, with pressure loads applied on the domes, it was possible to have a panoramic view of the elasto-plastic behavior of three-dimensional structures with node deviation imperfections. The results showed that with higher node deviations, the domes are more

prone to fail due to a snap-trough buckling (nodal buckling with minor displacement of neighborhood nodes). Furthermore, it was also determined that in three-dimensional domes with rigidly jointed connections, the support conditions in the perimeter of the dome pose virtually no effect on the elasto-plastic buckling load.

Gidófalvy and Katula (2010) described the buckling behavior of shallow three-dimensional structures with rigid nodal connections giving special attention to geometric imperfections. Geometrical imperfections considered in the research were beam curvature and node deviation. For the member curvature imperfection, researchers concluded that, if a member has an initial defectiveness with a curvature in sinusoidal shape, the structure is more prone to fail as compared to a member with a shorter or a more elongated length as compared to perfect member. Furthermore, researchers concluded that node deviation may be very dangerous because of the possibility of snap-through buckling.

Fan et al. (2012b) studied how the curvature of members affects the elasto-plastic stability of three-dimensional domes. In the study, the researchers simulated imperfect members with initial curvature and used a finite element analysis software to calculate the elasto-plastic buckling load of three-dimensional domes assuming rigidly jointed connections. According to the authors, initial curvature of members can decrease the elasto-plastic buckling load of three-dimensional domes by 12.80% as compared to the ideal perfect structure. Furthermore, initial curvature of members modeled along with initial deviation of node locations can reduce the elasto-plastic buckling load of domes by 9.44% as compared to a structure considering only member curvature as initial imperfection.

The semi-rigidity of jointing systems and their effect on the buckling behavior and capacity of three-dimensional structures has been reviewed in the past. **Section 2.4.2** presents a review of

research studies regarding the evaluation of the buckling behavior of three-dimensional structures including the semi-rigid behavior of different jointing systems.

#### 2.4.2 Buckling of Semi-Rigid Jointed Three-Dimensional Structures

A description of studies performed, using FEA software, to model and predict the buckling behavior of three-dimensional structures considering the semi-rigidity behavior of the connections were reviewed. A description of the methods and/or modeling techniques and types of analyses performed in the past are reported in this section.

Amiri and Davodi (2002) proposed a method, using a finite element software, to include the semi-rigid behavior of the MERO jointing system in the buckling analysis of three-dimensional structures. According to the authors, a beam element together with non-linear spring elements at both ends of the beam element can be used to represent the behavior of tubular member and connections, respectively, as shown in **Figure 2.11**

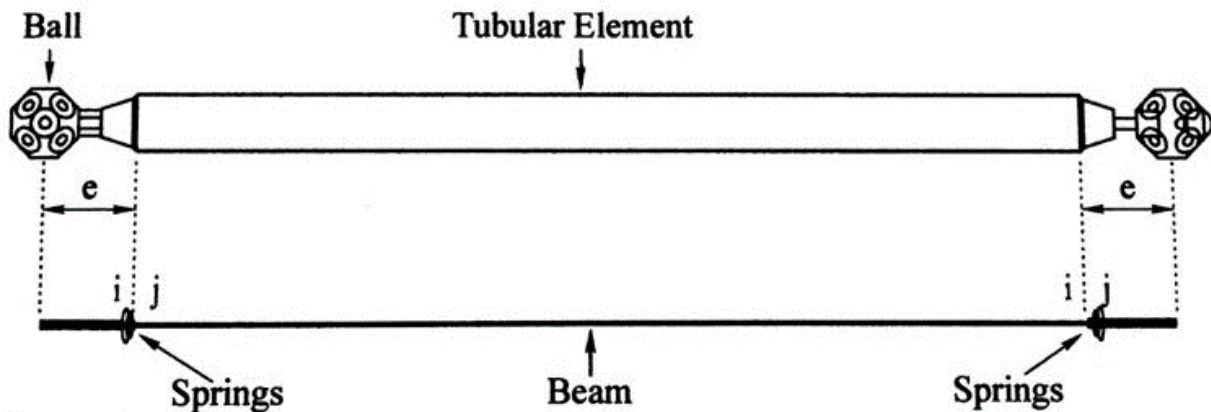


**Figure 2.11** Members and End Connections Modeled by Amiri and Davodi (2002)

In the analysis, the buckling capacity of single layer three-dimensional structures was obtained. The analyses of the domes were carried out assuming: (1) the semi-rigid behavior of the

jointing system; and assuming (2) completely rigid connections. The results of the analyses showed that including the stiffness of the MERO jointing system can decrease the buckling capacity of three-dimensional structures about 40% when compared to structures with completely rigid connections.

López et al. (2007a; 2007c) proposed a joint-beam element to represent the ORTZ jointing system (**Figure 2.12**) in the buckling analysis of three-dimensional structures using common finite element analysis components.



**Figure 2.12** ORTZ Jointing System (López et al. 2007a)

The proposed element, shown in **Figure 2.13**, is modeled as follows: The ball is modeled as an infinite rigidity beam element. The tube is assumed to be elastic with the same cross-sectional area and moment of inertia as the real tube. The bolt is represented with a cylinder element between the beam and the balls with the same area and moment of inertia as the real bolt.

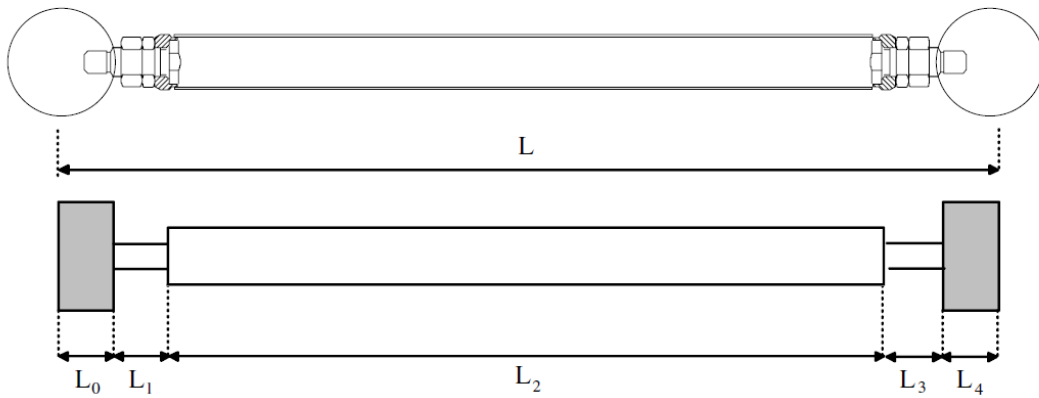


**Figure 2.13** Members and Connections Modeled by López et al. (2007a; 2007c)

In the analysis, the load-deflection behavior of a seven-meter diameter three-dimensional dome was obtained using a finite element analysis software. The analyses of the dome were carried out assuming rigid joints and including the proposed beam element. The results showed that including the semi-rigid behavior of the ORTZ connections can decrease the buckling capacity of three-dimensional structures approximately 10% when compared to structures with completely rigid connections.

Fan et al. (2010b) conducted finite element analyses to obtain the mechanical properties of the bolt-ball jointing system shown in **Figure 2.14**.



**Figure 2.14** Bolt-Ball Jointing System (Fan et al. 2012a)

In addition, the elasto-plastic buckling capacity of single layer three-dimensional domes was obtained using a finite element analysis software. The analyses of the domes were conducted including bending stiffness of the jointing system and assuming a completely rigid connection. The bending stiffness of the jointing systems was included in the analyses by means of non-linear spring elements at the end of each beam element as shown in **Figure 2.15**.

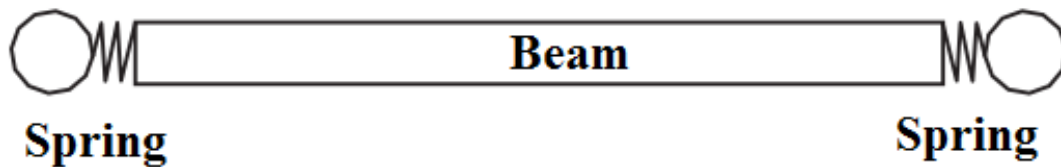


**Figure 2.15** Finite Element Model Developed by Fan et al. (After 2010b)

The results of the analyses indicated that including the bending stiffness of the bolt-ball jointing system can decrease the buckling capacity of three-dimensional structures up to 40% when compared to structures with completely rigid connections.

Hwang et al.(2009) conducted a study to determine how different size bolt holes/clearances of four different bolted connections, used in three-dimensional structures (**Figure 2.16**), influence the buckling capacity of the structures.

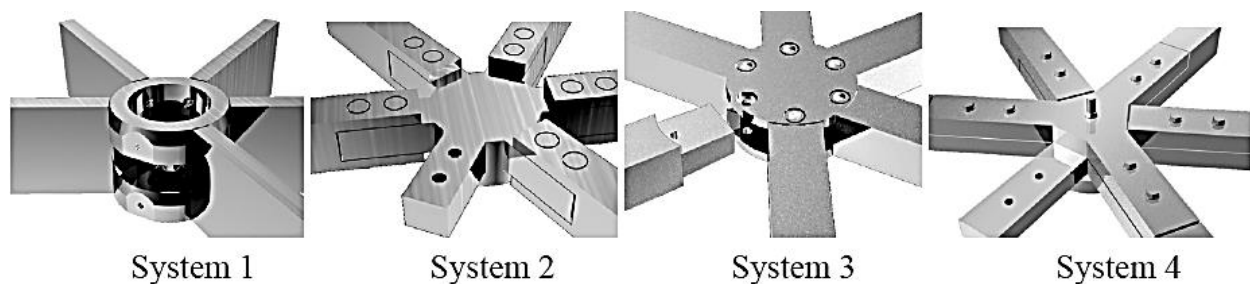


**Figure 2.16** Bolted Connections (Hwang et al.2009)

First, finite element analyses were carried out to obtain the bending and axial semi-rigid behavior of the connections of each system modeled with different bolt size clearances. **Figure 2.17** and **2.18** show the moment-rotation and load-displacement curves for the different types of jointing systems analyzed in the study, respectively. It can be observed, from the figures, that the designed bolt clearance of the connection influences the stiffness and load capacity of the same type of jointing system.

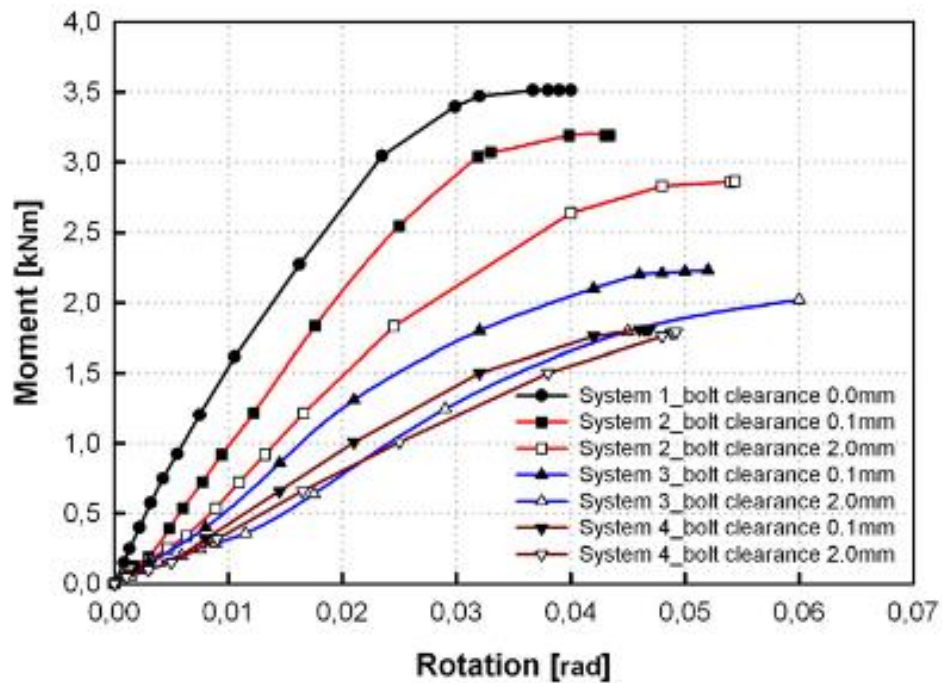


**Figure 2.17** Moment-Rotation Curves of Jointing System (Hwang et al.2009)

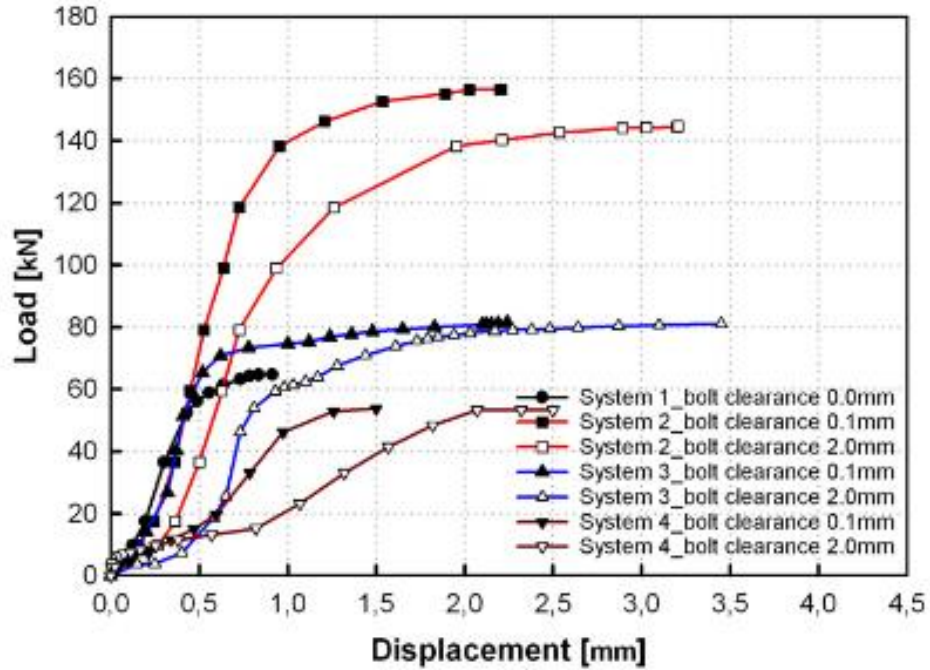


**Figure 2.18** Load- Displacement of Axial Loading Tests (Hwang et al.2009)

Next, numerical simulations were conducted to estimate the elasto-plastic buckling capacity of three-dimensional domes considering the semi-rigidity of the jointing systems. The semi-rigid behavior of the jointing systems was included in the analyses by means of non-linear spring elements at the end of each beam element to represent the behavior of tubular member and connections, respectively as shown in **Figure 2.19**.

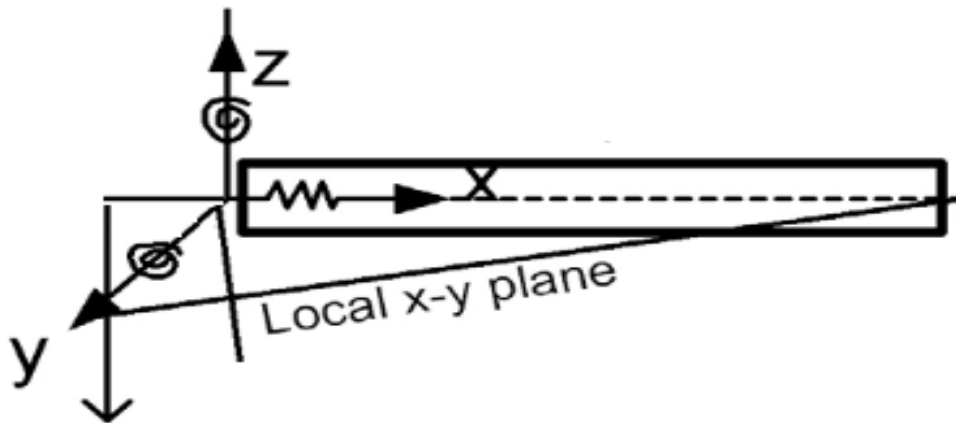


**Figure 2.19** Finite Element Model Developed by Hwang et al.(2009)

The results of the analyses proved that jointing systems with larger bolt clearances exhibit a decrease in load capacities. Furthermore, structures analyzed with larger bolt clearances experienced a decrease in the buckling capacity up to 13%.

Fan et al. (2011) proposed a classification system of the socket jointing system utilized in three-dimensional structures (**Figure 2.20**).



**Figure 2.20** Socket Jointing System (Fan et al. 2012a)

Following this classification system, the joints can be distinguished to exhibit a rigid, semi-rigid or pinned behavior. First, it is necessary to obtain the mechanical characteristics of the jointing system including bending stiffness ( $k$ ) and moment capacity ( $M_j$ ) through numerical simulations or by experimental studies (see **Figure 2.21**).

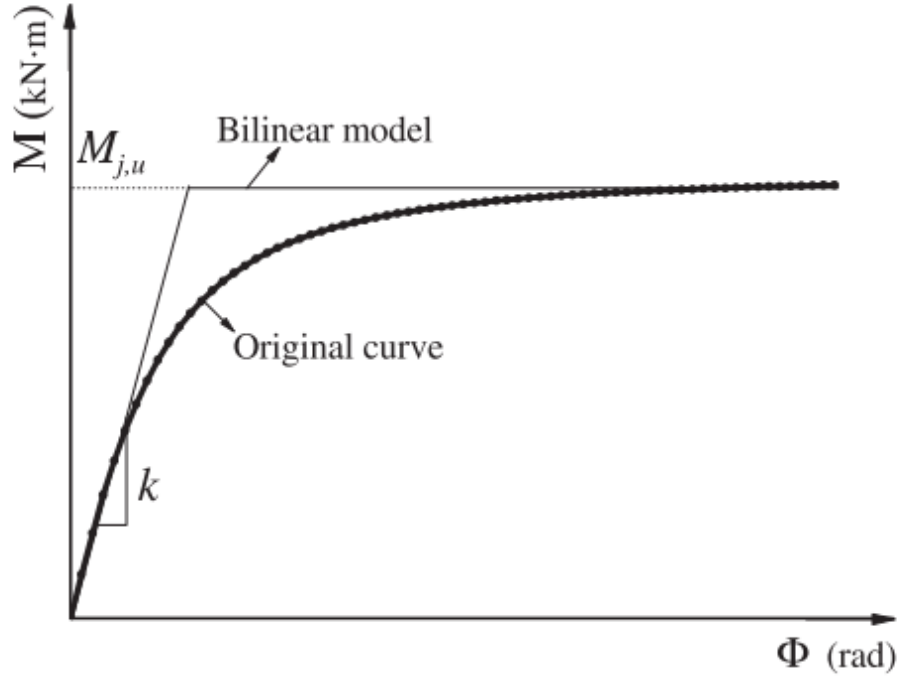


**Figure 2.21** Simplification of the Bending-Rotation Curves by Fan et al. (2011)

Next, the stiffness coefficient ( $\alpha$ ) needs to be defined as follows:

$$\alpha = \frac{k}{\frac{EI}{l}} \quad (2.8)$$

where  $E$ ,  $I$ , and  $l$  represent the modulus of elasticity, moment of inertia and length of the beam element, respectively.

In addition, the moment capacity coefficient ( $\beta$ ) needs to be defined as follows:

$$\beta = \frac{M_j}{M_e} \quad (2.9)$$

where  $M_e$  is the plastic moment capacity of the beam element connected to the joint.

At the end, the jointing system can be classified to behave as rigid, semi-rigid, or pinned connection using **Table 2.1**.

**Table 2.1** Joint Classification Based on  $\alpha$  and  $\beta$  (After Fan et al. 2011)

| Categories | Determination coefficients $\alpha$ and $\beta$ |
|------------|---|
| Rigid      | $\alpha \geq 5$ and $\beta \geq 0.5$            |
| Semi-rigid | $5 > \alpha > 0.5$ and $0.01 < \beta < 0.5$     |
| Pin        | $\alpha \leq 0.5$ and $\beta \leq 0.01$         |

Ma et al. (2013b) obtained the bending stiffness of socket joints (**Figure 2.20**) through laboratory experiments and included the results of the semi-rigid behavior of the joints in the finite element analysis of single layer three-dimensional structures. The semi-rigid behavior of the socket jointing system was included in the analyses by means of non-linear spring elements at the end of each beam element to characterize the behavior of tubular member and connections, respectively as shown in **Figure 2.22**.

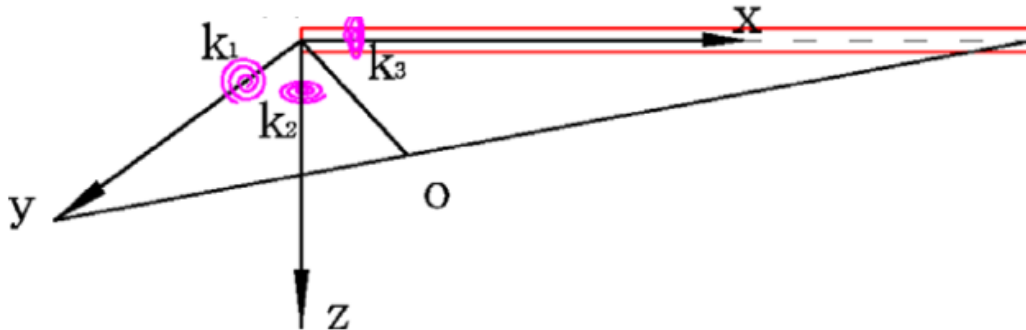


**Figure 2.22** Finite Element Model Developed by Ma et al. (2013b)

Finite element simulations of single layer three-dimensional structures were carried out including in the analysis the semi-rigid behavior of the jointing system and assuming completely rigid connections. According to the results, including the semi-rigid behavior of the socket jointing system in the buckling analysis of three-dimensional structures can decrease the elasto-plastic

buckling capacity of the structures up to 50% when compared to structures modeled assuming completely rigid connections.

Han et al. (2016) analyzed the influence of the semi-rigid behavior of the welded hollow spherical joints (**Figure 2.23**) on the stability of single layer three-dimensional structures.

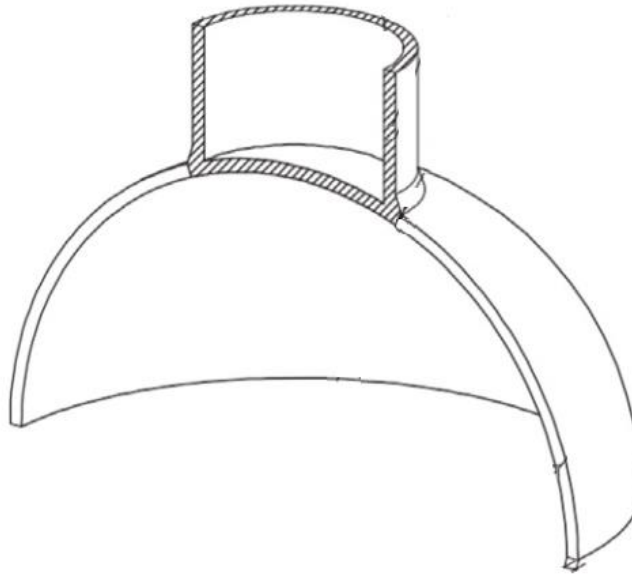


**Figure 2.23** Welded Hollow Spherical Joint (After Han et al. 2016)

Finite element analyses were carried out including the semi-rigid properties of the hollow spherical joints and assuming rigid connections. The results showed that the buckling capacity is reduced approximately 5% using semi-rigid connections compared with the structures with ideal rigid joints.

The utilization of finite element software programs, to model and estimate the buckling capacity of three-dimensional structures is nowadays commonly used by researchers and designers. Verification of such models require experimental testing under representative conditions similar to the finite element model simulations. **Section 2.5** presents different experimental studies to characterize the stability behavior of three-dimensional structures.

## 2.5 Experimental Studies to Characterize Buckling Stability of 3D Structures

The scope of this section is to report the types/methodologies of experimental studies, performed in the past, to characterize the load carrying capacity of three-dimensional structures.

Wright (1969) built a model of a dome with a base diameter (span) of 259 inches in order to determine the buckling capacity of three-dimensional structures connected by means of the fir-tree jointing system. The beam sections chosen were aluminum tubes of wall thickness of 0.022 inches with diameters of 3/8 inches, 7/16 inches and/or 1/2 inches in different regions of the structure. **Figure 2.24** shows the three-dimensional model developed by Wright (1969).

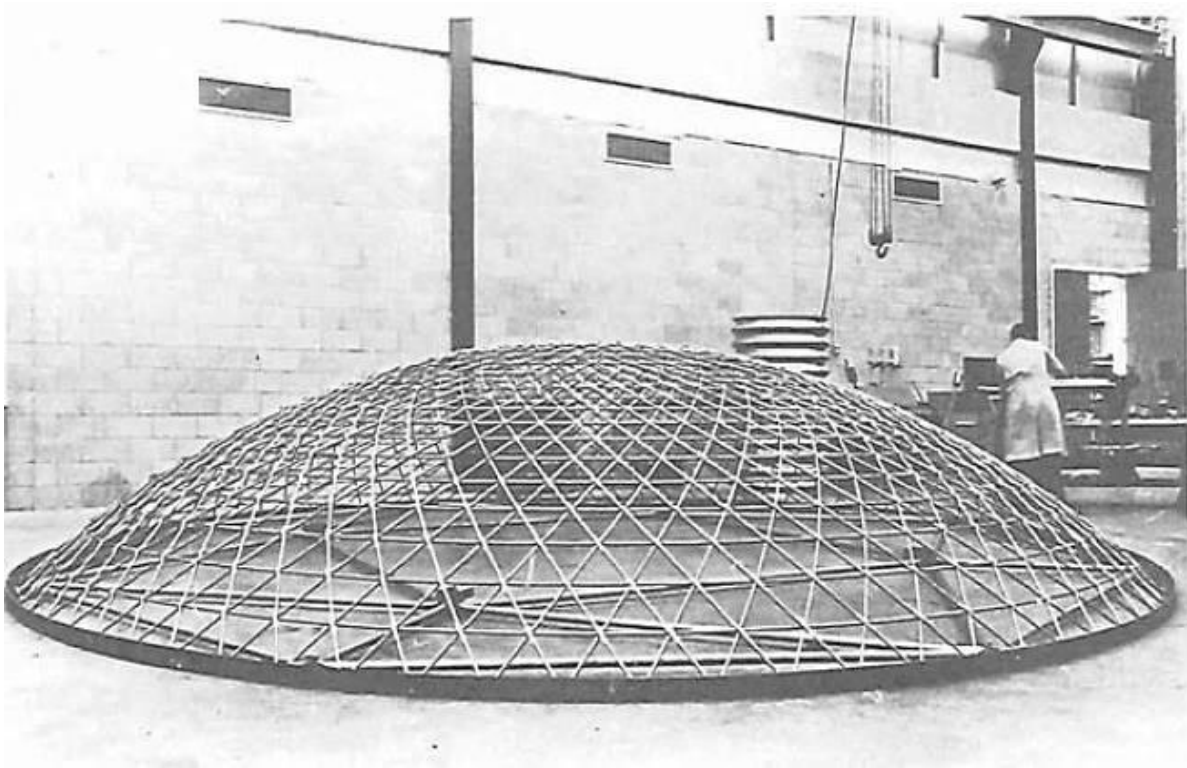


**Figure 2.24.** Model of Aluminum Space Frame Dome Developed by Wright (1969)

The structural model was loaded by evacuating a plastic bag that had been placed over the dome and sealed to the floor. According to the results of the experiments, at a pressure of 0.639 psi there was a sudden loss of stability with the structure imploding (collapsing in an inward direction) as shown in **Figure 2.25**.

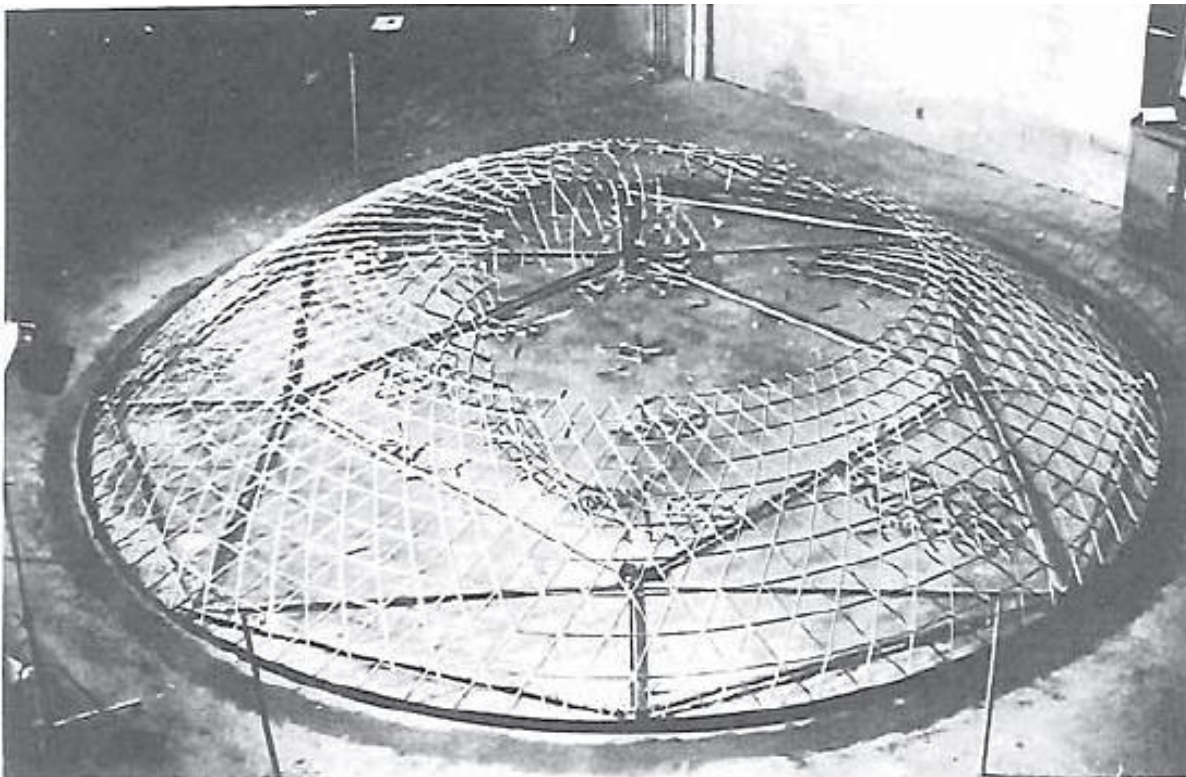


**Figure 2.25** Implosion Stability Failure of Space Frame Dome (Wright 1969)

Subsequently a second model of the same base diameter was built using slightly heavier members (7/16 inches diameter by 0.065 inches wall thickness). By following the same testing procedure as the first test, this dome was able to withstand a pressure load of 0.960 psi, and instead of implosion failure, the structure became dimpled (deformation of a large area of the structure), as shown in **Figure 2.26**.

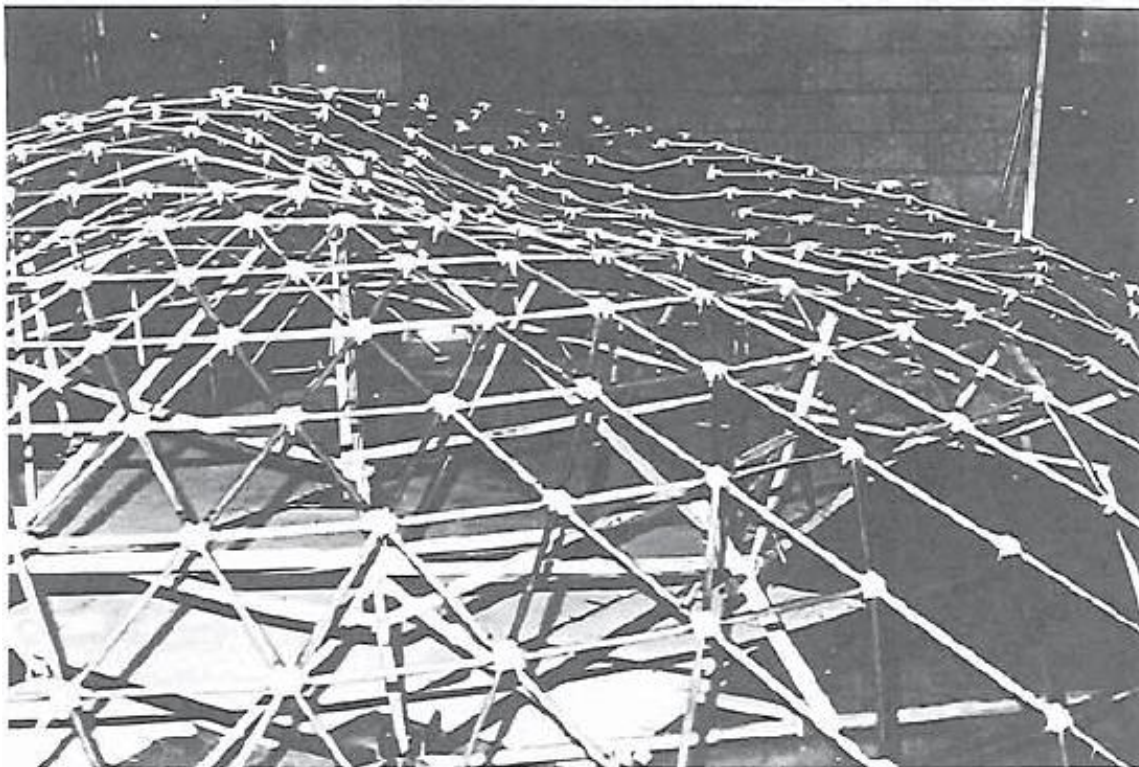


**Figure 2.26** Dimpled Stability Failure of Space Frame Dome (Wright 1969)

Wright (1969) described that an attempt was made to determine the influence of asymmetric loads on three-dimensional structures by placing a mixture of sand and gravel with enough water to induce buckling on one half of the structure alone. However, the test was not completed as it was impossible to accumulate enough material on the structure without it sliding off. The results of this experimental study confirmed that the type of connectors and members used in three-dimensional structures have an impact on the buckling load capacity of the latter.

Shibata et al. (1993) described an experimental research conducted to estimate the effect of the MERO jointing system semi-rigid properties on the ultimate strength of single layer three-dimensional structures. A total of eight structures were tested considering different length of members ( $l$ ), subtended half angle of the structure ( $\theta_0$ ), slenderness ratio of each members ( $\lambda_0$ ) and different jointing systems dimensions and/or semi-rigid behaviors. During the investigation,

the structures were loaded by controlling the displacement at the central crown node. As illustrated in **Figure 2.27**, the tested structures had seven joints and twelve members; the node number 4 located at the crown of the dome was free to move while nodes 3 and 5 were roller supported in the X direction. Finally, nodes 1, 2, 6, and 7 were roller supported in both the X and Y directions.

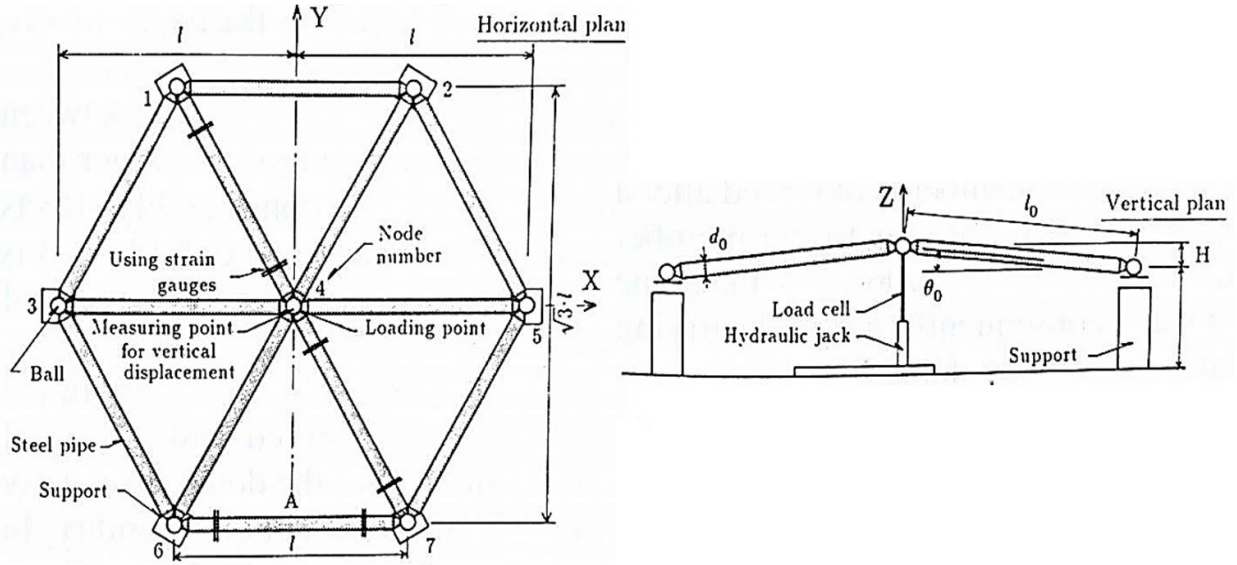


**Figure 2.27** Schematic Dome Test Arrangement Shibata et al. (1993)

During the experiment, a vertical load was applied to node number 4, located at the crown, by using a hydraulic jack and spherical support. The force level was measured by a load cell and implemented by controlling the displacements at the crown connection. The results obtained from the experiments confirmed that the jointing system behavior plays an important role on the ultimate buckling load capacity of three-dimensional structures. With the increment in the bending rigidity of the MERO jointing system, the three-dimensional structures obtained higher load carrying capacities.

López et al. (2007a; 2007c) tested a seven-meter diameter single layer three-dimensional dome with three rings, a rise to span ratio equal to 1/6, and connected using the ORTZ jointing system (**Figure 2.12**). The dome rested on plastic supports which allowed free displacement in the radial direction of the 24 outer perimeter nodes. The load was applied on the upper vertex by means of a hydraulic cylinder with 50 kN of maximum capacity and a total stroke of 500 mm. The force acted under displacement control conditions at quasi-static speed of 4 mm/minute. Vertical displacements of some of the nodes were measured through steel thread sensors fixed to the ceiling of the laboratory. Finally, a load cell was introduced between the vertex and the hydraulic cylinder to register the applied load. **Figure 2.28** shows the experimental set up of the dome.



**Figure 2.28** General Experimental Set Up (López et al. 2007a; c)

**Figure 2.29** shows a comparison of the results between the load-displacement curves obtained experimentally and with numerical analyses.

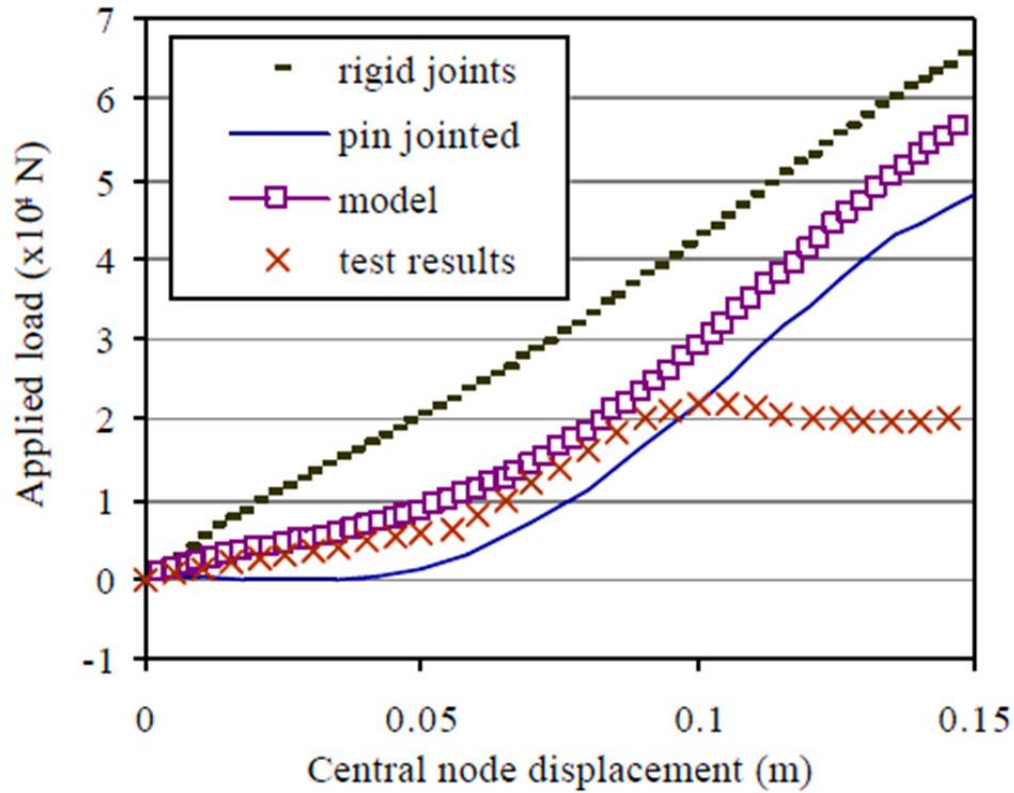


**Figure 2.29** Experimental and Numerical Results (López et al. 2007a; c)

As it can be seen from **Figure 2.29**, the experimental results are very close to the results of numerical analysis modeled with semi-rigid joints during the first 100 mm of displacement. The researchers concluded that the experimental results deviated from analytical results after the first 100 mm of displacement due to lack of tightening of some of the beam members joined to the connectors (see **Figure 2.12**).

Fong et al. (2012) built a single layer shallow three-dimensional dome with a depth of 0.27 and a span of 4.76 meters using bolted connections. The model was constructed to study the behavior and to determine the snap-through buckling load of semi-rigid jointed shallow domes. The structure consisted of 90 members and 37 connections. Stainless steel circular hollow tubes of 19 mm and a diameter of 0.8 mm thick were used as the members of the structure. To test the

structure, a rigid bar was used to connect the central node to a hydraulic jack. During the test, the vertical displacement of the central node was increased gradually by using the hydraulic jack, and the vertical deflection of the central node was measured by means of a displacement transducer. A load cell was also placed at the central node of the structure to record the applied force under an increasing displacement. The deflection of the central node was documented at intervals of 0.1 kN load increments before buckling was reached and at 0.05 kN load increments after buckling. The results of the experimental study were compared with finite element analysis results. **Figure 2.30** shows a comparison of the results between the load-displacement curves obtained experimentally and with numerical analyses. As can be observed, the numerical model including the semi-rigid behavior of the jointing system predicted accurately the actual experimental behavior of the structure compared to the model assuming rigid connections.

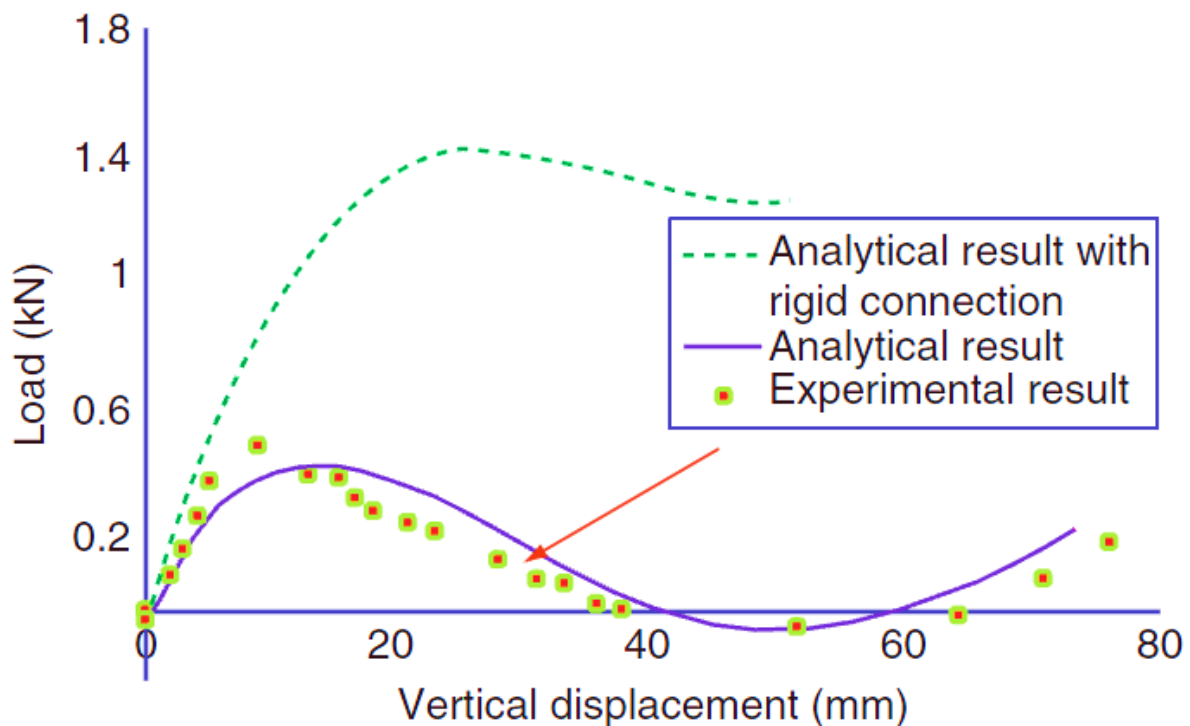


**Figure 2.30** Load-Deflection Curves Obtained by Fong et al. (2012)

As indicated in **Section 2.4.2** of this literature review, the modeling and analysis of three-dimensional structures must include the semi-rigidity behavior of the jointing system, that will be utilized to build the real structure, to accurately predict its behavior. According to Narayanan (2007), there are more than 250 different types of jointing systems that have been used to connect three-dimensional structures. This dissertation is limited to the analysis of single layer three-dimensional structures connected using extruded aluminum connectors featuring fir-tree slots joining tubular structural members (known as fir-tree jointing system). **Section 2.6** presents a description of the fir-tree jointing system. Furthermore, an explanation of the experimental and numerical studies performed in the past to characterize the semi-rigid load carrying capacity of these type of jointing system is reviewed.

## **2.6 Review of the Fir-Tree Jointing System**

This section describes the fir-tree jointing system and the types of experimental and analytical studies performed in the past to characterize the mechanical properties this joint.

### **2.6.1 Description of the Fir-Tree Jointing System**

The fir-tree jointing system consists of an extruded aluminum connector with serrated keyway slots (**Figure 2.31**) and tubular members with their ends pressed to form a coined edge (**Figure 2.32**) that fits in the connector keyway slots. Besides, the non-loaded slots of the connector can be filled with aluminum filler shim elements. The jointing system is finished when the beam coined pressed ends or filler shims are inserted in the fir-tree slots, a screw bolt is placed on the center of the connector, and washers are placed at each end of the connector, as illustrated in **Figure 2.33** (Lan 2005). This particular system was developed in the late 1950's by Arthur Fentiman (Geometrica® 2015). *r*

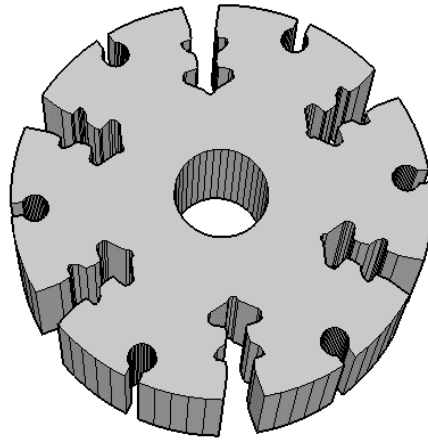


**Figure 2.31** Fir-Tree Extruded Aluminum Connector

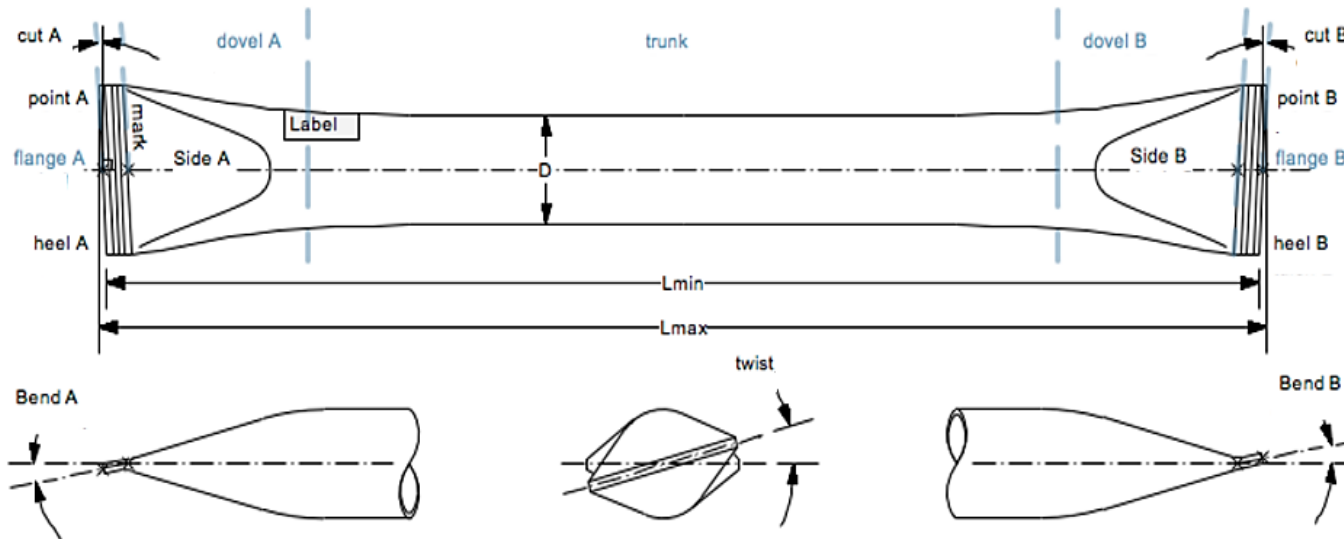


**Figure 2.32** Coined Pressed Ends Tubular Element (Geometrica® 2015)

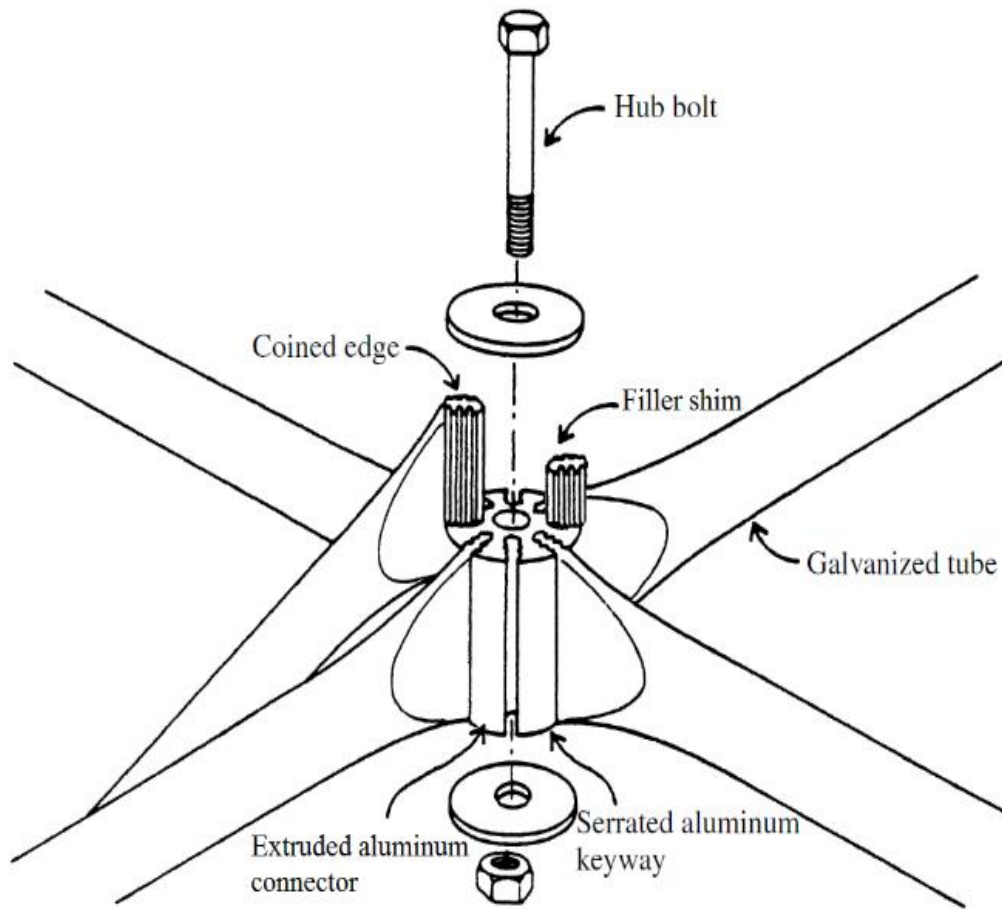


**Figure 2.33** Fir-Tree Jointing System (After Narayanan 2007)

### 2.6.2 Fir-Tree Jointing System: Previous Analytical and Experimental Studies

Sugizaki and Kohmura (1994) conducted a study to obtain the fir-tree jointing system semi-rigid characteristics. During the study, the authors conducted tension, compression, in-plane bending, and out-of-plane bending tests of the jointing system. **Figure 2.34** shows the results of the semi-rigid behavior of the fir-tree jointing system.

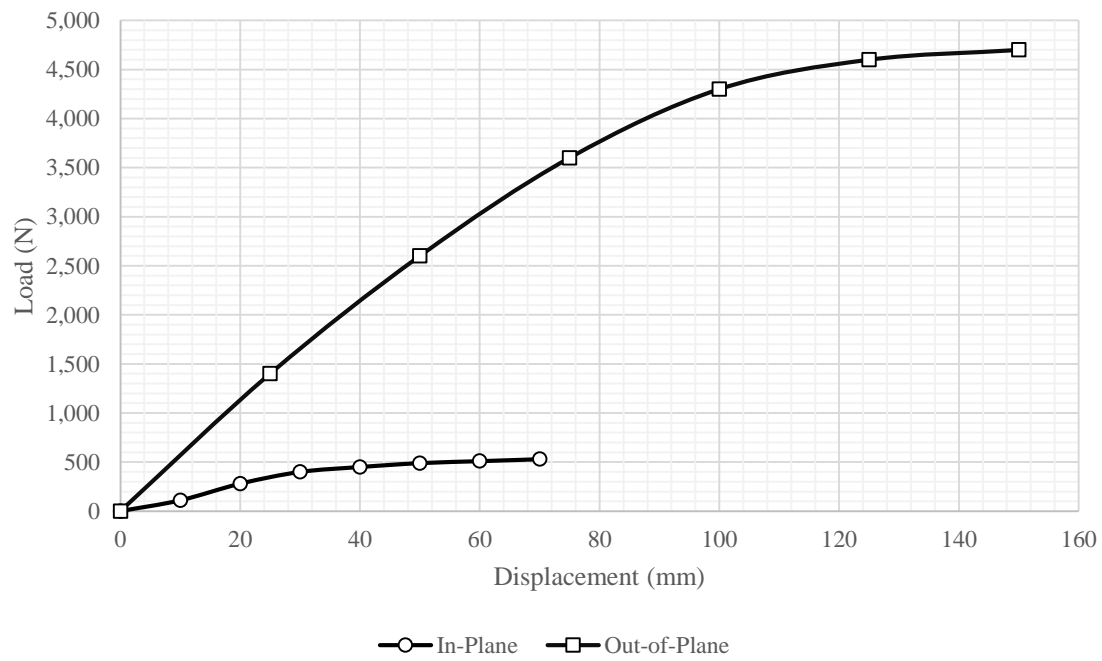
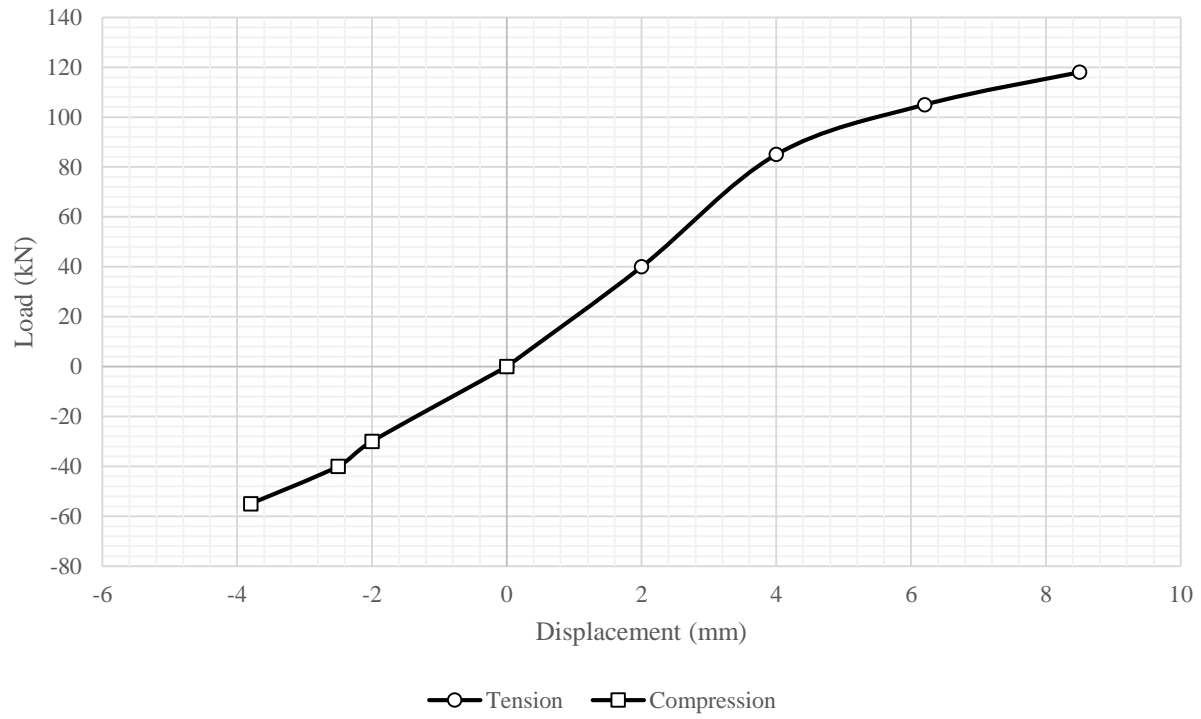


**Figure 2.34** Behavior of Fir-Tree Jointing System (Afer Sugizaki and Kohmura 1994)

From the experimental results, it was concluded that the fir-tree jointing system can be modeled with out-of-plane rigid joints and in-plane hinged joints. Furthermore, experimental studies were conducted in a complete structure to capture the buckling mode of three-dimensional structures connected using this jointing system. According to the results, the buckling capacity of three-dimensional structures using the fir-tree jointing system is reached due to the hub's rotation (rotated node buckling) as shown in **Figure 2.35**.



**Figure 2.35** Failure Mode of Dome with Fir-Tree Joint (Sugizaki and Kohmura 1994)

Doran (1997) conducted a series of mechanical tests to characterize the strength of the Geometrica® 6-6090 fir-tree jointing system. The mechanical tests were conducted to find the behavior and load capacity under tensile load of the system, the compression end-crippling load capacity of the system, and the bending capacity of the jointing system. **Figure 2.36** shows a typical set of the load-deformation curves obtained during the tensile study.

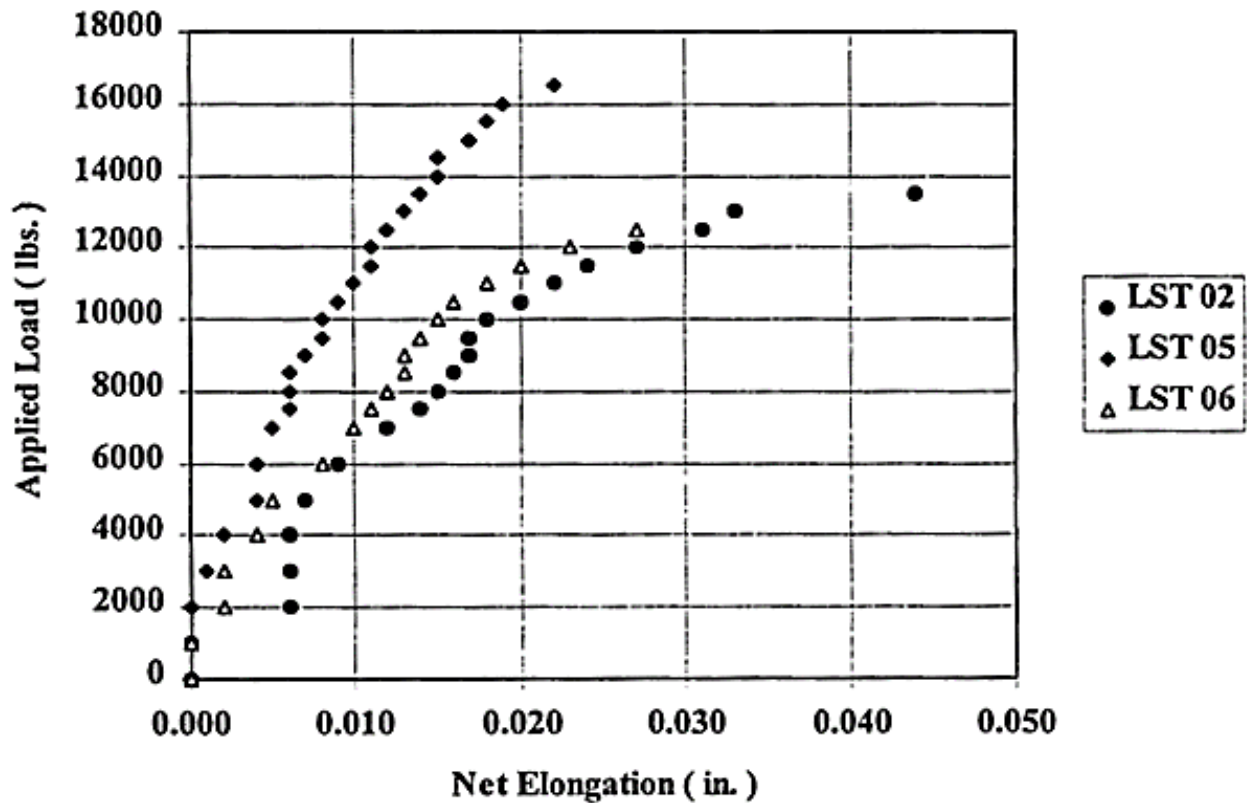


**Figure 2.36** Tension Load-Deformation Curves Obtained Experimentally by Doran (1997)

As future work recommendations, Doran (1997) suggested to conduct a study to inspect the real dimensions of the fir-tree jointing system elements to more accurately predict its structural performance.

A similar study was conducted by Ferregut and Carrasco (1998). The researchers performed laboratory and analytical experiments to characterize the tension and compression load capacity of the Geometrica® the 6Zd-00 fir-tree jointing system. Furthermore, the researchers developed a finite element model of the jointing system shown in **Figure 2.37**.

V1  
L5  
C1

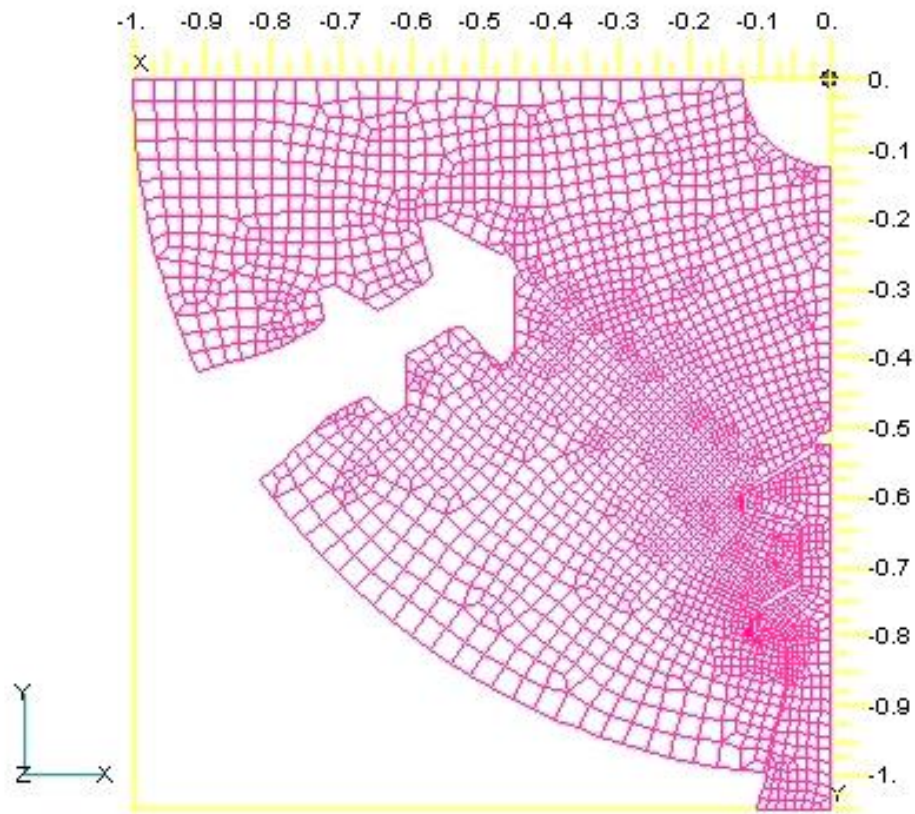


**Figure 2.37** Geometrica® 6Zd-00 Jointing System FEM (Ferregut and Carrasco 1998)

The analysis of the finite element model was conducted to simulate contact between the connector slots and the tubular element of the jointing system when the system is loaded under tension forces. The results included the force-displacement curve of the jointing system, as illustrated in **Figure 2.38**.

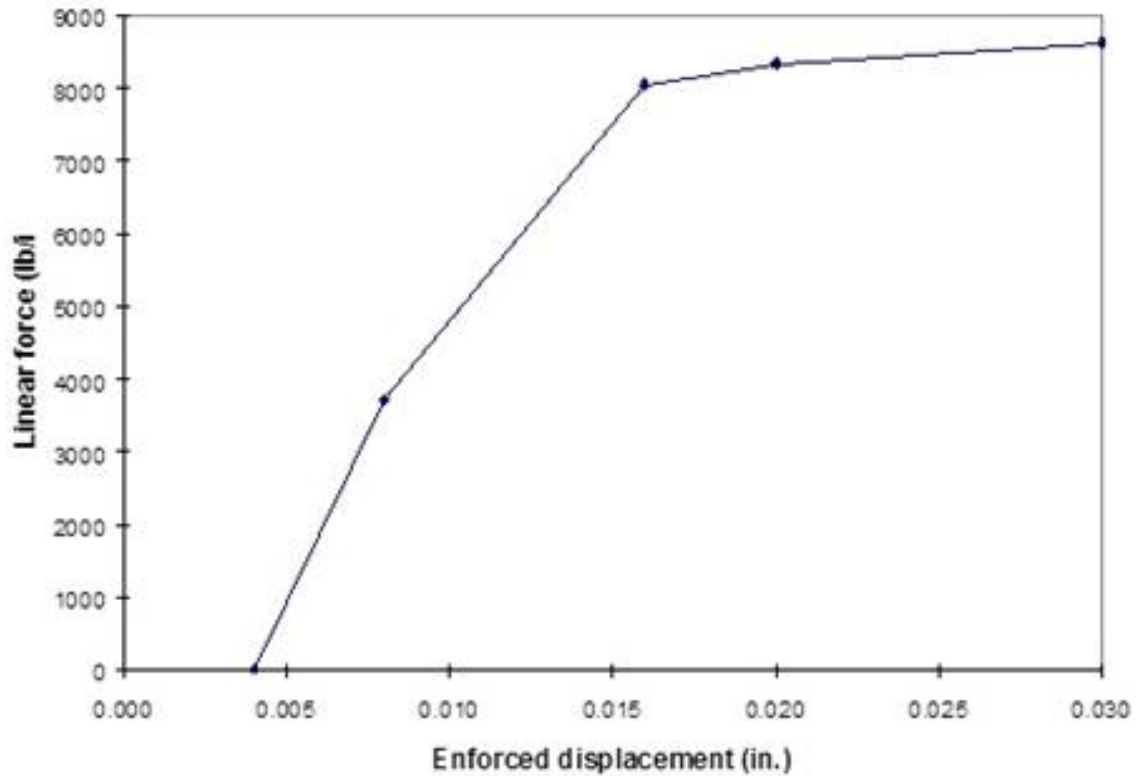


**Figure 2.38** Load-Displacement Curve of Geometrica® 6Zd-00 Jointing System (Ferregut and Carrasco 1998)

From their analysis, Ferregut and Carrasco (1998) concluded that the fir-tree jointing system exhibits a semi-rigid behavior and that further analysis is required to fully characterize the mechanical behavior of the jointing system.

### 2.6.3 Geometrica 6Sd-00 Fir-Tree Jointing System: Concurrent Numerical Study

Garcia (2017) conducted numerical simulations to obtain the axial (tension and compression) and in-plane bending semi-rigid behavior of the Geometrica® 6Sd-00 fir-tree jointing system shown in **Figure 2.39** and **2.40**, respectively.

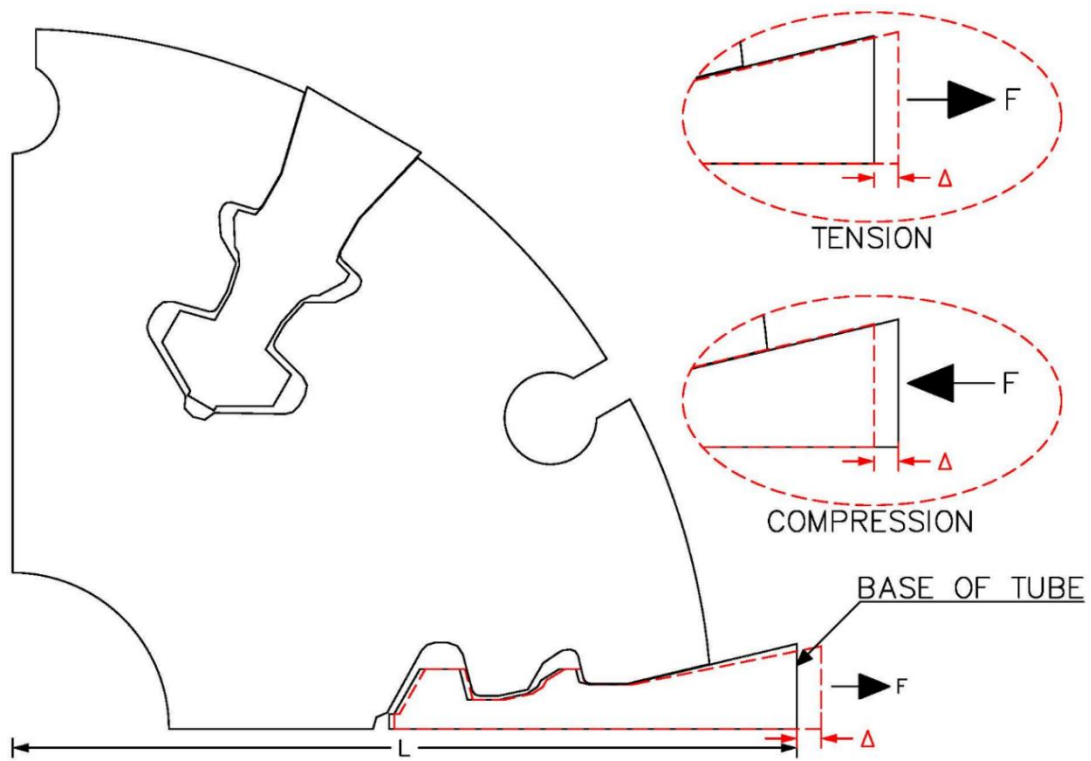


**Figure 2.39** Geometrica® 6Sd-00 Jointing System Axial Semi-Rigid Configuration

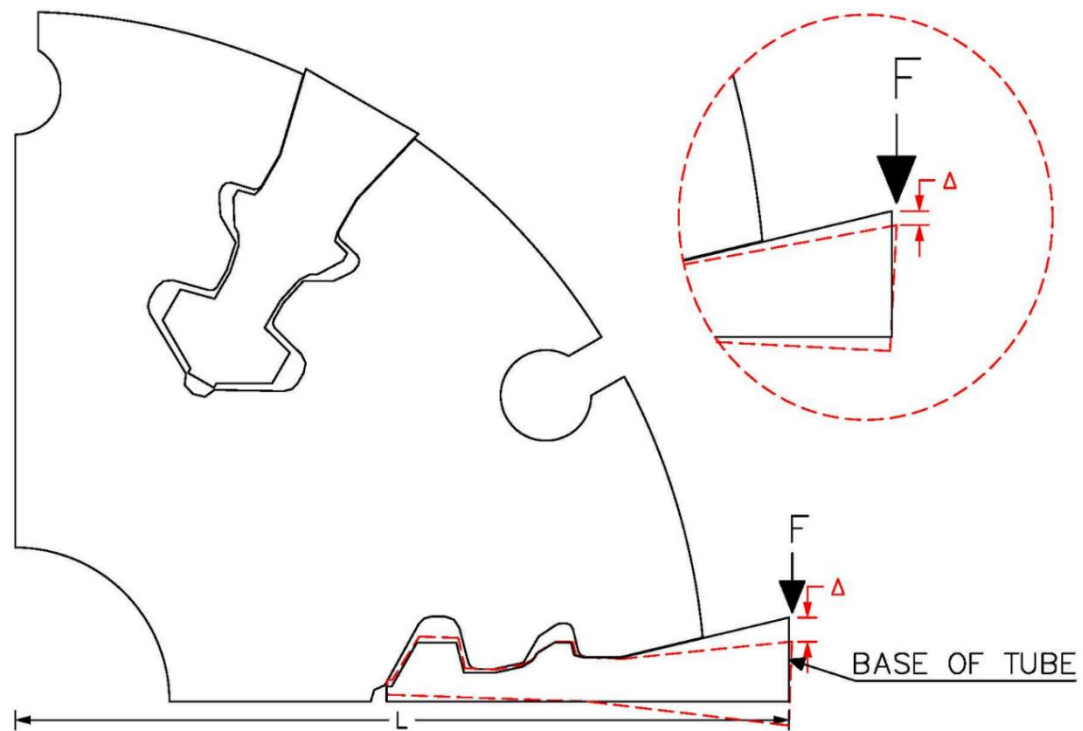


**Figure 2.40** Geometrica® 6Sd-00 Jointing System In-Plane Bending Semi-Rigid Configuration

Since the Geometrica® 6Sd-00 connector slots can accommodate three different tubular coined pressed end thicknesses being: 0.090 inches, 0.104 inches, and 0.120 inches; Garcia (2017) obtained the axial and in-plane bending semi-rigid behavior of the jointing system considering the three possible tubular thickness combinations. The simulations were conducted, first, using the “as-designed” dimensions and, then, using the “as-built” dimensions (considering manufacturing geometric imperfections) of the jointing system elements (connector slots and tubular coined pressed ends). The as-designed jointing system dimensions were obtained from the Geometrica® shop drawings, while the as-built jointing system dimensions were obtained by measuring manufactured samples of the jointing system elements.

Three as-designed semi-rigid behaviors of the Geometrica 6Sd-00 fir-tree jointing system were obtained numerically. **Table 2.2** shows the as-designed jointing system combinations, including the material of the connecting elements.

**Table 2.2** As-Designed Jointing System Combinations (After Garcia 2017)

| Jointing System                       | Tube Thickness 0.090 in<br>A500 Grade B | Tube Thickness 0.104 in<br>A653 SS 37 steel | Tube Thickness 0.120 in<br>A653 SS 37 steel |
|---------------------------------------|---|---|---|
| Hub Connector<br>A6061-T6<br>Aluminum | d-090                                   | d-104                                       | d-120                                       |

From **Table 2.2**, “d” defines “as-designed jointing system”; while the numbering defines the tube thickness. For instance, d-090 refers to “as-designed jointing system with a tube thickness of 0.090 inches.

To obtain the axial and in-plane bending semi-rigid behavior of the as-built Geometrica® 6Sd-00 fir-tree jointing system, Garcia (2017) measured three connector slots (named A-C) and three tubular coined pressed ends (named A-C) per tubular thickness resulting in a total of 27 connector-tube combinations. Then, 27 as-built semi-rigid behaviors (9 per each tube thickness) were obtained numerically. **Table 2.3** displays the as-built jointing system combinations and the material of the connecting elements.

**Table 2.3** As-Built Jointing System Combinations (After Garcia 2017)

| Jointing System                    |   | Tube Thickness 0.090 in<br>A500 Grade B |             |             | Tube Thickness 0.104 in<br>A653 SS 37 steel |             |             | Tube Thickness 0.120 in<br>A653 SS 37 steel |             |             |
|------------------------------------|---|---|-------------|-------------|---|-------------|-------------|---|-------------|-------------|
|                                    |   | A                                       | B           | C           | A   | B           | C           | A   | B           | C           |
| Hub Connector<br>A6061-T6 Aluminum | A | b-AA<br>090                             | b-AB<br>090 | b-AC<br>090 | b-AA<br>104                                 | b-AB<br>104 | b-AC<br>104 | b-AA<br>120                                 | b-AB<br>120 | b-AC<br>120 |
|                                    | B | b-BA<br>090                             | b-BB<br>090 | b-BC<br>090 | b-BA<br>104                                 | b-BB<br>104 | b-BC<br>104 | b-BA<br>120                                 | b-BB<br>120 | b-BC<br>120 |
|                                    | C | b-CA<br>090                             | b-CB<br>090 | b-CC<br>090 | b-CA<br>104                                 | b-CB<br>104 | b-CC<br>104 | b-CA<br>120                                 | b-CB<br>120 | b-CC<br>120 |

From **Table 2.3**, “b” defines “as-built jointing system”; the first letter refers to the measured connector; the second letter refers to the measured tube end; and the numbering define the tube thickness. For instance, b-CB 090 refers to “as-built jointing system, connector C and tube B with a thickness of 0.090 inches.

From the comparison of the simulation results, Garcia (2017) concluded that, in general, the as-built jointing system exhibits some differences in displacements, rotations, and capacities when compared to the as-designed jointing system semi-rigid behavior. However, the difference in the semi-rigid behavior of the connections due to manufacturing imperfections can affect the overall buckling behavior and capacity of three-dimensional structures since, accordingly to the presented literature review, joint behavior plays a critical role in the buckling stability behavior of three-dimensional structures.

This research incorporates the results of the as-designed and as-built semi-rigid behavior of the fir-tree jointing system with a tube thickness of 0.090 inches obtained by Garcia (2017) in the buckling analysis of three-dimensional structures. The objective is to understand/quantify the effect that manufacturing geometric imperfections in the jointing system produce in the buckling behavior of three-dimensional structures.

## **2.7 Summary of Literature Review**

Past research studies to predict the structural behavior of three-dimensional structures have been reviewed in this chapter. Researchers have considered node deviation and member curvature as initial geometric imperfections in the buckling analysis of three-dimensional structures. These types of imperfections tend to change the buckling mode and decrease the load capacity of three-dimensional structures. In addition, the semi-rigidity of jointing systems and their effect on the buckling behavior of three-dimensional structures have, also, been studied in the past. According to these research works; the semi-rigid behavior of jointing systems can decrease the buckling capacity from 10% to 50% as compared to perfectly rigid three-dimensional structures. Recently, Garcia (2017) considered how manufacturing geometric imperfections (as-built condition) affect the semi-rigid behavior and load capacity of the fir-tree jointing system as compared to an ideal (as-designed condition) jointing system. However, the semi-rigid behavior, including manufacturing geometric imperfections, of the jointing system components has never been included in the buckling analysis of 3D structures.

This research is the first work dedicated to characterizing the buckling behavior of three-dimensional structures considering the semi-rigid behavior of perfect and manufactured imperfect

jointing systems. The comparison of results will help to understand how manufacturing geometric imperfections of jointing systems affect the buckling behavior of three-dimensional structures.

### **Chapter 3: Modeling of 3D Structures and Laboratory Test Verification**

Laboratory tests are essential to understand the real behavior of structural systems (i.e. the load carrying capacity of 3D structures). These physical tests need to be scaled down to a size appropriate for the dimensions and capability of the laboratory equipment available for the researchers. Small-scaled laboratory tests can be referred as bench-scale tests (Battaini et al. 2000).

Hence, to capture the buckling behavior of 3D structures built using the Geometrica® 6Sd-00 fir-tree connection, physical laboratory tests were conducted on bench-scale 3D structures. A total of three tests were conducted to ensure that the conditions and procedures of the test produced consistent results. This chapter presents a description of the laboratory tests including the: (1) laboratory equipment and instrumentation used to conduct the tests; (2) geometry and dimensions of the bench-scale 3D structures; (3) construction procedure of the models; (4) test procedures; and (5) tests results.

In addition to laboratory tests, modern computer capabilities have offered the opportunity to investigate the complex buckling phenomena of structures using non-linear numerical analysis. However, to precisely estimate the buckling stability of 3D structures using finite element analysis, it is important to accurately model: (1) the shape of the structure; and (2) the actual jointing system behavior (Kato et al. 2005). Common design practices assume that joints in three-dimensional structures are completely rigid. Nevertheless, the actual semi-rigid behavior of the connections needs to be incorporated into the analysis of the structure to accurately predict its buckling stability (Ma et al. 2013).

Therefore, this chapter also describes two 3D structure finite element models identical in geometry and loading conditions to the bench-scale test models developed to capture their buckling

stability behavior. The different models were developed using the Patran/Nastran software (MSC 2014) and include:

- 1) A model using rigid joint connections; and
- 2) A model using the semi-rigid behavior of the fir-tree jointing system.

The description of the models includes the: (1) geometry; (2) material properties; (3) boundary and loading conditions; (4) jointing system modeling technique; and (5) finite element analysis results.

In the last part of this chapter, the laboratory tests and finite element simulation results reported herein are compared to:

- 1) Capture the real behavior of 3D structures built using the Geometrica® fir-tree jointing system;
- 2) Assess how the rigidity of this jointing system influences the buckling behavior of 3D structures; and
- 3) Assess the accuracy of the finite element simulation results obtained from the structure modeled using the semi-rigid behavior of the Geometrica® 6Sd-00 fir-tree jointing system.

### **3.1 Laboratory Tests of Bench-Scale 3D Structures**

#### **3.1.1 Laboratory Facilities, Equipment, and Instrumentation**

To capture the real buckling behavior stability of 3D structures built using the Geometrica® 6Sd-00 jointing system, three laboratory tests on bench-scale structural models were performed. The tests were conducted at the Center for Transportation Infrastructure Systems (CTIS) of The University of Texas at El Paso (UTEP) with a MTS load frame testing machine (shown in **Figure 3.1**). The MTS load frame assembly has the following dimensions and capabilities:

- 1) A maximum space of 4 feet between columns;
- 2) A mounted load cell to measure applied load with maximum capacity of 220 kips;
- 3) A displacement transducer to measure movement/deformations; and
- 4) An adjustable loading rate.



**Figure 3.1** MTS Universal Testing Machine

### 3.1.2 Geometry

**Figure 3.2** presents a detailed drawing of the bench-scale structures tested in this research. The final geometry and size of the structures were designed based on the dimensions and capability of the equipment available to conduct the laboratory tests. From the figure, it can be observed that scale structures had a hexagonal form with a span of 41.80 inches (3.5 feet) and a height of 4.18 inches at the crown node; hence, having a rise to span ratio of 1/10. The description and dimensions of the elements used to construct the structural bench-scale models are as follows:

- 1) Twelve 0.104-inch wall thickness Geometrica® beam elements made of A500 Grade B steel:
  - a. The six perimeter beam elements had a total designed length of 20.88 inches; and
  - b. The six beam elements connecting the outside ring with the crown connector of the structure had a total designed length of 21.29 inches;
- 2) Seven 2.25-inch diameter and 3.60-inch long Geometrica® 6Sd-00 connectors made of A6061-T6 aluminum;
- 3) Filler shim elements made of A6061-T6 aluminum;
- 4) Six 5-inch x 5-inch x 1/2-inch base plate supports made of A36 steel. These plates had round bar to receive the perimeter connectors of the structure;
- 5) One 5-inch x 5-inch x 1/2-inch plate made of A36 steel on the top to serve as a load transfer mechanism from the MTS loading machine to the bench-scale structures;
- 6) All plates had four 5/8-inch diameter holes; and
- 7) Threaded rods, nuts and washers used to secure the jointing system after tubular members were inserted into the connector slots.

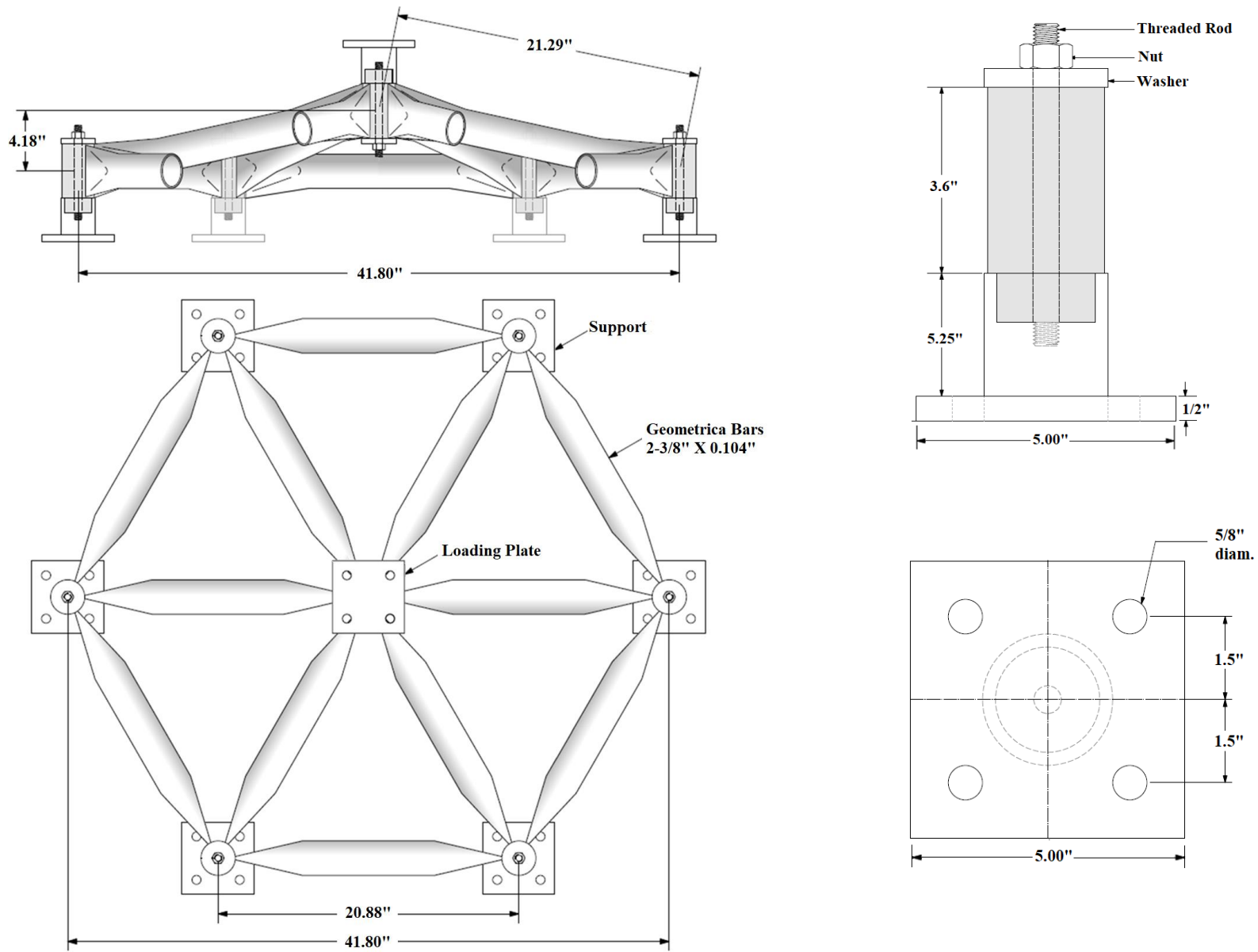


**Figure 3.2** Geometry of Bench-Scale Tested Structures

### 3.1.3 Construction

Three-dimensional structures are built using slender, lightweight metal tubes, and connectors. To build each bench-scale structure, the tubular members were inserted into the fir-tree slots of the connectors. Once the required tubular members were inserted into each connector, the plates were placed on the perimeter and crown joints. The jointing systems were secured using threaded rods, washers and nuts. The step-by-step procedure to build these structures is shown in **Figure 3.3**.

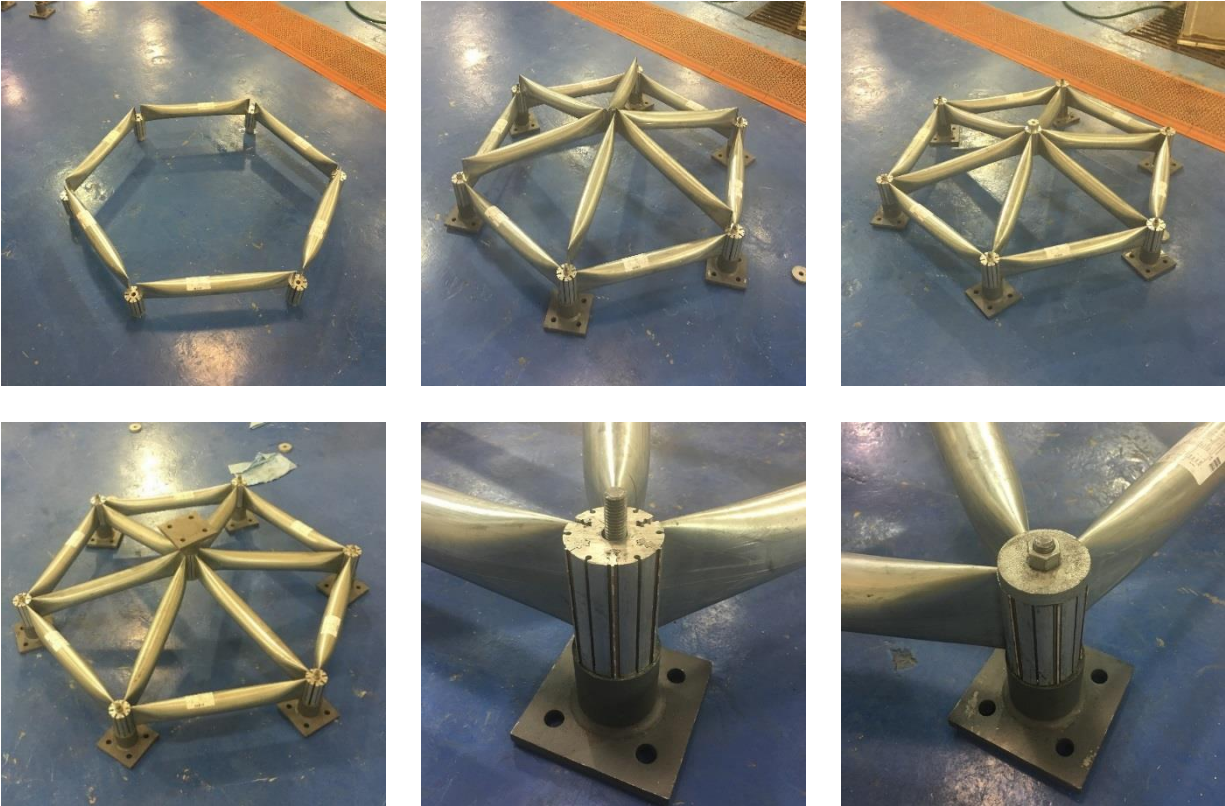


**Figure 3.3** Construction of Bench-Scale Tested Structures

### 3.1.4 Test Procedures

As stated in **Section 3.1.1**, the laboratory tests were conducted with a MTS load frame testing machine with 4 feet space between columns, a maximum load capacity of 220 kips, adjustable loading rate, and a displacement transducer to measure deformations. Each test was conducted under the configuration of the structure and MTS machine illustrated in **Figure 3.4**.

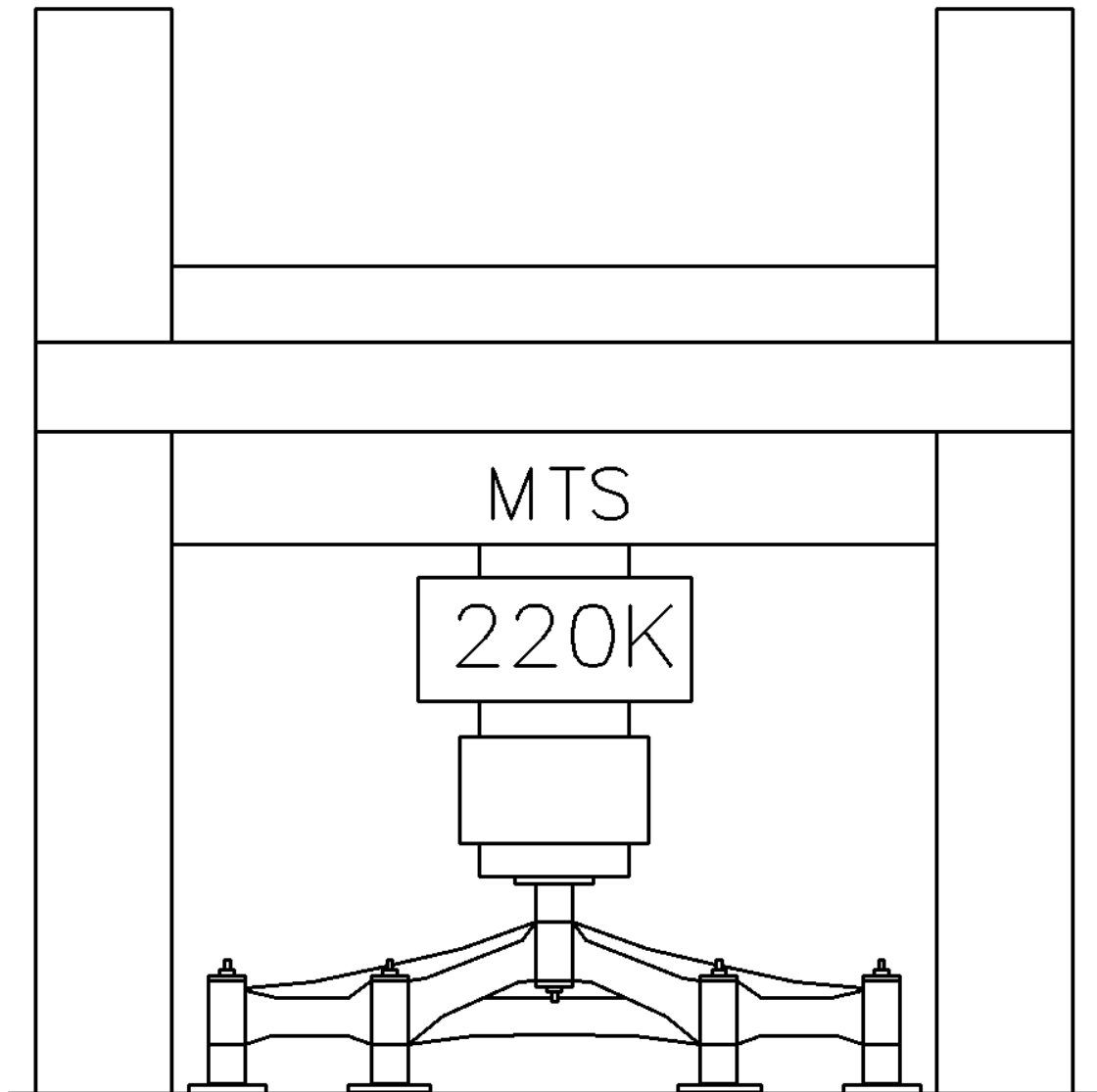


**Figure 3.4** MTS Universal Testing Machine and Bench-Scale Structure Configuration

To provide an adequate surface to fix the six-perimeter base plate supports of the bench-scale structures to the floor, a 4'x4' steel plate was placed and secured to the bottom frame under the loading jack of the MTS machine using anchor bolts. Next, the six perimeter base plates of the bench-scale structure specimens were welded to already fixed bearing plate. **Figure 3.5** shows a typical structural specimen with the perimeter base plates welded to the supporting steel plate.



**Figure 3.5** Supporting Conditions of Bench-Scale Tested Structures

To obtain the applied load-displacement buckling behavior of the experimental structures, a quasi-static load was applied on the upper crown connector under displacement control conditions at a speed of 0.02 in/minute. The data acquisition system of the MTS machine recorded the applied load-displacement data of the crown connector during the duration of each test. **Figure 3.6** shows a bench-scale specimen being tested while the load is being applied at the crown connector of the structure.



**Figure 3.6** Laboratory Test of Bench-Scale Structure in Progress

### 3.1.5 Test Results

**Table 3.1** summarizes the data of the applied load-displacement of the crown connector in 2,000 pounds increments and **Table 3.2** presents the applied load-displacement at failure of the three tested specimens.

**Table 3.1** Applied Load-Displacement of Crown Connector of Tested Structures

| Load<br>(lb.) | Displacement (in) |        |        |
|---------------|-------------------|--------|--------|
|               | Test 1            | Test 2 | Test 3 |
| 0             | 0.000             | 0.000  | 0.000  |
| 2,000         | 0.018             | 0.023  | 0.016  |
| 4,000         | 0.037             | 0.043  | 0.035  |
| 6,000         | 0.056             | 0.063  | 0.061  |
| 8,000         | 0.077             | 0.084  | 0.081  |
| 10,000        | 0.097             | 0.103  | 0.098  |
| 12,000        | 0.116             | 0.118  | 0.113  |
| 14,000        | 0.131             | 0.131  | 0.127  |
| 16,000        | 0.144             | 0.144  | 0.140  |
| 18,000        | 0.157             | 0.156  | 0.151  |
| 20,000        | 0.168             | 0.167  | 0.161  |
| 22,000        | 0.179             | 0.177  | 0.170  |
| 24,000        | 0.189             | 0.187  | 0.179  |
| 26,000        | 0.200             | 0.197  | 0.188  |
| 28,000        | 0.211             | 0.207  | 0.198  |
| 30,000        | 0.224             | 0.218  | 0.208  |
| 32,000        | 0.236             | 0.229  | 0.219  |
| 34,000        | 0.248             | 0.241  | 0.231  |
| 36,000        | 0.263             | 0.256  | 0.246  |
| 38,000        | 0.280             | 0.274  | 0.264  |

**Table 3.2** Failure Load-Displacement of Crown Connector of Tested Structures

|            | Test 1 | Test 2 | Test 3 |
|------------|--------|--------|--------|
| Load (lb.) | 38,813 | 41,179 | 39,696 |
| Disp. (in) | 0.290  | 0.331  | 0.285  |

In the three tests, only one failure mode was observed. Failure of the structures was determined when the load considerably dropped due to rotation of the crown connector. **Figure 3.7** shows the failure mode of the structures. From the figure, it can be observed that the crown connector rotated clockwise around the direction normal to the surface of the bench-scale structures when the beam members' ends, adjacent to the connector, reached local yielding.

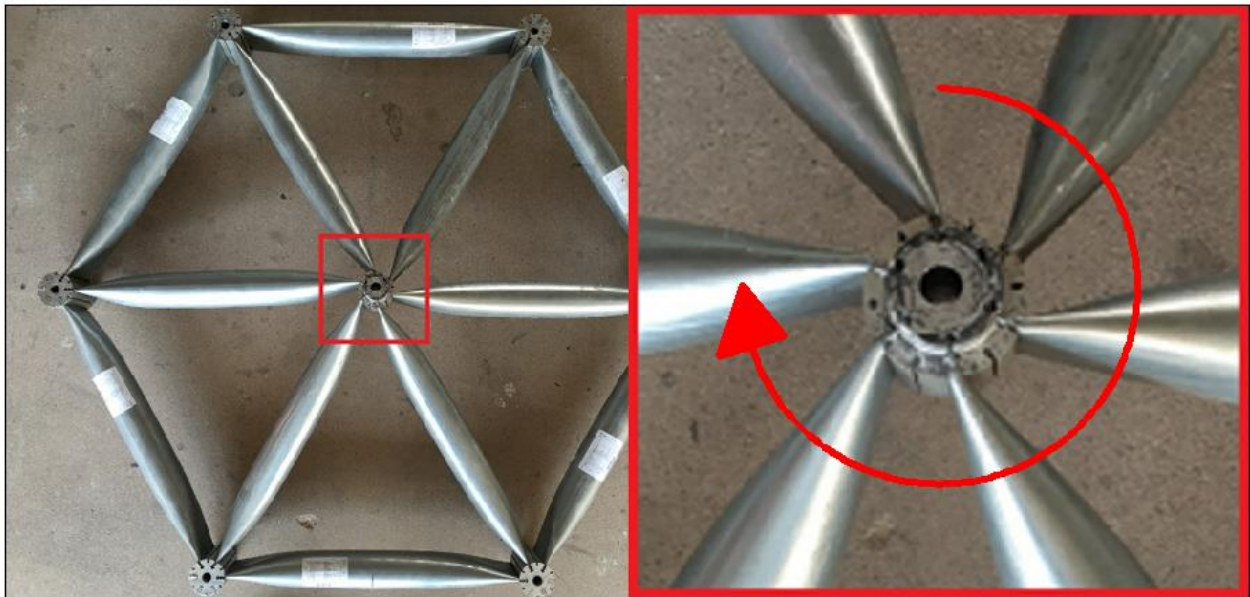


**Figure 3.7** Rotated Nodal Buckling Failure of Tested Bench-Scale Structures

Three laboratory tests were conducted to capture the actual buckling behavior of 3D structures. However, few researchers and designers have facilities and funds readily available to them to test full-scale structures. Conversely, the finite element method provides faster and more economical results than experimental analysis. Consequently, two finite element models identical in geometry and loading conditions to the bench-scale structures were developed. One model was developed using rigid joint connections and a second model was developed using the semi-rigid behavior of the Geometrica® 6Sd-00 fir-tree jointing system. These models were created to analytically: (1) assess how the rigidity of this jointing system influences the buckling behavior of 3D structures; and (2) predict the actual buckling behavior of 3D structures built with these joints.

## 3.2 Finite Element Simulation: Bench-Scale Structures

### 3.2.1 Geometry

**Figure 3.8** presents the bench-scale finite element model of the structure having a hexagonal form with a span of 41.80 inches and a height of 4.18 inches at the crown node. The modeled structure is composed of a total of twelve beam elements with the same dimensions described in **Section 3.1.2**.

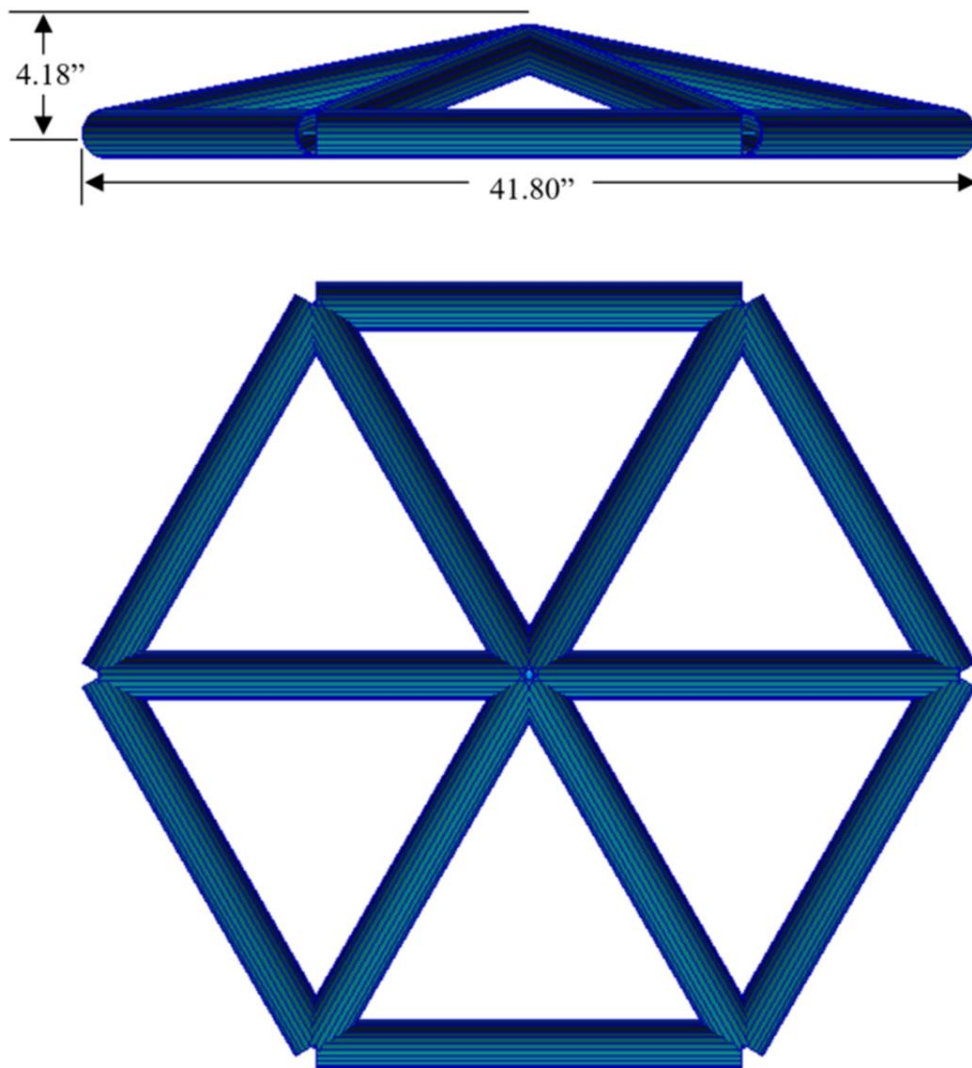


**Figure 3.8** Finite Element Model of Bench-Scale Structure

### 3.2.2 Material Properties

The bench-scale structures were modeled considering the following elements:

- 1) The Geometrica® 6Sd-00 connector element made of A6061-T6 aluminum;
- 2) A 2-3/8-inch tube with a 0.104-inch wall thickness made of A500 Grade B steel; and
- 3) Filler shim elements made of A6061-T6 aluminum.

To find the material properties of the aluminum and steel, one coupon tension test for each of the materials was performed according to ASTM standards (ASTM 2016). **Figure 3.9** shows a coupon tension test in progress.

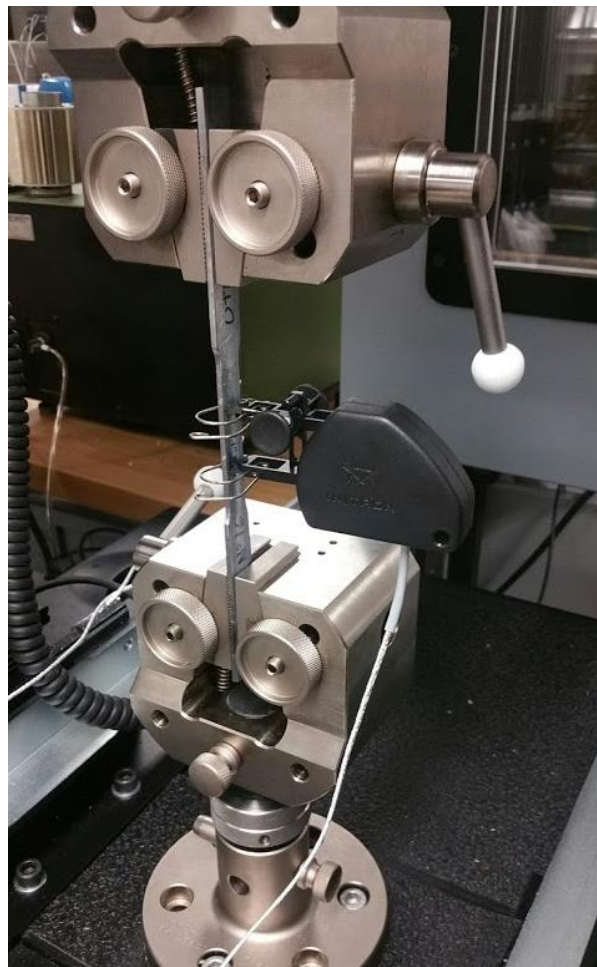


**Figure 3.9** Coupon Tension Test in Progress

**Figure 3.10** and **3.11** show the stress-strain curve of aluminum A6061-T6 and A500 Grade B steel obtained through the tension tests, respectively. These curves were smoothed to eliminate potential problems during the numerical non-linear finite element analysis.

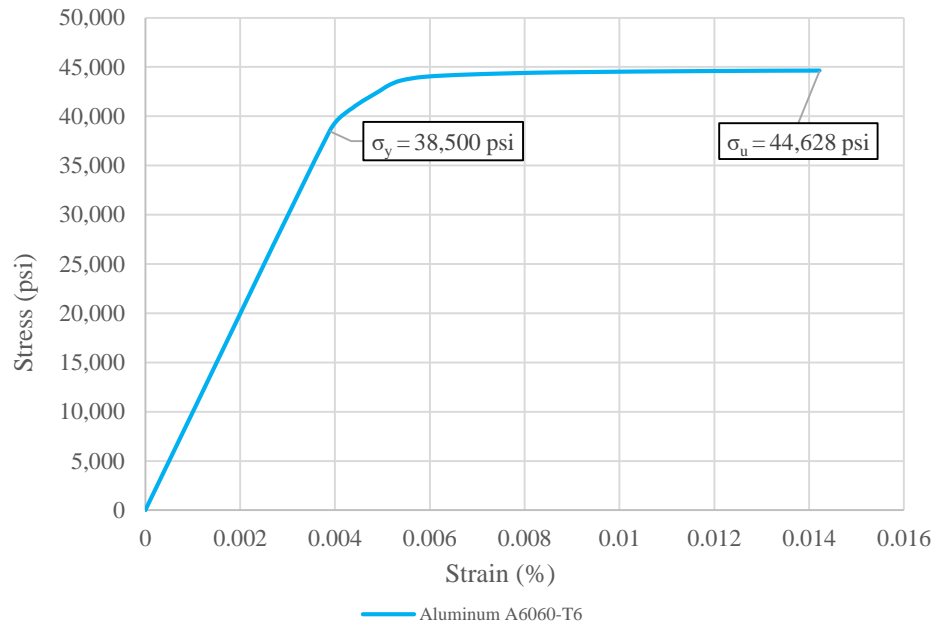


**Figure 3.10** Bench-Scale Structure Material Properties: Aluminum A6061-T6

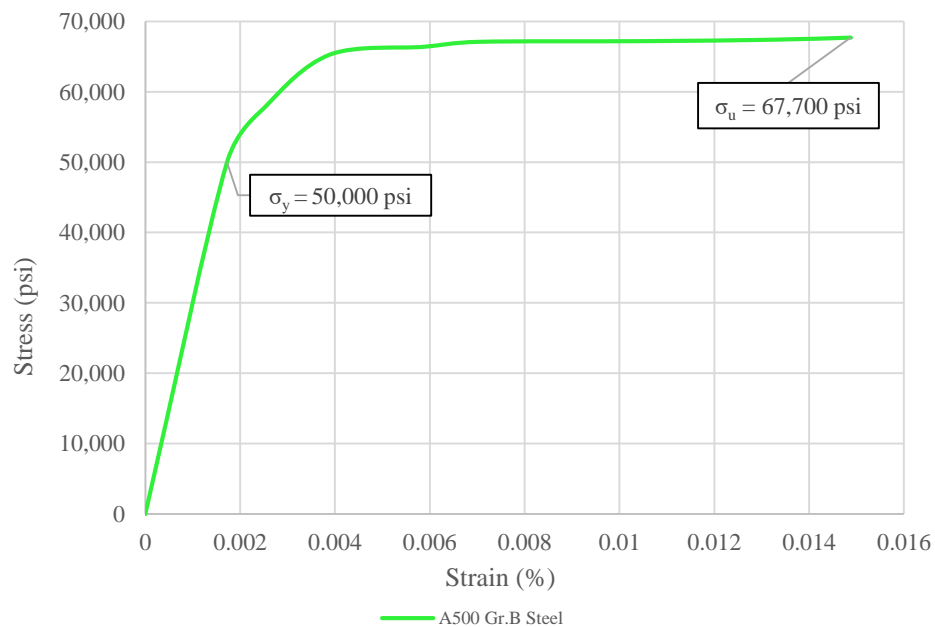


**Figure 3.11** Bench-Scale Structure Material Properties: Steel A500 Grade B

The stress-strain curves were used to estimate the elastic modulus (E), yield strength ( $\sigma_y$ ), and ultimate tensile strength ( $\sigma_u$ ) of the two materials. Results are shown in **Table 3.3**.

**Table 3.3** Material Properties of Modeled Bench-Scale Structures

| Component                                  | Material           | E(psi)*           | $\mu^+$ | $\sigma_y$ (psi)* | $\sigma_u$ (psi)* |
|--|--------------------|-------------------|---------|-------------------|-------------------|
| 6Sd-00 Connector                           | A6061-T6 Aluminum  | $9.9 \times 10^6$ | 0.34    | 38,500            | 44,628            |
| 2-3/8" x 0.104" Tube<br>Coined Pressed End | A500 Grade B Steel | $29 \times 10^6$  | 0.29    | 50,000            | 67,700            |
| 6Sd-00 Connector Filler<br>Shims           | A6061-T6 Aluminum  | $9.9 \times 10^6$ | 0.34    | 38,500            | 44,628            |

\* Obtained through experimental test.

+ Typical Poisson's ratio values (Ferregut and Carrasco 1998)

### 3.2.3 Boundary and Loading Conditions

To mimic the laboratory test conditions, the bench-scale structures simulated in this section were modeled and analyzed using fully restrained boundary conditions in the periphery nodes. The applied load was a static force on the crown node of the structure as shown in **Figure 3.12**.

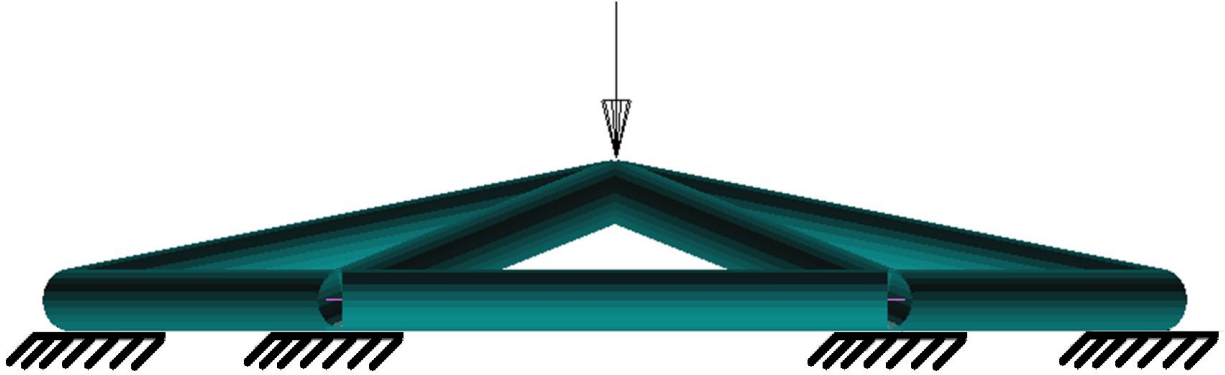


**Figure 3.12** Boundary and Loading Conditions of Modeled Bench-Scale Structures

### 3.2.4 Jointing System Modeling

To analytically assess how the rigidity of this jointing system influences the buckling behavior of 3D structures and to accurately predict the actual buckling behavior of 3D structures, the jointing system behavior of the bench-scale structure was modeled as follows:

- 1) A model with rigid jointing system connections: r-104; and
- 2) A model with semi-rigid jointing system connections: s-104.

#### 3.2.4.1 Modeling of the Rigid Jointing System

For the model of the structure considering rigid jointing system connections, beam elements (Nastran CBEAM elements) were connected to a central node to represent a rigid connection. **Figure 3.13** displays the FEM of the bench-scale structure with rigid jointing system connections.

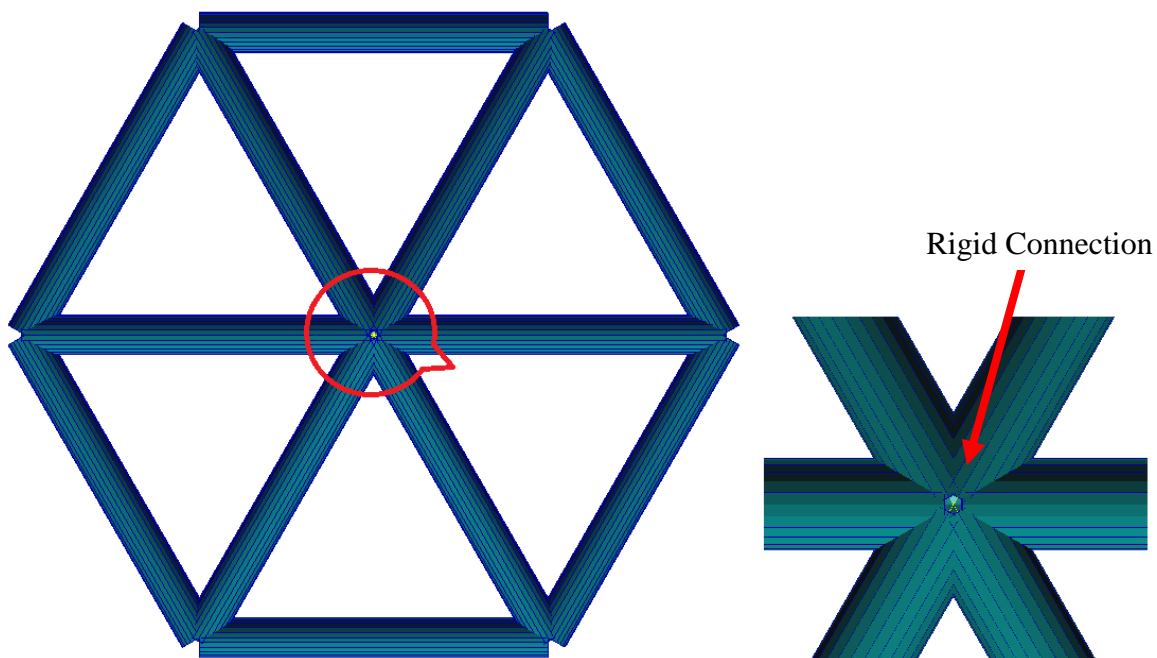


**Figure 3.13** Rigid Jointing System: FEM of Bench-Scale Structure

### 3.2.4.2 Modeling of the Semi-Rigid Jointing System

To simulate the semi-rigid characteristics jointing system, non-linear spring elements (Nastran CBUSH elements) with axial and in-plane rotational stiffness properties were added at the end of each CBEAM element. These spring elements had a length equivalent to the radius of the connector. Therefore, the length of the beam elements was reduced an equivalent of the radius of the connector from each of their two ends. **Figure 3.14** displays the FEM of the bench-scale structure with semi-rigid jointing system connections modeled with non-linear spring elements at the end of each beam element.

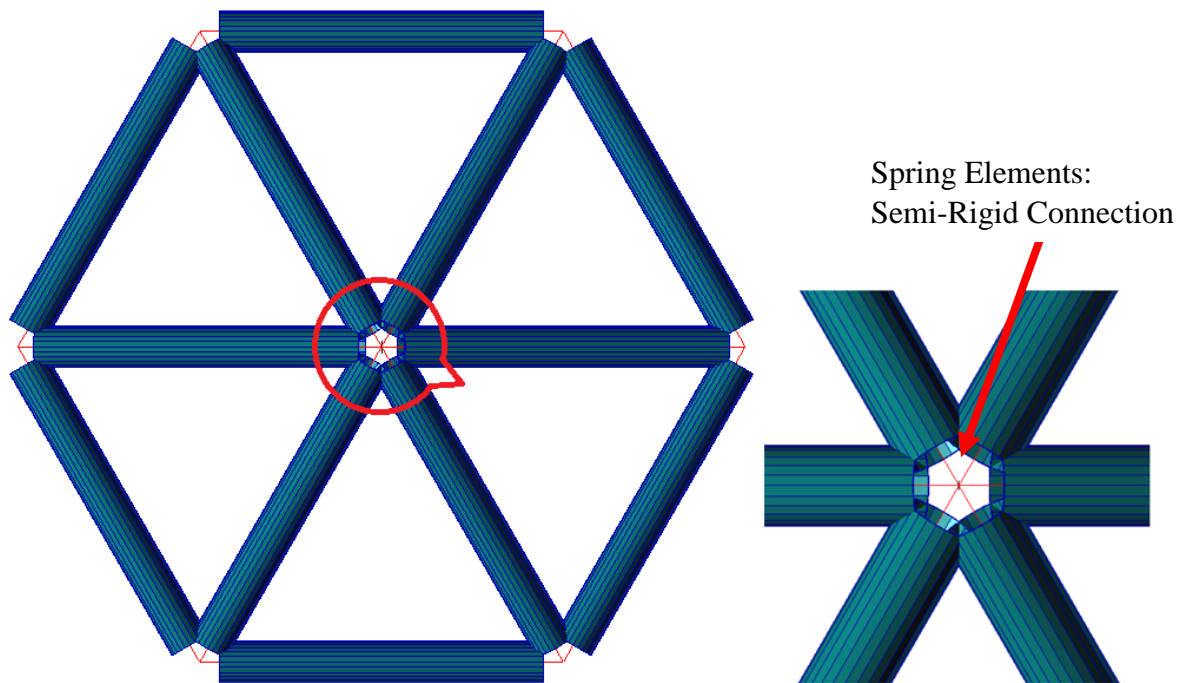


**Figure 3.14** Semi-Rigid Jointing System: FEM of Bench-Scale Structure

The semi-rigid behavior of the connections was obtained following the finite element modeling technique of the fir-tree jointing system proposed by Garcia (2017). **Figure 3.15** displays

the axial semi-rigid behavior of the jointing system modeled into the properties of the spring elements. This axial behavior is composed of two main zones. Zone 1 is the initial flat portion which represents the fit-gap tolerance between the mating parts of the jointing system. Zone 2 is observed once the mating parts become in contact, creating a non-linear tension or compression load vs. displacement behavior of the connection.

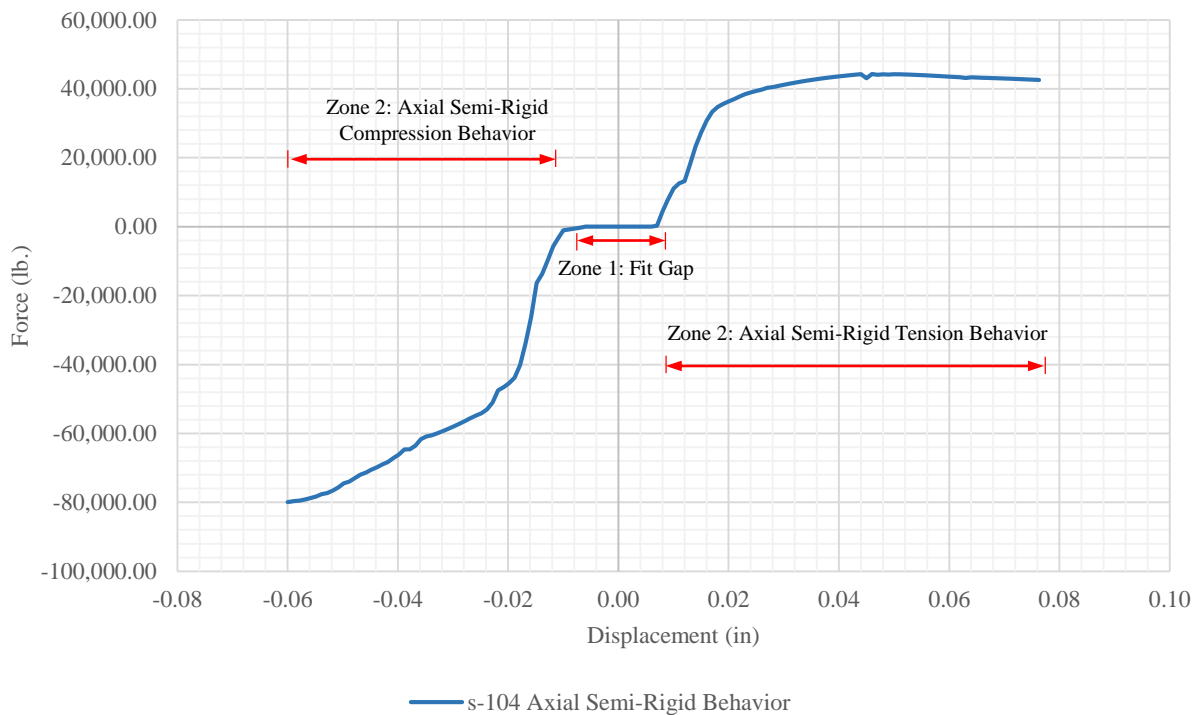


**Figure 3.15** Axial Semi-Rigid Behavior of the Jointing System: s-104

**Figure 3.16** illustrates the in-plane bending stiffness semi-rigid behavior of the jointing system modeled into the properties of the spring elements. This typical in-plane bending behavior is composed of two main zones. Zone 1 is the initial flat portion which represents the fit-gap tolerance between the mating parts of the jointing system. Zone 2 is observed once the mating

parts become in contact, creating a non-linear bending moment vs. rotation behavior of the connection.

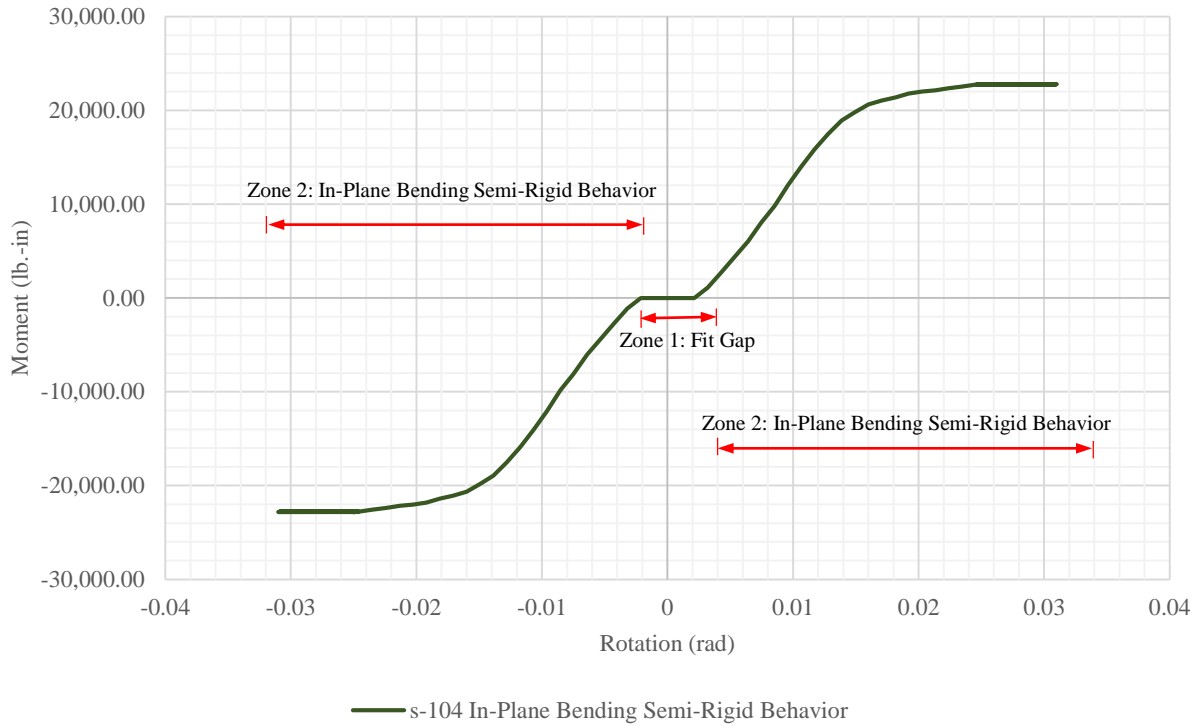


**Figure 3.16** In-Plane Bending Semi-Rigid Behavior of Jointing System: s-104

**Table 3.4** shows the Patran/Nastran elements utilized to model the bench-scale structures part of this dissertation.

**Table 3.4** Patran/Nastran Elements used to Model Bench-Scale Structures

| Three-Dimensional Structure Element            | Patran/Nastran Element | Nastran Properties |
|--|------------------------|--------------------|
| Tubular bars                                   | CBEAM                  | PBEAM              |
| Semi-Rigid Jointing System (Non-Linear Spring) | CBUSH                  | PBUSH              |

### 3.2.5 Selected Finite Element Simulation Results

Considering the concept of elasto-plastic buckling behavior of 3D structures, which is defined as the maximum point in the load-deformation curve equilibrium path/curve taking into account both the material nonlinear properties and the geometrical nonlinearity (Mohammadi et al. 2012), a non-linear finite element analysis was conducted on the two previously described finite element models. From the two FEA, the applied load (lb.) vs. displacement (in) history curves of the crown node were obtained.

In **Section 3.3**, the FEA results are presented and compared to assess how the rigidity of the Geometrica® fir-tree jointing system influences the buckling behavior of 3D structures. Furthermore, the FEA results are also compared with the results obtained from the three experimental tests. This comparison will be the base to assess the accuracy of the results obtained from the finite element model of the structure that includes the stiffness of the fir-tree jointing system.

### 3.3 Laboratory vs. Analytical Results: Comparative Analysis

The applied load-displacement curves obtained through the FEA (r-104 and s-104) and the laboratory tests are shown in **Figure 3.17**, **3.18**, and **3.19** for the tests one, two, and three, respectively. In the figures, the applied load-displacement history relationship of the central connector of the experimental bench-scale structures is represented by the pink square marks. The analytical applied load-displacement curve of the crown node is represented by the green solid line for the model using rigid connections (r-104) and by the blue solid line for the model that includes the semi-rigid behavior of the jointing system (s-104).

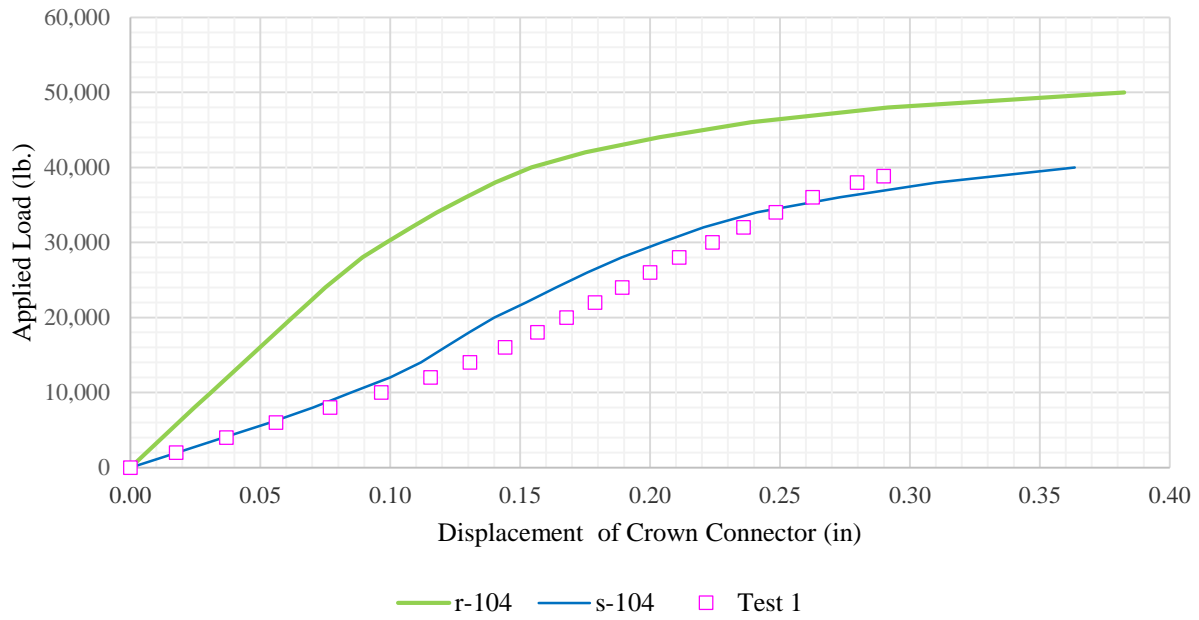


**Figure 3.17** Load-Displacement of Bench Scale Structure: r-104 vs. s-104 vs. Test 1

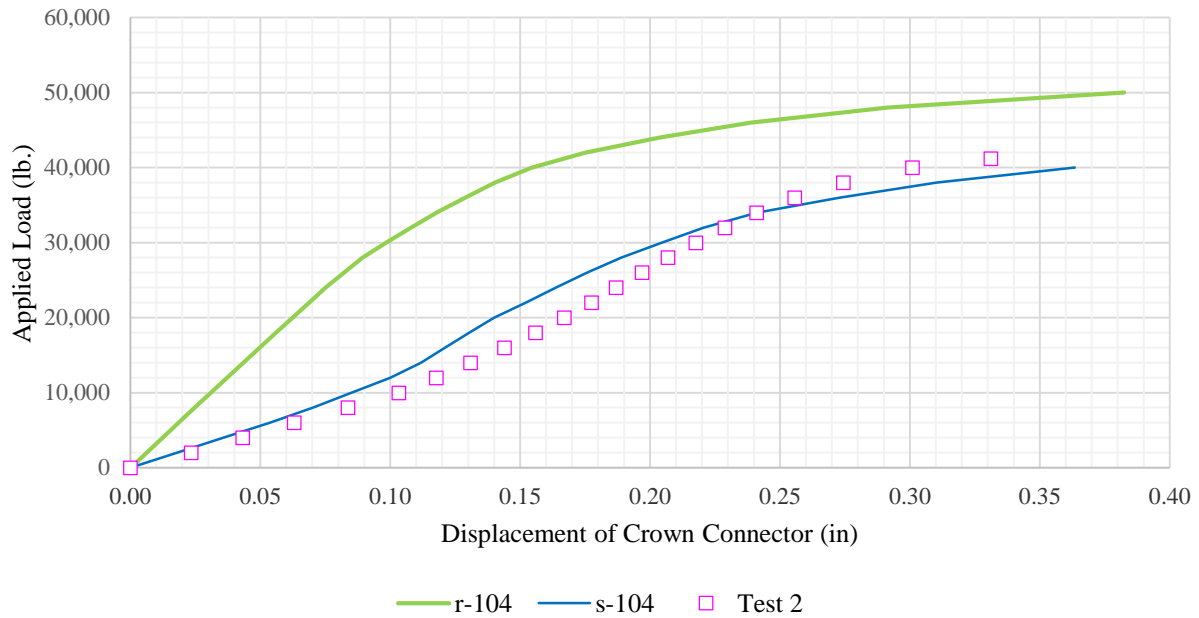


**Figure 3.18** Load-Displacement of Bench Scale Structure: r-104 vs. s-104 vs. Test 2

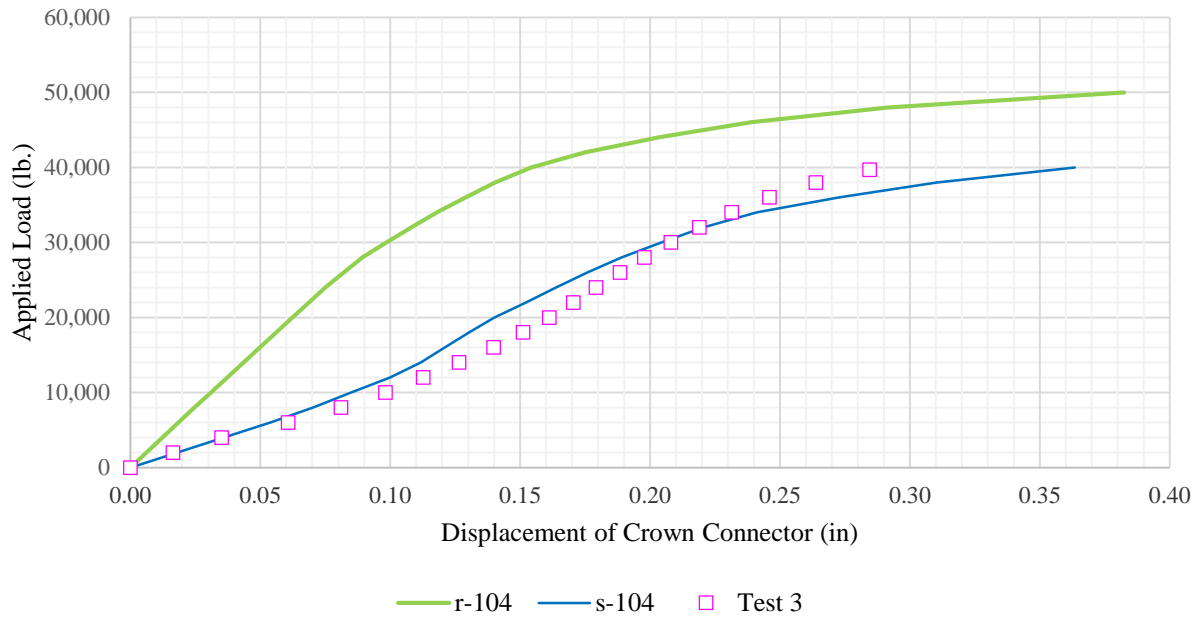


**Figure 3.19** Load-Displacement of Bench Scale Structure: r-104 vs. s-104 vs. Test 3

The following conclusions are obtained from the comparison of the laboratory tests vs. analytical results of the applied load-displacement plots of the bench-scale structure presented in **Figure 3.17, 3.18, and 3.19**:

- In the applied-displacement curves of the three laboratory tests, the increase in deflection is nearly linear from initial loading until the applied load reaches around 10,000 lbs. At this point, the curve becomes non-linear until failure load is reached at 38,813 lb., 41,179 lb., and 39,696 lb. for test 1, 2, and 3, respectively;
  - The applied load-displacement curve of the s-104 finite element model follows a similar path as compared to the obtained behavior curve of the three bench-scale structures tested;
- and

- Conversely, the applied load-displacement curve of the r-104 finite element structural model overestimates the strength of the structure compared to the results of the three laboratory tests. Hence, proving that common design practices based on the assumption that the fir-tree connections are rigid, might be un-conservative.

The preceding interpretations prove the accuracy of results obtained from the developed FEM of bench-scale 3D structure that uses the semi-rigid properties of the fir-tree jointing system. Therefore, this modeling technique will be used to create models of large span three-dimensional structures considering:

- 1) The as-designed behavior of the jointing system (**Chapter 5**); and
- 2) The as-built behavior of the jointing system (**Chapter 6**).

Subsequently, non-linear finite element analyses will be conducted on the previously mentioned 3D structure models to capture their buckling behavior. In **Chapter 7**, the buckling behavior of the as-designed vs. the as-built 3D structures will be compared to evaluate how the imperfections in the fir-tree jointing system affect the overall buckling stability of three-dimensional structures.

## **Chapter 4: Finite Element Modeling of a Large Span Three-Dimensional Structure**

As stated in **Chapter 3**, in this research, the finite element method was chosen as a technique of analysis to predict the buckling behavior of three-dimensional structures as it provides more precise and faster results than conventional analysis. This chapter describes the finite element models of large span three-dimensional structures including the geometry, material properties, loads and boundary conditions, jointing system modeling, and the different models developed using the Patran/Nastran software (MSC 2014). Furthermore, selected results of the finite element analyses to be presented in **Chapters 5** and **Chapter 6** for the as-designed and as-built structures, respectively, are introduced during this chapter. These results will be used and compared in **Chapter 7** to quantify how manufacturing geometric imperfections of the jointing system influence the buckling behavior and capacity of three-dimensional structures.

## 4.1 Geometry

To create non-conventional and complex three-dimensional structural geometries using the Geometrica® 6Sd-00 fir-tree jointing system, tubular elements are constructed having different lengths and coined pressed ends having different angles of twist, angles of cut, and angles of bend (Geometrica® 2014). These physical parameters of the tubular element (shown in **Figure 4.1**) can have an impact in the buckling behavior and capacity of three-dimensional structures.

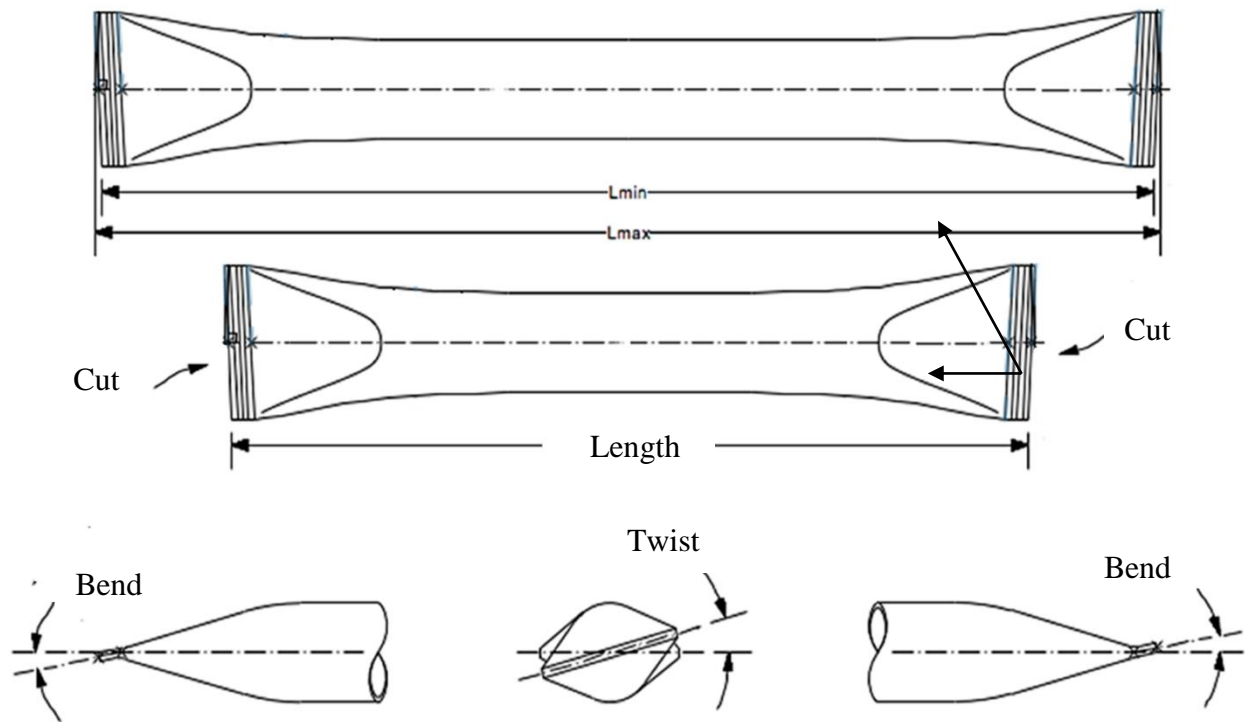


**Figure 4.1** Fir-Tree Jointing System Tubular Element Parameters

Since the main objective of this dissertation is to quantify how manufacturing geometric imperfections in the joints influence the buckling behavior of three-dimensional structures, it was preferred to model a structure with tubular elements having similar lengths and coined pressed ends with a minimum angle of twist, cut, and bends. This was accomplished by modeling a

structure having a hexagonal shape created by connecting linear elements to each of the six 60 degrees rotated slots of the Geometrica® 6Sd-00 connector (See **Figure 1.7**). As a result, the geometry configuration shown in **Figure 4.2** was chosen. The structure has a hexagonal shape with three rings, a span of 30 feet. (360 inches), and a height of 5 feet. (60 inches) at the central crown node; thus, having a rise to span ratio of 1/6. The modeled three-dimensional structure has a total of ninety beam elements and thirty-seven node connectors.

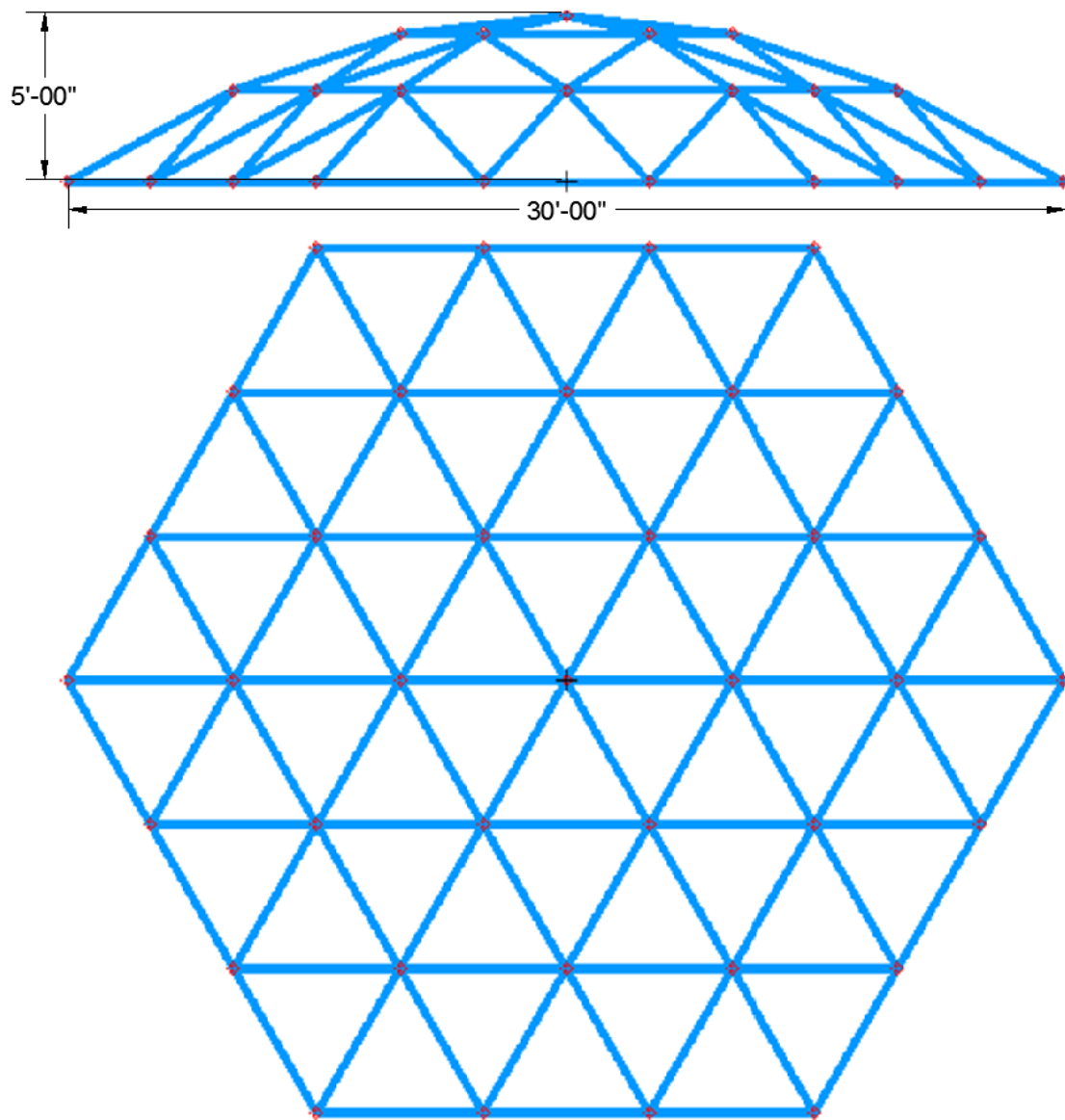


**Figure 4.2** Three-Dimensional Structure Finite Element Model

## 4.2 Material Properties

The different finite element models of the large span three-dimensional structure were developed considering:

- 1) The Geometrica® 2-3/8-inch-inch tube size with a 0.090-inch wall thickness of A500 Grade B steel;
- 2) The Geometrica® 6Sd-00 connector element made of A6061-T6 aluminum; and
- 1) The filler shim elements made of A6061-T6 aluminum.

To find the material properties, one coupon tension test for each of the materials was conducted following ASTM standards (ASTM 2016). The material stress-strain curves of the aluminum connector and filler shims elements and the steel tubular elements were obtained through the tension tests. **Figure 4.3** shows one of the tension tests in progress.

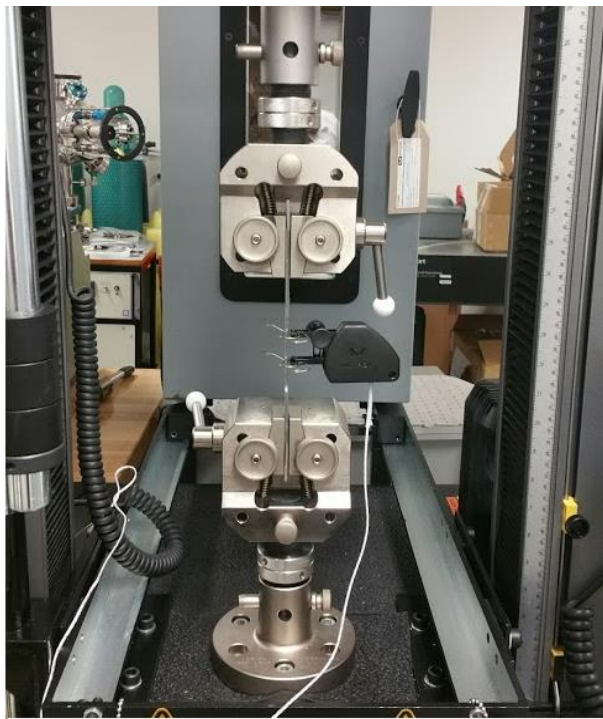


**Figure 4.3** ASTM Tension Test in Progress

**Figure 4.4** and **4.5** show the stress-strain curves of A6061-T6 aluminum and A-500 Grade B steel, respectively. These curves were smoothed to eliminate potential problems during the numerical non-linear finite element analysis.

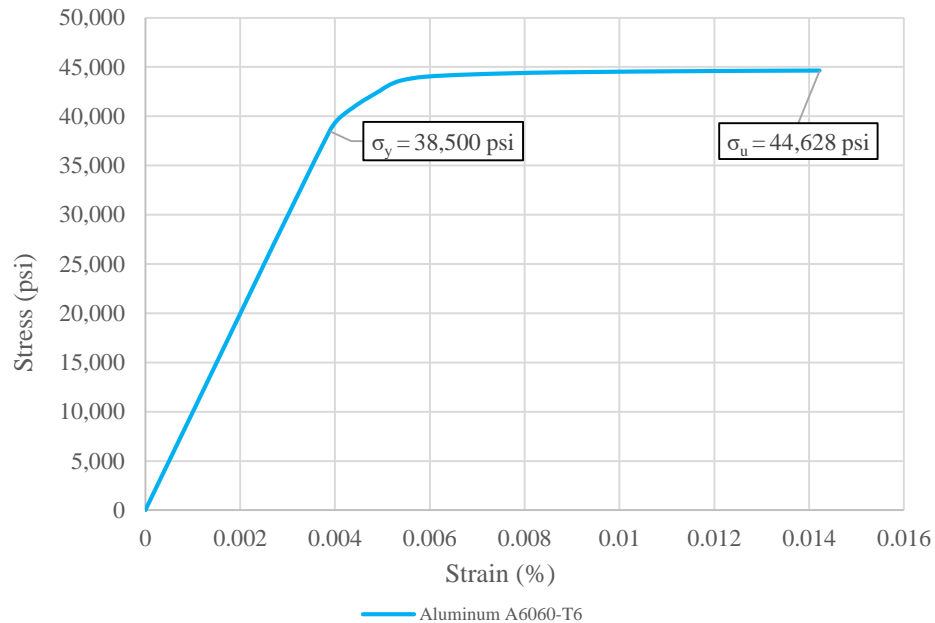


**Figure 4.4** Stress-Strain Curve of Aluminum A6061-T6

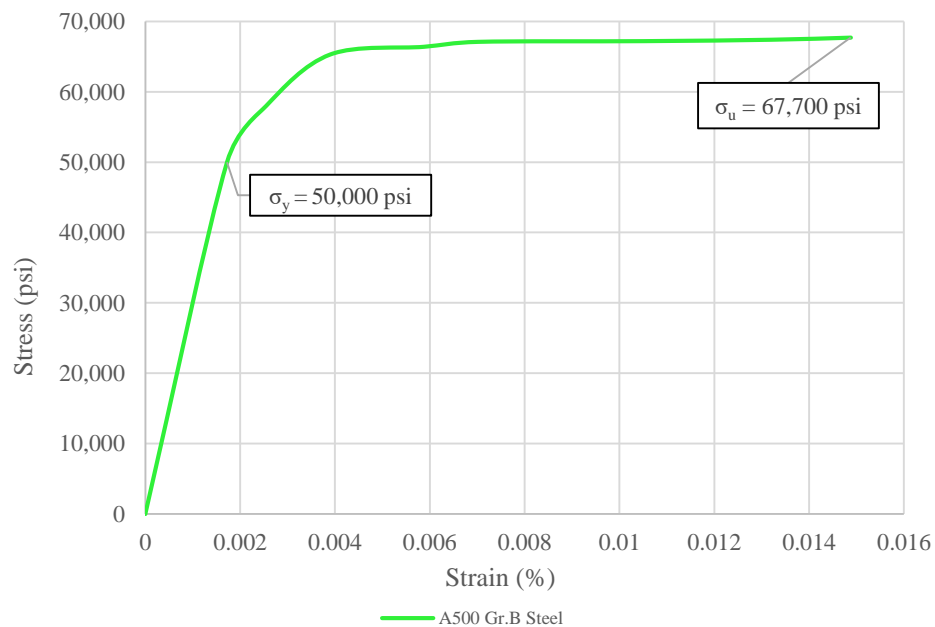


**Figure 4.5** Stress-Strain Curve of Steel A500 Grade B

The material stress-strain curves were used to estimate the elastic modulus (E), yield strength ( $\sigma_y$ ), and ultimate tensile strength ( $\sigma_u$ ) of the two materials. Results are shown in **Table 4.1**.

**Table 4.1** Material Properties of Structural Elements

| Component                                  | Material           | E(psi)*           | $\mu^+$ | $\sigma_y$ (psi)* | $\sigma_u$ (psi)* |
|--|--------------------|-------------------|---------|-------------------|-------------------|
| 6Sd-00 Connector                           | A6061-T6 Aluminum  | $9.9 \times 10^6$ | 0.34    | 38,500            | 44,628            |
| 2-3/8" x 0.090" Tube<br>Coined Pressed End | A500 Grade B Steel | $29 \times 10^6$  | 0.29    | 50,000            | 67,700            |
| 6Sd-00 Connector Filler<br>Shims           | A6061-T6 Aluminum  | $9.9 \times 10^6$ | 0.34    | 38,500            | 44,628            |

\* Obtained through experimental test.

+ Typical Poisson's ratio values (Ferregut and Carrasco 1998)

### 4.3 Boundary and Loading Conditions

As a case of study, the three-dimensional structures were modeled and analyzed using simply supported boundary conditions in the periphery nodes of the structure (as shown in **Figure 4.6**) and under snow loads.

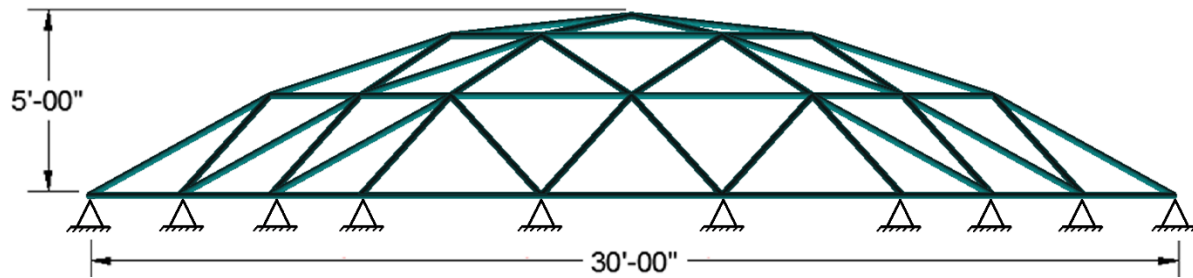


**Figure 4.6** Three-Dimensional Structure with Simply Supported Boundary Conditions

To estimate the magnitude of nominal snow loads, the Ferry County in Washington State was selected. For this study, the American Society of Civil Engineers 7-05 (ASCE 2006) provisions and data to determine the snow load magnitude were utilized as follows:

**Location:** Republic, Ferry County

**Elevation:** 2600'

**Ground Snow Load ( $P_g$ ):** 54.0 psf

**Building Type:** Unheated dry storage

**Building Exposure:** Forested (Sheltered)

**As per ASCE 7-05**

$$P_f = (0.7) (C_e) (C_t) (I) (P_g) \quad (4.1)$$

$C_e = 1.2$  (Terrain category B and sheltered)

$C_t = 1.2$  (Unheated dry storage)

$I = 1.0$  (Building category II)

$P_f = (0.7) (1.2) (1.2) (1.0) (54.0 \text{ psf}) = 54.4 \text{ psf}$

**Balance snow load**

$$P_s = (C_s) (P_f) \quad (4.2)$$

**Using Table 7-2c (ASCE 2006)**

$C_s = 1.0$  at  $15^\circ$

$P_s = (1.0) (54.4 \text{ psf}) = 54.4 \text{ psf}$ , use **54 psf**

$C_s = 0.71$  at  $30^\circ$

$P_s = (0.71) (54.4 \text{ psf}) = 38.624 \text{ psf}$ , use **39 psf**

$C_s = 0.63$  at  $35^\circ$  (structure eave)

$P_s = (0.63) (54.4 \text{ psf}) = 34.272 \text{ psf}$ , use **34 psf**

**Unbalanced snow load**

$a = \tan^{-1} (60''/180'') = 18.43^\circ$

$10^\circ < 18.43^\circ < 70^\circ$ , **therefore, unbalanced snow load must be considered**

$$P_s \text{ at crown} = (0.5) (P_f) \quad (4.3)$$

$$P_s = [(2) (P_f) (C_s)] / [C_e] \quad (4.4)$$

At crown point =  $0.5 (P_f) = (0.5) (54.4 \text{ psf}) = 27.2 \text{ psf}$ , use **27 psf**

At  $30^\circ$  point =  $[(2) (P_f) (C_s)] / [C_e] = [(2) (54.4 \text{ psf}) (0.71)] / [1.2] = 64.4 \text{ psf}$ , use **64 psf**

At  $35^\circ$  point =  $[(2) (P_f) (C_s)] / [C_e] = [(2) (54.4 \text{ psf}) (0.63)] / [1.2] = 57.12 \text{ psf}$ , use **57 psf**

Since the angle between the eave and the crown of the modeled 3D structures is between  $10^\circ$  and  $70^\circ$ , unbalanced snow loads were considered in the present study. **Figure 4.7** shows the calculated nominal unbalanced loading conditions applied to the three-dimensional structure models.

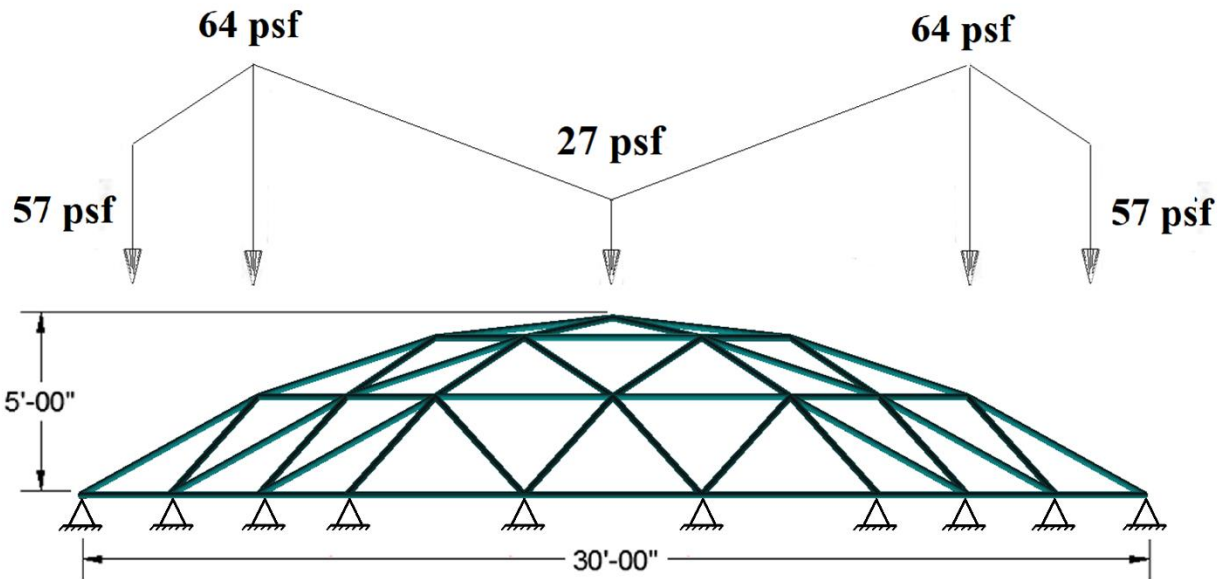


**Figure 4.7** Three-Dimensional Structure under Base Snow Load

However, since the actual nominal snow loads were not large enough make the structures reach their critical buckling capacity, the actual magnitude of the calculated snow loads, shown in **Figure 4.7**, were incremented by a factor of five (applied load was incremented 500%) in all simulations conducted in this investigation. Therefore, during the finite element simulations, first, the actual nominal snow load was applied from 0% to 100% (base calculated load); afterwards, the incremented snow loads were applied from 100% up to 500% or until the structures reached critical buckling capacity.

#### 4.4 Jointing System Modeling

To quantify how manufacturing geometric imperfections of the jointing system influence the buckling behavior and capacity of three-dimensional structures, the jointing system behavior was modeled in two ways being:

- 1) As-designed semi-rigid behavior; and
- 2) As-built semi-rigid behavior.

A total of eleven different models were developed for the 3D structure with 0.090-inch tube thickness, as described in the following list and shown in **Figure 4.8**:

- 1) A model with as-designed semi-rigid jointing system connection;
- 2) Nine models with each as-built semi-rigid jointing system connections (AA-CC; see **Table 2.3**); and
- 3) Also, one three-dimensional structure model was generated by randomly combining all the as-built jointing system connections; this analysis was performed to examine if different stiffness, in each of the joints, produce a larger impact on the buckling behavior/capacity on the three-dimensional structures.

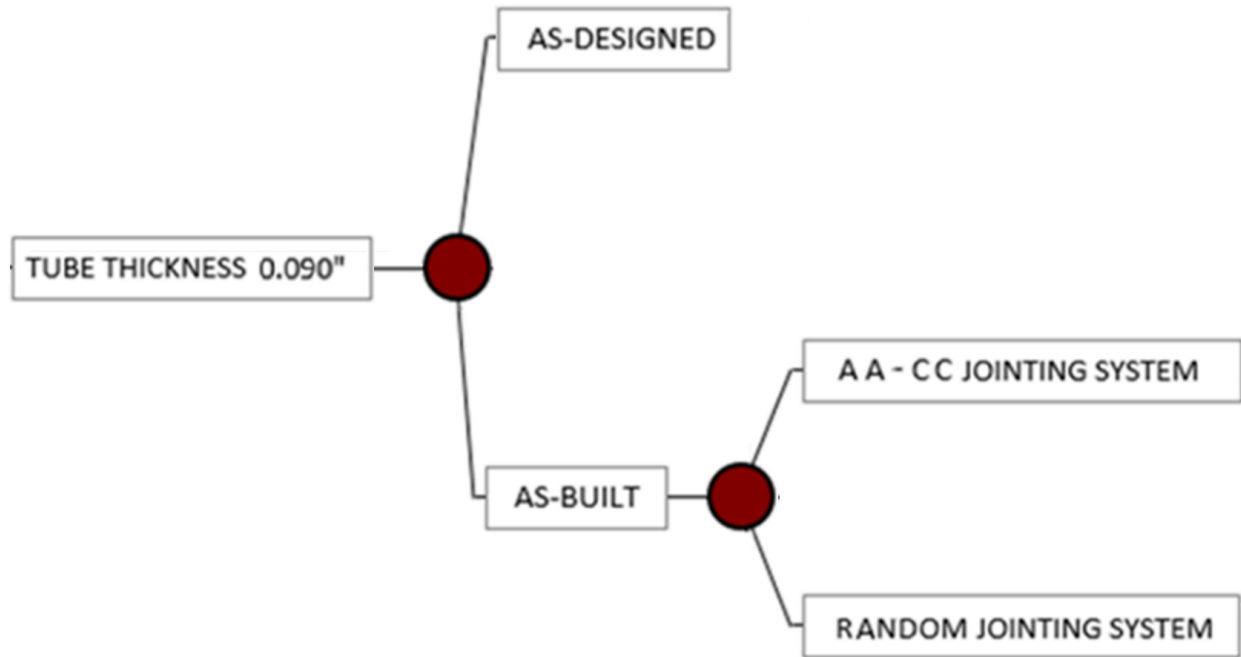


**Figure 4.8** Developed FEM of the Three-Dimensional Structure

From now on, a common terminology will be used to designate the different models in this dissertation. The large span three-dimensional structure models can be defined by the following details: (1) the type of connection considered (“d” for as-designed and “b” for as-built); (2) combination of tube-connector components (used only for as-built terminology); and (3) the tubular thicknesses (0.090 inches). For example:

- 1) d-090 is the 3D structure with as-designed jointing system connections and 0.090-inch tube thickness;
- 2) b-CB 090 defines a 3D structure with as-built jointing system connector C and tube B with a thickness of 0.090 inches; and
- 3) b-RD 090 defines the model with a random combination of as-built jointing system with a tube thickness of 0.090 inches.

#### 4.4.1 Modeling of the Semi-Rigid Jointing System

As explained in **Section 3.2.4.2**, to simulate the semi-rigid characteristics of the as-designed and/or the as-built jointing system, non-linear spring elements (Nastran CBUSH elements) with axial and in-plane rotational stiffness properties were added at the end of each CBEAM element. These spring elements had a length equivalent to the radius of the connector. **Figure 4.9** and **4.10** display the typical semi-rigid behavior curves of the Geometrica® 6Sd-00 connections obtained from the research conducted by Garcia (2017) and included in the models of the 3D structures. **Figure 4.9** shows a typical axial semi-rigid behavior of the jointing system modeled into the properties of the spring elements which composed of two main zones. Zone 1 is the initial flat portion which represents the fit-gap tolerance between the mating parts of the jointing system. Zone 2 is observed once the mating parts become in contact, creating a non-linear tension or compression load vs. displacement behavior of the connection.

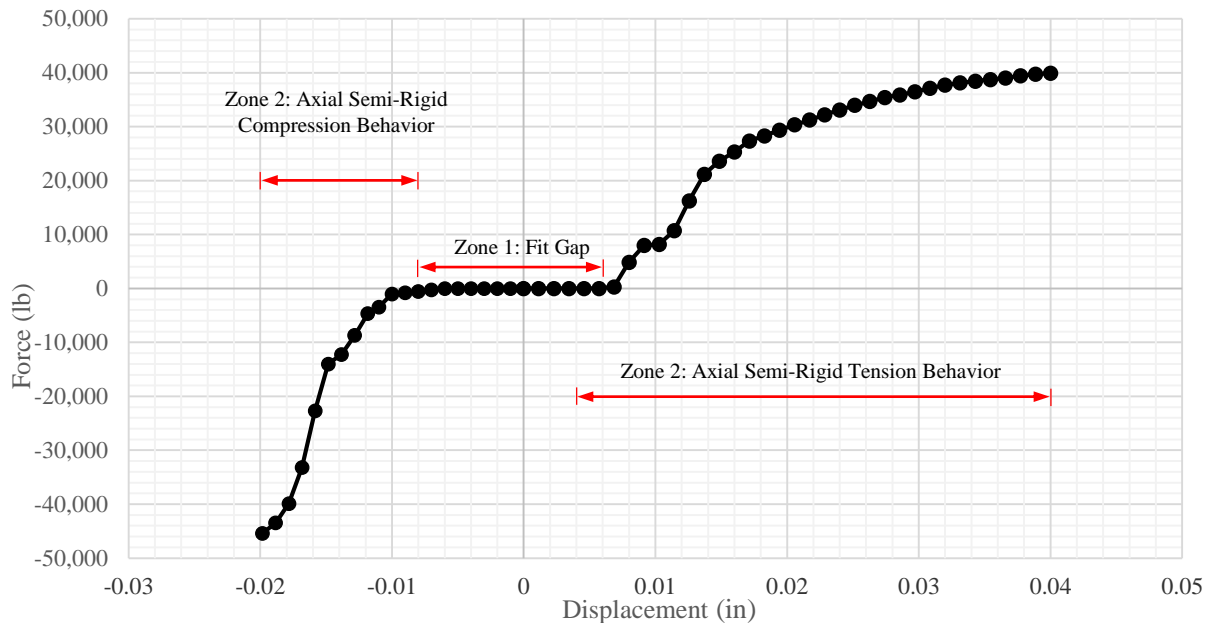


**Figure 4.9** Typical Axial Stiffness of the Jointing System (After Garcia 2017)

**Figure 4.10** shows a typical in-plane bending stiffness semi-rigid behavior of the jointing system modeled into the properties of the spring elements. This typical in-plane bending behavior is composed of two main zones. Zone 1 is the initial flat portion which represents the fit-gap tolerance between the mating parts of the jointing system. Zone 2 is observed once the mating parts become in contact, creating a non-linear bending moment vs. rotation behavior of the connection.

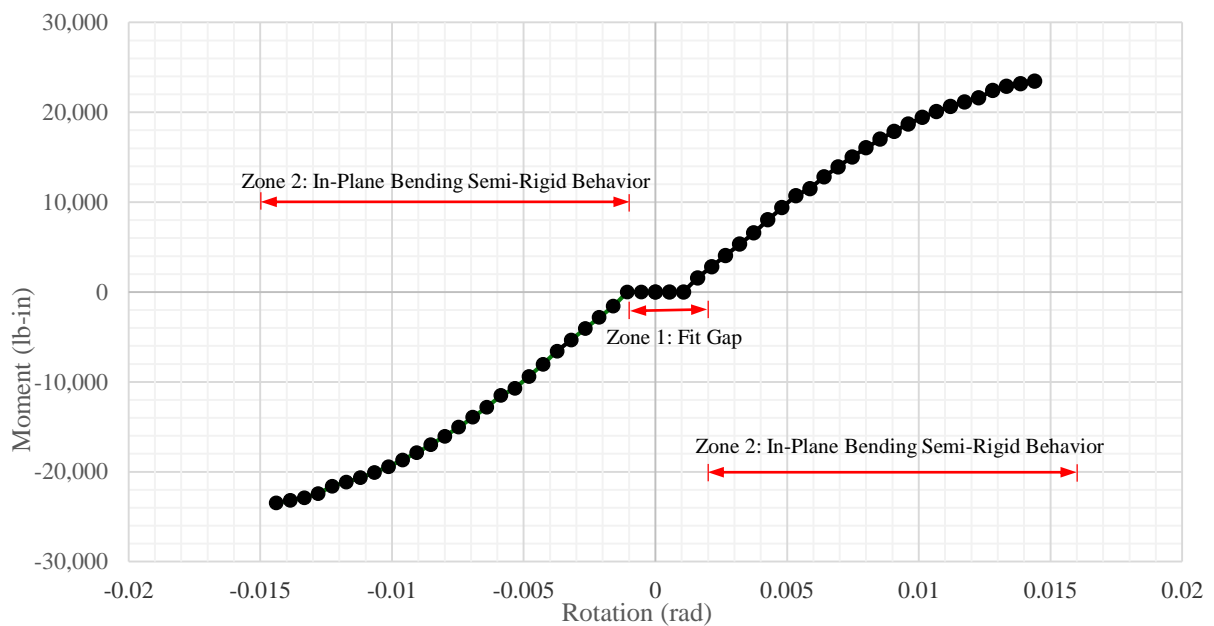


**Figure 4.10** Typical In-Plane Bending Stiffness of the Jointing System (After Garcia 2017)

**Table 4.2** shows the Patran/Nastran elements utilized to model the large span three-dimensional structures part of this dissertation.

**Table 4.2** Patran/Nastran Elements to Model Three-Dimensional Structures

| Three-Dimensional Structure<br>Element            | Patran/Nastran<br>Element | Nastran Properties |
|---|---------------------------|--------------------|
| Tubular bars                                      | CBEAM                     | PBEAM              |
| Semi-Rigid Jointing System<br>(Non-Linear Spring) | CBUSH                     | PBUSH              |

#### 4.5 Selected Finite Element Simulation Results

A non-linear finite element analysis was conducted on each the eleven previously mentioned models. From the simulations, one of the beam elements experiencing higher compression forces (element 62), was chosen to inspect its efficiency through the applied load-beam interaction index (see **Section 4.5.2**). Besides, one the extreme nodes of this beam element was chosen to inspect its applied load-displacement history (node 13), while the other extreme node of this beam element was chosen to inspect its applied load-rotation history (node 2). **Figure 4.11** displays the chosen beam and node elements. The selected elements and their stresses, displacements, and rotations obtained from the simulations of the structures modeled the as-designed behavior of the jointing system (shown in **Chapter 5**), and the as-built behavior of the jointing system (shown in **Chapter 6**) will be compared in **Chapter 7** to quantify how the manufacturing geometric imperfections influence the buckling behavior of three-dimensional structures.

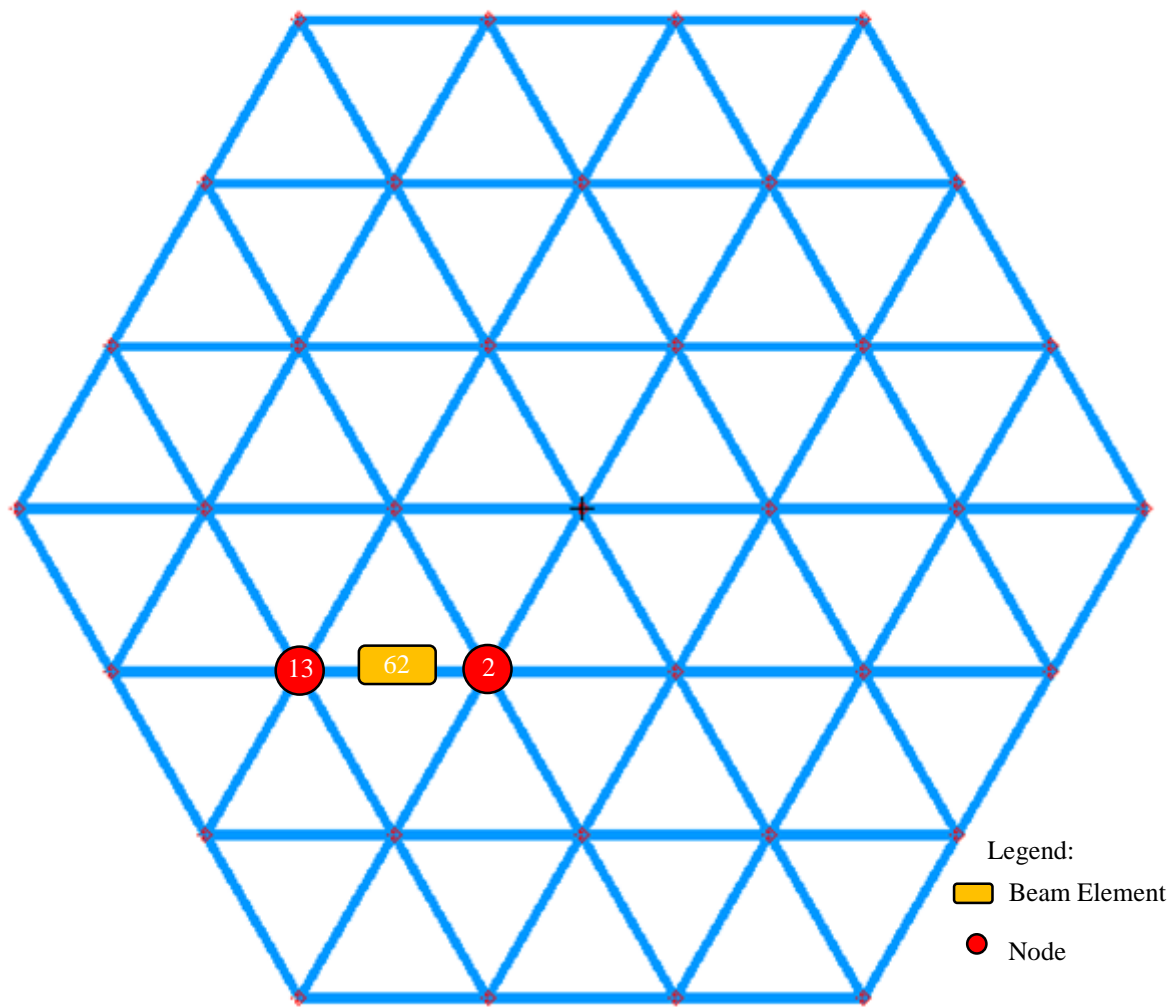


**Figure 4.11** Selected Members of the Structure to Study

#### 4.5.1 Applied Load-Displacement and Applied Load-Rotation

Elasto-plastic buckling load is defined as the maximum point in the load-deformation equilibrium path/curve taking into account both the material nonlinear properties and the geometrical nonlinearity (Mohammadi et al. 2012). Considering this concept, the percent applied load vs. displacement (in) and rotation (rad) curves and tabulated data of the selected nodes, from initial loading until critical load is reached, were obtained and are shown **Chapters 5** for the as-designed structures and **in Chapter 6** for the as-built structures.

#### 4.5.2 Applied Load-Interaction Index

Members subjected to axial compression and bending moment forces are referred as beam-column elements. The effect of combined loading leads to a buckling instability of the beam-column members at lower forces as compared to members loaded under compression forces only (Salmon et al. 2009). Since tubular bars in three-dimensional structures behave as members subjected to axial and bending forces, the interaction index for the selected bar was obtained from the finite element simulation results. To obtain the interaction index in both extreme nodes (nodes 13 and 2) of the chosen bar, the LRFD American Institute of Steel Construction (AISC 2005) equations were utilized as follows:

First, it was required to obtain the designed buckling strength of the tubular beams as follows:

#### Designed Buckling Strength of Beam Members

$$\phi P_{nx} = (0.90)(F_{cr})(A_g) \quad (4.5)$$

#### Critical Stress ( $F_{cr}$ ) of Beam Members Equation 1

$$\text{For } \frac{(K)(L)}{r} \leq 4.71 \sqrt{\frac{E}{F_y}}; \quad F_{cr} = \left(0.658 \frac{F_y}{F_e}\right) (F_y) \quad (4.6)$$

#### Critical Stress ( $F_{cr}$ ) of Beam Members Equation 2

$$\text{For } \frac{(K)(L)}{r} > 4.71 \sqrt{\frac{E}{F_y}}; \quad F_{cr} = (0.877)(F_e) \quad (4.7)$$

#### Elastic Buckling Stress ( $F_e$ ) of Beam Members

$$F_e = \frac{(\pi^2)(E)}{\left(\frac{(K)(L)}{r}\right)^2} \quad (4.8)$$

where  $A_g$  is gross area of member,  $F_y$  is the yield stress of member material,  $E$  is the modulus of elasticity of the member material,  $K$  is the effective length factor (taken as 1.0),  $L$  is the length of the member, and  $r$  is the radius of gyration of member.

Then, the interaction index was computed using the following equations:

Interaction Index Equation 1

$$\text{For } \frac{P_{ux}}{\phi P_{nx}} \geq 0.2; \quad \frac{P_{ux}}{\phi P_{nx}} + \frac{8}{9} \left( \frac{M_{uy}}{\phi M_{ny}} + \frac{M_{uz}}{\phi M_{nz}} \right) \leq 1 \quad (4.9)$$

Interaction Index Equation 2

$$\text{For } \frac{P_{ux}}{\phi P_{nx}} < 0.2; \quad \frac{P_{ux}}{2\phi P_{nx}} + \left( \frac{M_{uy}}{\phi M_{ny}} + \frac{M_{uz}}{\phi M_{nz}} \right) \leq 1 \quad (4.10)$$

where the designed bending strength of the beam members about the Y axis is calculated as follows:

$$\phi M_{ny} = (0.90)(F_y)(Z_y) \quad (4.11)$$

And the designed bending strength of the beam members about the Z axis is calculated as follows:

$$\phi M_{nz} = (0.90)(F_y)(Z_z) \quad (4.12)$$

where  $P_{ux}$  is the compression force of the beam member,  $M_{uy}$  is the moment about the Y axis of the beam member,  $M_{uz}$  is the moment about the Z axis of the beam member,  $Z_y$  is the plastic modulus of the beam member about the Y axis, and  $Z_z$  is the plastic modulus of the beam member about the Z axis.

Once the interaction index reaches a value of 1.0 in any of the two extreme nodes, the material strength of the column-beam element has reached capacity and failed. Therefore, the interaction index in the node experimenting higher stresses during all simulations (node 13) was computed and recorded at 25% applied load increments until the three-dimensional structure models reached their critical buckling capacity.

The finite element modeling of a large span three-dimensional structure and the different models developed during this dissertation were presented in this chapter. Also, the selected elements and their FEA results were introduced. These results are presented in **Chapters 5 and 6** for the as-designed and as-built structures, respectively. In **Chapter 7**, these results will be the base of comparison to quantify how manufacturing geometric imperfections of the jointing system influence the buckling behavior of three-dimensional structures.

## Chapter 5: Finite Element Simulation Results: As-Designed Structures

This chapter presents the finite element simulation results of the 3D structure modeled with as-designed jointing system connections and 0.090-inch tube thickness: d-090.

The results obtained from the finite element simulation include:

- 1) The applied load-displacement graph and tabulated data of node 13;
- 2) The applied load-rotation graph and tabulated data of node 2; and
- 3) The applied load-interaction index graph and tabulated data of beam element 62. This index was obtained from the extreme node of the beam experimenting higher stresses (node 13).

To include the semi-rigid characteristics of the as-designed jointing system connections, non-linear spring elements with axial (tension and compression) and in-plane rotational stiffness at the end of each beam element were used. The force-displacement and moment-rotation curves used during the simulation are also presented in this chapter.

In **Appendix A**, tables with the displacement, rotation, and bar efficiency data of the selected elements are presented at 25% load increments until critical load percentage is reached.

## 5.1 Applied Load-Displacement

**Figure 5.1** presents the applied load-displacement history graph of node 13 for the d-090 3D structure. In this plot, the vertical axis corresponds to the applied load history expressed in percentage while the horizontal axis displays the resultant displacement of the node in inches as the load is applied.

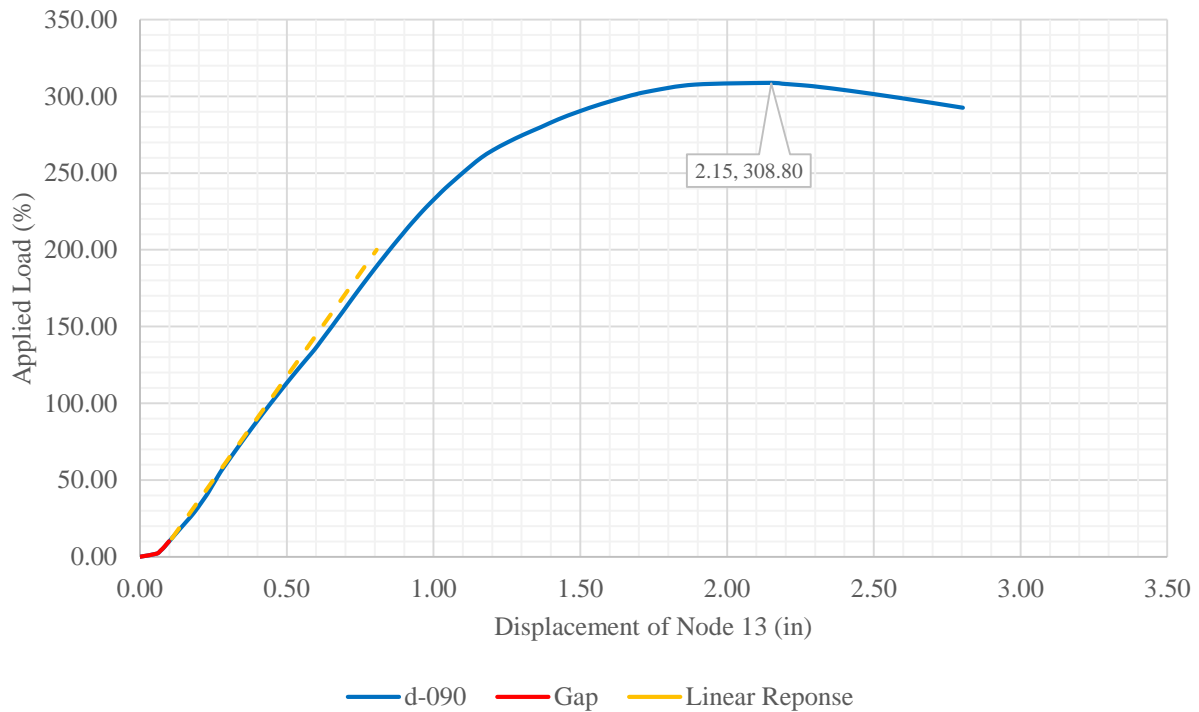


**Figure 5.1** Applied Load-Displacement of Node 13: d-090 3D Structure

In the 3D structure modeled with as-designed connections and 0.090-inch tube thicknesses, the applied load-displacement history graph of node 13 displays a non-linear response under initial loading which indicates the movement/closing of the jointing systems' gaps. After initial loading, the structure follows a linear response up to 150% of the load. Subsequently, the structure follows a non-linear behavior until critical capacity is reached at 308.80% of the applied load and at a displacement of 2.15 inches. Overall buckling is observed after critical capacity is reached.

## 5.2 Applied Load-Rotation

**Figure 5.2** presents the applied load-rotation history graph of node 2 for the d-090 3D structure. In this plot, the vertical axis corresponds to the applied load history expressed in percentage while the horizontal axis shows the resultant rotation of the node in radians as the load is applied.

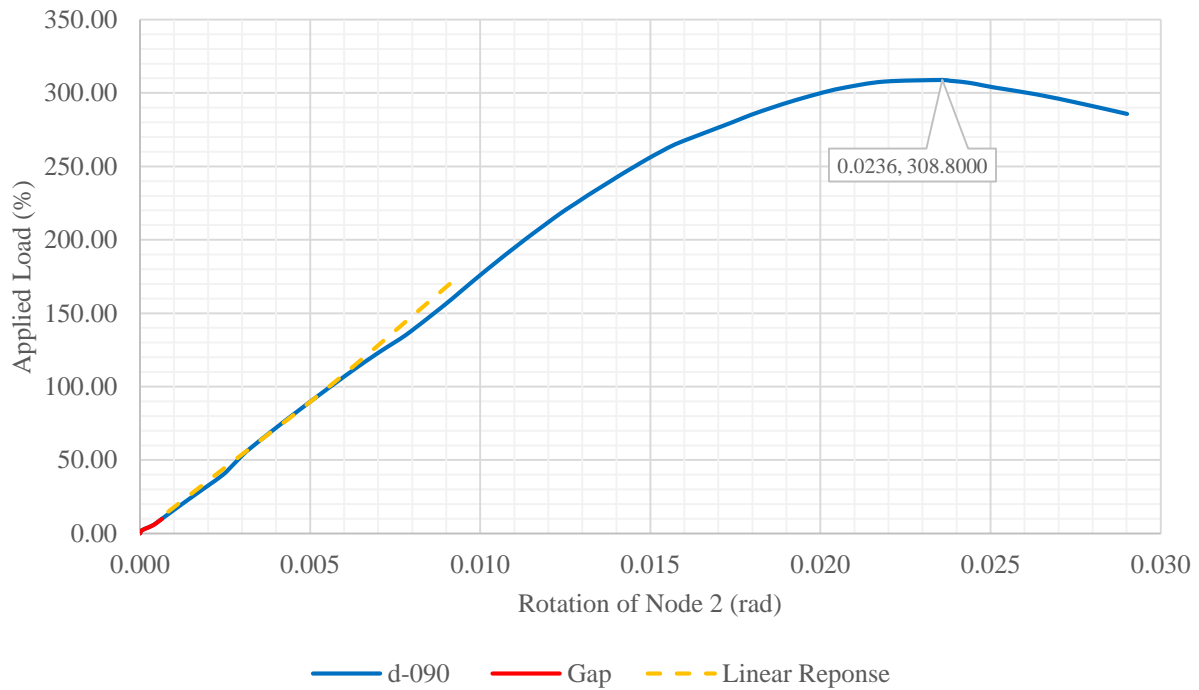


**Figure 5.2** Applied Load-Rotation of Node 2: d-090 3D Structure

In the 3D structure modeled with as-designed connections and 0.090-inch tube thicknesses, the applied load-rotation history plot of node 2 displays a non-linear response under initial loading which indicates the movement/closing of the jointing systems' gaps. After initial loading, the structure follows a linear response up to 150% of the load. Subsequently, the structure follows a non-linear response until critical capacity is reached at 308.80% of the applied load and at a rotation of 0.0236 radians. Overall buckling is observed after critical capacity is reached.

### 5.3 Applied Load-Interaction Index

**Figure 5.3** presents the applied load-interaction index plot of beam element 62 for the d-090 3D structure. In this graph, the vertical axis corresponds to the applied load history expressed in percentage while the horizontal axis shows the interaction index of the beam element as the load is applied. As in the load-displacement and load-rotation graphs of the d-090 3D structure, the applied load-interaction index graph displays a non-linear response under initial loading which indicates the movement/closing of the jointing systems' gaps. After initial loading, the applied load-interaction index plot of beam element 62 shows a linear response up to 150% of the applied load. Subsequently, a non-linear behavior of the element is observed until failure of the beam is reached at 241.47% of the applied load.

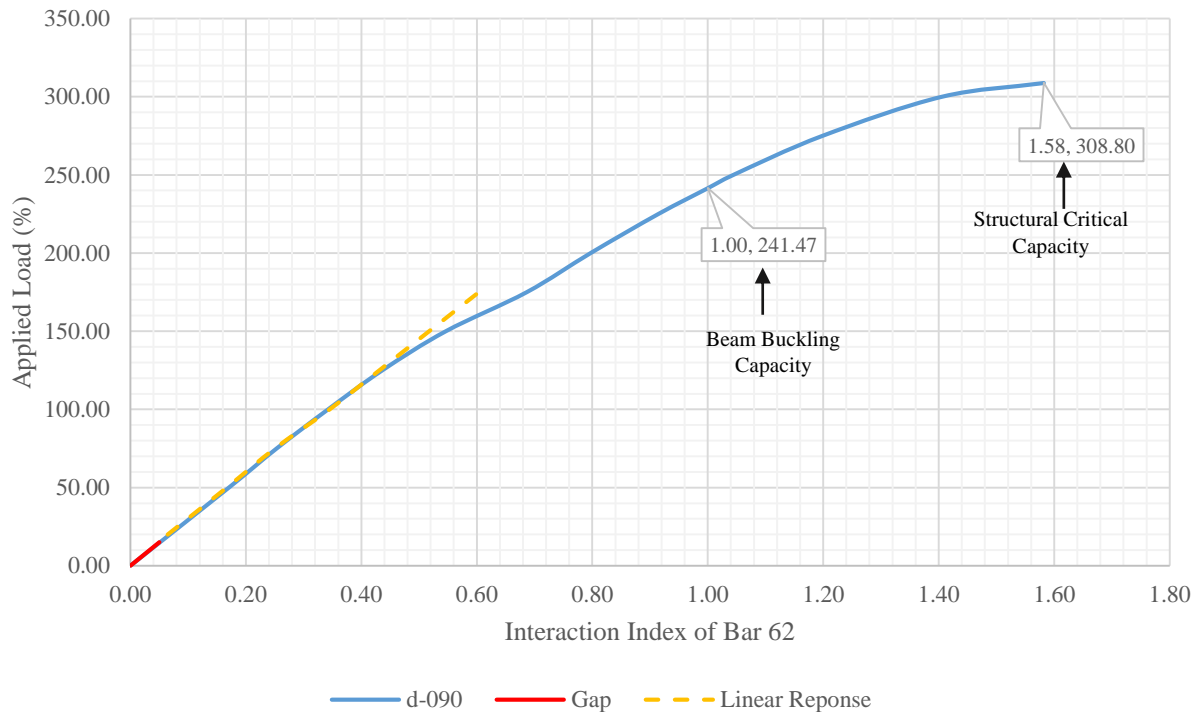


**Figure 5.3** Applied Load-Interaction Index of Beam Element 62: d-090 3D Structure

The axial compression forces and bending moments of beam element 62 in the d-090 3D structure at bar failure are:

- 1)  $P_{ux}$  is 9,609.94 lb.;
- 2)  $M_{uy}$  is 829.99 lb.-in; and
- 3)  $M_{uz}$  is 15,020.74 lb.-in.

As described in **Section 4.5.2**, in this investigation the compression force ( $P_{ux}$ ), moment about the Y axis ( $M_{uy}$ ), and moment about the Z axis ( $M_{uz}$ ) were considered to obtain the interaction index and failure load of beam element 62. In three-dimensional structures, these beam forces and moments are transferred to the connections. Therefore, the forces and moments experimented in the node with higher stresses (node 13) of the beam element 62 were compared with the force-displacement and moment-rotation curves used during the simulations to capture what proportion of the connection capacity is used when the beam element reaches failure load.

**Figure 5.4** shows the axial semi-rigid behavior of the jointing system used during the simulation of the d-090 3D structure. In this plot, the initial flat portion represents the fit-gap tolerance between the mating parts of the jointing system. Once the mating parts become in contact, a non-linear tension or compression load vs. displacement behavior of the connection is observed. Additionally, **Figure 5.4** displays that at beam failure, only 21.12% of the connection capacity in compression is reached.

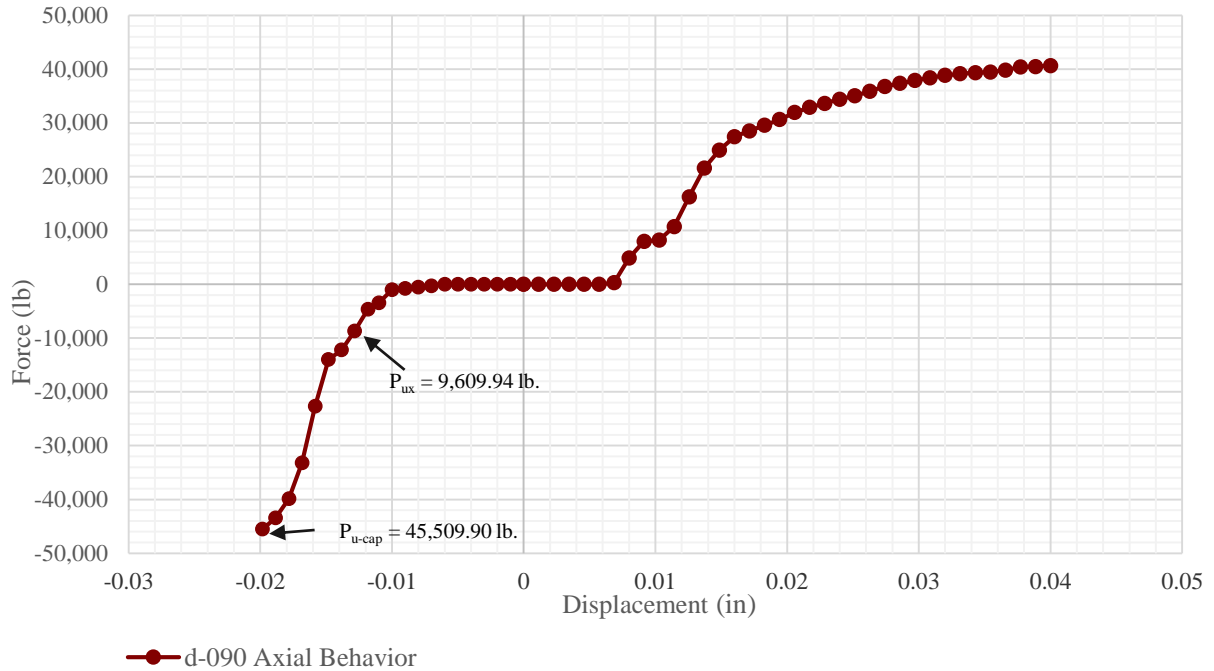


**Figure 5.4** Axial Semi-Rigid Behavior: d-090 (After Garcia 2017)

**Figure 5.5** shows the in-plane bending semi-rigid behavior of jointing system used during the simulation of the d-090 3D structure. In this plot, the initial flat portion represents the in-plane fit-gap tolerance between the mating parts of the jointing system. Once the mating parts become in contact, a non-linear bending moment vs. rotation behavior of the connection is observed. Additionally, **Figure 5.5** displays that at beam failure, only 3.13% of the connection in-plane bending capacity is reached.

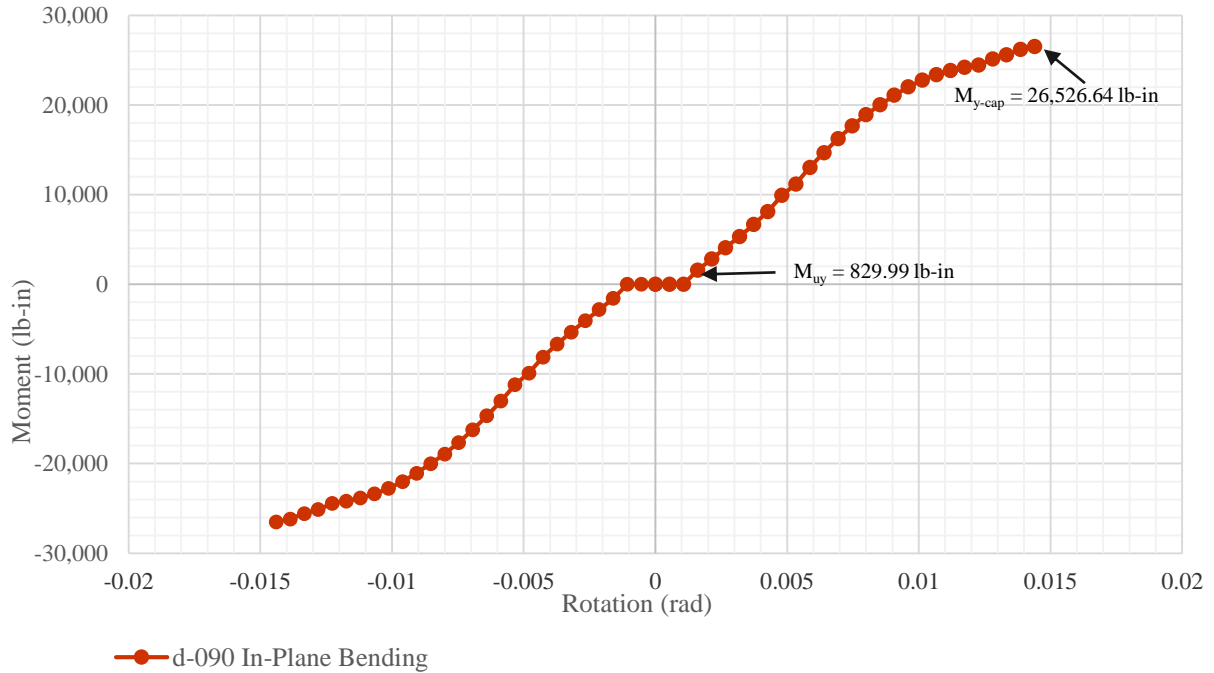


**Figure 5.5** In-Plane Bending Semi-Rigid Behavior: d-090 (After Garcia 2017)

In the 3D structure modeled with as-designed connections and 0.090-inch tube thicknesses, the buckling failure of the beam element occurs before the connection reaches its axial and moment capacity; thus, indicating that failure occurs due to beam member's ends buckling and not because of connection failure. Also, it can be noted that, even when the beam element has reached failure capacity, the redundancy of the structure allows the loads to be redistributed to adjacent members and node connections allowing the structure to keep carrying loads and avoiding catastrophic collapse (Fang and Fan 2011).

In **Chapter 7**, the results of the structures modeled with the as-designed behavior of the jointing systems (presented in this chapter) will be compared with the results or the structures modeled with as-built behavior of the jointing systems (presented in **Chapter 6**) to quantify how manufacturing geometric imperfections influence the buckling behavior of 3D structures.

## Chapter 6: Finite Element Simulation Results: As-Built Structures

**Section 2.6.3** describes how Garcia (2017) obtained the axial and in-plane bending semi-rigid behavior of the as-built Geometrica® 6Sd-00 fir-tree jointing system using three tubular thicknesses being: 0.090 inches, 0.104 inches, and 0.120 inches. During this research, only the semi-rigid properties of the as-built jointing systems composed the Geometrica® connector and a tube with a thickness of 0.090 inches were utilized to obtain the buckling behavior of the modeled 3D structures. A total of 10 different models were developed for the as-built structures (referred as model set) as follows:

- 1) Nine models with as-built semi-rigid jointing system connections (b-AA to b-CC); and
- 2) One 3D structure model was generated by randomly combining all the as-built jointing system connections. This analysis was performed to examine if different stiffness, in each of the joints, produce a larger impact on the buckling behavior/capacity on the 3D structures.

To include the semi-rigid characteristics of the as-built jointing system connections, non-linear spring elements with axial and in-plane rotational stiffness at the end of each beam element were used. A different spring stiffness was utilized for each of the 3D structure models.

For each of the finite element simulations, the results include:

- 1) The applied load-displacement graph and tabulated data of node 13;
- 2) The applied load-rotation graph and tabulated data of node 2; and
- 3) The applied load-interaction index graph and tabulated data of beam element 62. This index was obtained from the extreme node of the beam experimenting higher stresses (node 13).

The complete set of results for the ten three-dimensional structure models with as-built jointing system and tube thickness of 0.090 are shown in **Appendix B**.

This chapter presents the tabulated results of the ten 3D structures modeled with as-built connections and 0.090-inch tubular thickness. From the results, statistical information of the following data was obtained:

- 1) Displacement of node 13;
- 2) Rotation of node 2;
- 3) Critical load capacity of the structures;
- 4) Interaction index of beam element 62; and
- 5) Buckling load of the beam element 62.

The statistical parameters computed includes the:

- 1) Mean value ( $\mu$ ) to illustrate the central tendency of the data;
- 2) Standard deviation ( $\sigma$ ) to describe the dispersion of values; and
- 3) Coefficient of Variation (COV) to obtain a non-dimensional estimation of the dispersion of values in relation to the mean value.

## 6.1 Applied Load-Displacement: b-090 3D Structures Model Set

**Table 6.1** presents the tabulated data of the applied load-displacement history of node 13 from initial loading until critical capacity is reached at 25% load increments for the b-090 3D structures model set simulations. Besides, this table presents the mean, standard deviation, and COV of the:

- 1) Displacements of the model set at every load increment;
- 2) Load critical capacity of the model set; and
- 3) Displacement of the model set at load critical capacity.

**Table 6.1** Applied Load-Displacement and Statistical Properties of Node 13: b-090 3D Structures Model Set

| Structure         |      | Applied Load (%) |       |       |       |        |        |        |        |        |        |        |        |        | Crit. Load (%) | Crit. Disp. (in) |
|-------------------|------|------------------|-------|-------|-------|--------|--------|--------|--------|--------|--------|--------|--------|--------|----------------|------------------|
|                   |      | 0.00             | 25.00 | 50.00 | 75.00 | 100.00 | 125.00 | 150.00 | 175.00 | 200.00 | 225.00 | 250.00 | 275.00 | 300.00 |                |                  |
| Displacement (in) | b-AA | 0.000            | 0.152 | 0.235 | 0.323 | 0.418  | 0.517  | 0.605  | 0.698  | 0.797  | 0.904  | 1.037  | 1.226  | 1.568  | 310.31         | 1.870            |
|                   | b-AB | 0.000            | 0.159 | 0.245 | 0.342 | 0.444  | 0.550  | 0.665  | 0.780  | 0.898  | 1.028  | 1.187  | 1.455  | 1.970  | 301.81         | 2.267            |
|                   | b-AC | 0.000            | 0.160 | 0.249 | 0.346 | 0.448  | 0.553  | 0.666  | 0.782  | 0.891  | 1.007  | 1.143  | 1.353  | 1.768  | 305.97         | 2.052            |
|                   | b-BA | 0.000            | 0.161 | 0.245 | 0.334 | 0.427  | 0.525  | 0.628  | 0.720  | 0.819  | 0.932  | 1.074  | 1.285  | 1.661  | 308.34         | 2.141            |
|                   | b-BB | 0.000            | 0.174 | 0.263 | 0.359 | 0.457  | 0.568  | 0.687  | 0.814  | 0.943  | 1.073  | 1.236  | 1.507  | -      | 299.90         | 2.221            |
|                   | b-BC | 0.000            | 0.174 | 0.262 | 0.360 | 0.460  | 0.528  | 0.610  | 0.771  | 0.913  | 1.028  | 1.168  | 1.399  | 1.881  | 303.47         | 2.158            |
|                   | b-CA | 0.000            | 0.161 | 0.244 | 0.332 | 0.426  | 0.490  | 0.567  | 0.647  | 0.814  | 0.925  | 1.064  | 1.266  | 1.622  | 309.46         | 2.066            |
|                   | b-CB | 0.000            | 0.184 | 0.274 | 0.362 | 0.458  | 0.567  | 0.678  | 0.792  | 0.912  | 1.045  | 1.208  | 1.466  | 2.035  | 301.21         | 2.138            |
|                   | b-CC | 0.000            | 0.166 | 0.255 | 0.354 | 0.457  | 0.564  | 0.678  | 0.800  | 0.908  | 1.024  | 1.163  | 1.384  | 1.834  | 304.13         | 2.191            |
|                   | b-RD | 0.000            | 0.154 | 0.236 | 0.325 | 0.419  | 0.520  | 0.627  | 0.733  | 0.840  | 0.957  | 1.102  | 1.320  | 1.738  | 302.06         | 1.812            |
| Statistical Data  | μ    | 0.000            | 0.164 | 0.251 | 0.344 | 0.441  | 0.538  | 0.641  | 0.754  | 0.873  | 0.992  | 1.138  | 1.366  | 1.787  | 304.66         | 2.091            |
|                   | σ    | 0.000            | 0.010 | 0.013 | 0.015 | 0.017  | 0.026  | 0.040  | 0.053  | 0.051  | 0.058  | 0.066  | 0.093  | 0.158  | 3.672          | 0.148            |
|                   | COV  | -                | 0.060 | 0.050 | 0.043 | 0.039  | 0.049  | 0.062  | 0.070  | 0.059  | 0.058  | 0.058  | 0.068  | 0.089  | 0.012          | 0.071            |

The following conclusions are obtained from information of the applied load-displacement history of node 13 of the b-090 3D structures model set presented in **Table 6.1**:

- A low COV of nodal displacements fluctuating from 3.90% to 8.90% is observed at all load increments. At critical load, the COV of the displacement is 7.10%. Therefore, it can be concluded that the nodal displacements display a low dispersion in relation to the mean value from initial loading until buckling load is reached;
- The COV of the critical capacity is 1.20%; therefore, it can be concluded that manufacturing imperfections do not produce a significant impact in the buckling capacity among the b-090 3D structures model set; and
- It can be noted that the b-RD 3D structure model, with different as-built stiffness in each of the joints, shows similar displacements and fails at a slightly smaller load as compared to the mean failure load of the b-090 model set. These results indicate that modeling the 3D structures with different joint system behaviors in each of the connections do not produce a larger negative impact on the nodal displacement behavior and capacity of the 0.090-inch tube thickness as-built structures.

**Figure 6.1** presents a value plot of the applied load-displacement history of node 13 of the b-090 3D structures model set (b-AA – b-CC and b-RD) simulations at 25% applied load increments until critical load is reached in each of the simulations. Besides, the model set mean applied load-displacement history of node 13 is presented in this illustration.

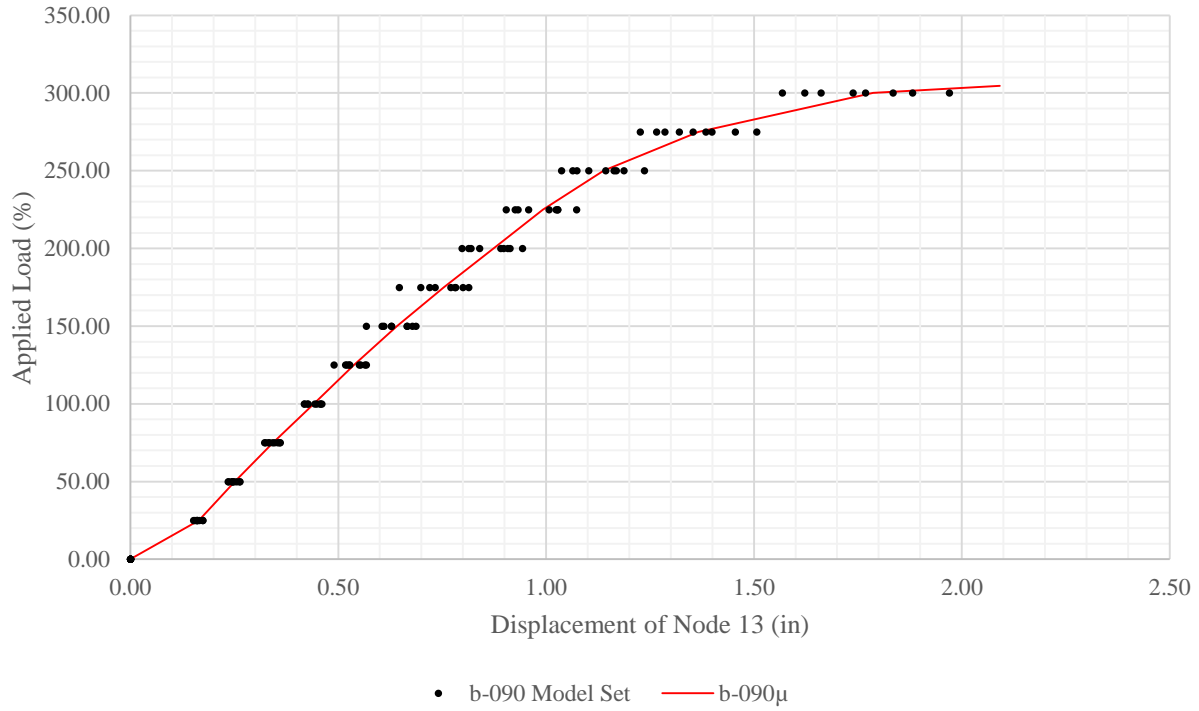


**Figure 6.1** Applied Load-Displacement of Node 13: b-090 3D Structures Model Set

Since the b-090 3D structures model set shows a low spread of values in relation to the central tendency of nodal displacements and critical capacity, the mean behavior of node 13, shown in **Figure 6.1**, will be used to represent the as-built applied load-displacement history of node 13 and will be referred as nodal displacement of the b-090μ 3D structure in **Chapter 7**.

## 6.2 Applied Load-Rotation: b-090 3D Structures Model Set

In **Table 6.2**, the results of the applied load-rotation history of node 2 from initial loading until critical capacity is reached at 25% load increments in each of the 3D structures of the b-090 model set are presented. Additionally, this table displays the mean, standard deviation, and COV of the:

- 1) Rotations of the model set at every load increment;
- 2) Load critical capacity of the model set; and
- 3) Rotation of the model set at critical capacity.

**Table 6.2** Applied Load-Rotation and Statistical Properties of Node 2: b-090 3D Structures Model Set

| Structure        |      | Applied Load (%) |        |        |        |        |        |        |        |        |        |        |        |        | Crit. Load (%) | Crit. Rot (rad) |
|------------------|------|------------------|--------|--------|--------|--------|--------|--------|--------|--------|--------|--------|--------|--------|----------------|-----------------|
|                  |      | 0.00             | 25.00  | 50.00  | 75.00  | 100.00 | 125.00 | 150.00 | 175.00 | 200.00 | 225.00 | 250.00 | 275.00 | 300.00 |                |                 |
| Rotation (rad)   | b-AA | 0.0000           | 0.0013 | 0.0025 | 0.0039 | 0.0053 | 0.0068 | 0.0081 | 0.0093 | 0.0107 | 0.0121 | 0.0138 | 0.0160 | 0.0190 | 310.31         | 0.0213          |
|                  | b-AB | 0.0000           | 0.0013 | 0.0026 | 0.0039 | 0.0055 | 0.0070 | 0.0087 | 0.0103 | 0.0119 | 0.0137 | 0.0156 | 0.0185 | 0.0227 | 301.81         | 0.0247          |
|                  | b-AC | 0.0000           | 0.0013 | 0.0026 | 0.0040 | 0.0056 | 0.0071 | 0.0087 | 0.0104 | 0.0119 | 0.0135 | 0.0152 | 0.0175 | 0.0211 | 305.97         | 0.0230          |
|                  | b-BA | 0.0000           | 0.0013 | 0.0026 | 0.0039 | 0.0053 | 0.0068 | 0.0083 | 0.0096 | 0.0110 | 0.0125 | 0.0143 | 0.0167 | 0.0201 | 308.34         | 0.0234          |
|                  | b-BB | 0.0000           | 0.0014 | 0.0026 | 0.0041 | 0.0056 | 0.0070 | 0.0088 | 0.0108 | 0.0127 | 0.0145 | 0.0165 | 0.0193 | -      | 299.90         | 0.0250          |
|                  | b-BC | 0.0000           | 0.0013 | 0.0026 | 0.0040 | 0.0056 | 0.0071 | 0.0088 | 0.0108 | 0.0123 | 0.0139 | 0.0156 | 0.0181 | 0.0222 | 303.47         | 0.0240          |
|                  | b-CA | 0.0000           | 0.0015 | 0.0026 | 0.0040 | 0.0054 | 0.0070 | 0.0083 | 0.0096 | 0.0110 | 0.0125 | 0.0143 | 0.0166 | 0.0198 | 309.46         | 0.0240          |
|                  | b-CB | 0.0000           | 0.0019 | 0.0031 | 0.0043 | 0.0055 | 0.0070 | 0.0086 | 0.0104 | 0.0121 | 0.0139 | 0.0158 | 0.0185 | 0.0234 | 301.21         | 0.0242          |
|                  | b-CC | 0.0000           | 0.0013 | 0.0026 | 0.0040 | 0.0057 | 0.0072 | 0.0089 | 0.0108 | 0.0124 | 0.0140 | 0.0157 | 0.0181 | 0.0220 | 304.13         | 0.0244          |
|                  | b-RD | 0.0000           | 0.0012 | 0.0024 | 0.0038 | 0.0053 | 0.0069 | 0.0085 | 0.0101 | 0.0117 | 0.0134 | 0.0152 | 0.0179 | 0.0223 | 302.06         | 0.0234          |
| Statistical Data | μ    | 0.0000           | 0.0014 | 0.0026 | 0.0040 | 0.0055 | 0.0070 | 0.0086 | 0.0102 | 0.0118 | 0.0134 | 0.0152 | 0.0177 | 0.0214 | 304.66         | 0.0238          |
|                  | σ    | 0.0000           | 0.0002 | 0.0002 | 0.0001 | 0.0001 | 0.0001 | 0.0003 | 0.0005 | 0.0007 | 0.0008 | 0.0008 | 0.0010 | 0.0015 | 3.672          | 0.0011          |
|                  | COV  | -                | 0.152  | 0.072  | 0.034  | 0.022  | 0.019  | 0.031  | 0.052  | 0.058  | 0.057  | 0.055  | 0.058  | 0.070  | 0.012          | 0.044           |

The following conclusions can be drawn from the tabulated information of the applied load-rotation history of node 2 of the b-090 3D structures model set presented in **Table 6.2**:

- A low COV of nodal rotations is observed at all load increments ranging from 1.90% to 15.20% for the b-090 3D structures model set. At critical load, the COV of the rotations is 4.40%. These low COV indicate a low dispersion of rotations in relation to the mean value from initial loading until reaching buckling load;
- The highest COV of nodal rotation occurs at the beginning of the applied load (25%) indicating that the in-plane fit-gap tolerance between the mating parts of the jointing system produce more dispersed rotational values during initial loading of the model set; and
- Finally, the b-RD 090 3D structure model shows similar rotations as compared to the mean values of the model set. These results indicate that modeling the 3D structures with different joint system behaviors in each joint do not produce a larger negative impact on the nodal rotational behavior of structures built with 0.090-inch tubular thickness beams.

**Figure 6.2** presents a value plot of the applied load-rotation history of node 2 of the b-090 3D structures model set (b-AA – b-CC and b-RD) simulations at 25% applied load increments until critical load is reached in each of the simulations. Besides, the model set mean applied load-rotation history of node 2 is presented in this illustration.

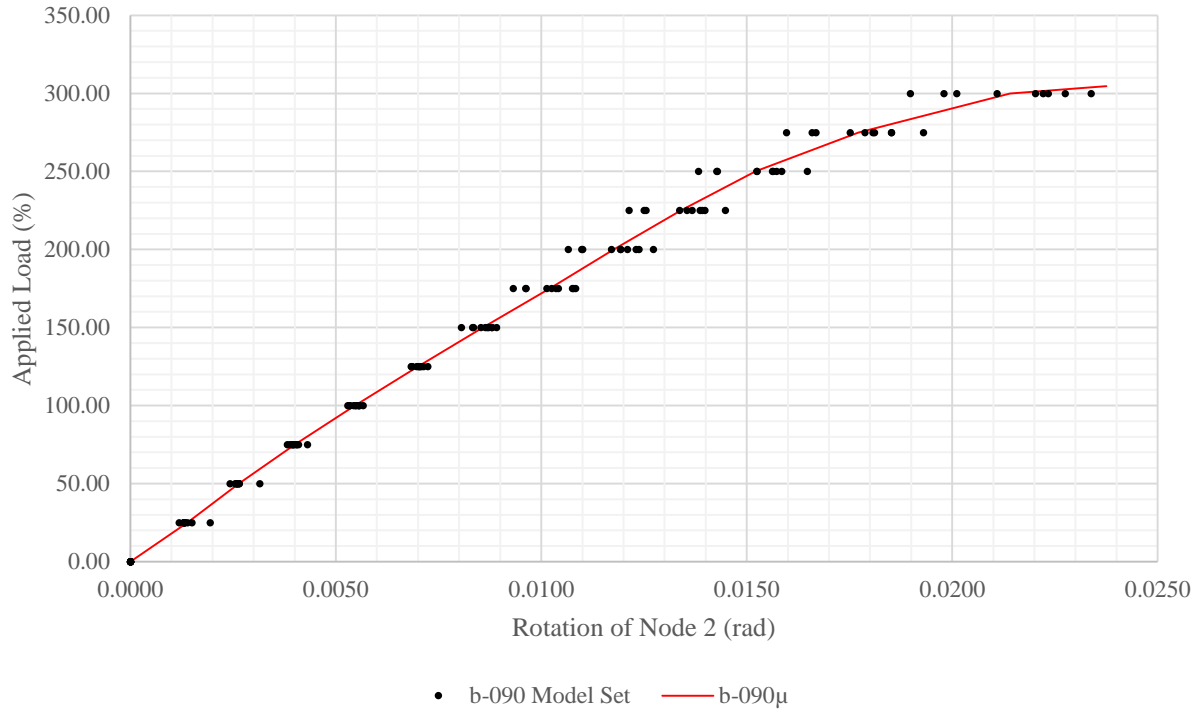


**Figure 6.2** Applied Load-Rotation of Node 2: b-090 3D Structures Model Set

Since the b-090 3D structures model set shows a low spread of values in relation to the central tendency of nodal rotations and critical capacity, the mean behavior of node 2, shown in **Figure 6.2**, will be used to characterize the as-built applied load-rotation history of node 2 and will be denoted as the nodal rotation of the b-090μ 3D structure during **Chapter 7**.

### 6.3 Applied Load-Interaction Index: b-090 3D Structures Model Set

**Table 6.3** presents the tabulated data of the applied load-interaction index history of beam element 62 from initial loading until beam failure is reached at 25% load increments for the b-090 3D structures model set simulations. Additionally, this table displays the model set mean, standard deviation, and COV of the:

- 1) Beam interaction index at all load increments; and
- 2) Applied load at failure of the beam element.

**Table 6.3** Applied Load-Interaction Index and Statistical Properties of Beam 62: b-090 3D Structures Model Set

| Structure         |      | Applied Load (%) |       |       |       |        |        |        |        |        |        | Failure Load (%) |
|-------------------|------|------------------|-------|-------|-------|--------|--------|--------|--------|--------|--------|------------------|
|                   |      | 0.00             | 25.00 | 50.00 | 75.00 | 100.00 | 125.00 | 150.00 | 175.00 | 200.00 | 225.00 |                  |
| Interaction Index | b-AA | 0.000            | 0.089 | 0.167 | 0.249 | 0.340  | 0.436  | 0.522  | 0.674  | 0.783  | 0.898  | 244.95           |
|                   | b-AB | 0.000            | 0.090 | 0.169 | 0.254 | 0.349  | 0.448  | 0.553  | 0.705  | 0.825  | 0.947  | 234.69           |
|                   | b-AC | 0.000            | 0.090 | 0.170 | 0.255 | 0.349  | 0.448  | 0.552  | 0.708  | 0.822  | 0.941  | 236.49           |
|                   | b-BA | 0.000            | 0.090 | 0.168 | 0.251 | 0.337  | 0.428  | 0.522  | 0.670  | 0.775  | 0.887  | 246.27           |
|                   | b-BB | 0.000            | 0.093 | 0.172 | 0.257 | 0.345  | 0.438  | 0.539  | 0.697  | 0.819  | 0.941  | 235.79           |
|                   | b-BC | 0.000            | 0.092 | 0.171 | 0.256 | 0.345  | 0.440  | 0.540  | 0.697  | 0.811  | 0.925  | 239.28           |
|                   | b-CA | 0.000            | 0.091 | 0.168 | 0.250 | 0.336  | 0.428  | 0.518  | 0.670  | 0.778  | 0.894  | 245.80           |
|                   | b-CB | 0.000            | 0.100 | 0.181 | 0.262 | 0.348  | 0.441  | 0.540  | 0.699  | 0.818  | 0.942  | 235.47           |
|                   | b-CC | 0.000            | 0.089 | 0.169 | 0.253 | 0.343  | 0.438  | 0.540  | 0.700  | 0.814  | 0.931  | 238.22           |
|                   | b-RD | 0.000            | 0.085 | 0.166 | 0.252 | 0.344  | 0.441  | 0.541  | 0.688  | 0.797  | 0.914  | 241.92           |
| Statistical Data  | μ    | 0.000            | 0.091 | 0.170 | 0.254 | 0.344  | 0.439  | 0.537  | 0.691  | 0.804  | 0.922  | 239.89           |
|                   | σ    | 0.000            | 0.004 | 0.004 | 0.004 | 0.005  | 0.007  | 0.012  | 0.015  | 0.019  | 0.022  | 4.514            |
|                   | COV  | -                | 0.042 | 0.024 | 0.015 | 0.013  | 0.016  | 0.023  | 0.021  | 0.024  | 0.024  | 0.019            |

The following observations are concluded from information of the applied load-interaction index history of beam element 62 of the b-090 3D structures model set presented in **Table 6.3**:

- The b-090 3D structures model set shows low COV of interaction indices at different applied loads being the lowest of 1.30% and the highest of 4.20%. Therefore, it can be determined that the interaction index displays a low dispersion in relation to the mean value from initial loading until reaching beam buckling load;
- The highest COV of 4.20% which is observed to occur at the beginning of the applied load indicates that the different movements of the gaps in each of the simulations produce more dispersed interaction indices values during initial loading of the b-090 model set;
- The COV of beam failure load is 1.90%. Therefore, it can be concluded that manufacturing imperfections do not produce a significant impact in the beam buckling capacity among the b-090 3D structures model set; and
- It can be noted that the b-RD 090 3D structure model, with different as-built stiffness in each of the joints, shows similar interaction indices in all the load increments as compared to the mean observations from the b-090 3D structures model set. In addition, the beam capacity of the b-RD 090 3D structure is slightly higher compared to the mean beam capacity of the model set. These results indicate that modeling the 3D structures with different joint system behaviors in each of the connections do not produce a larger negative impact on the beam buckling behavior and capacity.

**Table 6.4** presents the beam compression force ( $P_{ux}$ ), moment about the Y axis ( $M_{uy}$ ), and moment about the Z axis ( $M_{uz}$ ) at beam failure of the b-090 3D structures model set. Additionally, in this table the forces and moments experimented in beam element 62 in each of the simulations are compared with the corresponding force-displacement and moment-rotation capacities of the

jointing system used during each of the simulations to capture what proportion of the connection capacity is used when the beam element reaches failure load. Finally, this table shows the b-090 3D structures model set mean of the:

- 1) Force components of the beam element at failure load;
- 2) Compression and in-plane capacities of the jointing system; and
- 3) Utilized percentage of the connection capacity at beam failure.

**Table 6.4** Force Components and Statistical Properties of Beam 62 at Failure: b-090 3D Structures Model Set

| Structure | Beam Force Components |                          |                          | Connection Capacity       |                              | Utilized Percentage of Connection |      |
|-----------|-----------------------|--------------------------|--------------------------|---------------------------|------------------------------|-----------------------------------|------|
|           | P <sub>ux</sub> (lb.) | M <sub>uy</sub> (lb.-in) | M <sub>uz</sub> (lb.-in) | P <sub>ux-cap</sub> (lb.) | M <sub>uy-cap</sub> (lb.-in) | (%)                               | (%)  |
| b-AA      | 9,964.81              | 821.60                   | 14,735.53                | 43,839.61                 | 22,953.27                    | 22.73                             | 3.58 |
| b-AB      | 8,889.56              | 1,105.45                 | 15,341.29                | 45,169.47                 | 20,509.94                    | 19.68                             | 5.39 |
| b-AC      | 9,131.80              | 1,071.71                 | 15,174.61                | 43,885.83                 | 25,664.33                    | 20.81                             | 4.18 |
| b-BA      | 9,885.63              | 375.78                   | 15,246.86                | 43,464.51                 | 20,430.45                    | 22.74                             | 1.84 |
| b-BB      | 8,764.17              | 569.28                   | 15,981.20                | 43,702.65                 | 20,101.20                    | 20.05                             | 2.83 |
| b-BC      | 9,187.44              | 523.97                   | 15,676.32                | 43,857.30                 | 23,097.90                    | 20.95                             | 2.27 |
| b-CA      | 9,896.39              | 523.66                   | 15,090.07                | 42,996.74                 | 24,790.00                    | 23.02                             | 2.11 |
| b-CB      | 8,884.37              | 847.06                   | 15,603.98                | 43,342.47                 | 20,145.31                    | 20.50                             | 4.20 |
| b-CC      | 9,182.23              | 712.87                   | 15,491.72                | 44,208.53                 | 24,889.31                    | 20.77                             | 2.86 |
| b-RD      | 9,254.69              | 919.56                   | 15,225.08                | -                         | -                            | -                                 | -    |
| μ         | 9,304.11              | 747.09                   | 15,356.67                | 43,829.68                 | 22,509.08                    | 21.25                             | 3.25 |

The following conclusions are obtained from the information of the b-090 3D structures model set presented in **Table 6.4**:

- In all simulations of the b-090 3D structures model set, the buckling failure of the beam elements occurs before the connections reach their axial and in-plane moment capacity.

**Figure 6.3** shows the mean axial semi-rigid behavior and **Figure 6.4** displays the mean in-plane bending semi-rigid behavior of the jointing system used during simulations of the b-090 3D structures model set; which in average used only 21.25% and 3.25% of their capacity, respectively. These results indicate that failure occurs due to beam buckling and not connection failure in all the as-built structures.

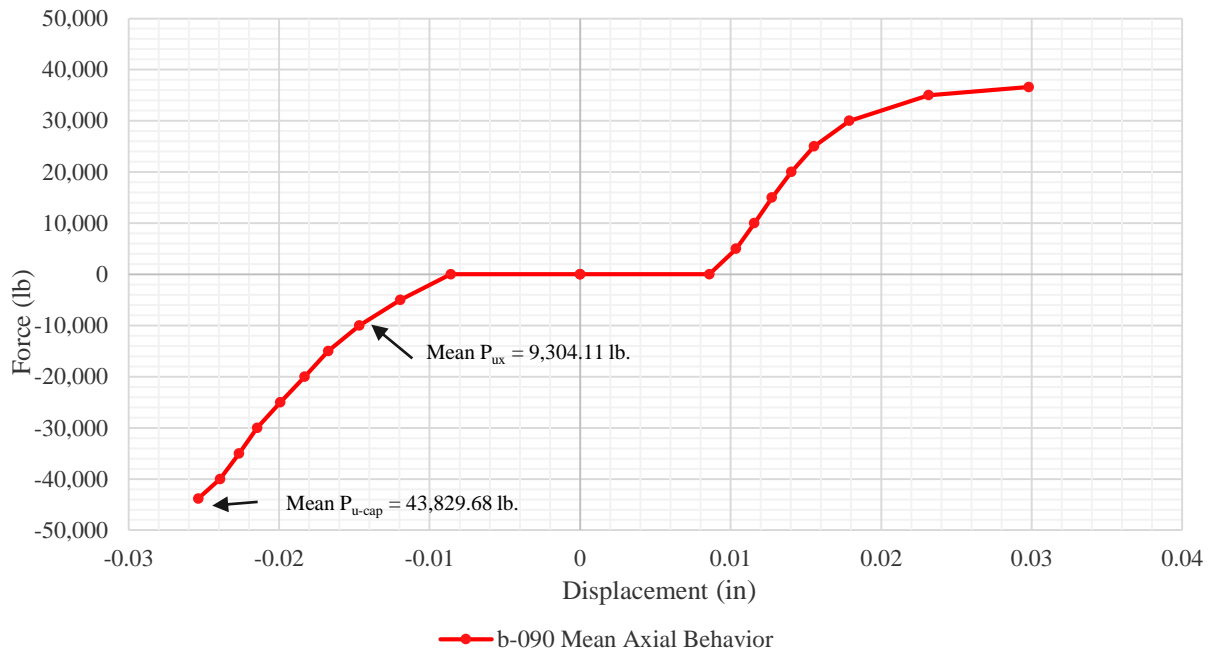


**Figure 6.3** Mean Axial Semi-Rigid Behavior: b-090 3D Structures Model Set

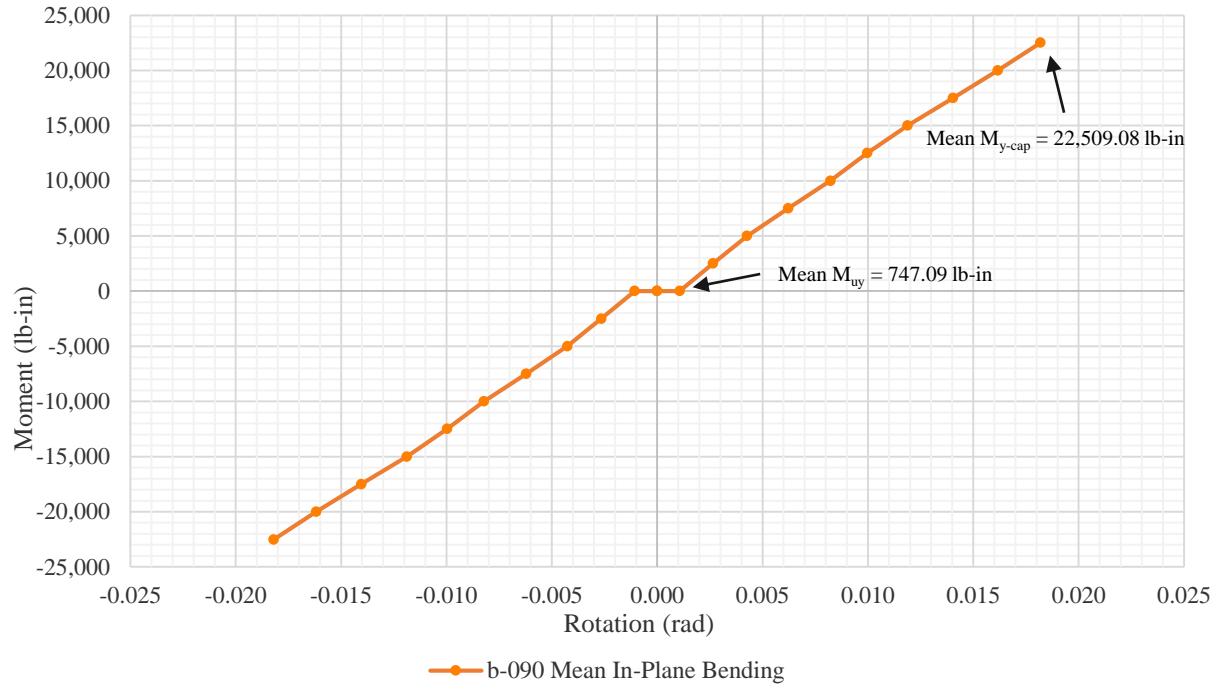


**Figure 6.4** Mean In-Plane Bending Semi-Rigid Behavior: b-090 3D Structures Model Set

**Figure 6.5** presents a value plot of the applied load-interaction index of beam element 62 of the b-090 3D structures model set (b-AA – b-CC and b-RD) simulations at 25% applied load increments until failure of the beam element is reached in each of the simulations. Furthermore, the model mean applied load-interaction index history of beam element is presented in this illustration.

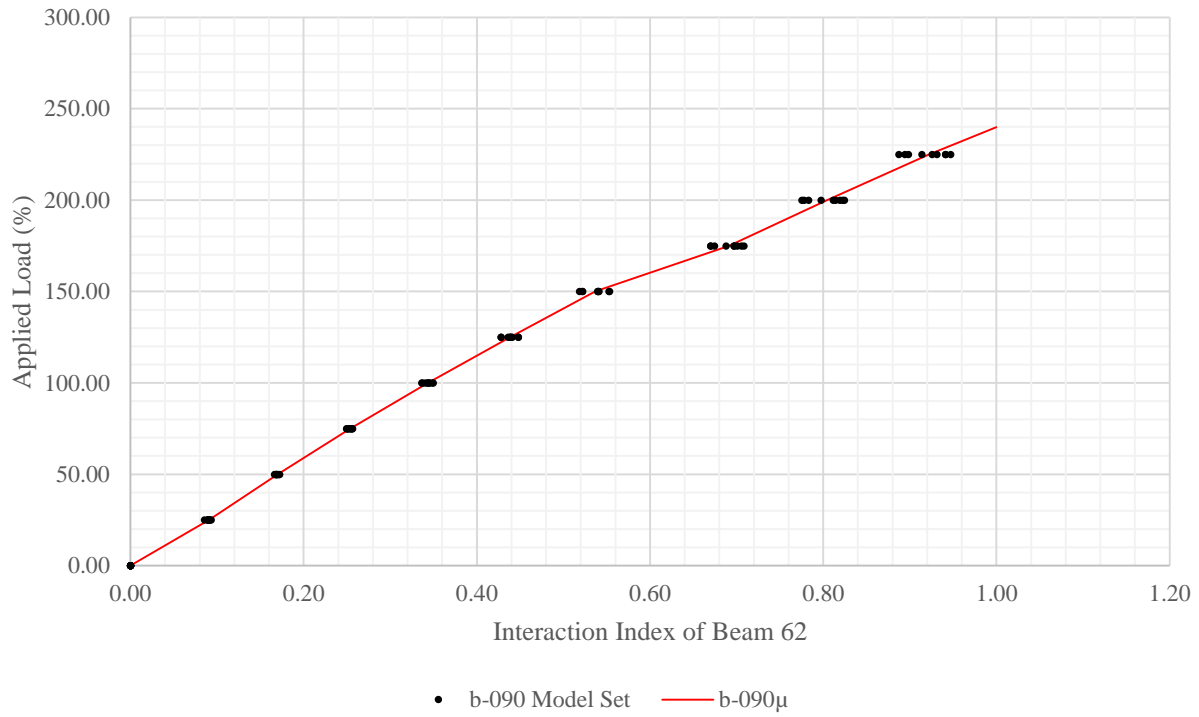


**Figure 6.5** Applied Load-Interaction Index of Beam 62: b-090 3D Structures Model Set

Since the b-090 3D structures model set displayed a low spread of values in relation to the central tendency of interaction indices, the mean behavior of beam element 62, shown in **Figure 6.5**, will be used to represent the as-built applied load-interaction index history of beam 62 and will be referred as the beam interaction index of the b-090μ 3D structure in the following chapter.

In conclusion, for each of the as-built model set of 3D structures, the results of: (1) the applied load-displacement of node 13; (2) the applied load-rotation of node 2; and (3) the applied load-bar efficiency (interaction index) of beam element 62, showed a low COV indicating a low dispersion of results away from the central tendency behavior of as-built structures. Accordingly, in **Chapter 7** the mean results obtained from the structures modeled with as-built jointing system connections (shown in this chapter) will be used and compared with the structures modeled with the as-designed behavior of the jointing system (shown in **Chapter 5**) to quantify how manufacturing geometric imperfections influence the buckling behavior of three-dimensional structures.

## **Chapter 7: Finite Element Simulation Results: Comparative Analysis**

The results of the structures modeled with the as-designed and as-built jointing system behavior were presented in **Chapter 5** and **Chapter 6**, respectively. For each structural model, the results included:

- 1) The applied load-displacement graph and tabulated data of node 13;
- 2) The applied load-rotation graph and tabulated data of node 2; and
- 3) The applied load-interaction index graph and tabulated data of beam element 62.

This chapter presents a comparison of results of the 3D structures modeled with the as-designed vs. the as-built jointing system behavior. The comparison will help assess how incorporating manufacturing geometric imperfections in the jointing system influence the buckling behavior and capacity of three-dimensional structures.

## 7.1 As-Designed vs. As-Built 3D Structures: Applied Load-Displacement

To assess how manufacturing geometric imperfections in the jointing system affect the nodal displacement behavior in three-dimensional structures, the results of the as-designed vs. the as-built 3D structures applied load-displacement history of node 13 are compared. The comparison is done using the following equations:

For critical load, the comparison is completed by subtracting the failure loads (expressed in percentage) as follows:

$$\Delta CL (\%) = (CL_{b\mu} - CL_d) \quad (7.1)$$

where  $\Delta CL$  is the change in critical load (%),  $CL_{b\mu}$  is the as-built 3D structures mean critical load (%); and  $CL_d$  is the as-designed 3D structure critical load (%).

For the nodal displacement, the comparison is completed by computing their ratios, subtracting 1.0, and expressing the change as a percentage as follows:

$$\Delta D (\%) = \left( \frac{D_{b\mu}}{D_d} - 1 \right) (100) \quad (7.2)$$

where  $\Delta D$  is the change in displacement (%),  $D_{b\mu}$  is the as-built 3D structures mean nodal displacement (in), and  $D_d$  is the as-designed 3D structure nodal displacement (in).

**Figure 7.1** presents the applied load-displacement history graphs of node 13 for the d-090 vs. the b-090 $\mu$  3D structures at 25% load increments from initial loading until critical load is reached in both models. In this plot, the vertical axis corresponds to the applied load history expressed in percentage while the horizontal axis displays the resultant displacement of the node in inches as the load is applied.

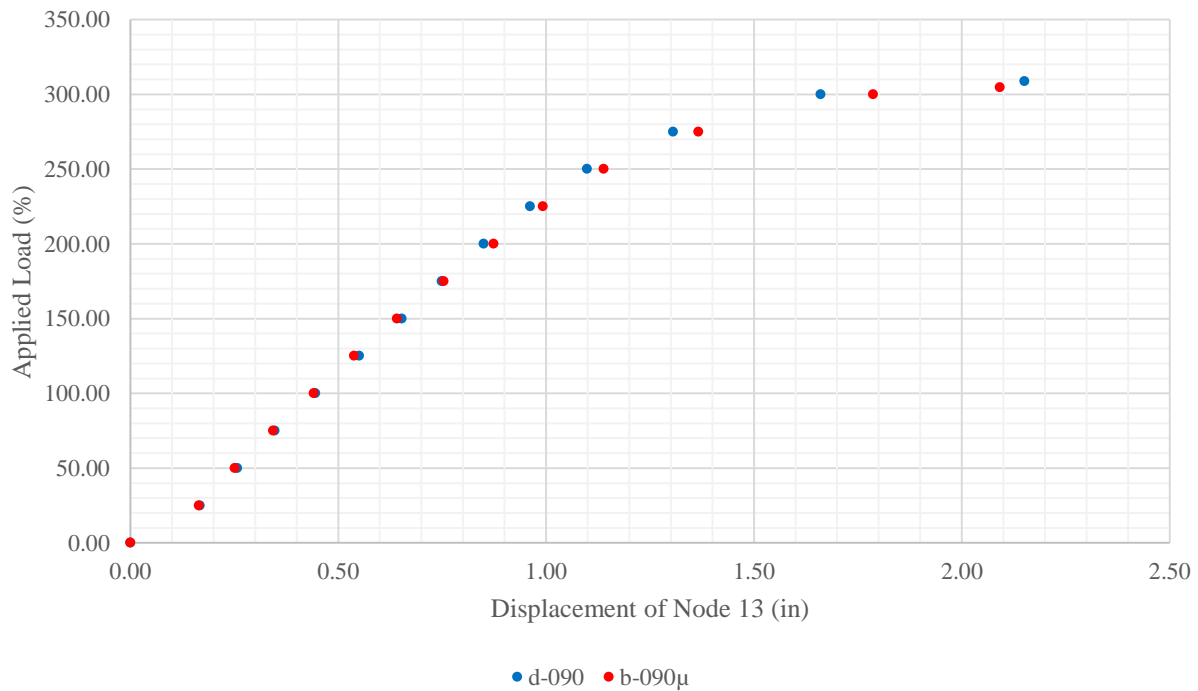


**Figure 7.1** Applied Load-Displacement of Node 13: d-090 vs. b-090 $\mu$  3D Structures

**Figure 7.1** shows that that both the d-090 and b-090 $\mu$  3D structure models follow very similar applied load-displacement histories. **Table 7.1** compares the change displacement of node 13 between the d-090 and the b-090 $\mu$  3D structure models at 25% load increments before critical load is reached, while **Table 7.2** compares the critical/maximum point in the applied load-displacement curves of the d-090 vs. the b-090 $\mu$  3D structure models.

**Table 7.1** Applied Load-Displacement of Node 13: 090 Comparison

| Applied Load (%) | D (in) | D (in)      | $\Delta D$ (%)        |
|------------------|--------|-------------|-----------------------|
|                  | d-090  | b-090 $\mu$ | d-090 vs. b-090 $\mu$ |
| 0.00             | 0.000  | 0.000       | -                     |
| 25.00            | 0.167  | 0.164       | (1.69)                |
| 50.00            | 0.257  | 0.251       | (2.46)                |
| 75.00            | 0.347  | 0.344       | (0.94)                |
| 100.00           | 0.445  | 0.441       | (0.81)                |
| 125.00           | 0.550  | 0.538       | (2.16)                |
| 150.00           | 0.653  | 0.641       | (1.82)                |
| 175.00           | 0.749  | 0.754       | 0.65                  |
| 200.00           | 0.850  | 0.873       | 2.78                  |
| 225.00           | 0.961  | 0.992       | 3.24                  |
| 250.00           | 1.098  | 1.138       | 3.66                  |
| 275.00           | 1.306  | 1.366       | 4.63                  |
| 300.00           | 1.661  | 1.787       | 7.58                  |

**Table 7.2** Critical Applied Load-Displacement of Node 13: 090 Comparison

|        | d-090  | b-090 $\mu$ | d-090 vs. b-090 $\mu$<br>( $\Delta\%$ ) |
|--------|--------|-------------|---|
| CL (%) | 308.80 | 304.66      | (4.14)                                  |
| D (in) | 2.151  | 2.091       | (2.77)                                  |

The interpretation of the preceding results are as follows:

- Table 7.1** shows that during the first 150% of the applied load, the b-090 $\mu$  3D structure model shows slightly lower nodal displacements in comparison to the d-090 3D structure model. Subsequently, the d-090 3D structure model becomes stiffer and the displacements start reducing gradually up to 300% of the applied load, where the as-designed structure experiences 7.58% less displacement as compared to the as-built model;

- **Table 7.2** shows that the critical load of the b-090 $\mu$  3D structure is 4.14% lower as compared to the d-090 3D structure model. Besides, at critical load, the node 13 in the b-090 $\mu$  3D structure shows 2.77% lower displacement as compared to the d-090 3D structure model; and
- In summary, minor changes in the applied load-displacement behavior of node 13 are observed between the d-090 and b-090 $\mu$  3D structure models due to manufacturing geometric imperfections in the jointing system. The difference in displacements is at the most in the order of magnitude of 1/10 of an inch (at 300% of applied load) and the critical load is reduced only 4.14% in the as-built model. Therefore, it can be concluded that manufacturing geometric imperfections of the joints do not produce a significant impact in the overall nodal displacement behavior of the currently analyzed large span hexagonal shape 3D structure modeled with 0.090-inch thickness tubular bars.

## 7.2 As-Designed vs. As-Built 3D Structures: Applied Load-Rotation

To evaluate the effect of manufactured imperfect jointing systems in the nodal rotation behavior in three-dimensional structures, the results of the as-designed vs. the as-built 3D structures applied load-rotation history of node 13 are compared. The comparison is done using **Equation 7.1** for the critical load. For the nodal rotation, the comparison is done by computing their ratios, subtracting 1.0, and expressing the change as a percentage as follows:

$$\Delta R (\%) = \left( \frac{R_{b\mu}}{R_d} - 1 \right) (100) \quad (7.3)$$

Where  $\Delta R$  is the change in rotation (%),  $R_{b\mu}$  is the as-built 3D structures mean nodal rotation (rad), and  $R_d$  is the as-designed 3D structure nodal rotation (rad).

**Figure 7.2** presents the applied load-rotation history graphs of node 2 for the d-090 vs. the b-090 $\mu$  3D structures at 25% load increments from initial loading until critical load is reached in both models. In this figure, the vertical axis corresponds to the applied load history expressed in percentage while the horizontal axis displays the resultant rotation of node 2 in radians as the load is applied.

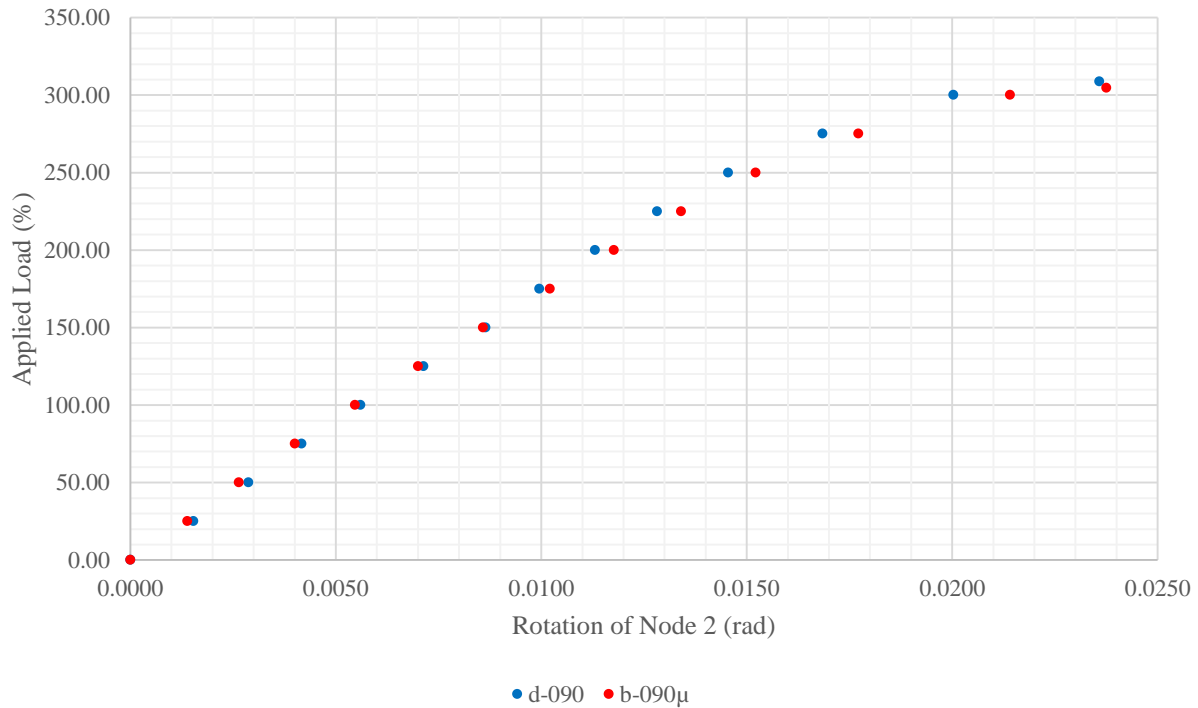


**Figure 7.2** Applied Load-Rotation of Node 2: d-090 vs. b-090 $\mu$  3D Structures

**Figure 7.2** shows that both the d-090 and b-090 $\mu$  3D structure models follow very similar applied load-rotation histories. **Table 7.3** compares the change rotation of node 2 between the d-090 and the b-090 $\mu$  models at 25% load increments before critical load is reached and **Table 7.4** compares the critical/maximum point in the applied load-rotation curves of the d-090 vs. the b-090 $\mu$  3D structure models.

**Table 7.3** Applied Load-Rotation of Node 2: 090 Comparison

| Applied Load (%) | R (rad) | R (rad)     | $\Delta R$ (%)        |
|------------------|---------|-------------|-----------------------|
|                  | d-090   | b-090 $\mu$ | d-090 vs. b-090 $\mu$ |
| 0.00             | 0.0000  | 0.0000      | -                     |
| 25.00            | 0.0015  | 0.0014      | (9.93)                |
| 50.00            | 0.0029  | 0.0026      | (8.09)                |
| 75.00            | 0.0042  | 0.0040      | (4.05)                |
| 100.00           | 0.0056  | 0.0055      | (2.32)                |
| 125.00           | 0.0071  | 0.0070      | (1.84)                |
| 150.00           | 0.0086  | 0.0086      | (0.75)                |
| 175.00           | 0.0100  | 0.0102      | 2.59                  |
| 200.00           | 0.0113  | 0.0118      | 4.10                  |
| 225.00           | 0.0128  | 0.0134      | 4.54                  |
| 250.00           | 0.0145  | 0.0152      | 4.62                  |
| 275.00           | 0.0168  | 0.0177      | 5.17                  |
| 300.00           | 0.0200  | 0.0214      | 6.89                  |

**Table 7.4** Critical Applied Load-Rotation of Node 2: 090 Comparison

|         | d-090  | b-090 $\mu$ | d-090 vs. b-090 $\mu$ ( $\Delta\%$ ) |
|---------|--------|-------------|--------------------------------------|
| CL (%)  | 308.80 | 304.66      | (4.14)                               |
| R (rad) | 0.0236 | 0.0238      | 0.73                                 |

The interpretation of these results are as follows:

- **Table 7.3** shows that during the first 150% of the applied load, the b-090 $\mu$  3D structure model shows lower nodal rotations in comparison to the d-090 3D structure model. Afterwards, the d-090 3D structure model becomes stiffer and the rotations start to decrease progressively up to 300% of the applied load. At this load, the as-designed structure experiences 6.89% less rotation as compared to the as-built model;

- **Table 7.4** shows that node 2 in the b-090 $\mu$  3D structure experiences 0.73% higher magnitude of rotation as compared to the d-090 model at critical or failure load of the structures; and
- In summary, negligible changes in the applied load-rotation behavior of node 2 are observed between the d-090 and b-090 $\mu$  3D structure models due to manufacturing geometric imperfections of the joints. The maximum difference in rotations of 0.0014 radians is observed to occur at 300% of the applied load. Therefore, it can be concluded that manufacturing geometric imperfections of the connections do not produce a significant impact in the overall nodal rotation behavior of the currently studied large span 3D structure modeled with 0.090-inch thickness tubular bars.

### 7.3 As-Designed vs. As-Built 3D Structures: Applied Load-Interaction Index

To estimate the effect that jointing systems with manufacturing geometric imperfections produce in the beam buckling behavior in three-dimensional structures, the results of the as-designed vs. the as-built 3D structures applied load-interaction index history of beam 62 are compared using the following equations:

For the applied load required to cause beam failure, the comparison is done by subtracting the beam failure loads (expressed in percentage) as follows:

$$\Delta BFL (\%) = (BFL_{b\mu} - BFL_d) @ interaction index = 1 \quad (7.4)$$

where  $\Delta BFL$  is the change in beam failure load (%),  $BFL_{b\mu}$  is the as-built 3D structures mean beam failure load (%), and  $BFL_d$  is the as-designed 3D structure beam failure load (%).

For the change in interaction index at every applied load increment, the comparison is done by computing their ratios, subtracting 1.0, and expressing the change as a percentage as follows:

$$\Delta II (\%) = \left( \frac{II_{b\mu}}{II_d} - 1 \right) (100) \quad (7.5)$$

where  $\Delta II$  is the change in interaction index (%),  $II_{b\mu}$  is the as-built 3D structures mean beam interaction index, and  $II_d$  is the as-designed 3D structure beam interaction index.

Besides, to estimate the effect that manufacturing geometric imperfections in the connections produce in the beam compression force ( $P_{ux}$ ), moment about the Y axis ( $M_{uy}$ ), and moment about the Z axis ( $M_{uz}$ ) at beam failure, the results of the as-designed vs. the as-built force components of beam 62 are compared using the following equations:

For the change in compression force at beam failure, the comparison is done by computing their ratios, subtracting 1.0, and expressing the change as a percentage as follows:

$$\Delta P_{ux} (\%) = \left( \frac{P_{ux} b_{\mu}}{P_{ux} d} - 1 \right) (100) \quad (7.6)$$

where  $\Delta P_{ux}$  is the change in compression force of the beam element (%),  $P_{ux} b_{\mu}$  is the as-built mean compression force of the beam elements (lb.), and  $P_{ux} d$  is the as-designed compression force of the beam element (lb.).

For the change in moment about the Y axis at beam failure, the comparison is done by computing their ratios, subtracting 1.0, and expressing the change as a percentage as follows:

$$\Delta M_{uy} (\%) = \left( \frac{M_{uy} b_{\mu}}{M_{uy} d} - 1 \right) (100) \quad (7.7)$$

where  $\Delta M_{uy}$  is the change in moment about the Y axis of the beam element (%),  $M_{uy} b_{\mu}$  is the as-built mean moment about the Y axis of the beam elements (lb.-in), and  $M_{uy} d$  is the as-designed moment about the Y axis of the beam element (lb.-in).

For the change in moment about the Z axis at beam failure, the comparison is done by computing their ratios, subtracting 1.0, and expressing the change as a percentage as follows:

$$\Delta M_{uz} (\%) = \left( \frac{M_{uz} b_{\mu}}{M_{uz} d} - 1 \right) (100) \quad (7.8)$$

where  $\Delta M_{uz}$  is the change in moment about the Z axis of the beam element (%),  $M_{uz} b_{\mu}$  is the as-built mean moment about the Z axis of the beam elements (lb.-in), and  $M_{uz} d$  is the as-designed moment about the Z axis of the beam element (lb.-in).

**Figure 7.3** shows the applied load-interaction index graphs of beam element 62 for the d-090 vs. the b-090 $\mu$  3D structures at 25% load increments from initial loading until beam failure load is reached in both models. In this figure, the vertical axis corresponds to the applied load history expressed in percentage while the horizontal axis displays the interaction index of beam element 62 as the load is applied. **Figure 7.3** shows that both the d-090 and b-090 $\mu$  3D structure models follow very similar applied load-interaction index histories.

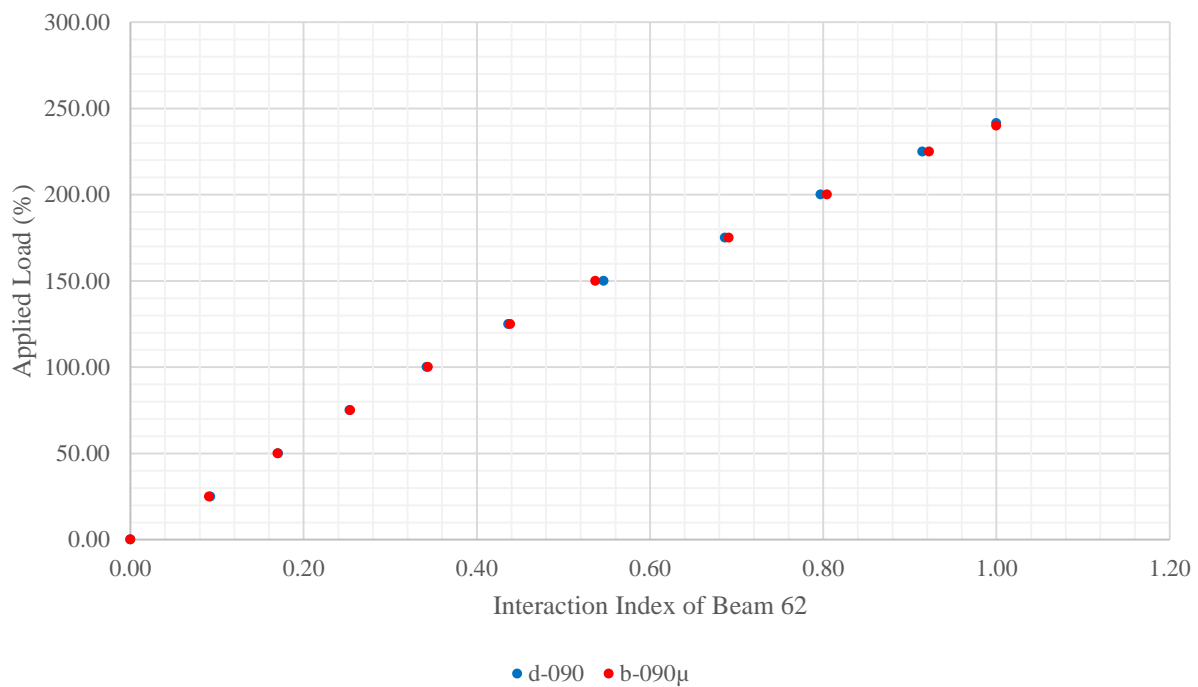


**Figure 7.3** Applied Load-Interaction Index of Beam 62: d-090 vs. b-090 $\mu$  3D Structures

**Figure 7.4** displays the compression forces and **Figure 7.5** shows the in-plane bending moments experienced in the Geometrica® fir-tree connections of the d-090 and the b-090 $\mu$  3D structures when the failure of beam 62 is reached.

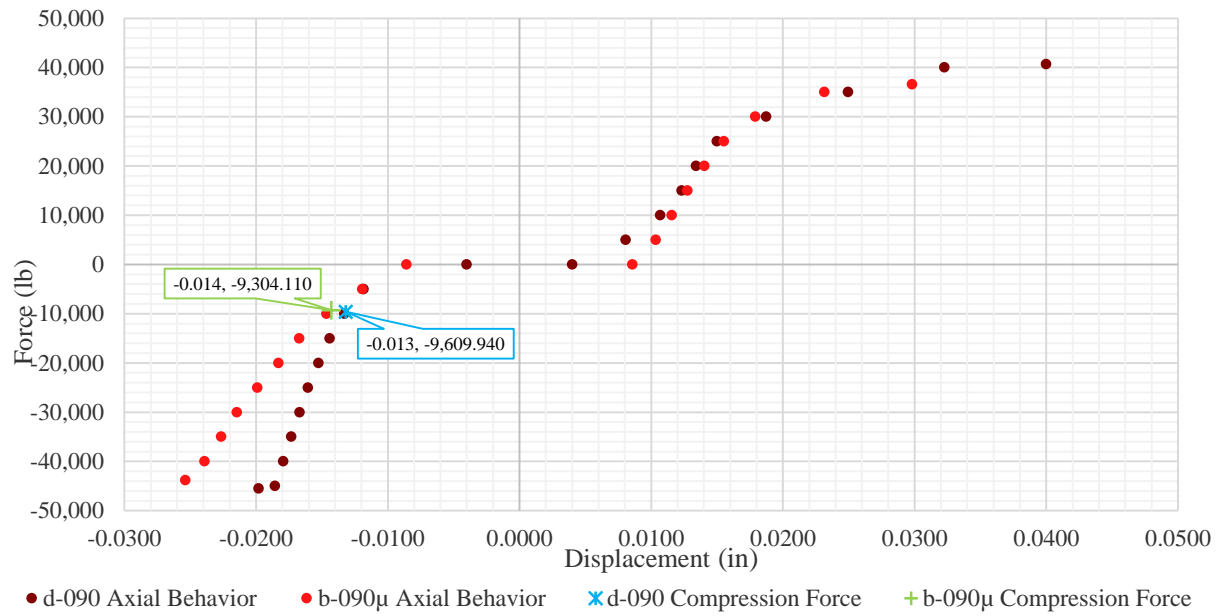


**Figure 7.4** Axial Semi-Rigid Behavior: d-090 vs. b-090 $\mu$  3D Structures

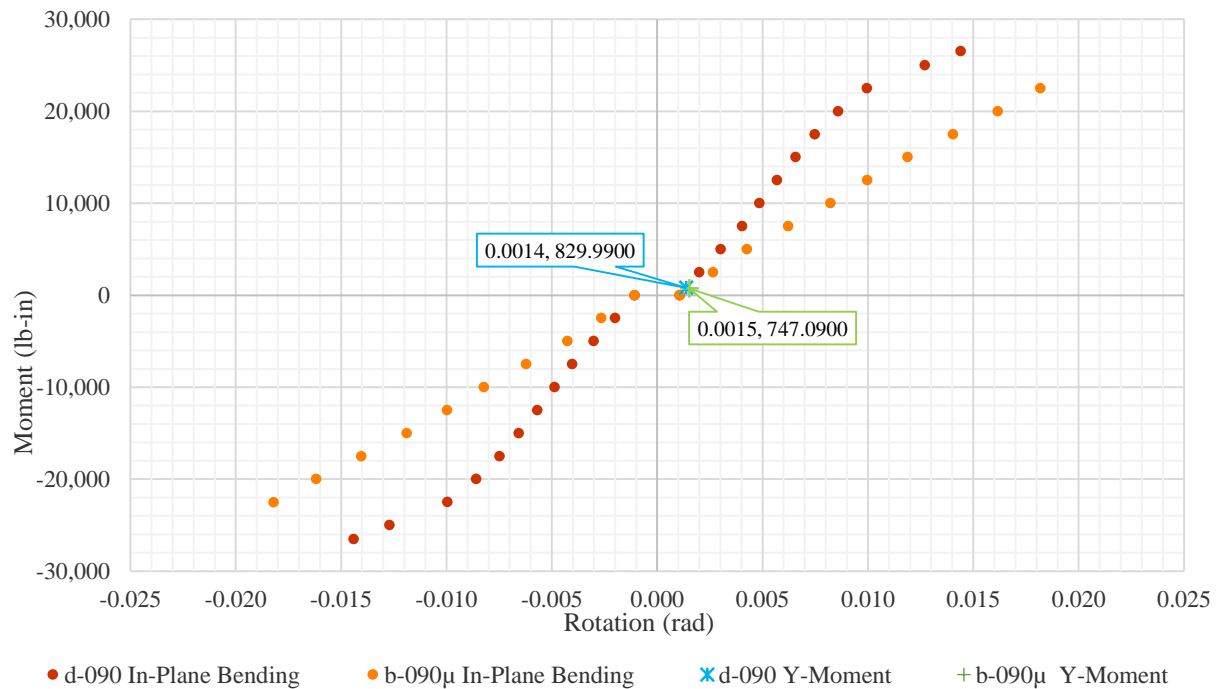


**Figure 7.5** In-Plane Bending Semi-Rigid Behavior: d-090 vs. b-090 $\mu$  3D Structures

From **Figure 7.4** it is observed that the connections in the d-090 and b-090 $\mu$  models experience similar compression forces and displacements when beam 62 reaches an interaction index of 1.0 in both models. Accordingly, **Figure 7.5** shows that the connections in the d-090 and b-090 $\mu$  3D structures experience similar in-plane bending moments and rotations when beam 62 fails. Additionally, from the previously mentioned figures, it is observed that the connections did not reach loads large enough to make manufacturing geometric imperfections produce an impact in the semi-rigid behavior of the joints and therefore, in the overall buckling behavior of the modeled structure.

**Table 7.5** compares the change interaction index of beam element 62 between d-090 and b-090 $\mu$  3D structure models at 25% load increments before beam failure load is reached. **Table 7.6** compares the required percentage of applied load required to make beam 62 reach a failure state between the d-090 vs. the b-090 $\mu$  models. Finally, **Table 7.7** presents the comparison of force components between the d-090 vs. the b-090 $\mu$  3D structures when both models reached an interaction index of 1.0.

**Table 7.5** Applied Load-Interaction Index of Beam 62: 090 Comparison

| Applied Load (%) | II    | II          | $\Delta$ II (%)       |
|------------------|-------|-------------|-----------------------|
|                  | d-090 | b-090 $\mu$ | d-090 vs. b-090 $\mu$ |
| 0.00             | 0.000 | 0.000       | -                     |
| 25.00            | 0.092 | 0.091       | (1.46)                |
| 50.00            | 0.171 | 0.170       | (0.33)                |
| 75.00            | 0.253 | 0.254       | 0.20                  |
| 100.00           | 0.342 | 0.344       | 0.36                  |
| 125.00           | 0.436 | 0.439       | 0.51                  |
| 150.00           | 0.546 | 0.537       | (1.75)                |
| 175.00           | 0.687 | 0.691       | 0.61                  |
| 200.00           | 0.797 | 0.804       | 0.89                  |
| 225.00           | 0.914 | 0.922       | 0.84                  |

**Table 7.6** Applied Load at Failure of Beam 62: 090 Comparison

|         | d-090  | b-090 $\mu$ | d-090 vs. b-090 $\mu$<br>( $\Delta\%$ ) |
|---------|--------|-------------|---|
| BFL (%) | 241.47 | 239.89      | (1.58)                                  |

**Table 7.7** Force Components of Beam 62 at Buckling Failure Load: 090 Comparison

| Beam Force Component     | d-090     | b-090 $\mu$ | d-090 vs. b-090 $\mu$<br>( $\Delta\%$ ) |
|--------------------------|-----------|-------------|---|
| P <sub>ux</sub> (lb.)    | 9,609.94  | 9,304.11    | (3.18)                                  |
| M <sub>uy</sub> (lb.-in) | 829.99    | 747.09      | (9.99)                                  |
| M <sub>uz</sub> (lb.-in) | 15,020.74 | 15,356.67   | 2.24                                    |

The preceding results show:

- **Table 7.5** shows that the d-090 and b-090 $\mu$  3D structure models follow slightly different the interaction index histories;
- **Table 7.6** shows that only 1.58% less applied load in the b-090 $\mu$  model is required to make beam 62 reach failure as compared the d-090 model;
- **Table 7.7** shows that the highest change of force components between models is observed to occur in the M<sub>uy</sub>, which shows a reduction of 9.99% in the b-090 $\mu$  as compared to the d-090 model. However, the magnitude of the M<sub>uy</sub> is the smallest force component contributing to the calculation of the interaction index, and therefore the percent change in this moment does not produce a large impact in the overall behavior of the beam; and

- In summary, negligible changes in the applied load-interaction index behavior of beam 62 are observed between the d-090 and b-090 $\mu$  3D structure models due to manufacturing geometric imperfections of the joints. The maximum difference in interaction index is 1.75% at 150% of the applied load. Therefore, it can be concluded that manufacturing geometric imperfections of the connections do not produce a significant impact in the overall beam buckling behavior of the large span 3D structure modeled with 0.090-inch thickness tubular bars.

#### **7.4 Conclusion of Comparisons**

In summary, for each of the comparisons of as-designed vs as-built models of the 3D structure, the results of: (1) the applied load-displacement node 13; (2) the applied load-rotation node 2; and (3) the applied load-bar efficiency (interaction index) of beam element 62, showed a negligible change between models due to the incorporation of the semi-rigid behavior of imperfectly manufactured jointing systems. Therefore, it can be concluded that the buckling stability of the large span 3D structure modeled during this dissertation is not sensitive to manufacturing geometric imperfections of the joints. However, contemporary architectural designs have led to the construction of many irregularly shaped three-dimensional structures around the world. Numerous of these structures are being built in high seismic risk areas, in windy cities and/or along coastal areas. As a result, these interesting and new structural systems are subject to extreme loading conditions which can make the jointing system connections reach higher compressive forces and bending moments where the stiffness behavior is influenced by manufacturing geometric imperfections. Consequently, these geometric imperfections of the joints could produce an impact on the overall buckling behavior of such structures.

## **Chapter 8: Summary, Conclusions, and Recommendations**

This chapter summarizes and presents the conclusions of the research reported in this dissertation. Furthermore, this chapter also describes the contributions of the study to the engineering profession. At the end, recommendations for future work are given.

### **8.1 Summary**

Three-dimensional structures, as their name suggests, are structural systems constructed using linear elements arranged for the forces to be transferred in a three-dimensional manner (Lan 2005). The buckling behavior of these types of structures is influenced by the effect of three main factors being: (1) the shape of the structure itself; (2) the jointing system semi-rigid behavior; and (3) the existence of geometric imperfections of the structural elements due to construction errors (Ma et al. 2013). Nevertheless, no attention had been directed to incorporate manufacturing geometric imperfections of the joints in the buckling analysis of three-dimensional structures. Thus, the study presented in this dissertation was conducted to understand the effect that these initial imperfections of the joints have in the buckling behavior and critical capacity of 3D structures.

In this research, physical laboratory tests were conducted on bench-scale structures to capture the actual buckling behavior of 3D structures built using the Geometrica® 6Sd-00 fir-tree connection. Subsequently, two finite element models identical in geometry and loading conditions to the bench-scale tested structures were developed. One model was created using rigid joint connections while the other model was developed including the semi-rigid behavior of the Geometrica® 6Sd-00 fir-tree jointing system. These models were created to analytically: (1) assess how the rigidity of this jointing system influences the buckling behavior of 3D structures; and (2)

predict the actual buckling behavior of 3D structures built with these joints. The comparison of analytical to experimental results indicated that the FEM that includes the semi-rigid properties of the fir-tree connections better predicted the experimentally observed buckling behavior of the 3D structures than the model that uses completely rigid connections.

After the accuracy of results obtained from the FEM of the bench-scale structure that included the semi-rigid properties of the fir-tree jointing system was validated, finite element models of a 30-foot span 3D structure were developed using the same semi-rigid modeling technique to conduct non-linear buckling FEA considering:

- 1) The as-designed behavior of the jointing system; and
- 2) The as-built behavior of the jointing system.

From the previously described models, the results included:

- 1) The applied load-displacement graph and tabulated data of node 13;
- 2) The applied load-rotation graph and tabulated data of node 2; and
- 3) The applied load-interaction index graph and tabulated data of beam element 62. This index was obtained from the extreme node of the beam experimenting higher stresses (node 13).

The comparison of FEA results of the as-designed vs. the as-built 3D structures helped to assess how incorporating manufacturing geometric imperfections in the jointing system influence the buckling behavior and capacity of three-dimensional structures.

## 8.2 Conclusions

This research has provided a method to consider the effect of imperfectly manufactured jointing systems in the buckling analysis of three-dimensional structures. Based on the results obtained through laboratory tests and finite element analyses conducted, the following is concluded:

- 1) Comparing the laboratory vs. analytical results of the bench-scale structure shows that the FEM that considered the stiffness characteristics of the fir-tree jointing system better predicted the experimentally observed buckling behavior of the structure than the model using completely rigid connections. Hence, proving that common design practices based on the assumption that fir-tree joints are rigid, underestimates the deflections and overestimates the buckling capacity of 3D structures;
- 2) The finite element simulation results of the as-designed and as-built structures modeled with fir-tree connections showed that the buckling failure of the beam elements occurs before the overall buckling capacity of the structures is reached. However, even when the beam elements have reached failure capacity, the redundancy of the structures allows the loads to be redistributed to adjacent members and node connections allowing the structure to keep carrying loads and avoiding catastrophic collapse;
- 3) The finite element simulation results of the as-designed and as-built structures modeled during this study showed that, at beam failure, the fir-tree connections do not reach their axial and moment capacity indicating that failure occurs due to beam members' end buckling and not because of connection failure;
- 4) A statistical analysis was performed on the results obtained from the ten different as-built structural models developed (referred as model set) during this investigation. From the

statistical analysis of results and due to the low COVs calculated for each of the variables involved, it was determined that the mean values of: (1) displacement; (2) rotation; (3) beam interaction index; (4) beam buckling capacity; and (5) overall critical capacity can be used to characterize the performance of 3D structures with manufactured imperfect joints;

- 5) Modeling 3D structures with different as-built stiffness in each of the joints do not produce a larger negative impact on the buckling behavior and capacity of such structures; and
- 6) The comparison of finite element simulation results of the as-designed vs. mean results of the as-built hexagonal shape 3D structure modeled during this study demonstrated that manufacturing geometric imperfections in the jointing system do not have a remarkable effect on the:
  - a. Applied load-displacement behavior of 3D structural elements;
  - b. Applied load-rotation behavior of the 3D structural elements;
  - c. Applied load-buckling stability of beam members of the 3D structure; or
  - d. Overall critical capacity of the 3D structure.

### **8.3 Contribution of the Study**

The major contribution of this research was the development of an enhanced finite element modeling technique that can incorporate the manufacturing geometric imperfections of the jointing system in the analysis of three-dimensional structures using the Patran/Nastran software. The significant highlight contributions in this study are:

- 1) Developed a more realistic modeling approach to consider imperfectly manufactured jointing systems in the buckling analysis of three-dimensional structures;
- 2) The methodology developed can serve as a procedure to help understand how the manufacturing geometric imperfections of the joints influence the buckling stability of any shape 3D structure under different loading conditions; and
- 3) Additionally, this methodology can be used to assess the global effect of manufacturing geometric imperfections of any type of connection used in 3D structural systems.

## 8.4 Future Work Recommendations

While this investigation has successfully addressed what is the influence of manufacturing geometric imperfections of the joints in the buckling behavior of hexagonal shape three-dimensional structures under symmetric loads, future investigations are required to expand the understanding of the behavior of these structural systems. The following recommendations are proposed:

- 1) Nowadays, there are many types of space frame structural shapes. This study can be extended to analyze contemporary non-conventional structures.
- 2) Include the semi-rigid behavior of as-built connections in the buckling analysis of 3D structures loaded under combined live and environmental forces to understand the significance of geometric imperfections under these extreme combined loading conditions;
- 3) In this dissertation, only the axial and in-plane bending rigidities of the fir-tree jointing system were considered. A further study can include the out-of-plane (strong axis) bending behavior of the fir-tree connection in the FEA of 3D structures; and
- 4) Combine nodal deviation, member curvature, and manufacturing geometric imperfections of the joints in the analysis to capture their collective consequence in the buckling capacity and behavior of 3D structures.

## References

- AISC. (2005). *Steel Construction Manual 13th Edition*. American Institute of Steel Construction, Chicago, IL.
- Amiri, V., and Davodi, M. R. (2002). "Modeling the semi-rigid behavior of the MERO Jointing System." *Space Structures 5(1)*, G. A. R. Parke and P. Disney, eds., Thomas Telford Ltd, 309–316.
- ASCE. (2006). "Snow Loads." *Minimum Design Loads for Buildings and Other Structures (ASCE/SEI 7-05)*, American Society of Civil Engineers, 81–93.
- ASTM. (2016). *ASTM E8/E8M-16a Standard Test Methods for Tension Testing of Metallic Materials*. ASTM International, West Conshohocken, PA.
- Battaini, M., Yang, G., and Spencer Jr., B. F. (2000). "Bench-Scale Experiment for Structural Control." *Engineering Mechanics*, ASCE, 126(February), 140–148.
- Chen, G., Zhang, H., Rasmussen, K. J. R., and Fan, F. (2016). "Modeling geometric imperfections for reticulated shell structures using random field theory." *Engineering Structures*, Elsevier Ltd, 126, 481–489.
- Doran, D. C. (1997). "Toward the Strength Characterization of Connections Employed in Reticulated Structures." Thesis presented to University of Texas at El Paso in partial fulfillment of the requirements for the degree of Master of Science.
- Fan, F., Cao, Z., and Shen, S. (2010a). "Elasto-Plastic Stability of Single-Layer Reticulated Shells." *Thin-Walled Structures*, Elsevier, 48, 827–836.

- Fan, F., Ma, H., Cao, Z., and Shen, S. (2010b). "Direct Estimation of Critical Load for Single-Layer Reticulated Domes with Semi-Rigid Joints." *International Journal of Space Structures*, SAGE, 25, 15–24.
- Fan, F., Ma, H., Cao, Z., and Shen, S. (2011). "A New Classification System for the Joints Used in Lattice Shells." *Thin-Walled Structures*, Elsevier, 49, 1544–1553.
- Fan, F., Ma, H., Chen, G., and Shen, S. (2012a). "Experimental study of semi-rigid joint systems subjected to bending with and without axial force." *Journal of Constructional Steel Research*, Elsevier, 68, 126–137.
- Fan, F., Yan, J., and Cao, Z. (2012b). "Stability of Reticulated Shells Considering Member Buckling." *Journal of Constructional Steel Research*, Elsevier Ltd, 77, 32–42.
- Fan, F., Yan, J., and Cao, Z. (2012c). "Elasto-Plastic Stability of Single-Layer Reticulated Domes with Initial Curvature of Members." *Thin-Walled Structures*, Elsevier, 60, 239–246.
- Fang, Z. X., and Fan, H. T. (2011). "Redundancy of Structural Systems in the Context of Structural Safety." *Procedia Engineering*, Elsevier, 14, 2172–2178.
- Ferregut, C., and Carrasco, C. (1998). *Strength Characterization of Geometrica Connector Type 6ZD-00*. Technical Report Submitted to Geometrica Inc.
- Fitch, J. R. (1968). "The Buckling and Post-Buckling Behavior of Spherical Caps Under Axisymmetric Load." *International Journal of Solid Structures*, Elsevier, 4, 421–446.
- Fong, M., Liu, Y. P., and Chan, S. L. (2012). "Second-Order Analysis and Experiments of Semi-Rigid and Imperfect Domes." *Advances in Structural Engineering*, SAGE, 15, 1537–1547.

- Fülöp, A., and Iványi, M. (2004). “Experimentally Analyzed Stability and Ductility Behaviour of a Space-Truss Roof System.” *Thin-Walled Structures*, Elsevier, 42, 309–320.
- Garcia, A. (2017). “Integrating Manufacturing Geometric Imperfections in the Inelastic Behavior Modeling of Joints Used in Three- Dimensional Structures.” Dissertation presented to University of Texas at El Paso in partial fulfillment of the requirements for the degree of Doctor of Philosophy in Civil Engineering.
- Geometrica®. (2014). “Geometrica Structure Assembly Process.”  
<<https://vimeo.com/102565601>> (Jan. 1, 2015).
- Geometrica®. (2015). “Geometrica.” <<http://www.geometrica.com/>> (Jan. 1, 2015).
- Gidófalvy, K., and Katula, L. (2010). “Imperfection for the Buckling Analysis of Grid Shells.” *Second Conference of Junior Researchers in Civil Engineering*, C. Tóth, ed., Emerald Group Publishing, Budapest, Hungary, 74–80.
- Han, Q., Liu, Y., and Xu, Y. (2016). “Stiffness characteristics of joints and influence on the stability of single-layer latticed domes.” *Thin Walled Structures*, Elsevier, 107, 514–525.
- Hwang, K., Knippers, J., and Park, S. (2009). “Influence of Various Types Node Connectors on the Buckling Loads of Grid Shells.” *Proceedings of the International Association for Shell and Spatial Structures (IASS) Symposium 2009 Evolution and Trends in Design, Analysis and Construction of Shell and Spatial Structures*, A. Domingo and C. Lazaro, eds., Valencia, 1841–1852.
- Jin, J. (2004). “Millennium Dome 1.”  
<<https://www.flickr.com/photos/jamesjin/58712717/in/photostream/>> (Nov. 11, 2016).

- Kartal, M. E., Başıağ, H. B., Bayraktar, A., and Muvafik, M. (2010). “Effects of Semi-Rigid Connection on Structural Responses.” *Electronic Journal of Structural Engineering*, 10, 22–35.
- Kashani, M., and Croll, J. G. a. (1994). “Lower Bounds for Overall Buckling of Spherical Space Domes.” *Journal of Engineering Mechanics*, ASCE, 949–970.
- Kato, S., Fujimoto, M., and Ogawa, T. (2005). “Buckling Load of Steel Single-Layer Reticulated Domes of Circular Plan.” *Journal of the International Association for Shell and Spatial Structures*, IASS, 46, 41–63.
- Kato, S., Mutoh, I., and Shomura, M. (1998). “Collapse of Semi-Rigidly Jointed Reticulated Domes with Initial Geometric Imperfections.” *Journal of Constructional Steel Research*, Elsevier, 48, 145–167.
- Lan, T. T. (2005). “Space Frame Structures.” *Handbook of Structural Engineering*, W. Chen and E. M. Lui, eds., CRC Press 2005, Beijing, 1–50.
- López, A., Puente, I., and Serna, M. (2007a). *Analysis of Single Layer Latticed Domes : a New Beam - Element*. Report from the Institute of Civil Engineering, University of Navarra, Spain.
- López, A., Puente, I., and Serna, M. (2007b). “Direct Evaluation of the Buckling Loads of Semi-Rigidly Jointed Single-Layer Latticed Domes under Symmetric Loading.” *Engineering Structures*, Elsevier, 29, 101–109.

- López, A., Puente, I., and Serna, M. (2007c). “Numerical Model and Experimental Tests on Single-Layer Latticed Domes with Semi-Rigid Joints.” *Computers & Structures*, Elsevier, 85, 360–374.
- Ma, H., Fan, F., Zhong, J., and Cao, Z. (2013). “Stability Analysis of Single-Layer Elliptical Paraboloid Latticed Shells with Semi-Rigid Joints.” *Thin-Walled Structures*, Elsevier, 72, 128–138.
- Makowski, Z. S. (1984). “A History of the Development of Domes and a Review of Recent Achievements World-Wide.” *Analysis Design and Construction of Braced Domes*, Nichols Publishing Company, New York, 1–85.
- Makowski, Z. S. (1993). “Space Structures - A Review of the Developments within the Last Decade.” *Space Structures 4(1)*, G. A. . Parke and C. M. Howard, eds., Thomas Telford, 1–15.
- Mohammadi, M., Abedi, K., and Taghizadeih, N. (2012). “Stability Analysis of Single- Layer Barrel Vault Space.” *Journal of Space Structures*, SAGE, 27, 203–218.
- MSC. (2014). “Patran/Nastran.” MSC Software Corporation, Santa Ana.
- Mullord, P. (1984). “Introduction to the Analysis of Braced Domes.” *Analysis Design and Construction of Braced Domes*, Nichols Publishing Company, 87–95.
- Narayanan, S. (2007). *Space Structures: Principles and Practice*. Multi Science Publishing Co Ltd.
- Nie, G., Fan, F., and Zhi, X. (2013). “Test on the Suspended Dome Structure and Joints of Dalian Gymnasium.” *Advances in Structural Engineering*, SAGE, 16, 467–486.

- Ogawa, T., and Kuwada, M. (1998). “Elasto-Plastic Buckling Behaviour of Rigidly Jointed Single-Layer Latticed Domes.” *International Association for Shell and Spatial Structures 1998 International Symposium*, J. S. Medwadowski, ed., IASS, Sidney, 460–467.
- Pugnale, S. (2013). “Buckling of gridshells from dome to free-form structures.” Thesis presented to Politecnico di Torino in partial fulfillment of the requirements for the degree of Master of Science.
- Ramaswamy, G. S., Eekhout, O. M., and Suresh, G. R. (2002). *Analysis, Design and Construction of Steel Space Frames*. Thomas Telford Publishing.
- Salcido, J. C., Abdul, A., and Ravi, S. (2016). “Comparison of Embodied Energy and Environmental Impact of Alternative Materials used in Reticulated Dome Construction.” *Building and Environment*, Elsevier, 96, 22–34.
- Salmon, C., Johnson, J., and Malhas, F. (2009). “Combined Bending and Axial Load.” *Steel Structures: Design and Construction*, T. M. Slaughter, ed., Pearson, 591–654.
- Shibata, R., Kato, S., Yamada, S., and Ueki, T. (1993). “Experimental Study on the Ultimate Strength of Single Layer Reticular Domes.” *Space Structures 4(1)*, G. A. R. Parke and C. M. Howard, eds., Thomas Telford Ltd, 387–395.
- Sugizaki, K., and Kohmura, S. (1994). “Experimental Study on the Buckling Behavior of Triodetic Aluminum Space Frame.” *IASS-ASCE International Symposium*, C. Penalba, ed., IASS, Atlanta, Georgia, United States, 478–487.

- Supple, W. J. (1984). “Stability and Collapse Analysis of Braced Domes.” *Analysis Design and Construction of Braced Domes*, Z. S. Makowski, ed., Nichols Publishing Company, 143–159.
- Wright, D. T. (1965). “Membrane Forces and Buckling in Reticulated Shells.” *Journal of the Structural Division*, ASCE, 91, 173–201.
- Wright, D. T. (1969). “Instability in Reticulated Spheroids; Experimental Results and the Effects of Nodal Imperfections.” *Structures Technology for Large Radio and Radar Telescope Systems*, J. Mar and H. Leibowitz, eds., MIT Press, Toronto, Canada, 369–379.
- Yan, G., Duan, Q., and Hua, X. (2000). “Instability signature for detecting snap-through buckling of dome structures.” *Journal of Engineering Mechanics*, ASCE, 126, 140–148.
- Yan, J., Qin, F., Cao, Z., Fan, F., and Mo, Y. L. (2016). “Mechanism of coupled instability of single-layer reticulated domes.” *Engineering Structures*, Elsevier, 114, 158–170.
- Zamanzadeh, Z., Abdolpour, H., and Behraves, A. (2010). “Investigating the Buckling Behaviour of Single Layer Dome Form of Space Structures.” *Challenges, Opportunities and Solutions in Structural Engineering and Construction*, N. Ghafoori, ed., CRC Press 2009, 399–404.

## **Appendix A**

### **Finite Element Simulation Results: As-Designed 3D Structure**

### **d-090 3D structure**

**Table A.1** summarizes the data of the applied load-displacement of node 13 at 25% load increments until critical load of the d-090 3D structure is reached at 38.80% of the applied load at a displacement of 2.15 inches.

**Table A.1** Applied Load-Displacement of Node 13: d-090 3D Structure

| Applied Load<br>(%) | d-090<br>Disp. (in) |
|---------------------|---------------------|
| 25.00               | 0.17                |
| 50.00               | 0.26                |
| 75.00               | 0.35                |
| 100.00              | 0.44                |
| 125.00              | 0.55                |
| 150.00              | 0.65                |
| 175.00              | 0.75                |
| 200.00              | 0.85                |
| 225.00              | 0.96                |
| 250.00              | 1.10                |
| 275.00              | 1.31                |
| 300.00              | 1.66                |
| 308.80              | 2.15                |

**Table A.2** summarizes the data of the applied load-rotation of node 2 at 25% load increments until critical load of the d-090 3D structure is reached at 308.80% of the applied load at a rotation of 0.0236 radians.

**Table A.2** Applied Load-Rotation of Node 2: d-090 3D Structure

| Applied Load<br>(%) | d-090<br>Rot. (rad) |
|---------------------|---------------------|
| 25.00               | 0.0015              |
| 50.00               | 0.0029              |
| 75.00               | 0.0042              |
| 100.00              | 0.0056              |
| 125.00              | 0.0071              |
| 150.00              | 0.0086              |
| 175.00              | 0.0100              |
| 200.00              | 0.0113              |
| 225.00              | 0.0128              |
| 250.00              | 0.0145              |
| 275.00              | 0.0168              |
| 300.00              | 0.0200              |
| 308.80              | 0.0236              |

**Table A.3** summarizes the data of the applied load-interaction index of both nodes of bar 62 at 25% load increments until critical load of the d-090 3D structure is reached at 308.80% of the applied load. Once one of the nodes of the bar reached an interaction index of 1.0 or greater the interaction index is highlighted with a red font

**Table A.3** Applied Load-Interaction Index of Beam 62: d-090 3D Structure

| Load (%)      | P <sub>ux</sub> (lb) |           | M <sub>uy</sub> (lb-in) |          | M <sub>uz</sub> (lb-in) |           | P <sub>ux</sub> /φP <sub>nx</sub> |        | Interaction Index |        | Bar Max |
|---------------|----------------------|-----------|-------------------------|----------|-------------------------|-----------|-----------------------------------|--------|-------------------|--------|---------|
|               | Node 13              | Node 2    | Node 13                 | Node 2   | Node 13                 | Node 2    | Node 13                           | Node 2 | Node 13           | Node 2 |         |
| <b>25.00</b>  | 797.15               | 797.15    | 23.11                   | 30.92    | 1,636.06                | 1,173.05  | 0.028                             | 0.028  | 0.092             | 0.071  | 0.092   |
| <b>50.00</b>  | 1,742.66             | 1,742.66  | 40.81                   | 61.95    | 2,929.18                | 2,282.00  | 0.061                             | 0.061  | 0.171             | 0.141  | 0.171   |
| <b>75.00</b>  | 2,653.81             | 2,653.81  | 60.61                   | 96.23    | 4,321.71                | 3,528.27  | 0.092                             | 0.092  | 0.253             | 0.217  | 0.253   |
| <b>100.00</b> | 3,542.77             | 3,542.77  | 85.17                   | 146.69   | 5,854.28                | 4,899.28  | 0.123                             | 0.123  | 0.342             | 0.300  | 0.342   |
| <b>125.00</b> | 4,432.66             | 4,432.66  | 104.08                  | 213.05   | 7,497.17                | 6,366.70  | 0.154                             | 0.154  | 0.436             | 0.388  | 0.436   |
| <b>150.00</b> | 5,410.06             | 5,410.06  | 479.08                  | 297.43   | 9,090.82                | 7,795.10  | 0.188                             | 0.188  | 0.546             | 0.477  | 0.546   |
| <b>175.00</b> | 6,518.72             | 6,518.72  | 401.90                  | 347.78   | 10,547.22               | 9,109.27  | 0.227                             | 0.227  | 0.687             | 0.624  | 0.687   |
| <b>200.00</b> | 7,650.47             | 7,650.47  | 543.05                  | 418.98   | 12,100.69               | 10,518.44 | 0.266                             | 0.266  | 0.797             | 0.725  | 0.797   |
| <b>225.00</b> | 8,803.45             | 8,803.45  | 700.57                  | 500.99   | 13,781.49               | 12,092.19 | 0.306                             | 0.306  | 0.914             | 0.835  | 0.914   |
| <b>250.00</b> | 10,027.75            | 10,027.75 | 897.03                  | 604.65   | 15,662.74               | 13,845.88 | 0.349                             | 0.349  | 1.044             | 0.956  | 1.044   |
| <b>275.00</b> | 11,381.20            | 11,381.20 | 1,151.40                | 722.69   | 17,964.44               | 16,176.61 | 0.396                             | 0.396  | 1.199             | 1.106  | 1.199   |
| <b>300.00</b> | 13,103.36            | 13,103.36 | 1,602.07                | 942.87   | 21,010.22               | 19,163.03 | 0.455                             | 0.455  | 1.406             | 1.300  | 1.406   |
| <b>308.80</b> | 14,390.68            | 14,390.68 | 2,016.84                | 1,202.91 | 23,738.09               | 22,486.72 | 0.500                             | 0.500  | 1.582             | 1.496  | 1.582   |

\*φP<sub>nx</sub> = 28,768.4 lb

\*φM<sub>ny</sub> = 21,156.9 lb-in

\*φM<sub>nz</sub> = 21,156.9 lb-in

## **Appendix B**

### **Finite Element Simulation Results: b-090 3D Structures Model Set**

## b-AA 090 3D Structure

**Figure B.1** presents the applied load-displacement plot of node 13 for the b-AA 090 3D structure. In this plot, the vertical axis corresponds to the applied load history expressed in percentage while the horizontal axis displays the resultant displacement of the node in inches as the load is applied. As observed in the figure, the applied load-displacement graph of node 13 displays a non-linear response under initial loading which indicates the movement/closing of the jointing systems' gaps. After initial loading, the structure follows a linear response up to 150% of the applied load. Subsequently, the b-AA 090 3D structure follows a non-linear behavior until critical capacity is reached at 310.31% of the applied load and at a displacement of 1.87 inches. Overall buckling is observed after critical capacity is reached.

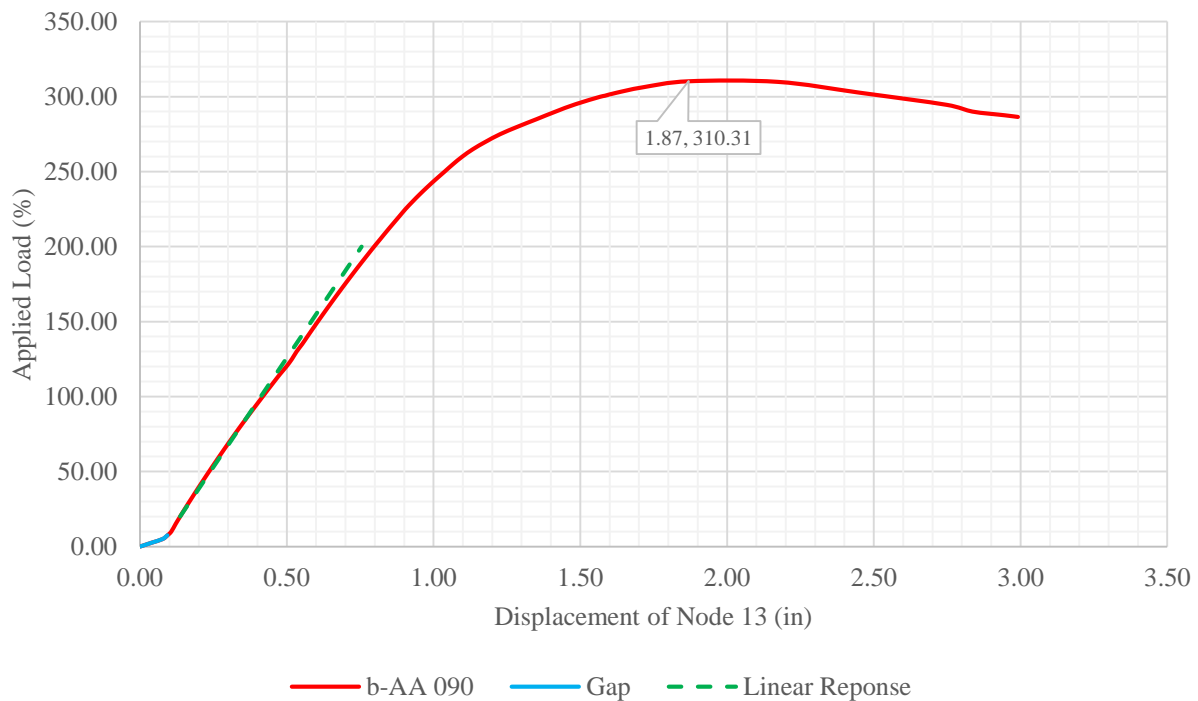


**Figure B.1** Applied Load-Displacement of Node 13: b-AA 090 3D Structure

**Figure B.2** presents the applied load-rotation plot of node 2 for the b-AA 090 3D structure. In this plot, the vertical axis corresponds to the applied load history expressed in percentage while the horizontal axis displays the resultant rotation of the node in radians as the load is applied. As observed in the figure, the applied load-rotation graph of node 2 displays a non-linear response under initial loading which indicates the movement/closing of the jointing systems' gaps. After initial loading, the structure follows a linear response up to 150% of the applied load. Subsequently, the b-AA 090 3D structure follows a non-linear behavior until critical capacity is reached at 310.30% of the applied load and at a rotation of 0.0213 radians. Overall buckling is observed after critical capacity is reached.

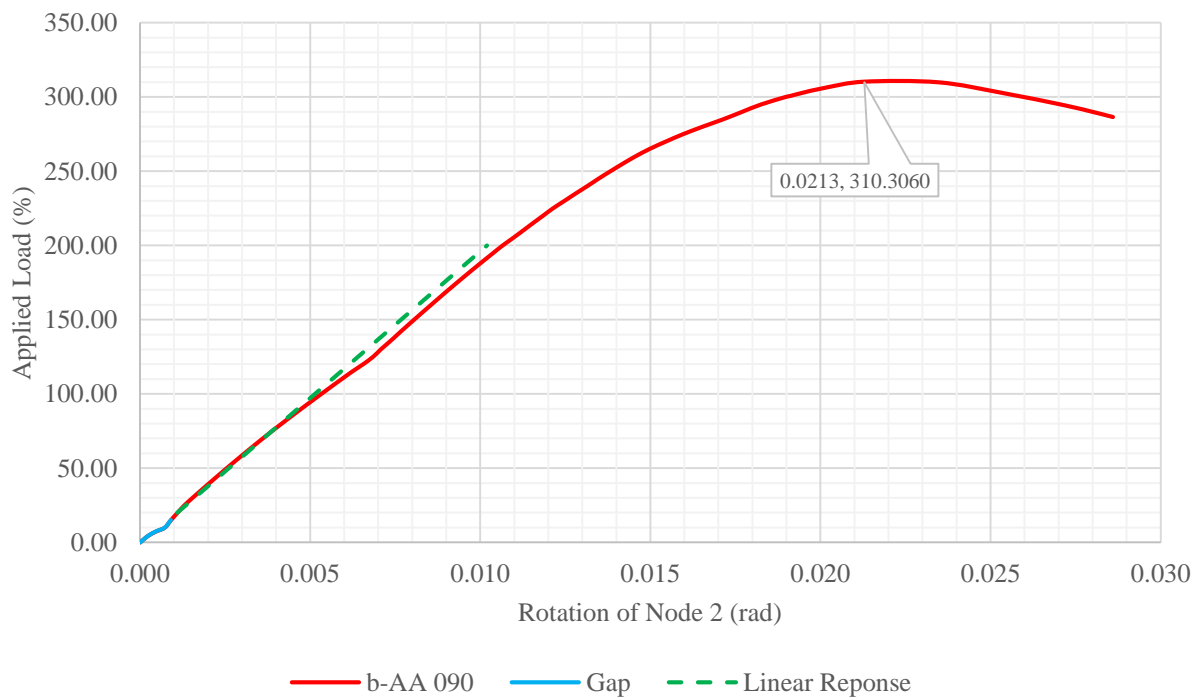


**Figure B.2** Applied Load-Rotation of Node 2: b-AA 090 3D Structure

**Table B.1** summarizes the data of the applied load-interaction index of both nodes of bar 62 at 25% load increments until critical load of the b-AA 090 3D structure is reached at 310.30% of the applied load.

**Table B.1** Applied Load-Interaction Index of Beam 62: b-AA 090 3D Structure

| 170                             | Load (%)  | P <sub>ux</sub> (lb)               |           | M <sub>uy</sub> (lb-in)            |           | M <sub>uz</sub> (lb-in) |           | P <sub>ux</sub> /φP <sub>nx</sub> |        | Interaction Index |        | Bar Max |
|---------------------------------|-----------|------------------------------------|-----------|------------------------------------|-----------|-------------------------|-----------|-----------------------------------|--------|-------------------|--------|---------|
|                                 |           | Node 13                            | Node 2    | Node 13                            | Node 2    | Node 13                 | Node 2    | Node 13                           | Node 2 | Node 13           | Node 2 |         |
|                                 | 25.00     | 843.77                             | 843.77    | 21.10                              | 28.07     | 1,546.89                | 1,175.48  | 0.029                             | 0.029  | 0.089             | 0.072  | 0.089   |
|                                 | 50.00     | 1,753.00                           | 1,753.00  | 38.07                              | 58.85     | 2,846.68                | 2,338.01  | 0.061                             | 0.061  | 0.167             | 0.144  | 0.167   |
|                                 | 75.00     | 2,664.16                           | 2,664.16  | 63.90                              | 103.88    | 4,231.22                | 3,574.95  | 0.093                             | 0.093  | 0.249             | 0.220  | 0.249   |
|                                 | 100.00    | 3,563.38                           | 3,563.38  | 159.01                             | 159.84    | 5,728.74                | 4,918.66  | 0.124                             | 0.124  | 0.340             | 0.302  | 0.340   |
|                                 | 125.00    | 4,467.62                           | 4,467.62  | 259.55                             | 221.86    | 7,322.39                | 6,353.27  | 0.155                             | 0.155  | 0.436             | 0.388  | 0.436   |
|                                 | 150.00    | 5,567.36                           | 5,567.36  | 340.01                             | 273.12    | 8,653.50                | 7,547.54  | 0.194                             | 0.194  | 0.522             | 0.466  | 0.522   |
|                                 | 175.00    | 6,679.56                           | 6,679.56  | 438.20                             | 324.42    | 10,081.43               | 8,839.01  | 0.232                             | 0.232  | 0.674             | 0.617  | 0.674   |
|                                 | 200.00    | 7,810.56                           | 7,810.56  | 555.61                             | 378.50    | 11,615.40               | 10,231.77 | 0.271                             | 0.271  | 0.783             | 0.717  | 0.783   |
|                                 | 225.00    | 8,978.71                           | 8,978.71  | 686.22                             | 463.27    | 13,267.72               | 11,726.91 | 0.312                             | 0.312  | 0.898             | 0.824  | 0.898   |
|                                 | 250.00    | 10,214.15                          | 10,214.15 | 855.83                             | 553.90    | 15,106.68               | 13,486.63 | 0.355                             | 0.355  | 1.026             | 0.945  | 1.026   |
|                                 | 275.00    | 11,539.48                          | 11,539.48 | 1,037.52                           | 665.08    | 17,313.74               | 15,689.31 | 0.401                             | 0.401  | 1.172             | 1.088  | 1.172   |
| 300.00                          | 13,245.56 | 13,245.56                          | 1,429.32  | 865.88                             | 20,295.49 | 18,608.35               | 0.460     | 0.460                             | 1.373  | 1.279             | 1.373  |         |
| 310.30                          | 14,309.11 | 14,309.11                          | 1,788.28  | 1,047.42                           | 22,464.91 | 20,830.20               | 0.497     | 0.497                             | 1.516  | 1.417             | 1.516  |         |
| *φP <sub>nx</sub> = 28,768.4 lb |           | *φM <sub>ny</sub> = 21,156.9 lb-in |           | *φM <sub>nz</sub> = 21,156.9 lb-in |           |                         |           |                                   |        |                   |        |         |

**Figure B.3** presents the applied load-interaction index plot of beam element 62 for the b-AA 090 3D structure. In this graph, the vertical axis corresponds to the applied load history expressed in percentage while the horizontal axis shows the interaction index of the beam element as the load is applied. The applied load-interaction index graph displays a non-linear response under initial loading which indicates the movement/closing of the jointing systems' gaps. After initial loading, the applied load-interaction index plot of beam element 62 shows a linear response up to 150% of the applied load. Subsequently, a non-linear behavior of the element is observed until failure of the beam is reached at 244.95% of the applied load. The forces and moments at bar failure are:

- 1)  $P_{ux}$  is 9,964.81 lb.;
- 2)  $M_{uy}$  is 821.60 lb.-in; and
- 3)  $M_{uz}$  is 14,735.53 lb.-in.

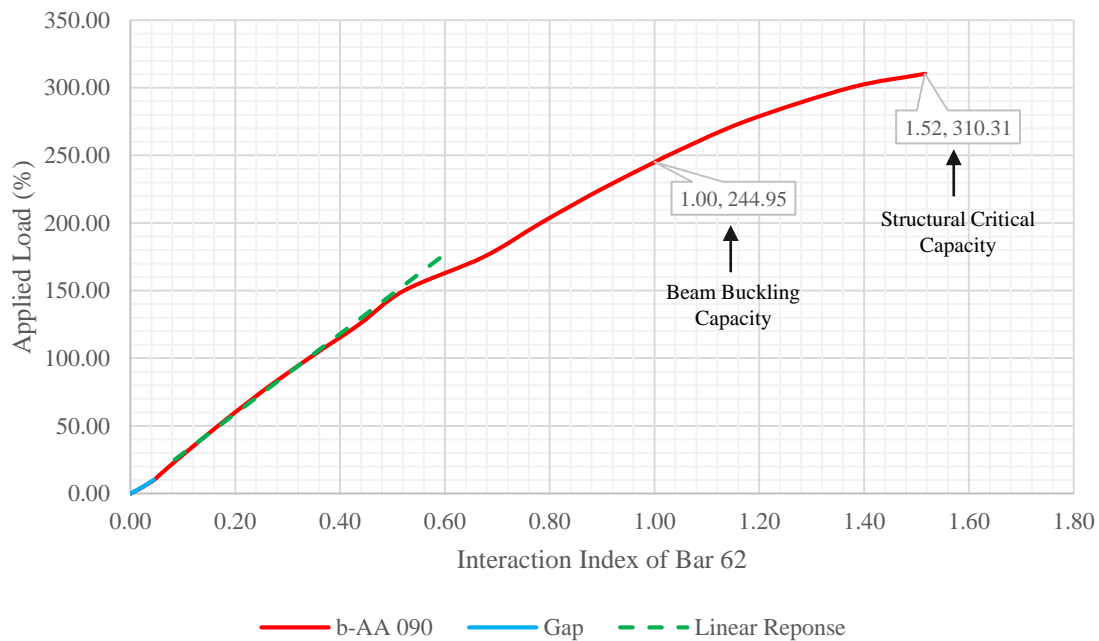


**Figure B.3** Applied Load-Interaction Index of Beam 62: b-AA 090 3D Structure

**Figure B.4** shows the axial semi-rigid behavior of the jointing system used during the simulation of the b-AA 090 3D structure. In this plot, the initial flat portion represents the fit-gap tolerance between the mating parts of the jointing system. Once the mating parts become in contact, a non-linear tension or compression load vs. displacement behavior of the connection is observed. Additionally, this figure displays that at beam failure, only 22.73% of the connection capacity in compression is reached.

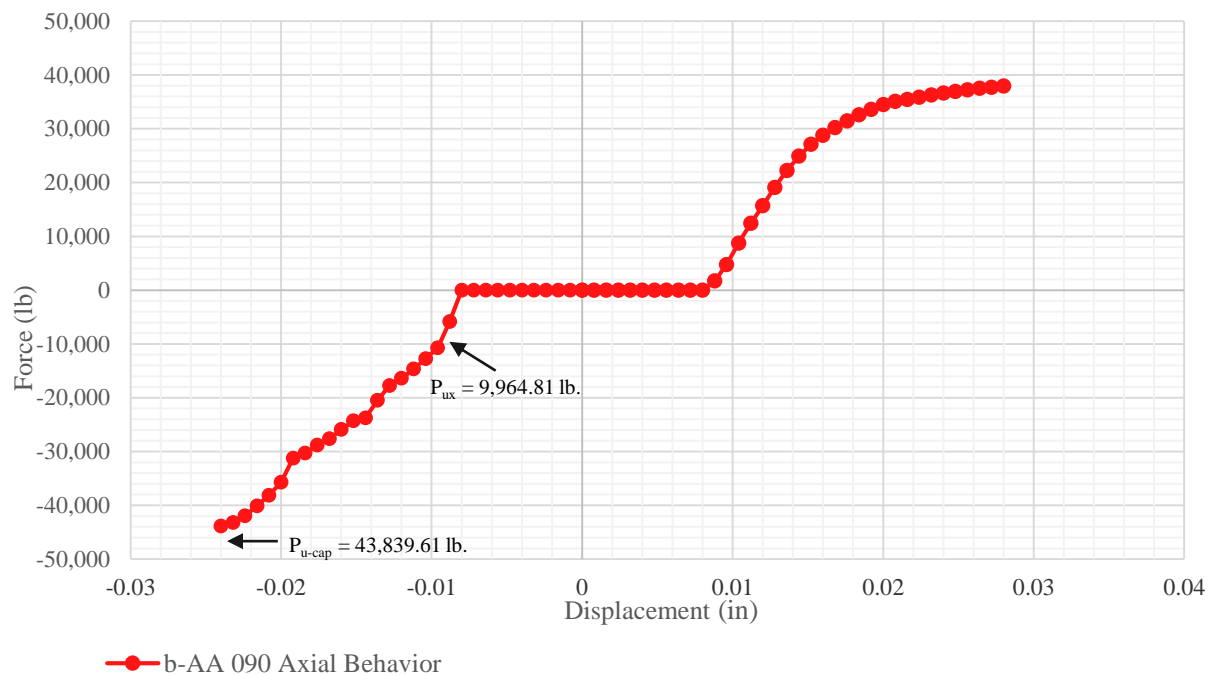


**Figure B.4** Axial Semi-Rigid Behavior: b-AA 090 (After Garcia 2017)

**Figure B.5** shows the in-plane bending semi-rigid behavior of jointing system used during the simulation of the b-AA 090 3D structure. In this plot, the initial flat portion represents the in-plane fit-gap tolerance between the mating parts of the jointing system. Once the mating parts become in contact, a non-linear bending moment vs. rotation behavior of the connection is observed. Additionally, this figure displays that at beam failure, only 3.58% of the connection in-plane bending capacity is reached.

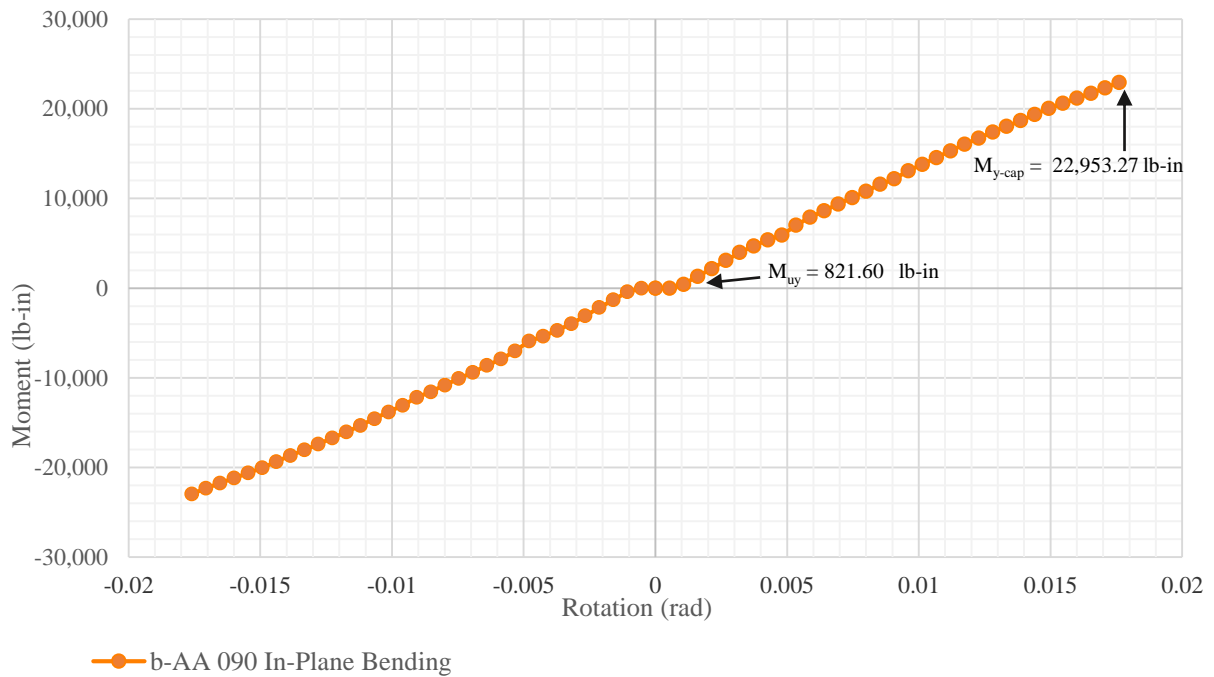


**Figure B.5** In-Plane Bending Semi-Rigid Behavior: b-AA 090 (After Garcia 2017)

## b-AB 090 3D Structure

**Figure B.6** presents the applied load-displacement plot of node 13 for the b-AB 090 3D structure. In this plot, the vertical axis corresponds to the applied load history expressed in percentage while the horizontal axis displays the resultant displacement of the node in inches as the load is applied. As observed in the figure, the applied load-displacement graph of node 13 displays a non-linear response under initial loading which indicates the movement/closing of the jointing systems' gaps. After initial loading, the structure follows a linear response up to 150% of the applied load. Subsequently, the b-AB 090 3D structure follows a non-linear behavior until critical capacity is reached at 301.81% of the applied load and at a displacement of 2.27 inches. Overall buckling is observed after critical capacity is reached.

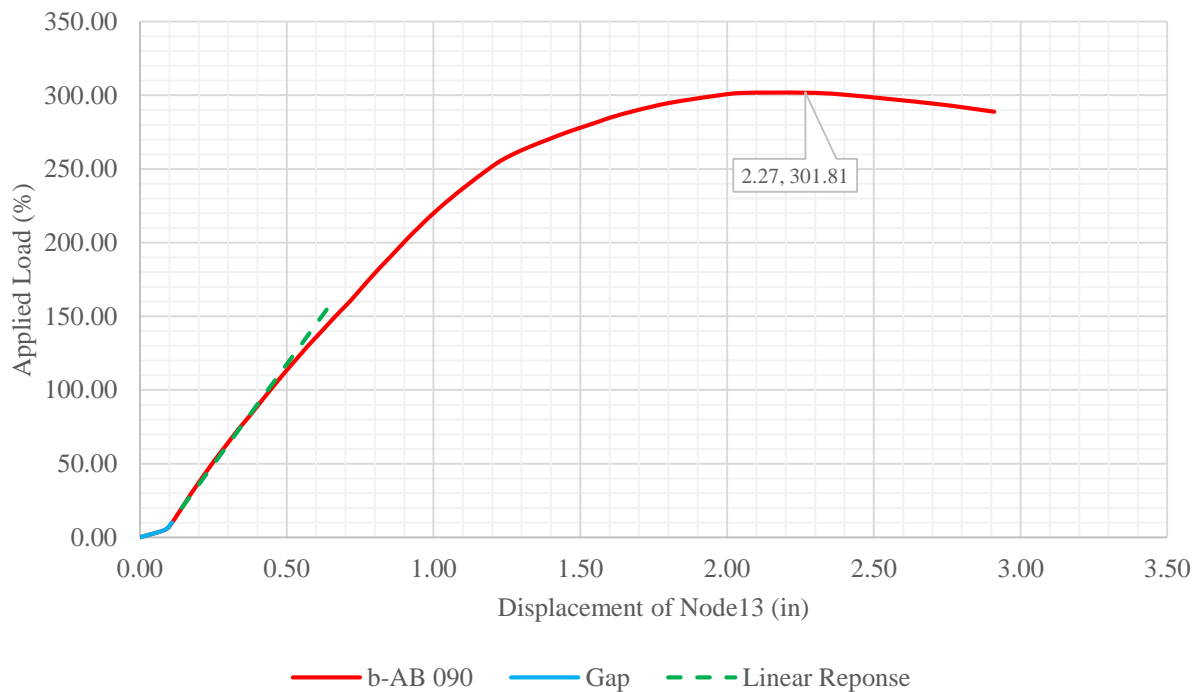


**Figure B.6** Applied Load-Displacement of Node 13: b-AB 090 3D Structure

**Figure B.7** presents the applied load-rotation plot of node 2 for the b-AB 090 3D structure. In this plot, the vertical axis corresponds to the applied load history expressed in percentage while the horizontal axis displays the resultant rotation of the node in radians as the load is applied. As observed in the figure, the applied load-rotation graph of node 2 displays a non-linear response under initial loading which indicates the movement/closing of the jointing systems' gaps. After initial loading, the structure follows a linear response up to 150% of the applied load. Subsequently, the b-AB 090 3D structure follows a non-linear behavior until critical capacity is reached at 301.81% of the applied load and at a rotation of 0.0247 radians. Overall buckling is observed after critical capacity is reached.

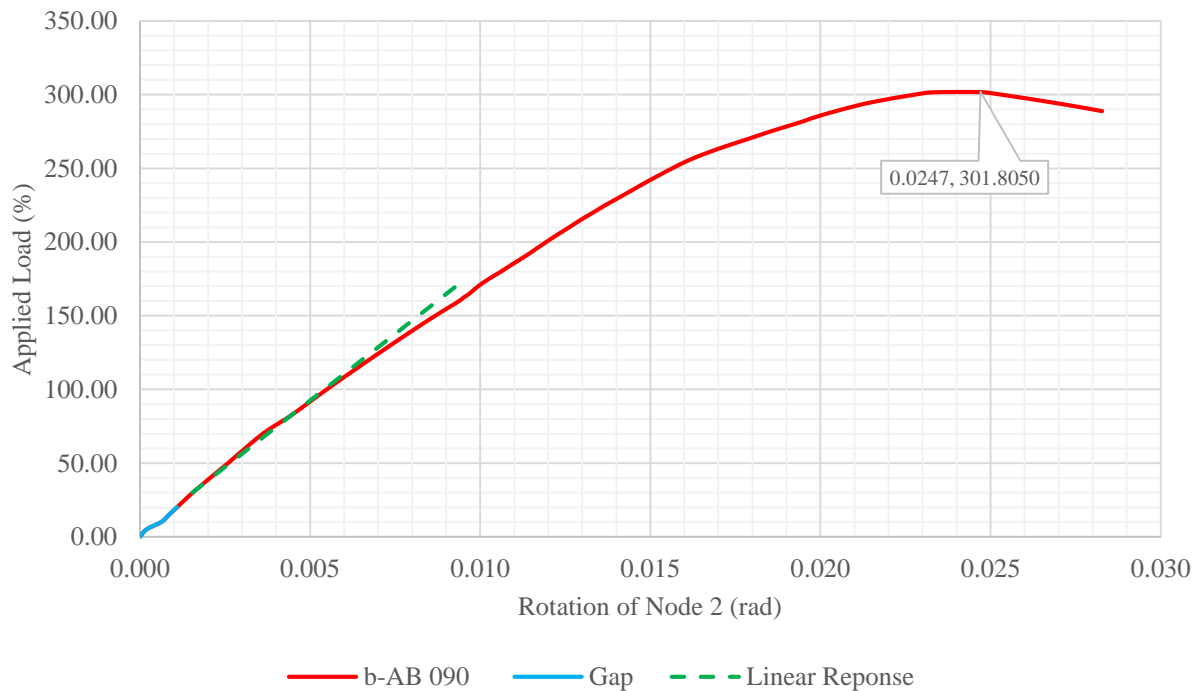


**Figure B.7** Applied Load-Rotation of Node 2: b-AB 090 3D Structure

**Table B.2** summarizes the data of the applied load-interaction index of both nodes of bar 62 at 25% load increments until critical load of the b-AB 090 3D structure is reached at 301.81% of the applied load.

**Table B.2** Applied Load-Interaction Index of Beam 62: b-AB 090 3D Structure

| Load (%)      | P <sub>ux</sub> (lb) |           | M <sub>uy</sub> (lb-in) |          | M <sub>uz</sub> (lb-in) |           | P <sub>ux</sub> /φP <sub>nx</sub> |        | Interaction Index |        | Bar Max |
|---------------|----------------------|-----------|-------------------------|----------|-------------------------|-----------|-----------------------------------|--------|-------------------|--------|---------|
|               | Node 13              | Node 2    | Node 13                 | Node 2   | Node 13                 | Node 2    | Node 13                           | Node 2 | Node 13           | Node 2 |         |
| <b>25.00</b>  | 850.30               | 850.30    | 38.70                   | 48.55    | 1,546.74                | 1,131.51  | 0.030                             | 0.030  | 0.090             | 0.071  | 0.090   |
| <b>50.00</b>  | 1,758.33             | 1,758.33  | 69.13                   | 99.93    | 2,859.53                | 2,288.77  | 0.061                             | 0.061  | 0.169             | 0.143  | 0.169   |
| <b>75.00</b>  | 2,648.41             | 2,648.41  | 110.90                  | 169.02   | 4,283.67                | 3,531.29  | 0.092                             | 0.092  | 0.254             | 0.221  | 0.254   |
| <b>100.00</b> | 3,545.57             | 3,545.57  | 248.26                  | 264.94   | 5,821.20                | 4,878.83  | 0.123                             | 0.123  | 0.349             | 0.305  | 0.349   |
| <b>125.00</b> | 4,437.16             | 4,437.16  | 393.37                  | 365.78   | 7,450.21                | 6,327.48  | 0.154                             | 0.154  | 0.448             | 0.393  | 0.448   |
| <b>150.00</b> | 5,323.96             | 5,323.96  | 546.86                  | 474.24   | 9,198.56                | 7,882.31  | 0.185                             | 0.185  | 0.553             | 0.488  | 0.553   |
| <b>175.00</b> | 6,362.52             | 6,362.52  | 680.50                  | 573.45   | 10,842.11               | 9,320.74  | 0.221                             | 0.221  | 0.705             | 0.637  | 0.705   |
| <b>200.00</b> | 7,375.85             | 7,375.85  | 855.36                  | 690.35   | 12,666.91               | 10,951.18 | 0.256                             | 0.256  | 0.825             | 0.745  | 0.825   |
| <b>225.00</b> | 8,452.24             | 8,452.24  | 1,033.36                | 817.62   | 14,514.38               | 12,691.76 | 0.294                             | 0.294  | 0.947             | 0.861  | 0.947   |
| <b>250.00</b> | 9,580.03             | 9,580.03  | 1,219.28                | 962.88   | 16,646.86               | 14,633.90 | 0.333                             | 0.333  | 1.084             | 0.988  | 1.084   |
| <b>275.00</b> | 10,833.95            | 10,833.95 | 1,534.07                | 1,186.36 | 19,420.61               | 17,433.68 | 0.377                             | 0.377  | 1.257             | 1.159  | 1.257   |
| <b>300.00</b> | 12,686.93            | 12,686.93 | 2,169.92                | 1,610.51 | 23,350.98               | 21,495.70 | 0.441                             | 0.441  | 1.513             | 1.412  | 1.513   |
| <b>301.81</b> | 13,429.31            | 13,429.31 | 2,241.43                | 1,817.48 | 24,790.52               | 23,325.55 | 0.467                             | 0.467  | 1.603             | 1.523  | 1.603   |

\*φP<sub>nx</sub> = 28,768.4 lb    \*φM<sub>ny</sub> = 21,156.9 lb-in    \*φM<sub>nz</sub> = 21,156.9 lb-in

**Figure B.8** presents the applied load-interaction index plot of beam element 62 for the b-AB 090 3D structure. In this graph, the vertical axis corresponds to the applied load history expressed in percentage while the horizontal axis shows the interaction index of the beam element as the load is applied. The applied load-interaction index graph displays a non-linear response under initial loading which indicates the movement/closing of the jointing systems' gaps. After initial loading, the applied load-interaction index plot of beam element 62 shows a linear response up to 150% of the applied load. Subsequently, a non-linear behavior of the element is observed until failure of the beam is reached at 234.69% of the applied load. The forces and moments at bar failure are:

- 1)  $P_{ux}$  is 8,889.56 lb.;
- 2)  $M_{uy}$  is 1,105.45 lb.-in; and
- 3)  $M_{uz}$  is 15,341.29 lb.-in.

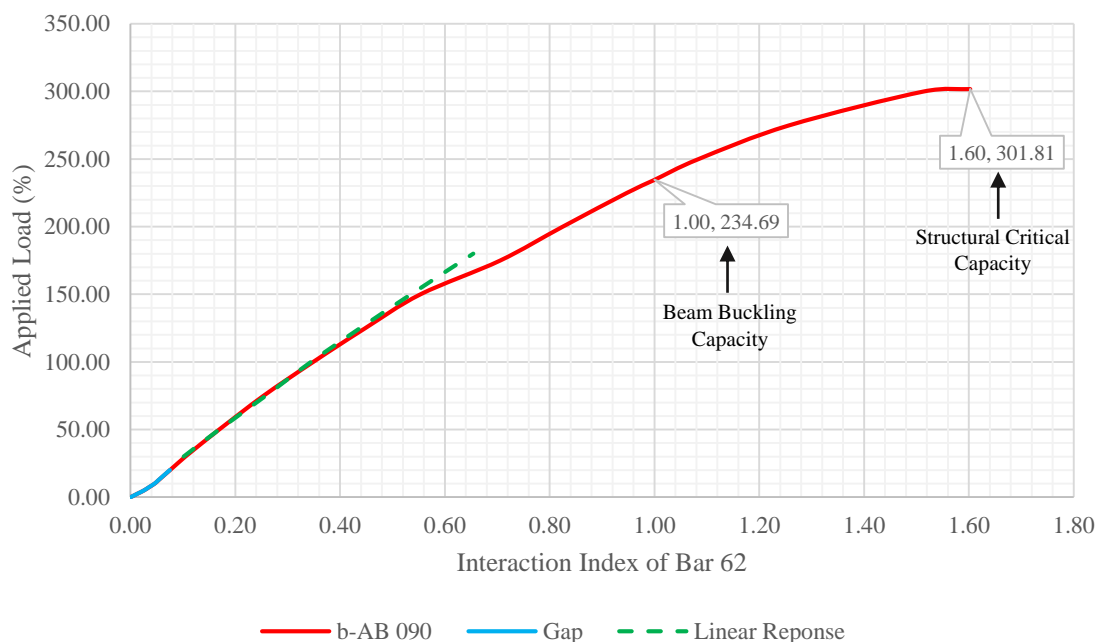


**Figure B.8** Applied Load-Interaction Index of Beam 62: b-AB 090 3D Structure

**Figure B.9** shows the axial semi-rigid behavior of the jointing system used during the simulation of the b-AB 090 3D structure. In this plot, the initial flat portion represents the fit-gap tolerance between the mating parts of the jointing system. Once the mating parts become in contact, a non-linear tension or compression load vs. displacement behavior of the connection is observed. Additionally, this figure displays that at beam failure, only 19.68% of the connection capacity in compression is reached.

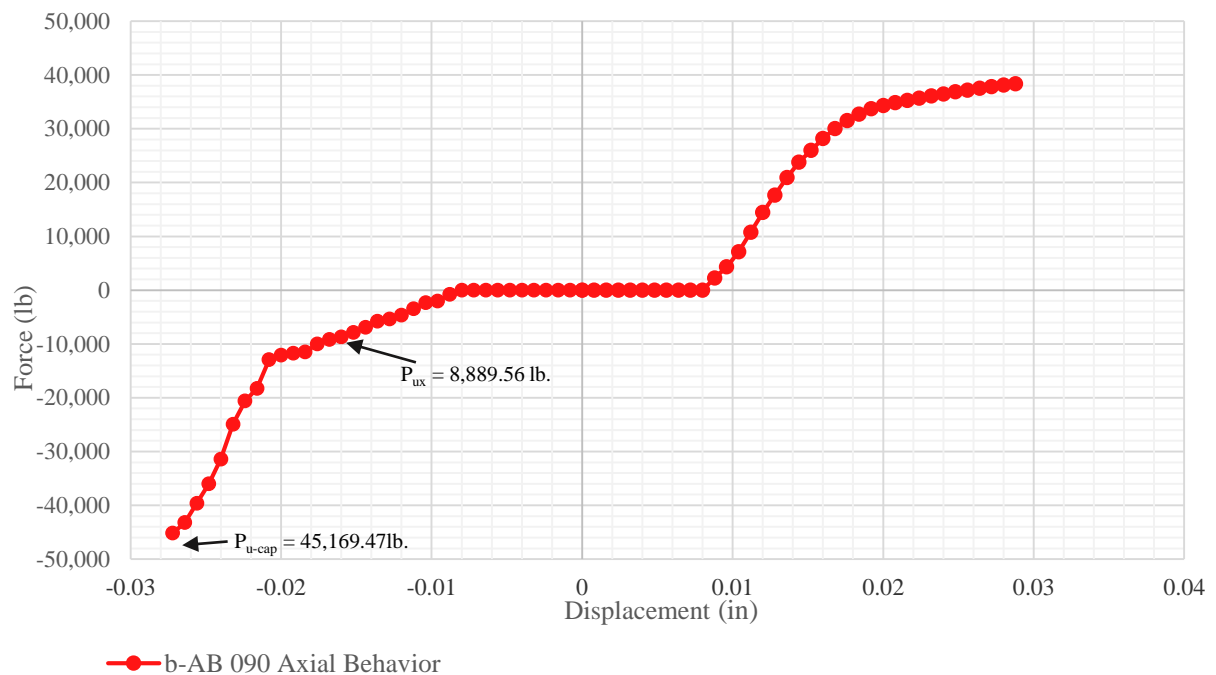


**Figure B.9** Axial Semi-Rigid Behavior: b-AB 090 (After Garcia 2017)

**Figure B.10** shows the in-plane bending semi-rigid behavior of jointing system used during the simulation of the b-AB 090 3D structure. In this plot, the initial flat portion represents the in-plane fit-gap tolerance between the mating parts of the jointing system. Once the mating parts become in contact, a non-linear bending moment vs. rotation behavior of the connection is observed. Additionally, this figure displays that at beam failure, only 5.39% of the connection in-plane bending capacity is reached.

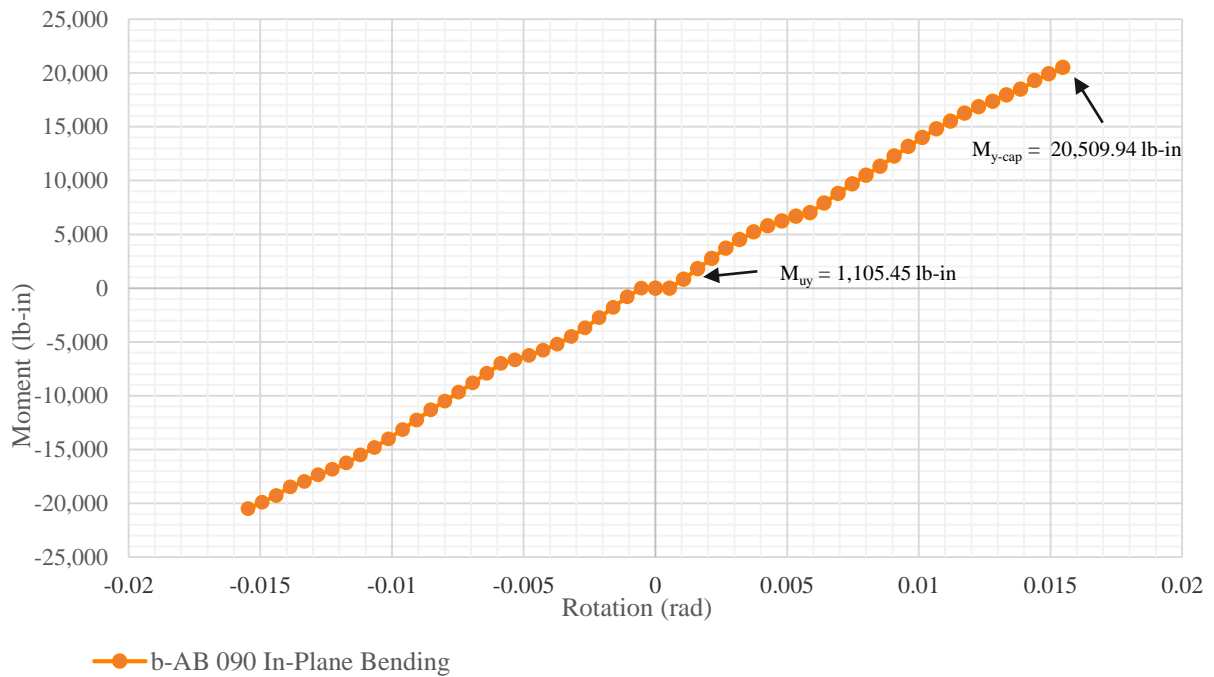


**Figure B.10** In-Plane Bending Semi-Rigid Behavior: b-AB 090 (After Garcia 2017)

## b-AC 090 3D Structure

**Figure B.11** presents the applied load-displacement plot of node 13 for the b-AC 090 3D structure. In this plot, the vertical axis corresponds to the applied load history expressed in percentage while the horizontal axis displays the resultant displacement of the node in inches as the load is applied. As observed in the figure, the applied load-displacement graph of node 13 displays a non-linear response under initial loading which indicates the movement/closing of the jointing systems' gaps. After initial loading, the structure follows a linear response up to 150% of the applied load. Subsequently, the b-AC 090 3D structure follows a non-linear behavior until critical capacity is reached at 305.97% of the applied load and at a displacement of 2.05 inches. Overall buckling is observed after critical capacity is reached.

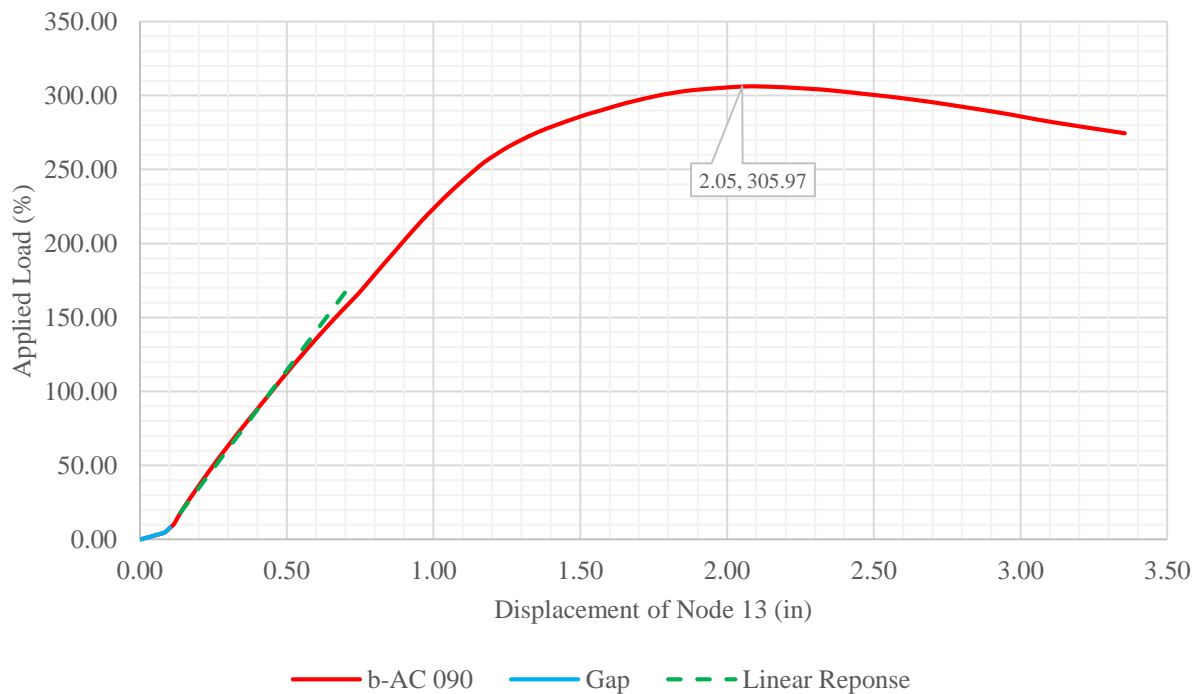


**Figure B.11** Applied Load-Displacement of Node 13: b-AC 090 3D Structure

**Figure B.12** presents the applied load-rotation plot of node 2 for the b-AC 090 3D structure. In this plot, the vertical axis corresponds to the applied load history expressed in percentage while the horizontal axis displays the resultant rotation of the node in radians as the load is applied. As observed in the figure, the applied load-rotation graph of node 2 displays a non-linear response under initial loading which indicates the movement/closing of the jointing systems' gaps. After initial loading, the structure follows a linear response up to 150% of the applied load. Subsequently, the b-AC 090 3D structure follows a non-linear behavior until critical capacity is reached at 305.97% of the applied load and at a rotation of 0.0230 radians. Overall buckling is observed after critical capacity is reached.

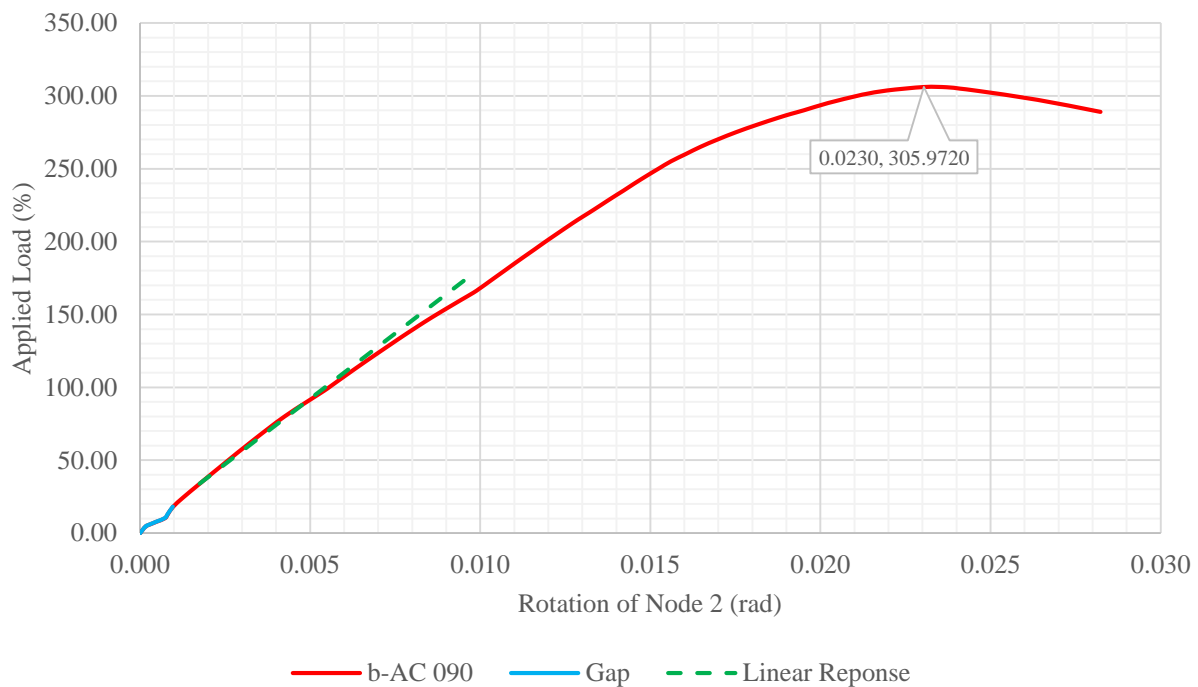


**Figure B.12** Applied Load-Rotation of Node 2: b-AC 090 3D Structure

**Table B.3** summarizes the data of the applied load-interaction index of both nodes of bar 62 at 25% load increments until critical load of the b-AC 090 3D structure is reached at 305.97% of the applied load.

**Table B.3** Applied Load-Interaction Index of Beam 62: b-AC 090 3D Structure

| Load (%)      | P <sub>ux</sub> (lb) |           | M <sub>uy</sub> (lb-in) |          | M <sub>uz</sub> (lb-in) |           | P <sub>ux</sub> /φP <sub>nx</sub> |        | Interaction Index |        | Bar Max |
|---------------|----------------------|-----------|-------------------------|----------|-------------------------|-----------|-----------------------------------|--------|-------------------|--------|---------|
|               | Node 13              | Node 2    | Node 13                 | Node 2   | Node 13                 | Node 2    | Node 13                           | Node 2 | Node 13           | Node 2 |         |
| <b>25.00</b>  | 845.61               | 845.61    | 36.90                   | 45.96    | 1,562.21                | 1,152.02  | 0.029                             | 0.029  | 0.090             | 0.071  | 0.090   |
| <b>50.00</b>  | 1,742.97             | 1,742.97  | 66.35                   | 96.48    | 2,894.81                | 2,317.23  | 0.061                             | 0.061  | 0.170             | 0.144  | 0.170   |
| <b>75.00</b>  | 2,637.86             | 2,637.86  | 116.72                  | 163.75   | 4,318.43                | 3,555.44  | 0.092                             | 0.092  | 0.255             | 0.222  | 0.255   |
| <b>100.00</b> | 3,543.58             | 3,543.58  | 244.01                  | 255.22   | 5,845.80                | 4,881.18  | 0.123                             | 0.123  | 0.349             | 0.304  | 0.349   |
| <b>125.00</b> | 4,445.07             | 4,445.07  | 382.02                  | 350.05   | 7,460.63                | 6,320.04  | 0.155                             | 0.155  | 0.448             | 0.393  | 0.448   |
| <b>150.00</b> | 5,341.39             | 5,341.39  | 529.76                  | 453.70   | 9,193.09                | 7,865.81  | 0.186                             | 0.186  | 0.552             | 0.486  | 0.552   |
| <b>175.00</b> | 6,302.29             | 6,302.29  | 685.41                  | 564.55   | 10,962.79               | 9,436.24  | 0.219                             | 0.219  | 0.708             | 0.639  | 0.708   |
| <b>200.00</b> | 7,401.84             | 7,401.84  | 827.51                  | 663.57   | 12,618.04               | 10,919.59 | 0.257                             | 0.257  | 0.822             | 0.744  | 0.822   |
| <b>225.00</b> | 8,560.26             | 8,560.26  | 992.14                  | 775.41   | 14,324.74               | 12,545.71 | 0.298                             | 0.298  | 0.941             | 0.857  | 0.941   |
| <b>250.00</b> | 9,803.54             | 9,803.54  | 1,165.23                | 898.85   | 16,173.49               | 14,245.88 | 0.341                             | 0.341  | 1.069             | 0.977  | 1.069   |
| <b>275.00</b> | 11,212.97            | 11,212.97 | 1,390.42                | 1,066.49 | 18,414.72               | 16,541.36 | 0.390                             | 0.390  | 1.222             | 1.130  | 1.222   |
| <b>300.00</b> | 13,029.62            | 13,029.62 | 1,897.76                | 1,404.53 | 21,891.76               | 20,015.94 | 0.453                             | 0.453  | 1.452             | 1.353  | 1.452   |
| <b>305.97</b> | 13,858.48            | 13,858.48 | 2,102.46                | 1,628.90 | 23,636.29               | 21,939.31 | 0.482                             | 0.482  | 1.563             | 1.472  | 1.563   |

\*φP<sub>nx</sub> = 28,768.4 lb    \*φM<sub>ny</sub> = 21,156.9 lb-in    \*φM<sub>nz</sub> = 21,156.9 lb-in

**Figure B.13** presents the applied load-interaction index plot of beam element 62 for the b-AC 090 3D structure. In this graph, the vertical axis corresponds to the applied load history expressed in percentage while the horizontal axis shows the interaction index of the beam element as the load is applied. The applied load-interaction index graph displays a non-linear response under initial loading which indicates the movement/closing of the jointing systems' gaps. After initial loading, the applied load-interaction index plot of beam element 62 shows a linear response up to 150% of the applied load. Subsequently, a non-linear behavior of the element is observed until failure of the beam is reached at 236.49% of the applied load. The forces and moments at bar failure are:

- 1)  $P_{ux}$  is 9,131.80 lb.;
- 2)  $M_{uy}$  is 1,071.71 lb.-in; and
- 3)  $M_{uz}$  is 15,174.61 lb.-in.

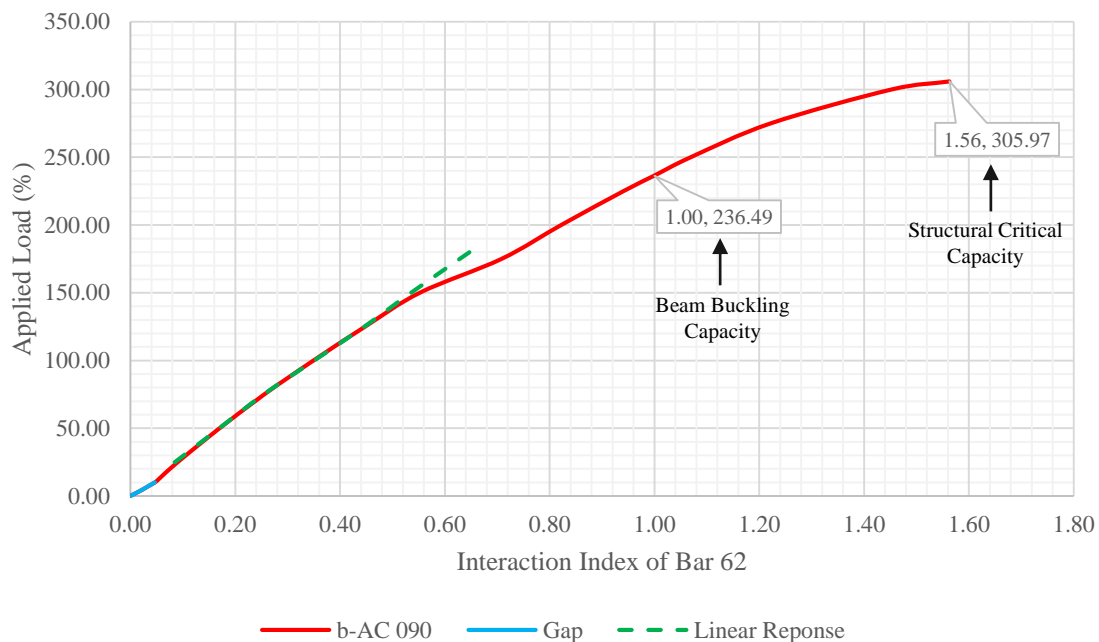


**Figure B.13** Applied Load-Interaction Index of Beam 62: b-AC 090 3D Structure

**Figure B.14** shows the axial semi-rigid behavior of the jointing system used during the simulation of the b-AC 090 3D structure. In this plot, the initial flat portion represents the fit-gap tolerance between the mating parts of the jointing system. Once the mating parts become in contact, a non-linear tension or compression load vs. displacement behavior of the connection is observed. Additionally, this figure displays that at beam failure, only 20.81% of the connection capacity in compression is reached.

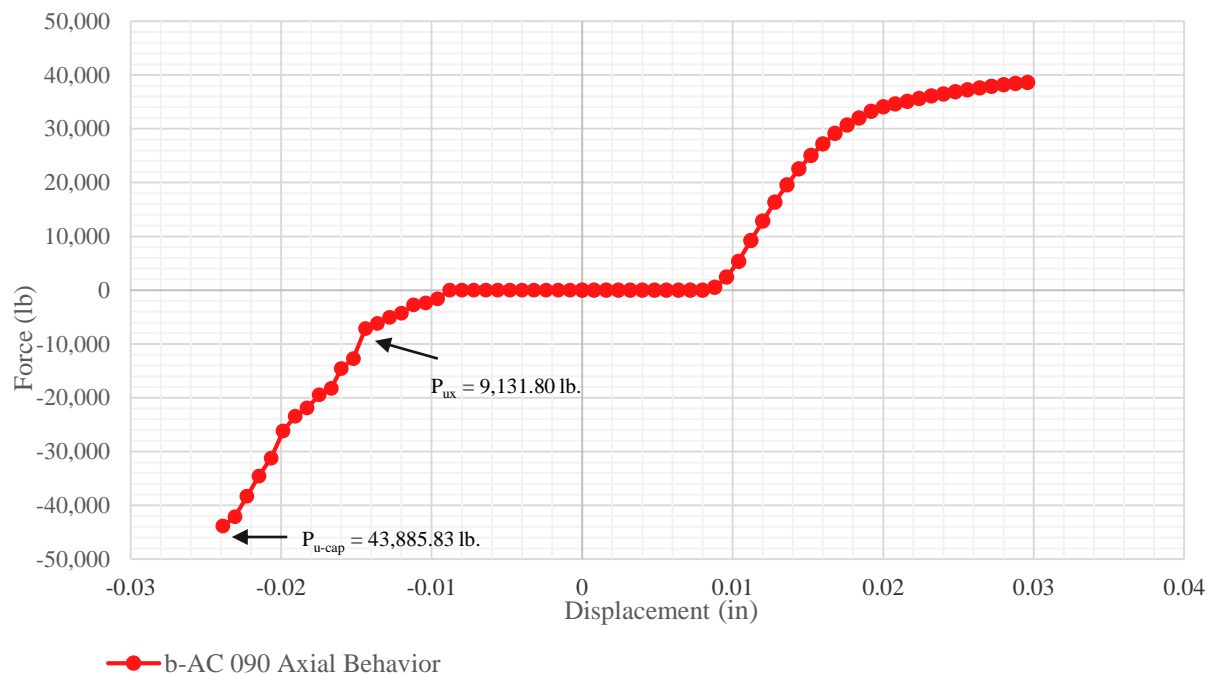


**Figure B.14** Axial Semi-Rigid Behavior: b-AC 090 (After Garcia 2017)

**Figure B.15** shows the in-plane bending semi-rigid behavior of jointing system used during the simulation of the b-AC 090 3D structure. In this plot, the initial flat portion represents the in-plane fit-gap tolerance between the mating parts of the jointing system. Once the mating parts become in contact, a non-linear bending moment vs. rotation behavior of the connection is observed. Additionally, this figure displays that at beam failure, only 4.18% of the connection in-plane bending capacity is reached.

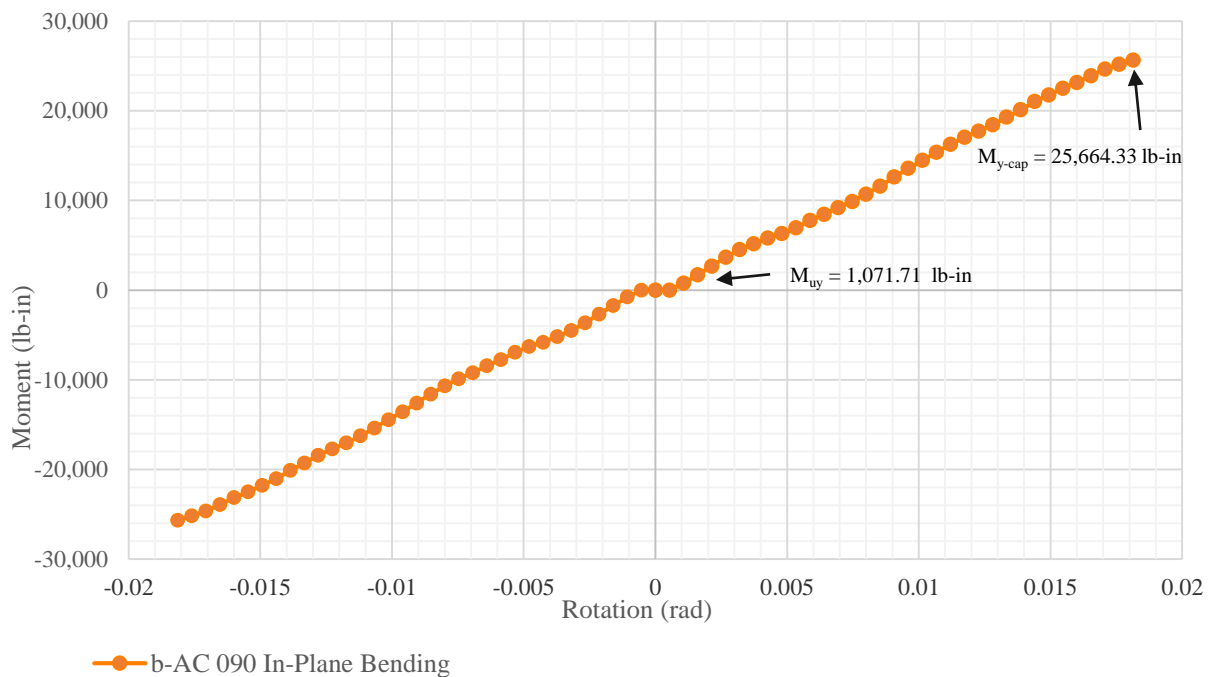


**Figure B.15** In-Plane Bending Semi-Rigid Behavior: b-AC 090 (After Garcia 2017)

## b-BA 090 3D Structure

**Figure B.16** presents the applied load-displacement plot of node 13 for the b-BA 090 3D structure. In this plot, the vertical axis corresponds to the applied load history expressed in percentage while the horizontal axis displays the resultant displacement of the node in inches as the load is applied. As observed in the figure, the applied load-displacement graph of node 13 displays a non-linear response under initial loading which indicates the movement/closing of the jointing systems' gaps. After initial loading, the structure follows a linear response up to 150% of the applied load. Subsequently, the b-BA 090 3D structure follows a non-linear behavior until critical capacity is reached at 308.34% of the applied load and at a displacement of 2.14 inches. Overall buckling is observed after critical capacity is reached.

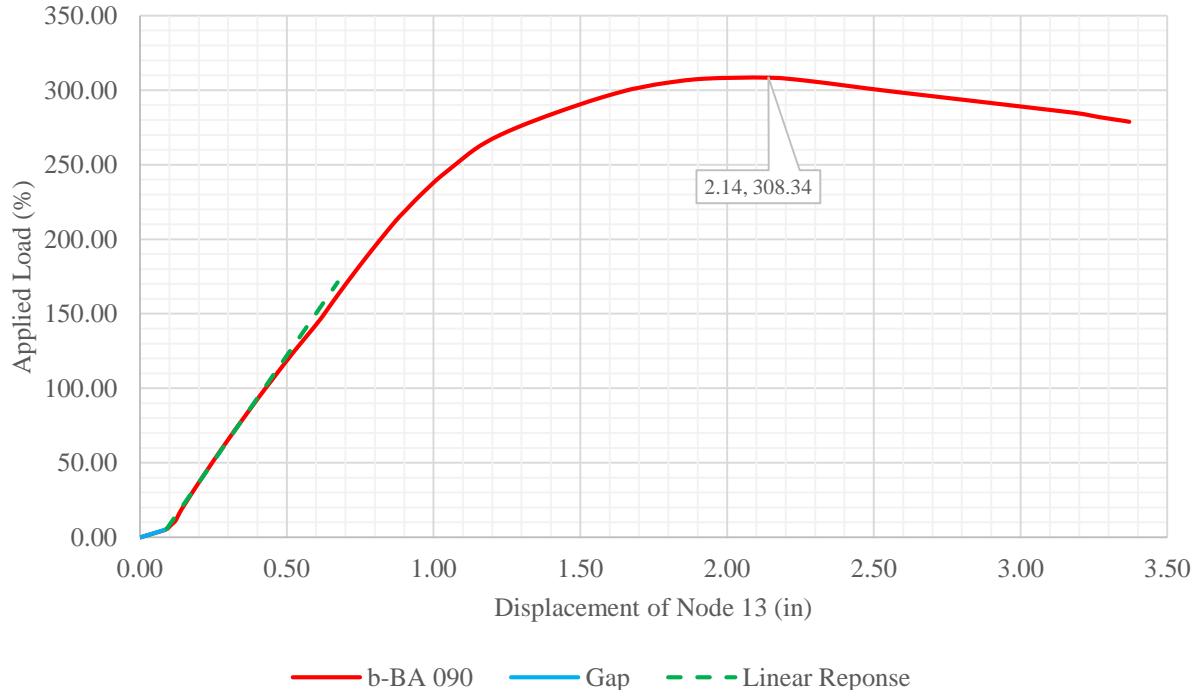


**Figure B.16** Applied Load-Displacement of Node 13: b-BA 090 3D Structure

**Figure B.17** presents the applied load-rotation plot of node 2 for the b-BA 090 3D structure. In this plot, the vertical axis corresponds to the applied load history expressed in percentage while the horizontal axis displays the resultant rotation of the node in radians as the load is applied. As observed in the figure, the applied load-rotation graph of node 2 displays a non-linear response under initial loading which indicates the movement/closing of the jointing systems' gaps. After initial loading, the structure follows a linear response up to 150% of the applied load. Subsequently, the b-BA 090 3D structure follows a non-linear behavior until critical capacity is reached at 308.34% of the applied load and at a rotation of 0.0234 radians. Overall buckling is observed after critical capacity is reached.

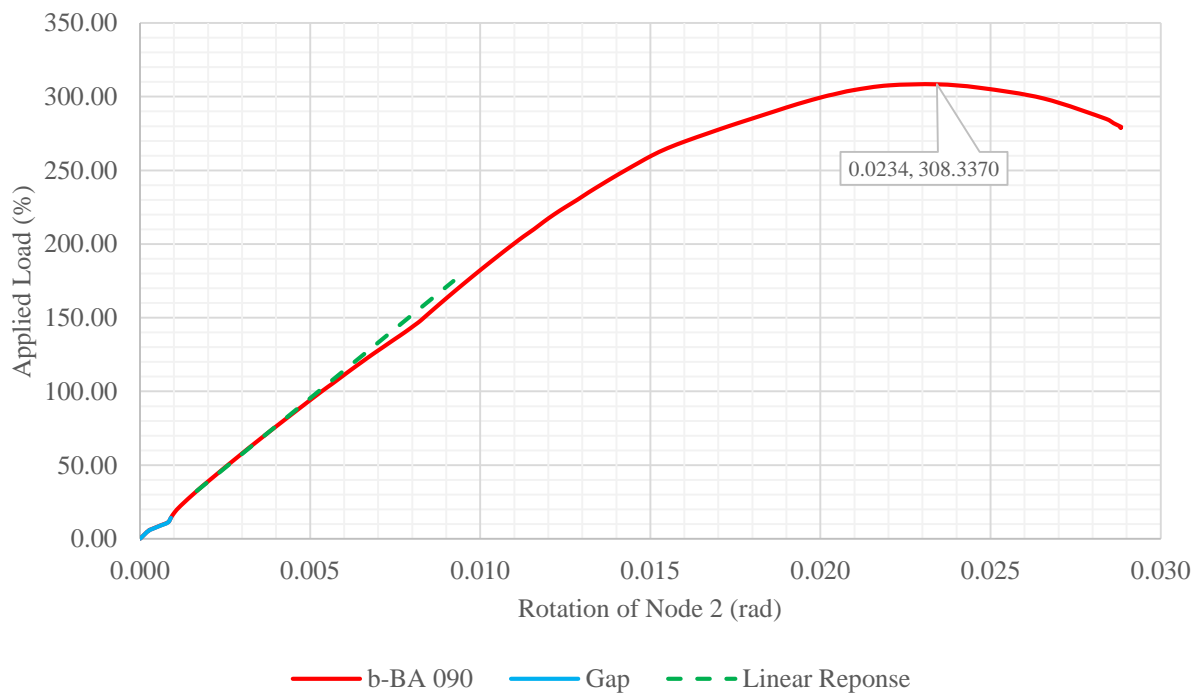


**Figure B.17** Applied Load-Rotation of Node 2: b-BA 090 3D Structure

**Table B.4** summarizes the data of the applied load-interaction index of both nodes of bar 62 at 25% load increments until critical load of the b-BA 090 3D structure is reached at 308.34% of the applied load.

**Table B.4** Applied Load-Interaction Index of Beam 62: b-BA 090 3D Structure

| Load (%)      | P <sub>ux</sub> (lb) |           | M <sub>uy</sub> (lb-in) |        | M <sub>uz</sub> (lb-in) |           | P <sub>ux</sub> /φP <sub>nx</sub> |        | Interaction Index |        | Bar Max |
|---------------|----------------------|-----------|-------------------------|--------|-------------------------|-----------|-----------------------------------|--------|-------------------|--------|---------|
|               | Node 13              | Node 2    | Node 13                 | Node 2 | Node 13                 | Node 2    | Node 13                           | Node 2 | Node 13           | Node 2 |         |
| <b>25.00</b>  | 842.39               | 842.39    | 16.64                   | 21.76  | 1,577.63                | 1,177.58  | 0.029                             | 0.029  | 0.090             | 0.071  | 0.090   |
| <b>50.00</b>  | 1,750.10             | 1,750.10  | 30.07                   | 46.07  | 2,889.64                | 2,357.60  | 0.061                             | 0.061  | 0.168             | 0.144  | 0.168   |
| <b>75.00</b>  | 2,657.80             | 2,657.80  | 45.84                   | 73.98  | 4,287.77                | 3,608.63  | 0.092                             | 0.092  | 0.251             | 0.220  | 0.251   |
| <b>100.00</b> | 3,577.06             | 3,577.06  | 63.71                   | 105.09 | 5,751.06                | 4,918.75  | 0.124                             | 0.124  | 0.337             | 0.300  | 0.337   |
| <b>125.00</b> | 4,498.67             | 4,498.67  | 84.70                   | 141.06 | 7,310.33                | 6,317.38  | 0.156                             | 0.156  | 0.428             | 0.383  | 0.428   |
| <b>150.00</b> | 5,473.79             | 5,473.79  | 108.64                  | 193.11 | 8,925.04                | 7,766.96  | 0.190                             | 0.190  | 0.522             | 0.471  | 0.522   |
| <b>175.00</b> | 6,595.31             | 6,595.31  | 130.94                  | 238.13 | 10,353.06               | 9,048.78  | 0.229                             | 0.229  | 0.670             | 0.619  | 0.670   |
| <b>200.00</b> | 7,734.40             | 7,734.40  | 157.88                  | 289.08 | 11,890.00               | 10,435.13 | 0.269                             | 0.269  | 0.775             | 0.719  | 0.775   |
| <b>225.00</b> | 8,874.35             | 8,874.35  | 168.15                  | 368.42 | 13,601.85               | 12,009.03 | 0.308                             | 0.308  | 0.887             | 0.829  | 0.887   |
| <b>250.00</b> | 10,062.99            | 10,062.99 | 412.19                  | 436.56 | 15,535.37               | 13,816.82 | 0.350                             | 0.350  | 1.020             | 0.949  | 1.020   |
| <b>275.00</b> | 11,374.91            | 11,374.91 | 616.89                  | 551.95 | 17,927.88               | 16,201.82 | 0.395                             | 0.395  | 1.175             | 1.099  | 1.175   |
| <b>300.00</b> | 13,079.13            | 13,079.13 | 1,030.69                | 780.10 | 21,191.23               | 19,389.70 | 0.455                             | 0.455  | 1.388             | 1.302  | 1.388   |
| <b>308.34</b> | 14,421.69            | 14,421.69 | 1,417.10                | 983.39 | 23,880.23               | 22,520.83 | 0.501                             | 0.501  | 1.564             | 1.489  | 1.564   |

\*φP<sub>nx</sub> = 28,768.4 lb    \*φM<sub>ny</sub> = 21,156.9 lb-in    \*φM<sub>nz</sub> = 21,156.9 lb-in

**Figure B.18** presents the applied load-interaction index plot of beam element 62 for the b-BA 090 3D structure. In this graph, the vertical axis corresponds to the applied load history expressed in percentage while the horizontal axis shows the interaction index of the beam element as the load is applied. The applied load-interaction index graph displays a non-linear response under initial loading which indicates the movement/closing of the jointing systems' gaps. After initial loading, the applied load-interaction index plot of beam element 62 shows a linear response up to 150% of the applied load. Subsequently, a non-linear behavior of the element is observed until failure of the beam is reached at 246.27% of the applied load. The forces and moments at bar failure are:

- 1)  $P_{ux}$  is 9,885.63 lb.;
- 2)  $M_{uy}$  is 375.78 lb.-in; and
- 3)  $M_{uz}$  is 15,246.86 lb.-in.

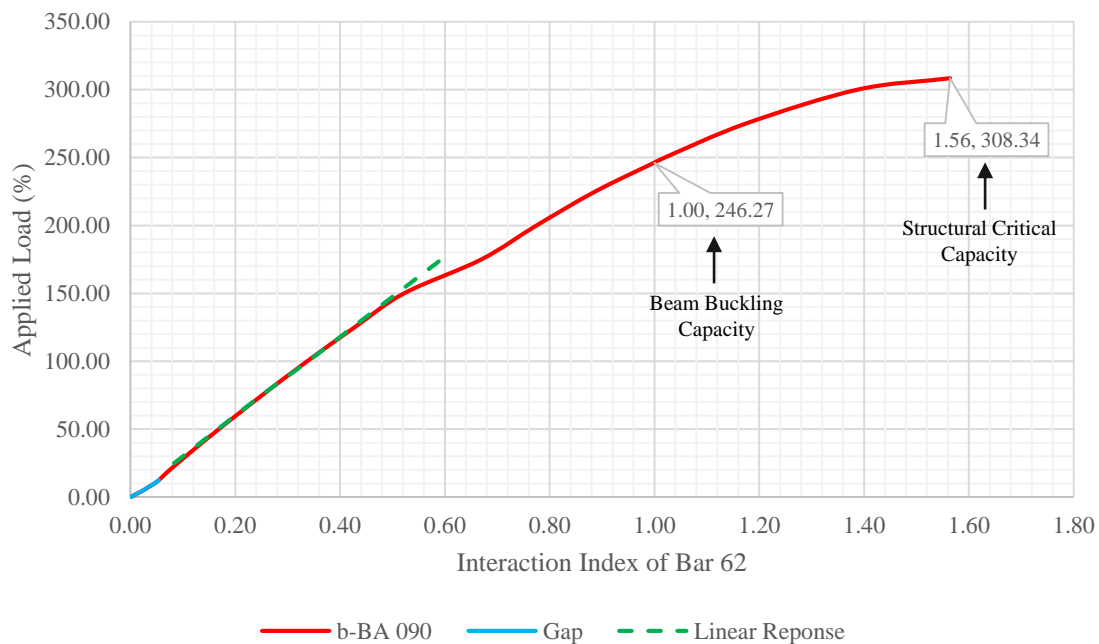


**Figure B.18** Applied Load-Interaction Index of Beam 62: b-BA 090 3D Structure

**Figure B.19** shows the axial semi-rigid behavior of the jointing system used during the simulation of the b-BA 090 3D structure. In this plot, the initial flat portion represents the fit-gap tolerance between the mating parts of the jointing system. Once the mating parts become in contact, a non-linear tension or compression load vs. displacement behavior of the connection is observed. Additionally, this figure displays that at beam failure, only 22.74% of the connection capacity in compression is reached.

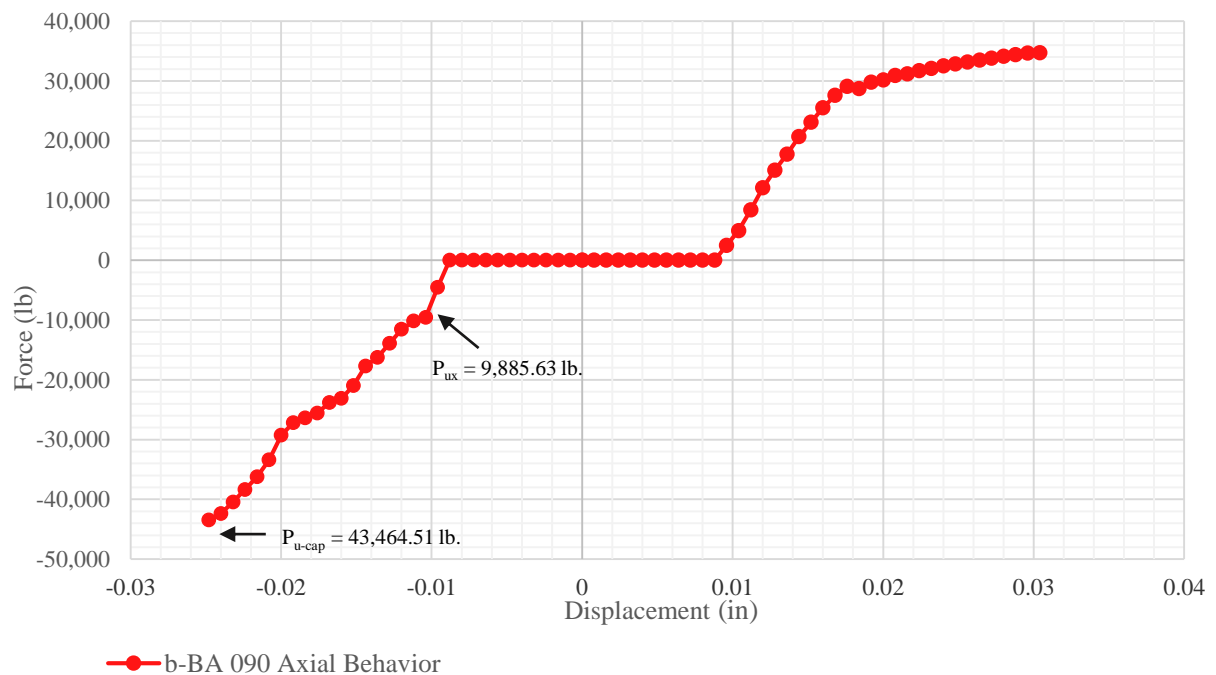


**Figure B.19** Axial Semi-Rigid Behavior: b-BA 090 (After Garcia 2017)

**Figure B.20** shows the in-plane bending semi-rigid behavior of jointing system used during the simulation of the b-BA 090 3D structure. In this plot, the initial flat portion represents the in-plane fit-gap tolerance between the mating parts of the jointing system. Once the mating parts become in contact, a non-linear bending moment vs. rotation behavior of the connection is observed. Additionally, this figure displays that at beam failure, only 1.84% of the connection in-plane bending capacity is reached.

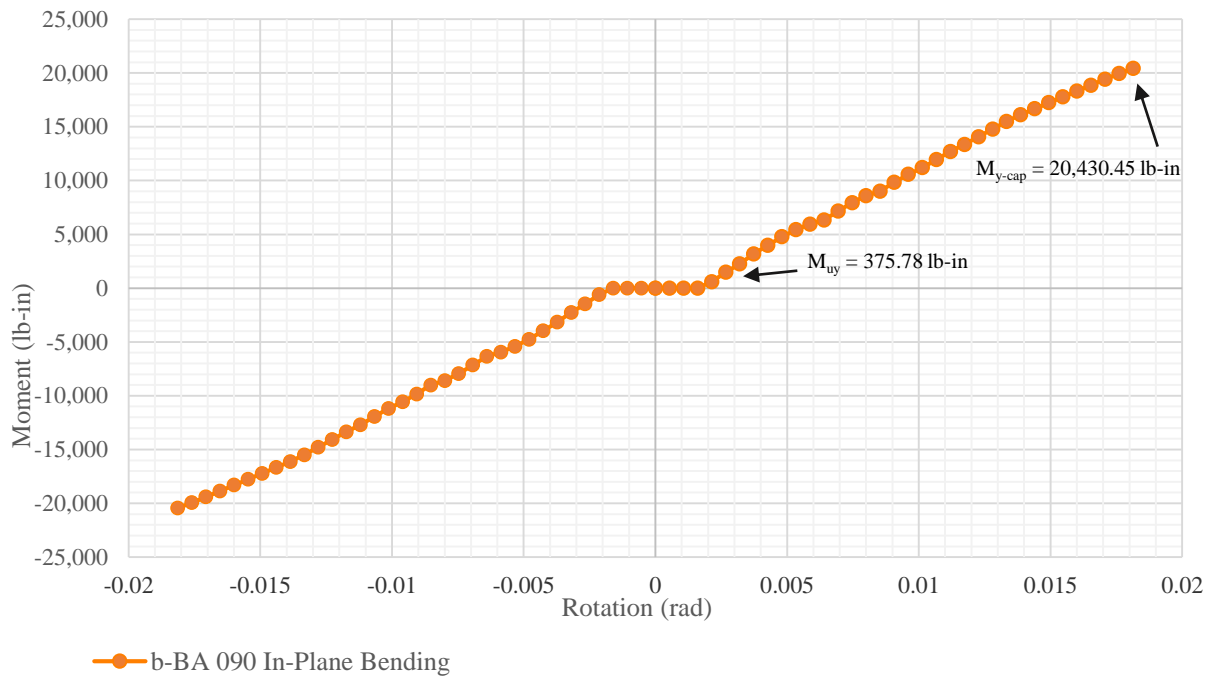


**Figure B.20** In-Plane Bending Semi-Rigid Behavior: b-BA 090 (After Garcia 2017)

## b-BB 090 3D Structure

**Figure B.21** presents the applied load-displacement plot of node 13 for the b-BB 090 3D structure. In this plot, the vertical axis corresponds to the applied load history expressed in percentage while the horizontal axis displays the resultant displacement of the node in inches as the load is applied. As observed in the figure, the applied load-displacement graph of node 13 displays a non-linear response under initial loading which indicates the movement/closing of the jointing systems' gaps. After initial loading, the structure follows a linear response up to 150% of the applied load. Subsequently, the b-BB 090 3D structure follows a non-linear behavior until critical capacity is reached at 299.90% of the applied load and at a displacement of 2.22 inches. Overall buckling is observed after critical capacity is reached.

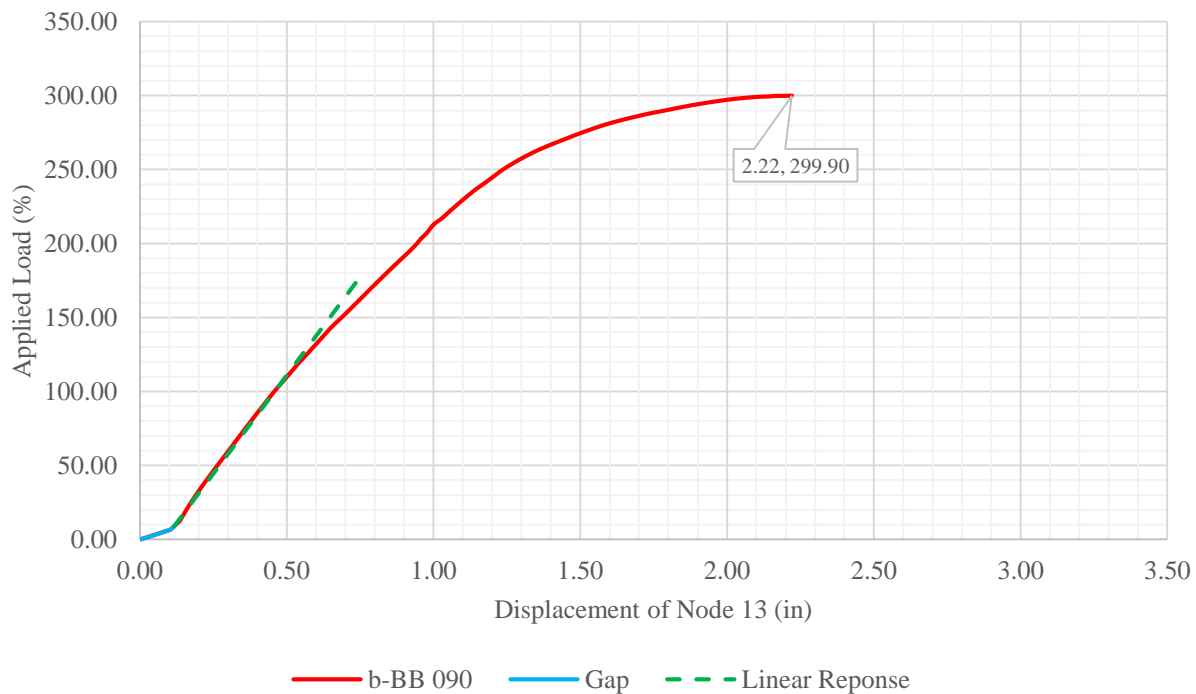


**Figure B.21** Applied Load-Displacement of Node 13: b-BB 090 3D Structure

**Figure B.22** presents the applied load-rotation plot of node 2 for the b-BB 090 3D structure. In this plot, the vertical axis corresponds to the applied load history expressed in percentage while the horizontal axis displays the resultant rotation of the node in radians as the load is applied. As observed in the figure, the applied load-rotation graph of node 2 displays a non-linear response under initial loading which indicates the movement/closing of the jointing systems' gaps. After initial loading, the structure follows a linear response up to 150% of the applied load. Subsequently, the b-BB 090 3D structure follows a non-linear behavior until critical capacity is reached at 299.90% of the applied load and at a rotation of 0.0250 radians. Overall buckling is observed after critical capacity is reached.

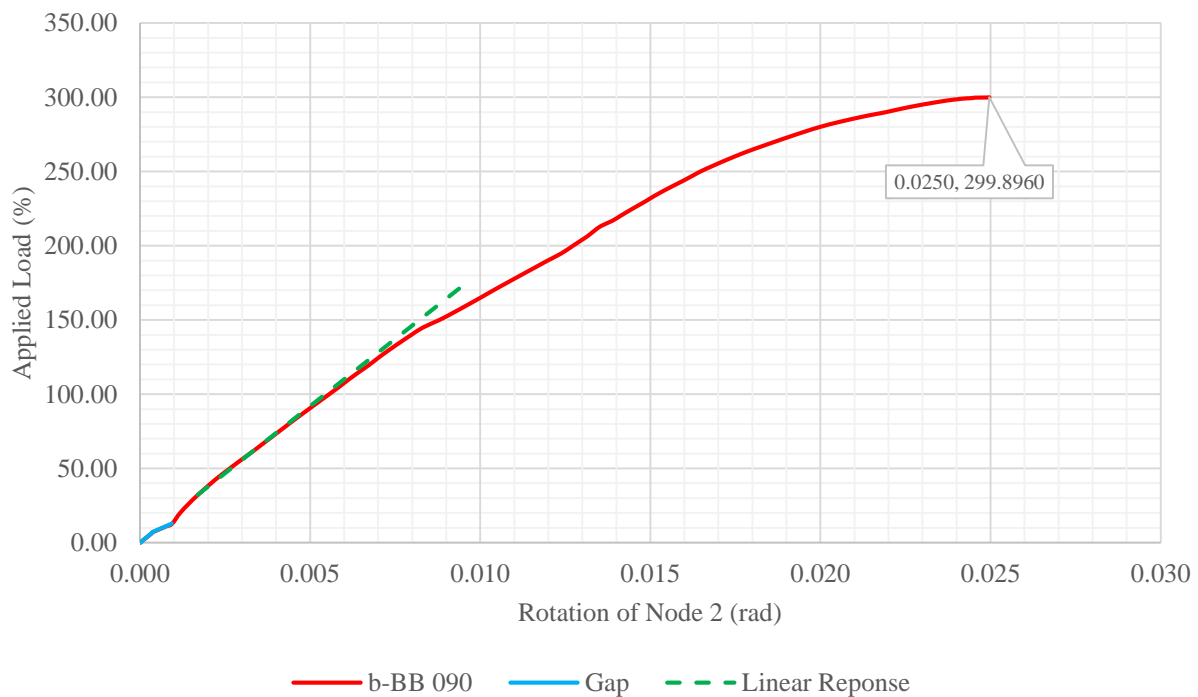


**Figure B.22** Applied Load-Rotation of Node 2: b-BB 090 3D Structure

**Table B.5** summarizes the data of the applied load-interaction index of both nodes of bar 62 at 25% load increments until critical load of the b-BB 090 3D structure is reached at 299.90% of the applied load.

**Table B.5** Applied Load-Interaction Index of Beam 62: b-BB 090 3D Structure

| Load (%)      | P <sub>ux</sub> (lb) |           | M <sub>uy</sub> (lb-in) |          | M <sub>uz</sub> (lb-in) |           | P <sub>ux</sub> /φP <sub>nx</sub> |        | Interaction Index |        | Bar Max |
|---------------|----------------------|-----------|-------------------------|----------|-------------------------|-----------|-----------------------------------|--------|-------------------|--------|---------|
|               | Node 13              | Node 2    | Node 13                 | Node 2   | Node 13                 | Node 2    | Node 13                           | Node 2 | Node 13           | Node 2 |         |
| <b>25.00</b>  | 825.57               | 825.57    | 25.03                   | 31.30    | 1,640.69                | 1,185.67  | 0.029                             | 0.029  | 0.093             | 0.072  | 0.093   |
| <b>50.00</b>  | 1,725.96             | 1,725.96  | 43.48                   | 63.45    | 2,963.69                | 2,353.88  | 0.060                             | 0.060  | 0.172             | 0.144  | 0.172   |
| <b>75.00</b>  | 2,630.52             | 2,630.52  | 65.61                   | 102.07   | 4,395.39                | 3,603.01  | 0.091                             | 0.091  | 0.257             | 0.221  | 0.257   |
| <b>100.00</b> | 3,535.61             | 3,535.61  | 90.09                   | 144.22   | 5,903.01                | 4,932.49  | 0.123                             | 0.123  | 0.345             | 0.301  | 0.345   |
| <b>125.00</b> | 4,425.47             | 4,425.47  | 116.90                  | 190.15   | 7,532.08                | 6,361.63  | 0.154                             | 0.154  | 0.438             | 0.387  | 0.438   |
| <b>150.00</b> | 5,330.62             | 5,330.62  | 151.49                  | 260.11   | 9,297.71                | 7,886.46  | 0.185                             | 0.185  | 0.539             | 0.478  | 0.539   |
| <b>175.00</b> | 6,243.64             | 6,243.64  | 193.25                  | 345.07   | 11,231.00               | 9,569.06  | 0.217                             | 0.217  | 0.697             | 0.634  | 0.697   |
| <b>200.00</b> | 7,191.00             | 7,191.00  | 332.03                  | 443.12   | 13,215.44               | 11,324.69 | 0.250                             | 0.250  | 0.819             | 0.744  | 0.819   |
| <b>225.00</b> | 8,290.11             | 8,290.11  | 490.83                  | 539.07   | 15,046.07               | 13,062.11 | 0.288                             | 0.288  | 0.941             | 0.860  | 0.941   |
| <b>250.00</b> | 9,388.68             | 9,388.68  | 672.64                  | 660.22   | 17,213.12               | 15,031.90 | 0.326                             | 0.326  | 1.078             | 0.986  | 1.078   |
| <b>275.00</b> | 10,734.32            | 10,734.32 | 984.85                  | 836.93   | 19,905.02               | 17,778.18 | 0.373                             | 0.373  | 1.251             | 1.155  | 1.251   |
| <b>299.90</b> | 12,932.19            | 12,932.19 | 1,759.89                | 1,298.09 | 24,695.06               | 22,960.79 | 0.450                             | 0.450  | 1.561             | 1.469  | 1.561   |

\*φP<sub>nx</sub> = 28,768.4 lb    \*φM<sub>ny</sub> = 21,156.9 lb-in    \*φM<sub>nz</sub> = 21,156.9 lb-in

**Figure B.23** presents the applied load-interaction index plot of beam element 62 for the b-BB 090 3D structure. In this graph, the vertical axis corresponds to the applied load history expressed in percentage while the horizontal axis shows the interaction index of the beam element as the load is applied. The applied load-interaction index graph displays a non-linear response under initial loading which indicates the movement/closing of the jointing systems' gaps. After initial loading, the applied load-interaction index plot of beam element 62 shows a linear response up to 150% of the applied load. Subsequently, a non-linear behavior of the element is observed until failure of the beam is reached at 235.79% of the applied load. The forces and moments at bar failure are:

- 1)  $P_{ux}$  is 8,764.17 lb.;
- 2)  $M_{uy}$  is 569.28 lb.-in; and
- 3)  $M_{uz}$  is 15,981.20 lb.-in.

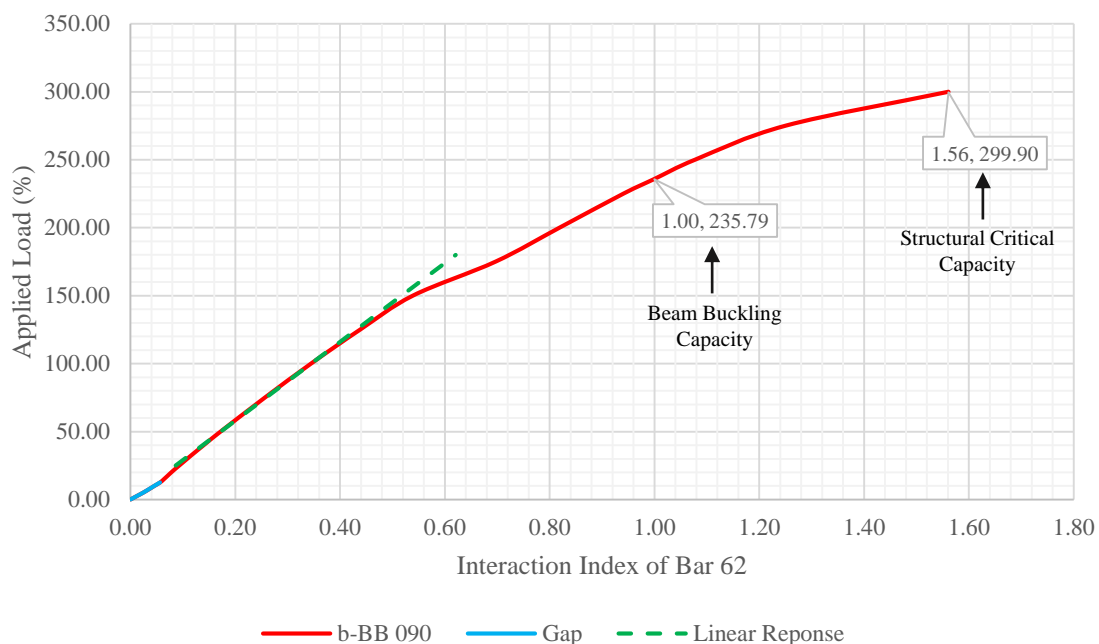


**Figure B.23** Applied Load-Interaction Index of Beam 62: b-BB 090 3D Structure

**Figure B.24** shows the axial semi-rigid behavior of the jointing system used during the simulation of the b-BB 090 3D structure. In this plot, the initial flat portion represents the fit-gap tolerance between the mating parts of the jointing system. Once the mating parts become in contact, a non-linear tension or compression load vs. displacement behavior of the connection is observed. Additionally, this figure displays that at beam failure, only 20.05% of the connection capacity in compression is reached.

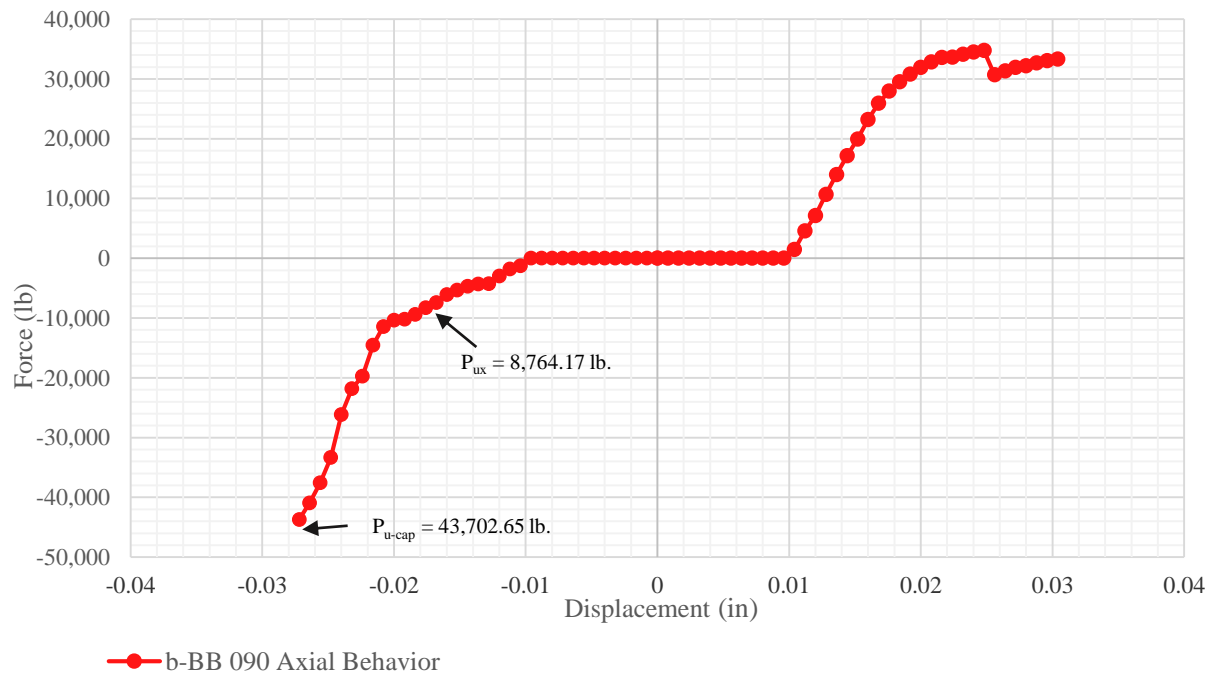


**Figure B.24** Axial Semi-Rigid Behavior: b-BB 090 (After Garcia 2017)

**Figure B.25** shows the in-plane bending semi-rigid behavior of jointing system used during the simulation of the b-BB 090 3D structure. In this plot, the initial flat portion represents the in-plane fit-gap tolerance between the mating parts of the jointing system. Once the mating parts become in contact, a non-linear bending moment vs. rotation behavior of the connection is observed. Additionally, this figure displays that at beam failure, only 2.83% of the connection of the in-plane bending capacity is reached.

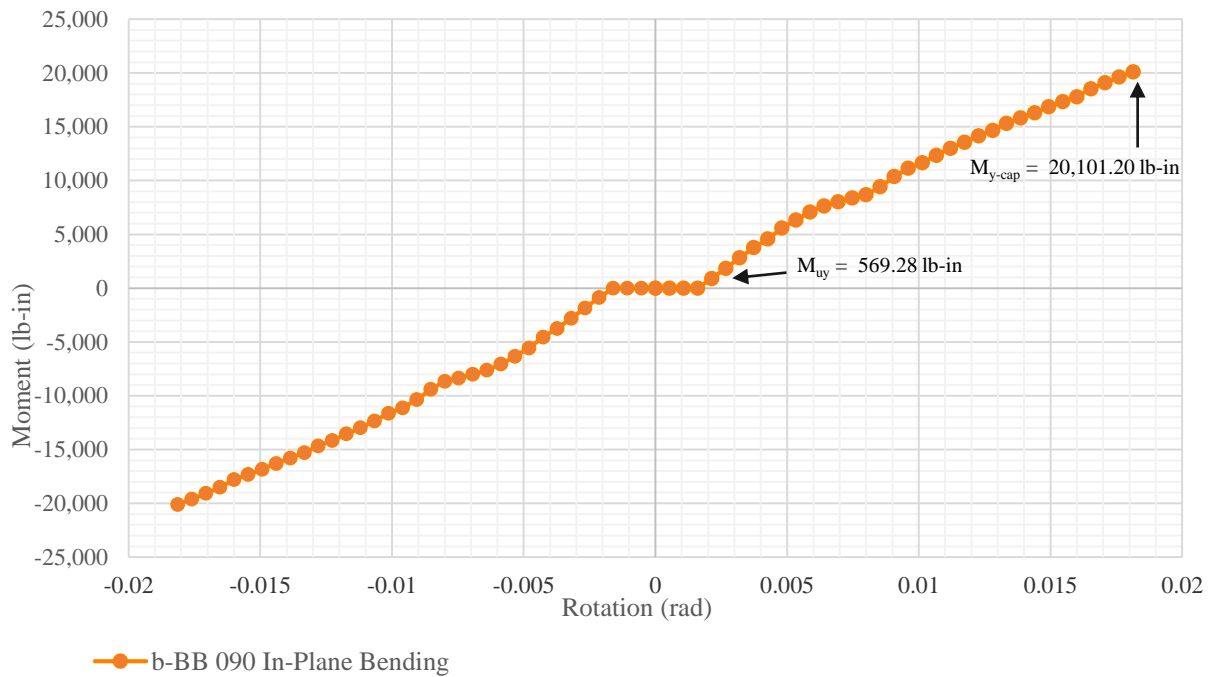


**Figure B.25** In-Plane Bending Semi-Rigid Behavior: b-BB 090 (After Garcia 2017)

## b-BC 090 3D Structure

**Figure B.26** presents the applied load-displacement plot of node 13 for the b-BC 090 3D structure. In this plot, the vertical axis corresponds to the applied load history expressed in percentage while the horizontal axis displays the resultant displacement of the node in inches as the load is applied. As observed in the figure, the applied load-displacement graph of node 13 displays a non-linear response under initial loading which indicates the movement/closing of the jointing systems' gaps. After initial loading, the structure follows a linear response up to 150% of the applied load. Subsequently, the b-BC 090 3D structure follows a non-linear behavior until critical capacity is reached at 303.47% of the applied load and at a displacement of 2.16 inches. Overall buckling is observed after critical capacity is reached.

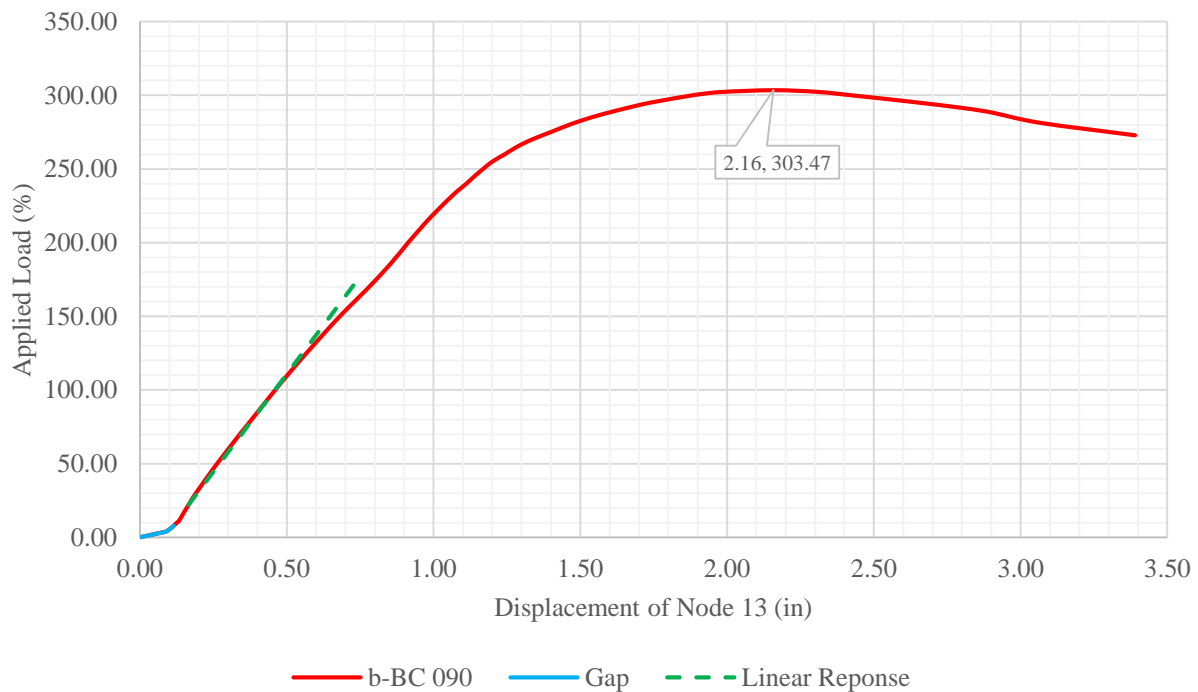


**Figure B.26** Applied Load-Displacement of Node 13: b-BC 090 3D Structure

**Figure B.27** presents the applied load-rotation plot of node 2 for the b-BC 090 3D structure. In this plot, the vertical axis corresponds to the applied load history expressed in percentage while the horizontal axis displays the resultant rotation of the node in radians as the load is applied. As observed in the figure, the applied load-rotation graph of node 2 displays a non-linear response under initial loading which indicates the movement/closing of the jointing systems' gaps. After initial loading, the structure follows a linear response up to 150% of the applied load. Subsequently, the b-BC 090 3D structure follows a non-linear behavior until critical capacity is reached at 303.47% of the applied load and at a rotation of 0.0240 radians. Overall buckling is observed after critical capacity is reached.

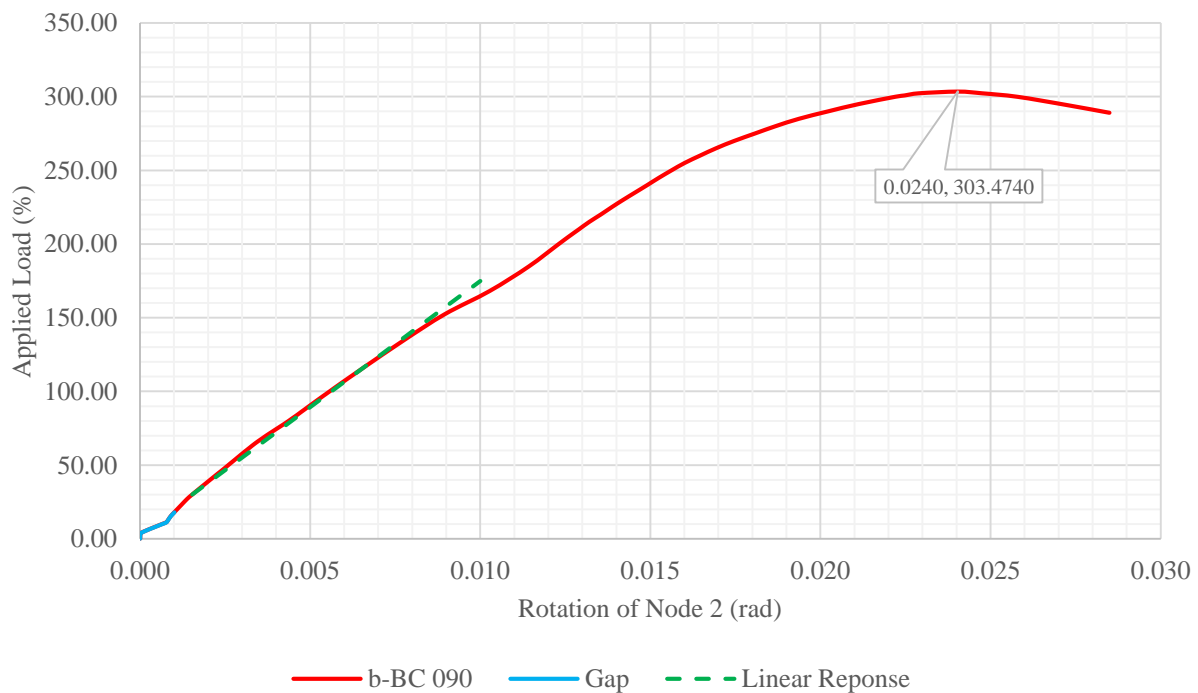


**Figure B.27** Applied Load-Rotation of Node 2: b-BC 090 3D Structure

**Table B.6** summarizes the data of the applied load-interaction index of both nodes of bar 62 at 25% load increments until critical load of the b-BC 090 3D structure is reached at 303.47% of the applied load.

**Table B.6** Applied Load-Interaction Index of Beam 62: b-BC 090 3D Structure

| Load (%)      | P <sub>ux</sub> (lb) |           | M <sub>uy</sub> (lb-in) |          | M <sub>uz</sub> (lb-in) |           | P <sub>ux</sub> /φP <sub>nx</sub> |        | Interaction Index |        | Bar Max |
|---------------|----------------------|-----------|-------------------------|----------|-------------------------|-----------|-----------------------------------|--------|-------------------|--------|---------|
|               | Node 13              | Node 2    | Node 13                 | Node 2   | Node 13                 | Node 2    | Node 13                           | Node 2 | Node 13           | Node 2 |         |
| <b>25.00</b>  | 842.05               | 842.05    | 25.03                   | 30.30    | 1,610.43                | 1,158.90  | 0.029                             | 0.029  | 0.092             | 0.071  | 0.092   |
| <b>50.00</b>  | 1,746.83             | 1,746.83  | 43.99                   | 63.72    | 2,928.86                | 2,317.83  | 0.061                             | 0.061  | 0.171             | 0.143  | 0.171   |
| <b>75.00</b>  | 2,640.55             | 2,640.55  | 66.33                   | 102.54   | 4,369.14                | 3,567.53  | 0.092                             | 0.092  | 0.256             | 0.219  | 0.256   |
| <b>100.00</b> | 3,537.39             | 3,537.39  | 92.41                   | 147.37   | 5,911.65                | 4,924.78  | 0.123                             | 0.123  | 0.345             | 0.301  | 0.345   |
| <b>125.00</b> | 4,435.79             | 4,435.79  | 121.77                  | 196.10   | 7,552.05                | 6,377.82  | 0.154                             | 0.154  | 0.440             | 0.388  | 0.440   |
| <b>150.00</b> | 5,338.55             | 5,338.55  | 154.64                  | 248.61   | 9,297.55                | 7,923.09  | 0.186                             | 0.186  | 0.540             | 0.479  | 0.540   |
| <b>175.00</b> | 6,270.76             | 6,270.76  | 200.95                  | 350.01   | 11,192.90               | 9,577.54  | 0.218                             | 0.218  | 0.697             | 0.635  | 0.697   |
| <b>200.00</b> | 7,336.02             | 7,336.02  | 356.76                  | 441.35   | 12,886.11               | 11,111.75 | 0.255                             | 0.255  | 0.811             | 0.740  | 0.811   |
| <b>225.00</b> | 8,494.80             | 8,494.80  | 422.74                  | 522.53   | 14,574.76               | 12,731.73 | 0.295                             | 0.295  | 0.925             | 0.852  | 0.925   |
| <b>250.00</b> | 9,707.58             | 9,707.58  | 599.99                  | 627.30   | 16,503.54               | 14,489.30 | 0.337                             | 0.337  | 1.056             | 0.973  | 1.056   |
| <b>275.00</b> | 11,124.29            | 11,124.29 | 886.74                  | 778.48   | 18,882.90               | 16,948.15 | 0.387                             | 0.387  | 1.217             | 1.131  | 1.217   |
| <b>300.00</b> | 13,010.33            | 13,010.33 | 1,461.75                | 1,103.62 | 22,737.33               | 20,865.89 | 0.452                             | 0.452  | 1.469             | 1.375  | 1.469   |
| <b>303.47</b> | 13,691.03            | 13,691.03 | 1,617.55                | 1,279.59 | 24,235.56               | 22,569.96 | 0.476                             | 0.476  | 1.562             | 1.478  | 1.562   |

\*φP<sub>nx</sub> = 28,768.4 lb    \*φM<sub>ny</sub> = 21,156.9 lb-in    \*φM<sub>nz</sub> = 21,156.9 lb-in

**Figure B.28** presents the applied load-interaction index plot of beam element 62 for the b-BC 090 3D structure. In this graph, the vertical axis corresponds to the applied load history expressed in percentage while the horizontal axis shows the interaction index of the beam element as the load is applied. The applied load-interaction index graph displays a non-linear response under initial loading which indicates the movement/closing of the jointing systems' gaps. After initial loading, the applied load-interaction index plot of beam element 62 shows a linear response up to 150% of the applied load. Subsequently, a non-linear behavior of the element is observed until failure of the beam is reached at 239.28% of the applied load. The forces and moments at bar failure are:

- 1)  $P_{ux}$  is 9,187.44 lb.;
- 2)  $M_{uy}$  is 523.97 lb.-in; and
- 3)  $M_{uz}$  is 15,676.32 lb.-in.

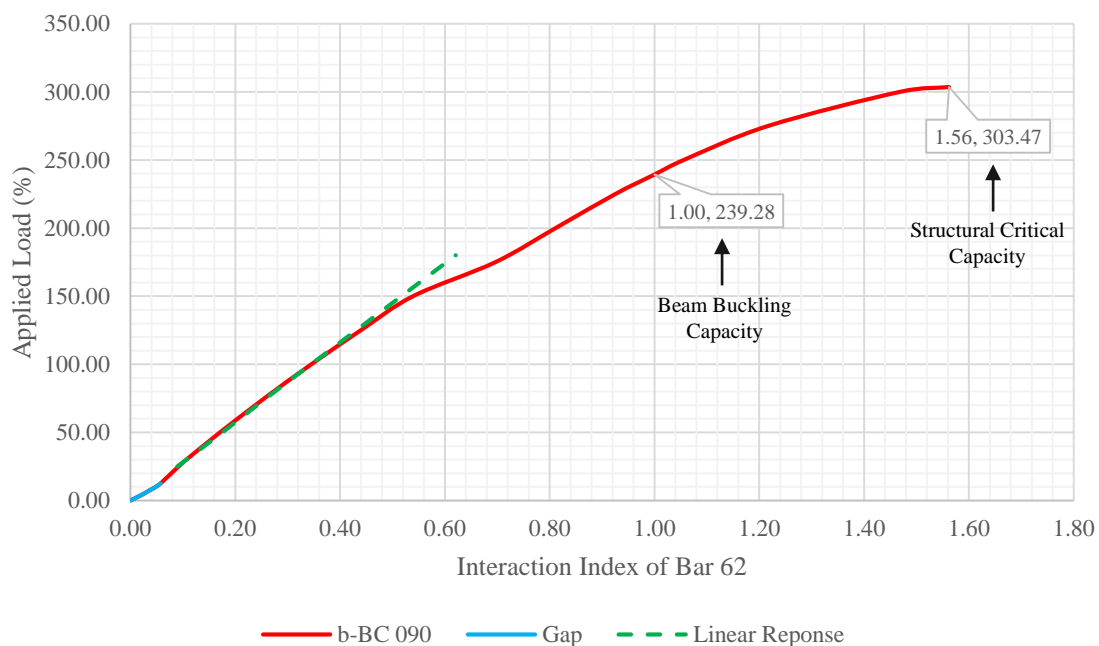


**Figure B.28** Applied Load-Interaction Index of Beam 62: b-BC 090 3D Structure

**Figure B.29** shows the axial semi-rigid behavior of the jointing system used during the simulation of the b-BC 090 3D structure. In this plot, the initial flat portion represents the fit-gap tolerance between the mating parts of the jointing system. Once the mating parts become in contact, a non-linear tension or compression load vs. displacement behavior of the connection is observed. Additionally, this figure displays that at beam failure, only 20.95% of the connection capacity in compression is reached.

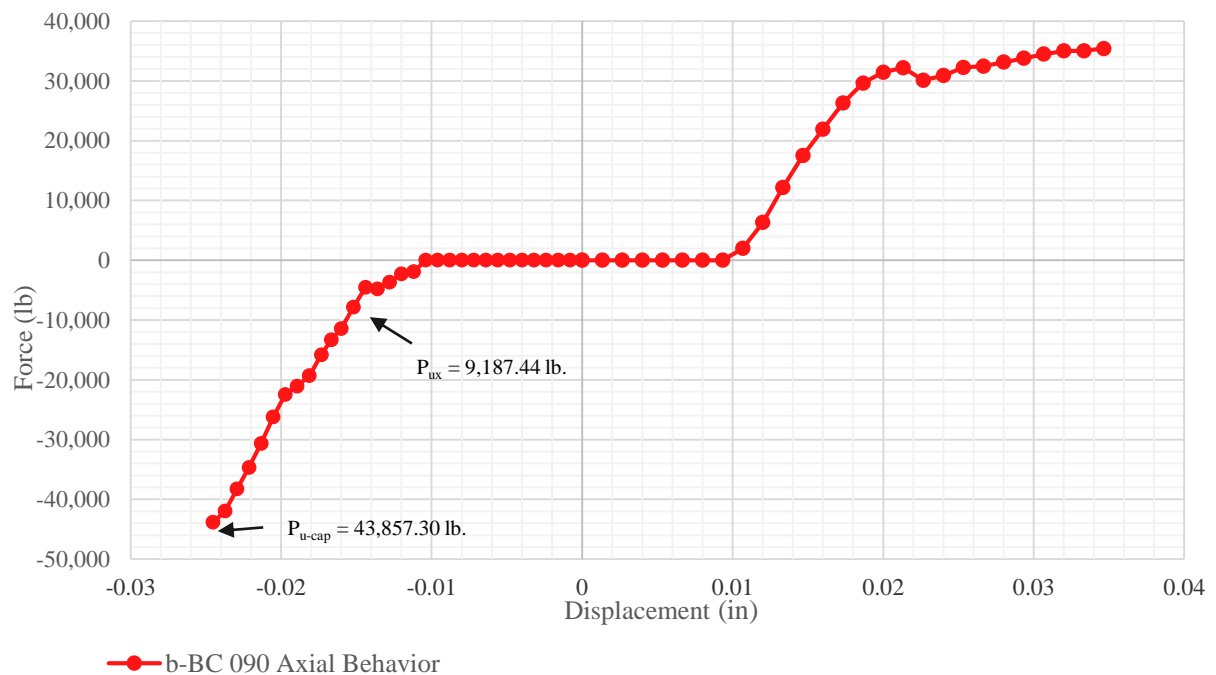


**Figure B.29** Axial Semi-Rigid Behavior: b-BC 090 (After Garcia 2017)

**Figure B.30** shows the in-plane bending semi-rigid behavior of jointing system used during the simulation of the b-BC 090 3D structure. In this plot, the initial flat portion represents the in-plane fit-gap tolerance between the mating parts of the jointing system. Once the mating parts become in contact, a non-linear bending moment vs. rotation behavior of the connection is observed. Additionally, this figure displays that at beam failure, only 2.27% of the connection in-plane bending capacity is reached.

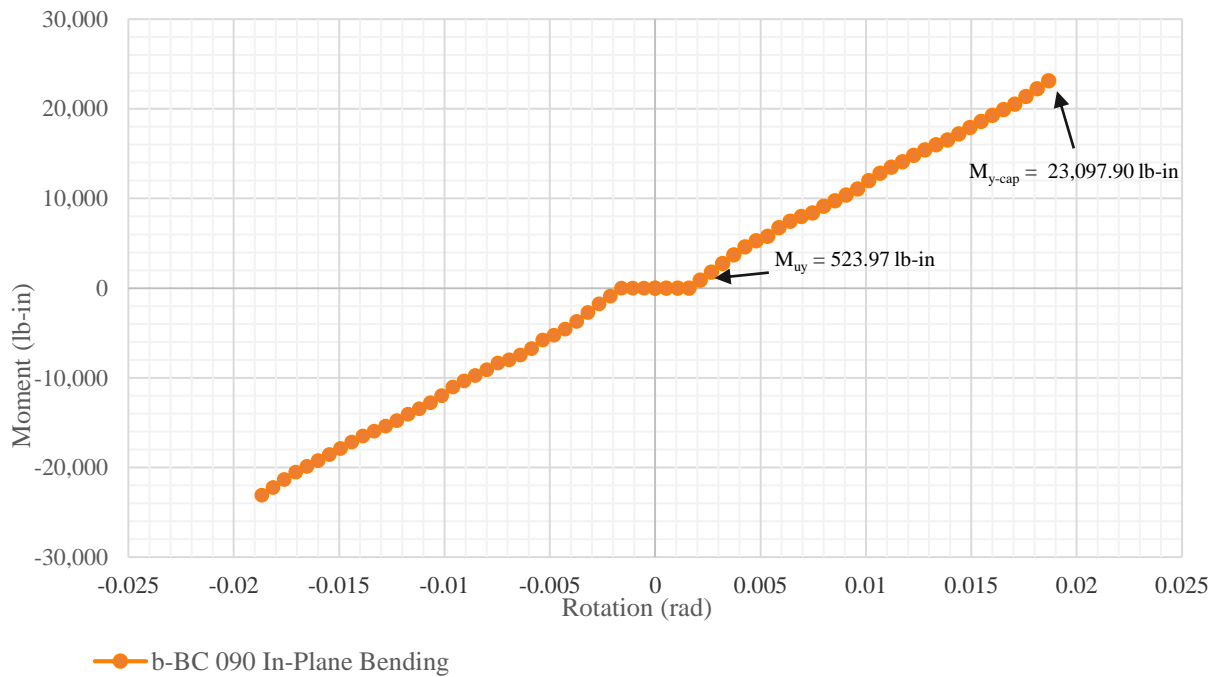


**Figure B.30** In-Plane Bending Semi-Rigid Behavior: b-BC 090 (After Garcia 2017)

## b-CA 090 3D Structure

**Figure B.31** presents the applied load-displacement plot of node 13 for the b-CA 090 3D structure. In this plot, the vertical axis corresponds to the applied load history expressed in percentage while the horizontal axis displays the resultant displacement of the node in inches as the load is applied. As observed in the figure, the applied load-displacement graph of node 13 displays a non-linear response under initial loading which indicates the movement/closing of the jointing systems' gaps. After initial loading, the structure follows a linear response up to 150% of the applied load. Subsequently, the b-CA 090 3D structure follows a non-linear behavior until critical capacity is reached at 309.46% of the applied load and at a displacement of 2.07 inches. Overall buckling is observed after critical capacity is reached.

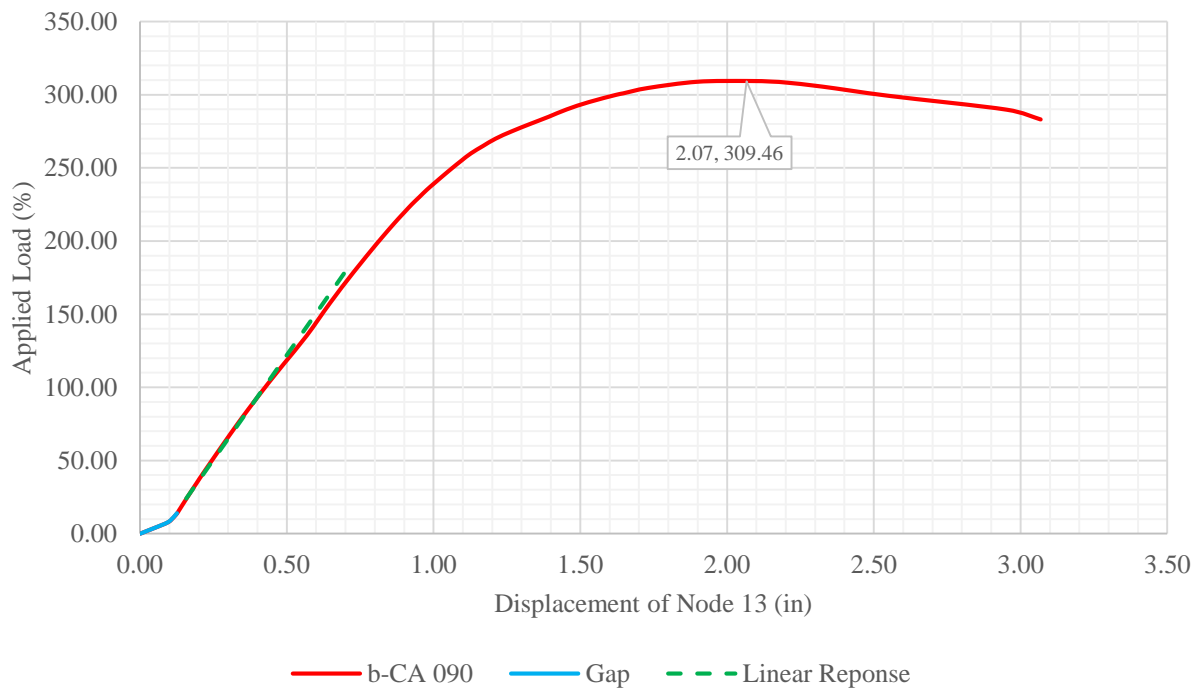


**Figure B.31** Applied Load-Displacement of Node 13: b-CA 090 3D Structure

**Figure B.32** presents the applied load-rotation plot of node 2 for the b-CA 090 3D structure. In this plot, the vertical axis corresponds to the applied load history expressed in percentage while the horizontal axis displays the resultant rotation of the node in radians as the load is applied. As observed in the figure, the applied load-rotation graph of node 2 displays a non-linear response under initial loading which indicates the movement/closing of the jointing systems' gaps. After initial loading, the structure follows a linear response up to 150% of the applied load. Subsequently, the b-CA 090 3D structure follows a non-linear behavior until critical capacity is reached at 309.46% of the applied load and at a rotation of 0.0237 radians. Overall buckling is observed after critical capacity is reached.

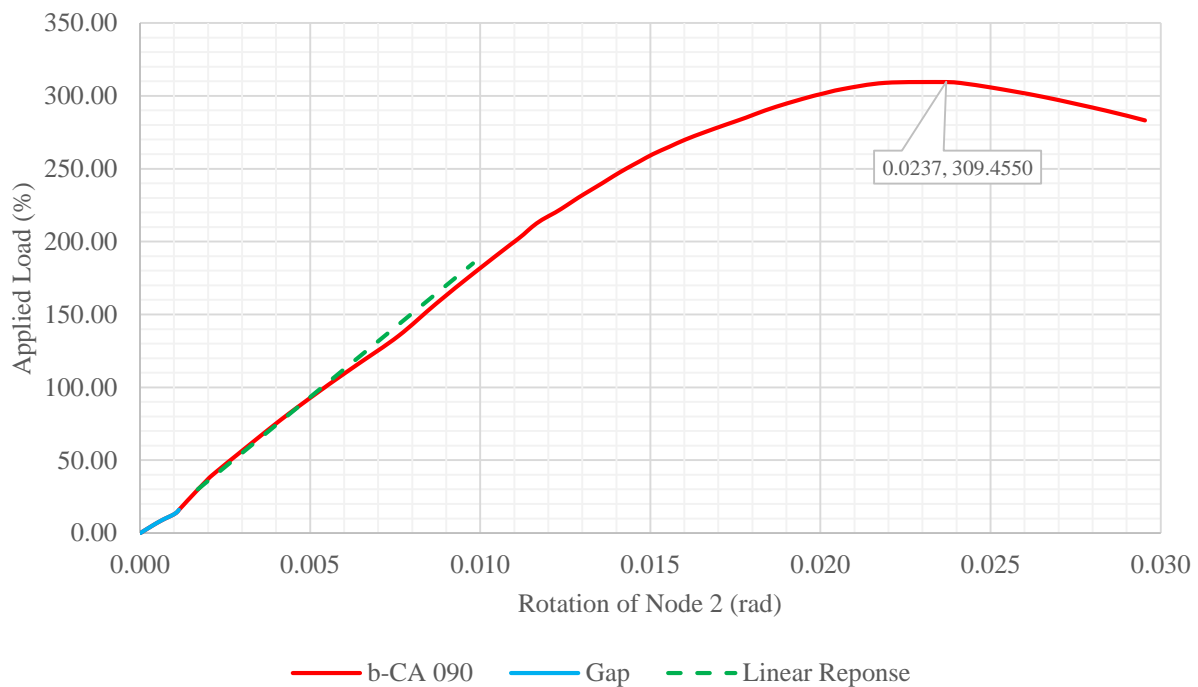


**Figure B.32** Applied Load-Rotation of Node 2: b-CA 090 3D Structure

**Table B.7** summarizes the data of the applied load-interaction index of both nodes of bar 62 at 25% load increments until critical load of the b-CA 090 3D structure is reached at 309.46% of the applied load.

**Table B.7** Applied Load-Interaction Index of Beam 62: b-CA 090 3D Structure

| Load (%)      | P <sub>ux</sub> (lb) |           | M <sub>uy</sub> (lb-in) |        | M <sub>uz</sub> (lb-in) |           | P <sub>ux</sub> /φP <sub>nx</sub> |        | Interaction Index |        | Bar Max |
|---------------|----------------------|-----------|-------------------------|--------|-------------------------|-----------|-----------------------------------|--------|-------------------|--------|---------|
|               | Node 13              | Node 2    | Node 13                 | Node 2 | Node 13                 | Node 2    | Node 13                           | Node 2 | Node 13           | Node 2 |         |
| <b>25.00</b>  | 817.71               | 817.71    | 7.59                    | 10.79  | 1,614.10                | 1,199.09  | 0.028                             | 0.028  | 0.091             | 0.071  | 0.091   |
| <b>50.00</b>  | 1,735.12             | 1,735.12  | 14.14                   | 22.25  | 2,904.79                | 2,367.15  | 0.060                             | 0.060  | 0.168             | 0.143  | 0.168   |
| <b>75.00</b>  | 2,655.04             | 2,655.04  | 22.70                   | 37.12  | 4,281.36                | 3,597.25  | 0.092                             | 0.092  | 0.250             | 0.218  | 0.250   |
| <b>100.00</b> | 3,564.96             | 3,564.96  | 33.52                   | 61.12  | 5,770.29                | 4,927.85  | 0.124                             | 0.124  | 0.336             | 0.298  | 0.336   |
| <b>125.00</b> | 4,483.88             | 4,483.88  | 49.46                   | 89.94  | 7,353.37                | 6,344.75  | 0.156                             | 0.156  | 0.428             | 0.382  | 0.428   |
| <b>150.00</b> | 5,519.80             | 5,519.80  | 115.82                  | 119.67 | 8,822.25                | 7,662.71  | 0.192                             | 0.192  | 0.518             | 0.464  | 0.518   |
| <b>175.00</b> | 6,631.70             | 6,631.70  | 202.88                  | 151.71 | 10,251.74               | 8,949.11  | 0.231                             | 0.231  | 0.670             | 0.613  | 0.670   |
| <b>200.00</b> | 7,758.47             | 7,758.47  | 296.37                  | 185.74 | 11,799.20               | 10,345.89 | 0.270                             | 0.270  | 0.778             | 0.712  | 0.778   |
| <b>225.00</b> | 8,892.89             | 8,892.89  | 416.73                  | 227.14 | 13,509.28               | 11,906.98 | 0.309                             | 0.309  | 0.894             | 0.819  | 0.894   |
| <b>250.00</b> | 10,099.26            | 10,099.26 | 545.28                  | 275.57 | 15,409.64               | 13,708.22 | 0.351                             | 0.351  | 1.021             | 0.939  | 1.021   |
| <b>275.00</b> | 11,453.83            | 11,453.83 | 748.58                  | 351.79 | 17,706.69               | 16,012.25 | 0.398                             | 0.398  | 1.174             | 1.086  | 1.174   |
| <b>300.00</b> | 13,187.44            | 13,187.44 | 1,146.77                | 480.12 | 20,813.61               | 19,060.38 | 0.458                             | 0.458  | 1.381             | 1.279  | 1.381   |
| <b>309.46</b> | 14,748.43            | 14,748.43 | 1,515.68                | 665.91 | 23,784.96               | 22,471.81 | 0.513                             | 0.513  | 1.576             | 1.485  | 1.576   |

\*φP<sub>nx</sub> = 28,768.4 lb    \*φM<sub>ny</sub> = 21,156.9 lb-in    \*φM<sub>nz</sub> = 21,156.9 lb-in

**Figure B.33** presents the applied load-interaction index plot of beam element 62 for the b-CA 090 3D structure. In this graph, the vertical axis corresponds to the applied load history expressed in percentage while the horizontal axis shows the interaction index of the beam element as the load is applied. The applied load-interaction index graph displays a non-linear response under initial loading which indicates the movement/closing of the jointing systems' gaps. After initial loading, the applied load-interaction index plot of beam element 62 shows a linear response up to 150% of the applied load. Subsequently, a non-linear behavior of the element is observed until failure of the beam is reached at 245.80% of the applied load. The forces and moments at bar failure are:

- 1)  $P_{ux}$  is 9,896.39 lb.;
- 2)  $M_{uy}$  is 523.66 lb.-in; and
- 3)  $M_{uz}$  is 15,090.07 lb.-in.

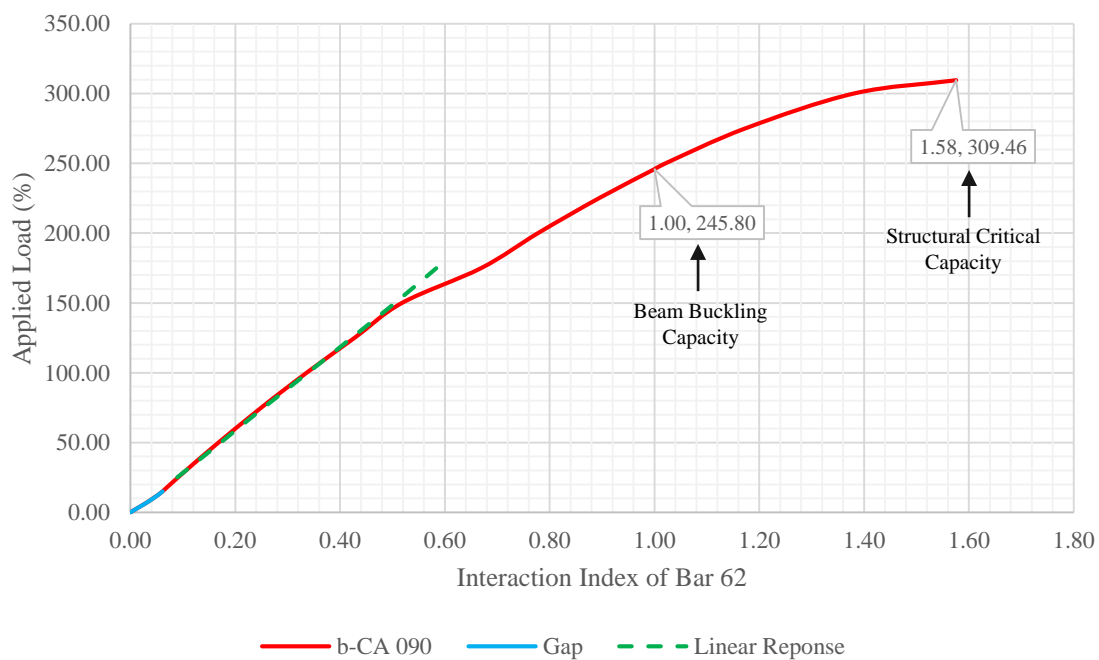


**Figure B.33** Applied Load-Interaction Index of Beam 62: b-CA 090 3D Structure

**Figure B.34** shows the axial semi-rigid behavior of the jointing system used during the simulation of the b-CA 090 3D structure. In this plot, the initial flat portion represents the fit-gap tolerance between the mating parts of the jointing system. Once the mating parts become in contact, a non-linear tension or compression load vs. displacement behavior of the connection is observed. Additionally, this figure displays that at beam failure, only 23.02% of the connection capacity in compression is reached.

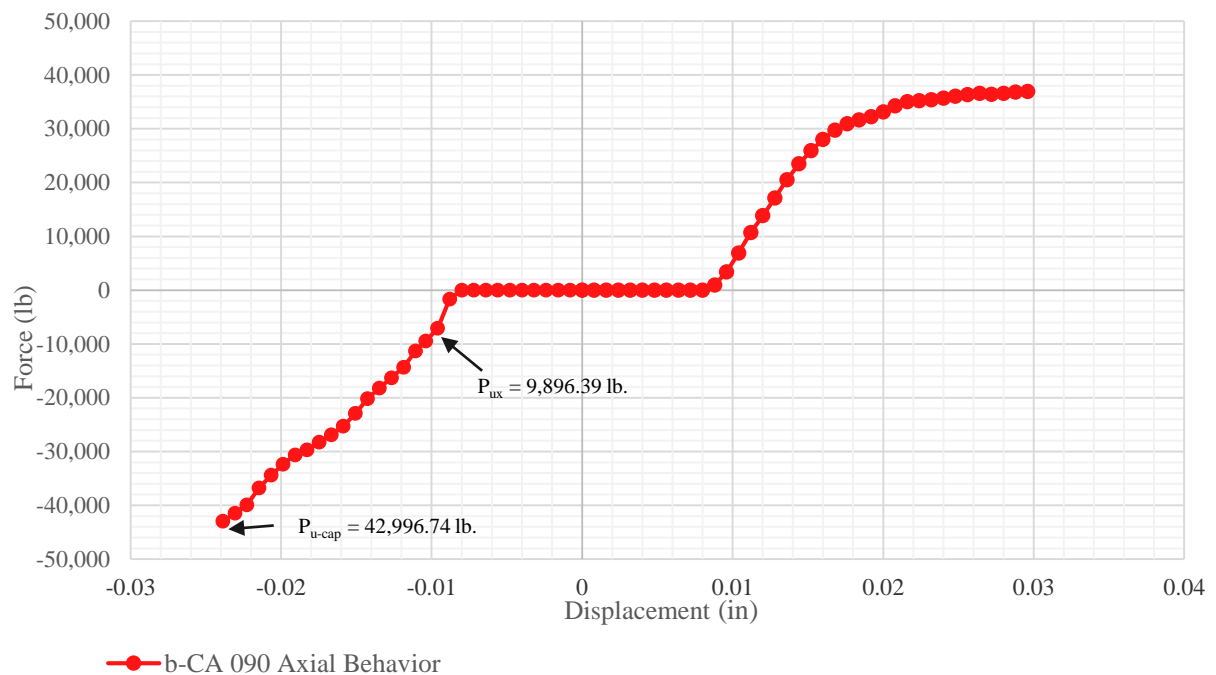


**Figure B.34** Axial Semi-Rigid Behavior: b-CA 090 (After Garcia 2017)

**Figure B.35** shows the in-plane bending semi-rigid behavior of jointing system used during the simulation of the b-CA 090 3D structure. In this plot, the initial flat portion represents the in-plane fit-gap tolerance between the mating parts of the jointing system. Once the mating parts become in contact, a non-linear bending moment vs. rotation behavior of the connection is observed. Additionally, this figure displays that at beam failure, only 2.11% of the connection in-plane bending capacity is reached.

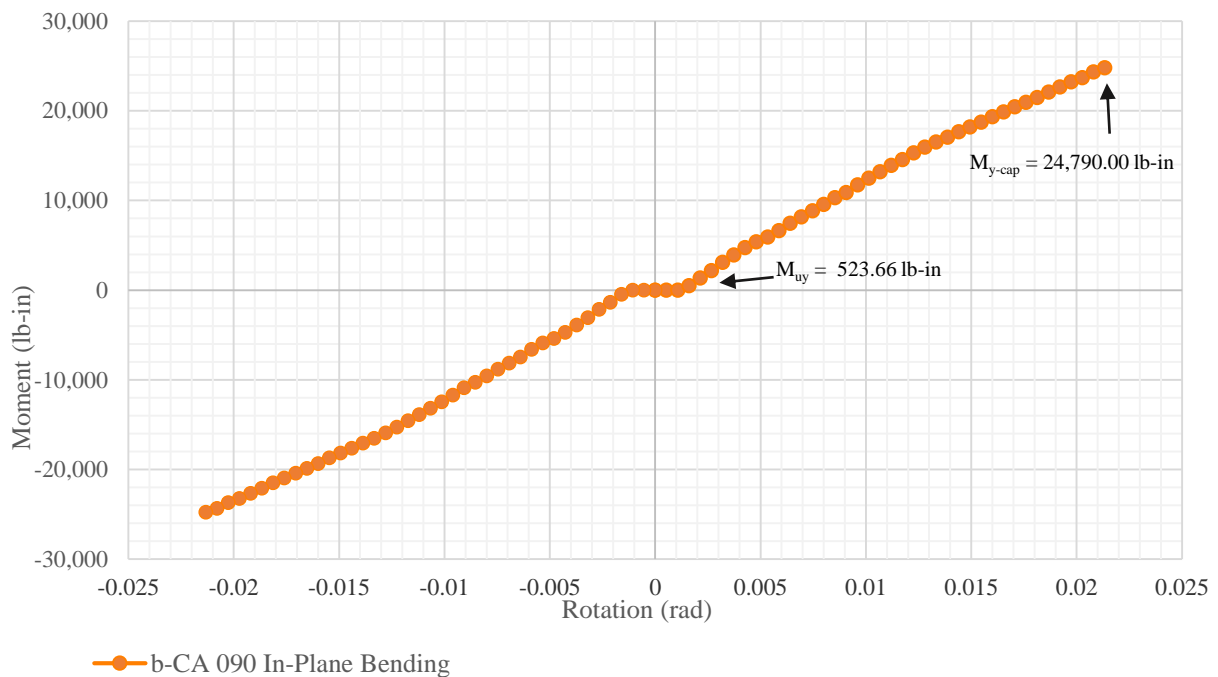


**Figure B.35** In-Plane Bending Semi-Rigid Behavior: b-CA 090 (After Garcia 2017)

## b-CB 090 3D Structure

**Figure B.36** presents the applied load-displacement plot of node 13 for the b-CB 090 3D structure. In this plot, the vertical axis corresponds to the applied load history expressed in percentage while the horizontal axis displays the resultant displacement of the node in inches as the load is applied. As observed in the figure, the applied load-displacement graph of node 13 displays a non-linear response under initial loading which indicates the movement/closing of the jointing systems' gaps. After initial loading, the structure follows a linear response up to 150% of the applied load. Subsequently, the b-CB 090 3D structure follows a non-linear behavior until critical capacity is reached at 301.21% of the applied load and at a displacement of 2.14 inches. Overall buckling is observed after critical capacity is reached.

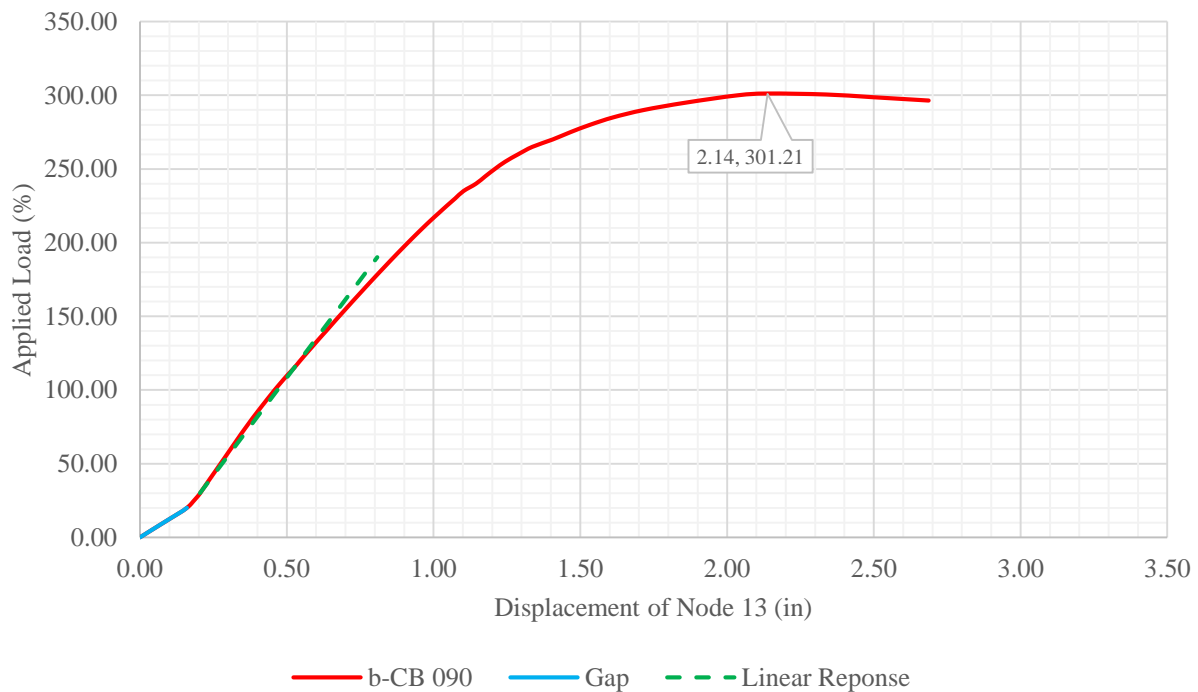


**Figure B.36** Applied Load-Displacement of Node 13: b-CB 090 3D Structure

**Figure B.37** presents the applied load-rotation plot of node 2 for the b-CB 090 3D structure. In this plot, the vertical axis corresponds to the applied load history expressed in percentage while the horizontal axis displays the resultant rotation of the node in radians as the load is applied. As observed in the figure, the applied load-rotation graph of node 2 displays a non-linear response under initial loading which indicates the movement/closing of the jointing systems' gaps. After initial loading, the structure follows a linear response up to 150% of the applied load. Subsequently, the b-CB 090 3D structure follows a non-linear behavior until critical capacity is reached at 301.21% of the applied load and at a rotation of 0.0242 radians. Overall buckling is observed after critical capacity is reached.

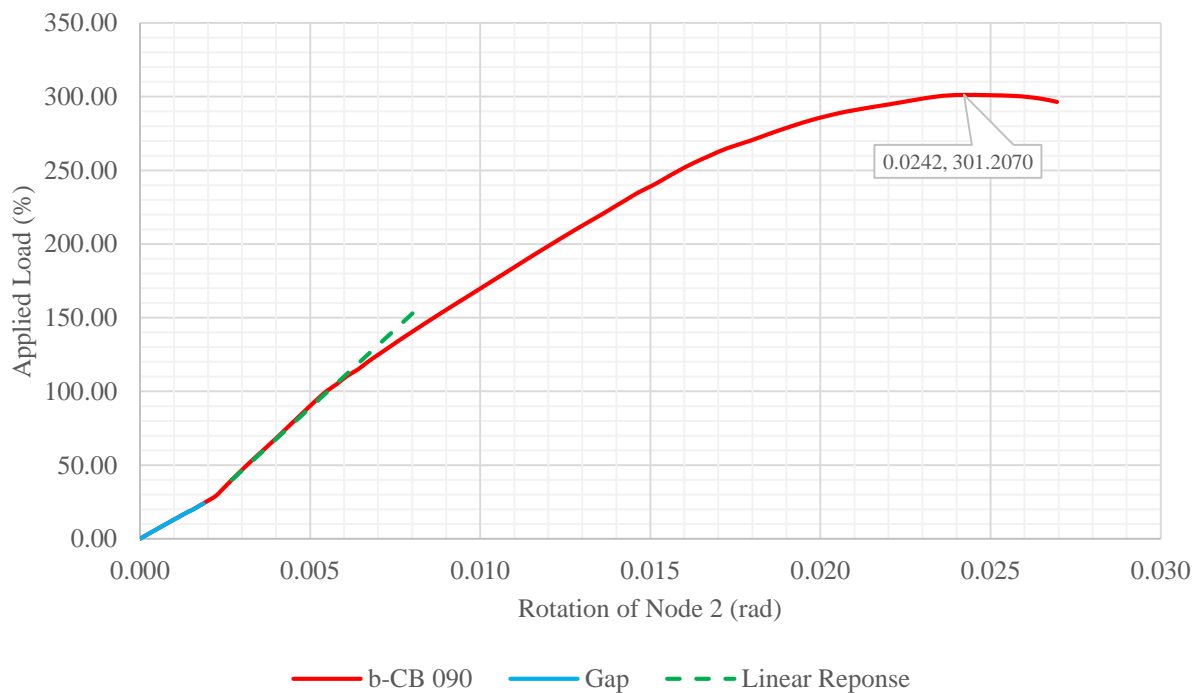


**Figure B.37** Applied Load-Rotation of Node 2: b-CB 090 3D Structure

**Table B.8** summarizes the data of the applied load-interaction index of both nodes of bar 62 at 25% load increments until critical load of the b-CB 090 3D structure is reached at 301.21% of the applied load.

**Table B.8** Applied Load-Interaction Index of Beam 62: b-CB 090 3D Structure

| Load (%)      | P <sub>ux</sub> (lb) |           | M <sub>uy</sub> (lb-in) |          | M <sub>uz</sub> (lb-in) |           | P <sub>ux</sub> /φP <sub>nx</sub> |        | Interaction Index |        | Bar Max |
|---------------|----------------------|-----------|-------------------------|----------|-------------------------|-----------|-----------------------------------|--------|-------------------|--------|---------|
|               | Node 13              | Node 2    | Node 13                 | Node 2   | Node 13                 | Node 2    | Node 13                           | Node 2 | Node 13           | Node 2 |         |
| <b>25.00</b>  | 725.67               | 725.67    | 46.58                   | 62.91    | 1,802.18                | 1,234.31  | 0.03                              | 0.025  | 0.100             | 0.074  | 0.100   |
| <b>50.00</b>  | 1,641.83             | 1,641.83  | 76.59                   | 112.79   | 3,139.17                | 2,431.18  | 0.06                              | 0.057  | 0.181             | 0.149  | 0.181   |
| <b>75.00</b>  | 2,582.62             | 2,582.62  | 107.80                  | 164.23   | 4,482.87                | 3,652.46  | 0.09                              | 0.090  | 0.262             | 0.225  | 0.262   |
| <b>100.00</b> | 3,503.94             | 3,503.94  | 140.94                  | 219.00   | 5,927.68                | 4,958.04  | 0.12                              | 0.122  | 0.348             | 0.306  | 0.348   |
| <b>125.00</b> | 4,428.85             | 4,428.85  | 184.14                  | 300.83   | 7,526.35                | 6,345.60  | 0.15                              | 0.154  | 0.441             | 0.391  | 0.441   |
| <b>150.00</b> | 5,394.88             | 5,394.88  | 263.29                  | 394.47   | 9,177.20                | 7,787.57  | 0.19                              | 0.188  | 0.540             | 0.480  | 0.540   |
| <b>175.00</b> | 6,390.91             | 6,390.91  | 422.98                  | 507.31   | 10,916.50               | 9,321.01  | 0.22                              | 0.222  | 0.699             | 0.635  | 0.699   |
| <b>200.00</b> | 7,390.24             | 7,390.24  | 588.05                  | 627.73   | 12,764.60               | 10,973.17 | 0.26                              | 0.257  | 0.818             | 0.744  | 0.818   |
| <b>225.00</b> | 8,424.81             | 8,424.81  | 767.25                  | 760.66   | 14,695.19               | 12,818.69 | 0.29                              | 0.293  | 0.942             | 0.863  | 0.942   |
| <b>250.00</b> | 9,522.09             | 9,522.09  | 957.81                  | 911.69   | 16,865.10               | 14,785.83 | 0.33                              | 0.331  | 1.080             | 0.991  | 1.080   |
| <b>275.00</b> | 10,807.96            | 10,807.96 | 1,245.69                | 1,114.60 | 19,478.66               | 17,447.74 | 0.38                              | 0.376  | 1.246             | 1.156  | 1.246   |
| <b>300.00</b> | 12,688.18            | 12,688.18 | 1,958.32                | 1,610.14 | 23,779.70               | 21,888.44 | 0.44                              | 0.441  | 1.522             | 1.428  | 1.522   |
| <b>301.21</b> | 12,916.58            | 12,916.58 | 2,044.50                | 1,693.36 | 24,296.63               | 22,452.18 | 0.45                              | 0.449  | 1.556             | 1.463  | 1.556   |

\*φP<sub>nx</sub> = 28,768.4 lb    \*φM<sub>ny</sub> = 21,156.9 lb-in    \*φM<sub>nz</sub> = 21,156.9 lb-in

**Figure B.38** presents the applied load-interaction index plot of beam element 62 for the b-CB 090 3D structure. In this graph, the vertical axis corresponds to the applied load history expressed in percentage while the horizontal axis shows the interaction index of the beam element as the load is applied. The applied load-interaction index graph displays a non-linear response under initial loading which indicates the movement/closing of the jointing systems' gaps. After initial loading, the applied load-interaction index plot of beam element 62 shows a linear response up to 150% of the applied load. Subsequently, a non-linear behavior of the element is observed until failure of the beam is reached at 235.47% of the applied load. The forces and moments at bar failure are:

- 1)  $P_{ux}$  is 8,884.37 lb.;
- 2)  $M_{uy}$  is 847.06 lb.-in; and
- 3)  $M_{uz}$  is 15,603.98 lb.-in.

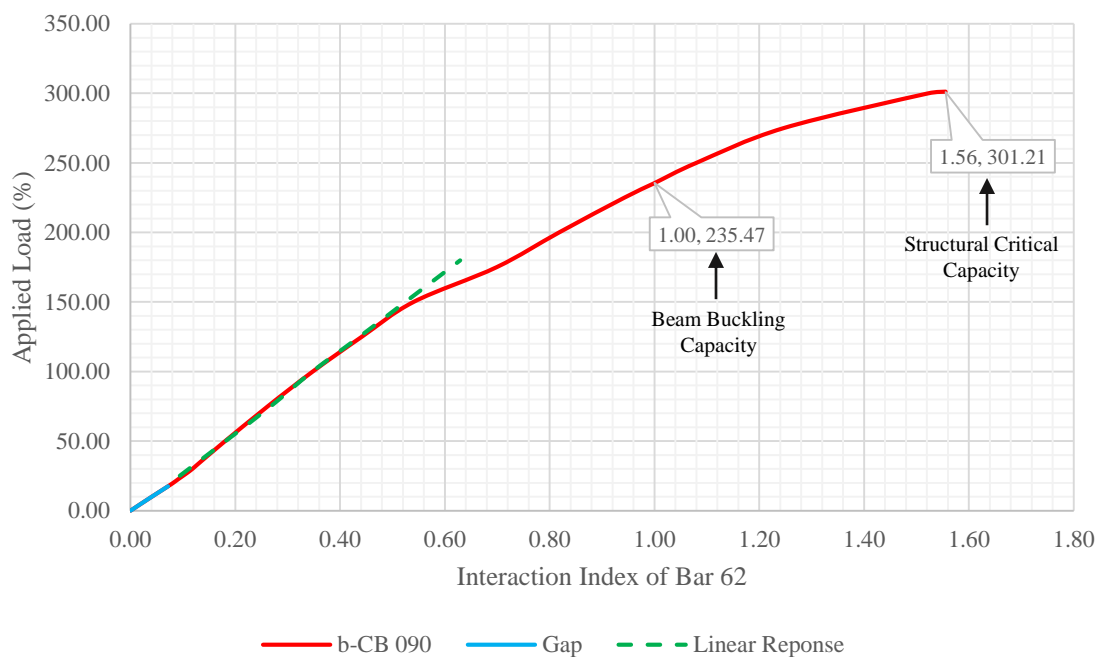


**Figure B.38** Applied Load-Interaction Index of Beam 62: b-CB 090 3D Structure

**Figure B.39** shows the axial semi-rigid behavior of the jointing system used during the simulation of the b-CB 090 3D structure. In this plot, the initial flat portion represents the fit-gap tolerance between the mating parts of the jointing system. Once the mating parts become in contact, a non-linear tension or compression load vs. displacement behavior of the connection is observed. Additionally, this figure displays that at beam failure, only 20.50% of the connection capacity in compression is reached.

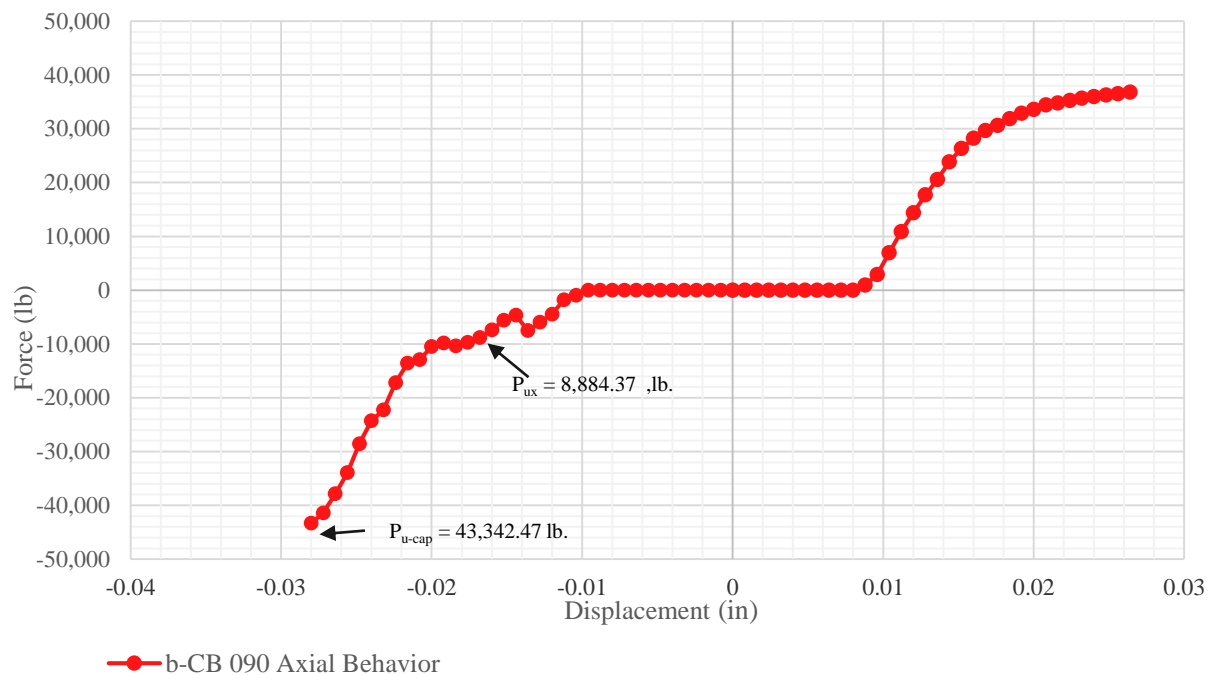


**Figure B.39** Axial Semi-Rigid Behavior: b-CB 090 (After Garcia 2017)

**Figure B.40** shows the in-plane bending semi-rigid behavior of jointing system used during the simulation of the b-CB 090 3D structure. In this plot, the initial flat portion represents the in-plane fit-gap tolerance between the mating parts of the jointing system. Once the mating parts become in contact, a non-linear bending moment vs. rotation behavior of the connection is observed. Additionally, this figure displays that, at beam failure, only 4.20% of the connection in-plane bending capacity is reached.

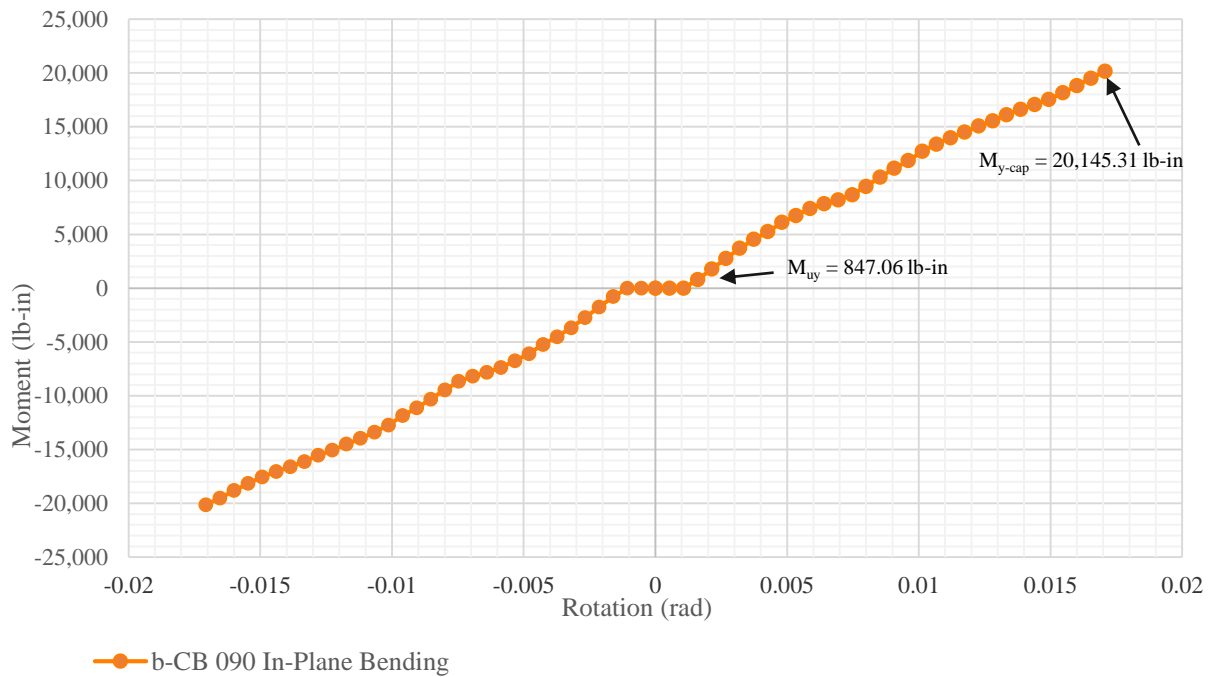


**Figure B.40** In-Plane Bending Semi-Rigid Behavior: b-CB 090 (After Garcia 2017)

## b-CC 090 3D Structure

**Figure B.41** presents the applied load-displacement plot of node 13 for the b-CC 090 3D structure. In this plot, the vertical axis corresponds to the applied load history expressed in percentage while the horizontal axis displays the resultant displacement of the node in inches as the load is applied. As observed in the figure, the applied load-displacement graph of node 13 displays a non-linear response under initial loading which indicates the movement/closing of the jointing systems' gaps. After initial loading, the structure follows a linear response up to 150% of the applied load. Subsequently, the b-CC 090 3D structure follows a non-linear behavior until critical capacity is reached at 304.13% of the applied load and at a displacement of 2.19 inches. Overall buckling is observed after critical capacity is reached.

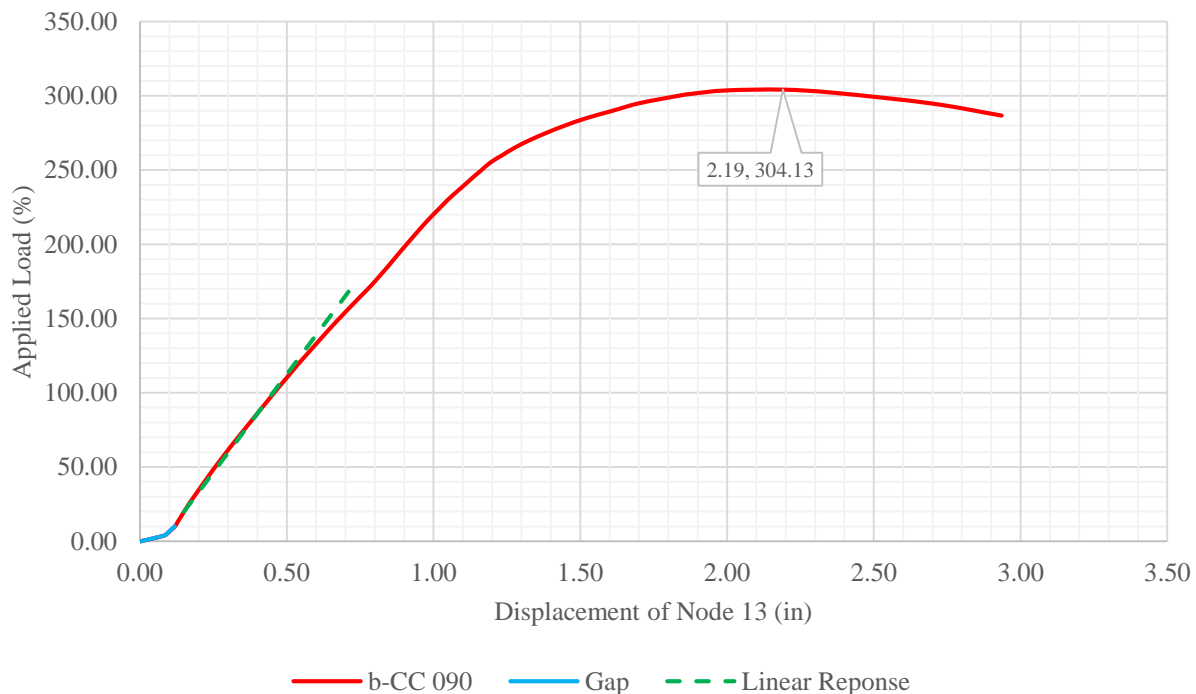


**Figure B.41** Applied Load-Displacement of Node 13: b-CC 090 3D Structure

**Figure B.42** presents the applied load-rotation plot of node 2 for the b-CC 090 3D structure. In this plot, the vertical axis corresponds to the applied load history expressed in percentage while the horizontal axis displays the resultant rotation of the node in radians as the load is applied. As observed in the figure, the applied load-rotation graph of node 2 displays a non-linear response under initial loading which indicates the movement/closing of the jointing systems' gaps. After initial loading, the structure follows a linear response up to 150% of the applied load. Subsequently, the b-CC 090 3D structure follows a non-linear behavior until critical capacity is reached at 304.13% of the applied load and at a rotation of 0.0244 radians. Overall buckling is observed after critical capacity is reached.

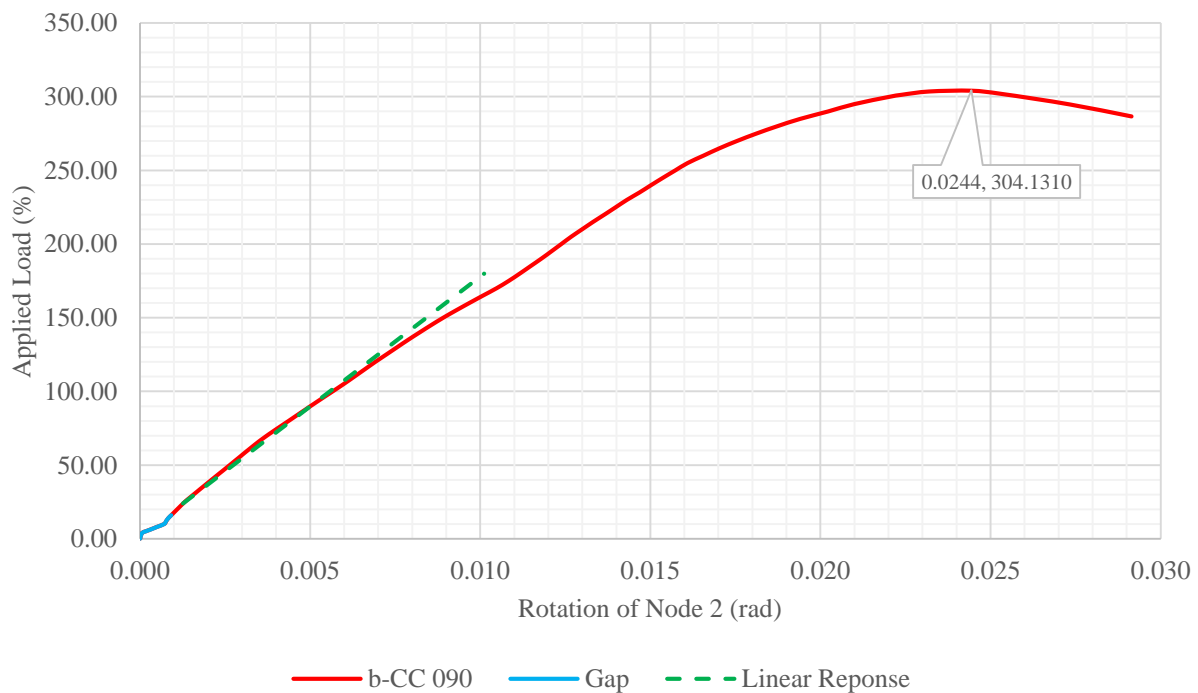


**Figure B.42** Applied Load-Rotation of Node 2: b-CC 090 3D Structure

**Table B.9** summarizes the data of the applied load-interaction index of both nodes of bar 62 at 25% load increments until critical load of the b-CC 0903D structure is reached at 304.13% of the applied load.

**Table B.9** Applied Load-Interaction Index of Beam 62: b-CC 090 3D Structure

| Load (%)      | P <sub>ux</sub> (lb) |           | M <sub>uy</sub> (lb-in) |        | M <sub>uz</sub> (lb-in) |           | P <sub>ux</sub> /φP <sub>nx</sub> |        | Interaction Index |        | Bar Max |
|---------------|----------------------|-----------|-------------------------|--------|-------------------------|-----------|-----------------------------------|--------|-------------------|--------|---------|
|               | Node 13              | Node 2    | Node 13                 | Node 2 | Node 13                 | Node 2    | Node 13                           | Node 2 | Node 13           | Node 2 |         |
| <b>25.00</b>  | 851.12               | 851.12    | 11.70                   | 15.13  | 1,567.52                | 1,146.01  | 0.030                             | 0.030  | 0.089             | 0.070  | 0.089   |
| <b>50.00</b>  | 1,747.31             | 1,747.31  | 21.79                   | 33.10  | 2,906.84                | 2,313.38  | 0.061                             | 0.061  | 0.169             | 0.141  | 0.169   |
| <b>75.00</b>  | 2,637.07             | 2,637.07  | 33.95                   | 54.21  | 4,347.74                | 3,557.60  | 0.092                             | 0.092  | 0.253             | 0.217  | 0.253   |
| <b>100.00</b> | 3,536.69             | 3,536.69  | 49.83                   | 89.27  | 5,902.07                | 4,901.95  | 0.123                             | 0.123  | 0.343             | 0.297  | 0.343   |
| <b>125.00</b> | 4,433.77             | 4,433.77  | 93.36                   | 131.98 | 7,538.72                | 6,341.29  | 0.154                             | 0.154  | 0.438             | 0.383  | 0.438   |
| <b>150.00</b> | 5,333.26             | 5,333.26  | 197.43                  | 176.36 | 9,272.03                | 7,878.52  | 0.185                             | 0.185  | 0.540             | 0.473  | 0.540   |
| <b>175.00</b> | 6,262.83             | 6,262.83  | 352.84                  | 241.33 | 11,136.25               | 9,516.50  | 0.218                             | 0.218  | 0.700             | 0.628  | 0.700   |
| <b>200.00</b> | 7,369.47             | 7,369.47  | 485.04                  | 291.99 | 12,788.11               | 10,992.85 | 0.256                             | 0.256  | 0.814             | 0.730  | 0.814   |
| <b>225.00</b> | 8,528.76             | 8,528.76  | 626.92                  | 348.02 | 14,479.58               | 12,614.18 | 0.296                             | 0.296  | 0.931             | 0.841  | 0.931   |
| <b>250.00</b> | 9,764.70             | 9,764.70  | 789.49                  | 415.77 | 16,393.90               | 14,368.86 | 0.339                             | 0.339  | 1.061             | 0.961  | 1.061   |
| <b>275.00</b> | 11,178.44            | 11,178.44 | 1,018.41                | 514.95 | 18,700.63               | 16,750.03 | 0.389                             | 0.389  | 1.217             | 1.114  | 1.217   |
| <b>300.00</b> | 13,046.78            | 13,046.78 | 1,542.19                | 717.70 | 22,373.28               | 20,440.69 | 0.454                             | 0.454  | 1.458             | 1.342  | 1.458   |
| <b>304.13</b> | 13,938.20            | 13,938.20 | 1,750.97                | 861.88 | 24,188.24               | 22,683.65 | 0.484                             | 0.484  | 1.574             | 1.474  | 1.574   |

\*φP<sub>nx</sub> = 28,768.4 lb    \*φM<sub>ny</sub> = 21,156.9 lb-in    \*φM<sub>nz</sub> = 21,156.9 lb-in

**Figure B.43** presents the applied load-interaction index plot of beam element 62 for the b-CC 090 3D structure. In this graph, the vertical axis corresponds to the applied load history expressed in percentage while the horizontal axis shows the interaction index of the beam element as the load is applied. The applied load-interaction index graph displays a non-linear response under initial loading which indicates the movement/closing of the jointing systems' gaps. After initial loading, the applied load-interaction index plot of beam element 62 shows a linear response up to 150% of the applied load. Subsequently, a non-linear behavior of the element is observed until failure of the beam is reached at 238.22% of the applied load. The forces and moments at bar failure are:

- 1)  $P_{ux}$  is 9,182.23 lb.;
- 2)  $M_{uy}$  is 712.87 lb.-in; and
- 3)  $M_{uz}$  is 15,491.72 lb.-in.

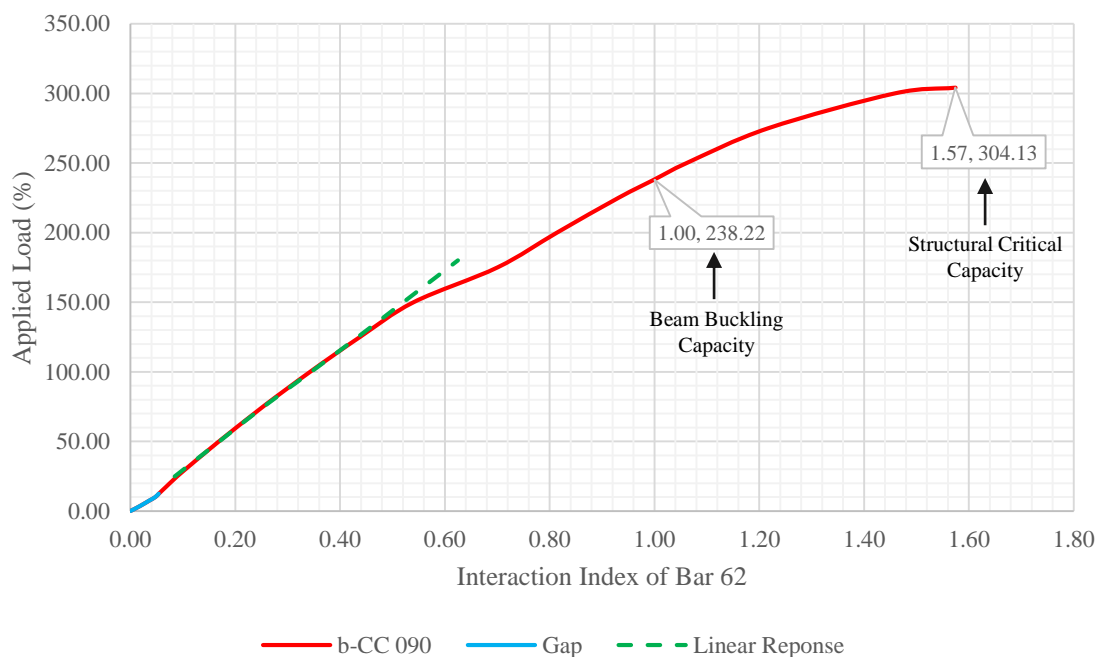


**Figure B.43** Applied Load-Interaction Index of Beam 62: b-CC 090 3D Structure

**Figure B.44** shows the axial semi-rigid behavior of the jointing system used during the simulation of the b-CC 090 3D structure. In this plot, the initial flat portion represents the fit-gap tolerance between the mating parts of the jointing system. Once the mating parts become in contact, a non-linear tension or compression load vs. displacement behavior of the connection is observed. Additionally, this figure displays that at beam failure, only 20.77% of the connection capacity in compression is reached.

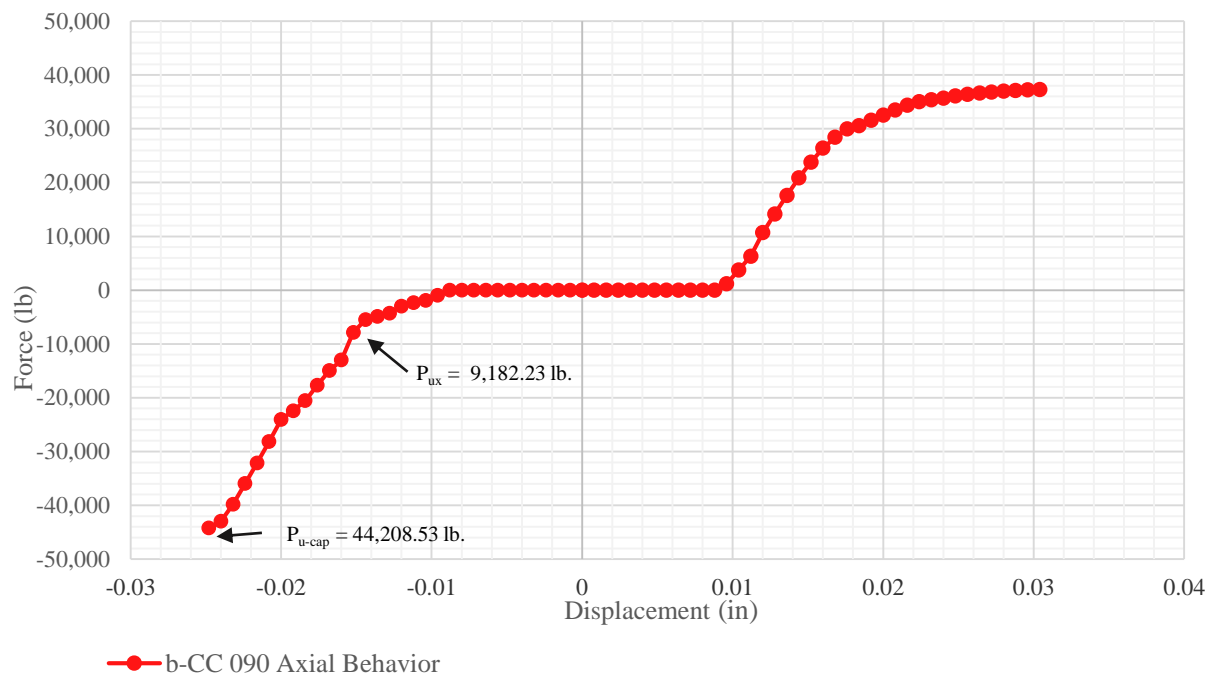


**Figure B.44** Axial Semi-Rigid Behavior: b-CC 090 (After Garcia 2017)

**Figure B.45** shows the in-plane bending semi-rigid behavior of jointing system used during the simulation of the b-CC 090 3D structure. In this plot, the initial flat portion represents the in-plane fit-gap tolerance between the mating parts of the jointing system. Once the mating parts become in contact, a non-linear bending moment vs. rotation behavior of the connection is observed. Additionally, this figure displays that at beam failure, only 2.86% of the connection in-plane bending capacity is reached.

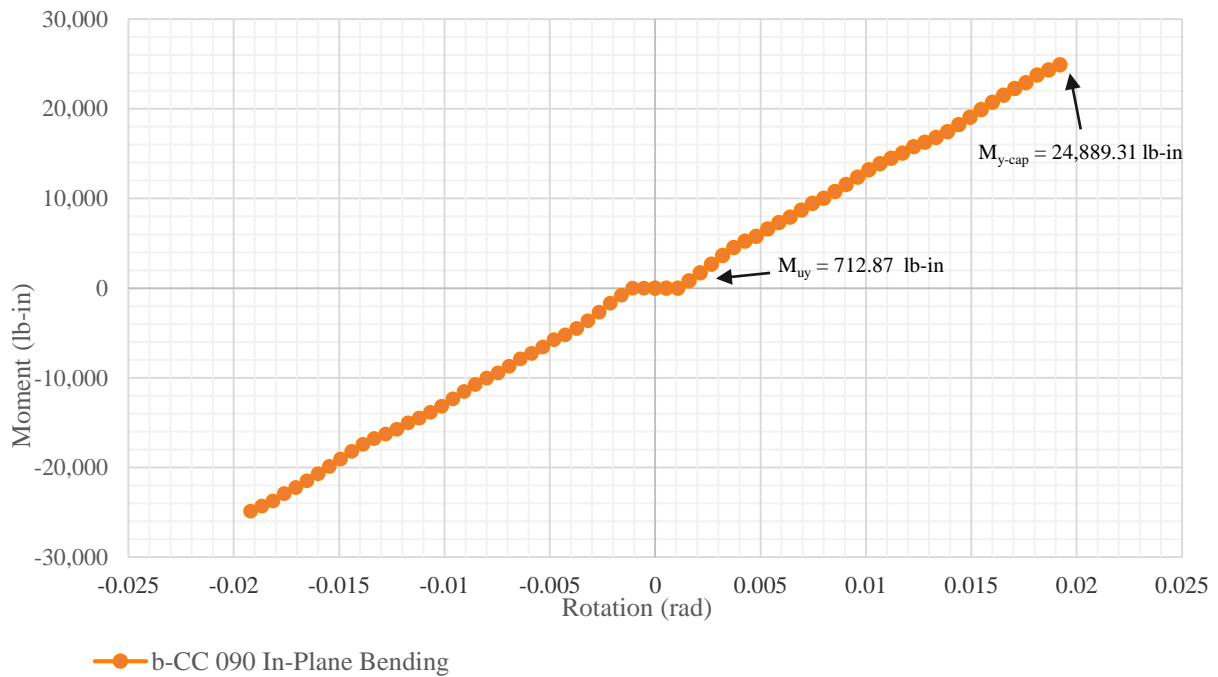


**Figure B.45** In-Plane Bending Semi-Rigid Behavior: b-CC 090 (After Garcia 2017)

## b-RD 090 3D Structure

**Figure B.46** presents the applied load-displacement plot of node 13 for the b-RD 090 3D structure. In this plot, the vertical axis corresponds to the applied load history expressed in percentage while the horizontal axis displays the resultant displacement of the node in inches as the load is applied. As observed in the figure, the applied load-displacement graph of node 13 displays a non-linear response under initial loading which indicates the movement/closing of the jointing systems' gaps. After initial loading, the structure follows a linear response up to 150% of the applied load. Subsequently, the b-RD 090 3D structure follows a non-linear behavior until critical capacity is reached at 302.06% of the applied load and at a displacement of 1.81 inches. Overall buckling is observed after critical capacity is reached.

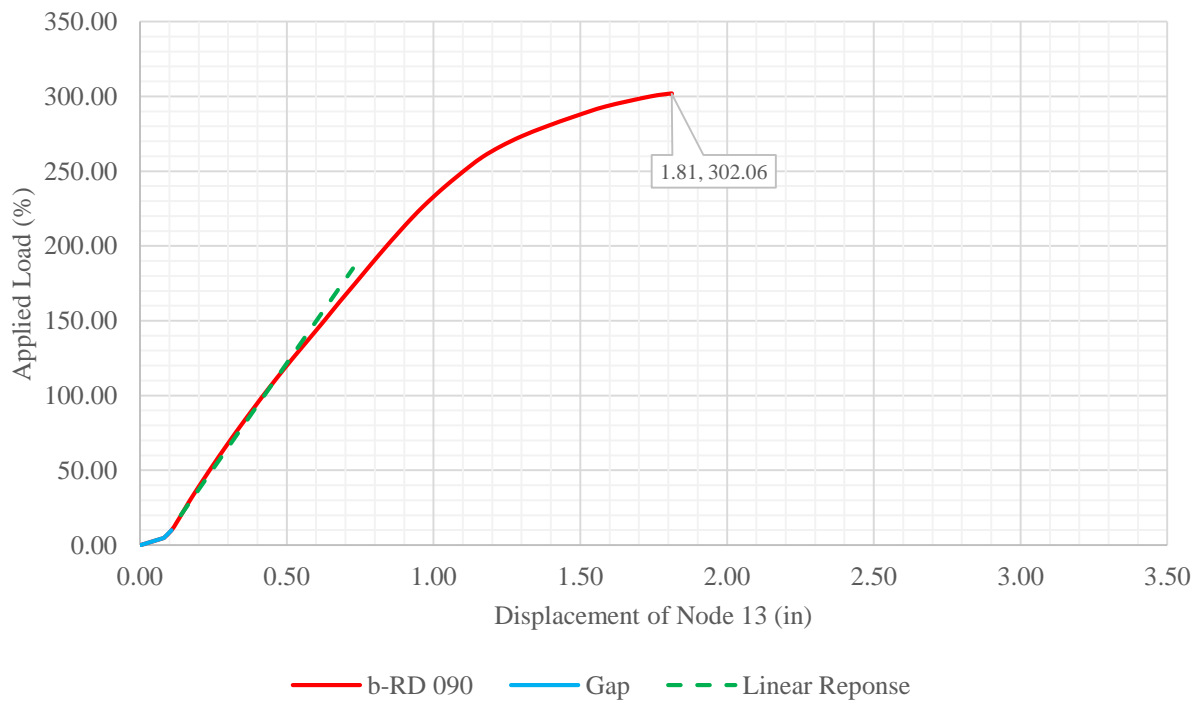


**Figure B.46** Applied Load-Displacement of Node 13: b-RD 090 3D Structure

**Figure B.47** presents the applied load-rotation plot of node 2 for the b-RD 090 3D structure. In this plot, the vertical axis corresponds to the applied load history expressed in percentage while the horizontal axis displays the resultant rotation of the node in radians as the load is applied. As observed in the figure, the applied load-rotation graph of node 2 displays a non-linear response under initial loading which indicates the movement/closing of the jointing systems' gaps. After initial loading, the structure follows a linear response up to 150% of the applied load. Subsequently, the b-RD 090 3D structure follows a non-linear behavior until critical capacity is reached at 302.06% of the applied load and at a rotation of 0.0234 radians. Overall buckling is observed after critical capacity is reached.

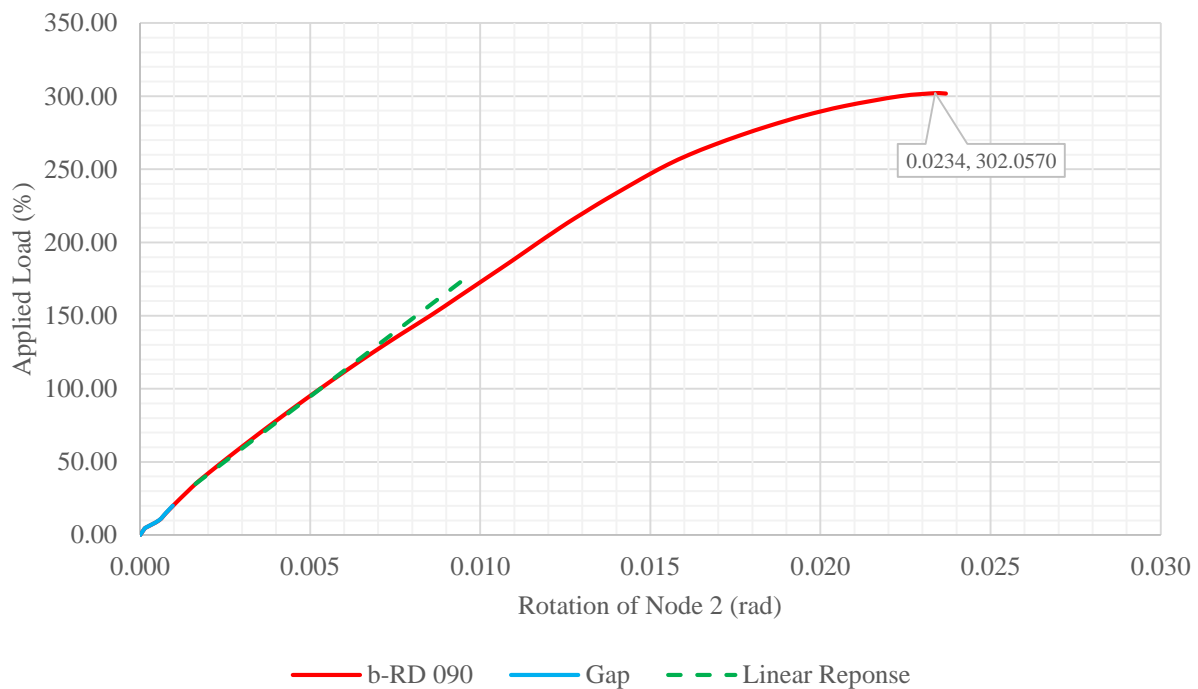


**Figure B.47** Applied Load-Rotation of Node 2: b-RD 090 3D Structure

**Table B.10** summarizes the data of the applied load-interaction index of both nodes of bar 62 at 25% load increments until critical load of the b-RD 090 3D structure is reached at 302.06% of the applied load.

**Table B.10** Applied Load-Interaction Index of Beam 62: b-RD 090 3D Structure

| Load (%)      | P <sub>ux</sub> (lb) |           | M <sub>uy</sub> (lb-in) |          | M <sub>uz</sub> (lb-in) |           | P <sub>ux</sub> /φP <sub>nx</sub> |        | Interaction Index |        | Bar Max |
|---------------|----------------------|-----------|-------------------------|----------|-------------------------|-----------|-----------------------------------|--------|-------------------|--------|---------|
|               | Node 13              | Node 2    | Node 13                 | Node 2   | Node 13                 | Node 2    | Node 13                           | Node 2 | Node 13           | Node 2 |         |
| <b>25.00</b>  | 795.33               | 795.33    | 31.36                   | 41.01    | 1,479.62                | 1,152.95  | 0.028                             | 0.028  | 0.085             | 0.070  | 0.085   |
| <b>50.00</b>  | 1,680.37             | 1,680.37  | 57.54                   | 81.23    | 2,839.08                | 2,355.44  | 0.058                             | 0.058  | 0.166             | 0.144  | 0.166   |
| <b>75.00</b>  | 2,569.60             | 2,569.60  | 96.53                   | 128.93   | 4,280.09                | 3,626.80  | 0.089                             | 0.089  | 0.252             | 0.222  | 0.252   |
| <b>100.00</b> | 3,467.92             | 3,467.92  | 193.13                  | 185.73   | 5,800.16                | 4,980.70  | 0.121                             | 0.121  | 0.344             | 0.304  | 0.344   |
| <b>125.00</b> | 4,362.29             | 4,362.29  | 309.61                  | 249.49   | 7,413.01                | 6,421.31  | 0.152                             | 0.152  | 0.441             | 0.391  | 0.441   |
| <b>150.00</b> | 5,262.11             | 5,262.11  | 430.02                  | 318.08   | 9,081.23                | 7,914.93  | 0.183                             | 0.183  | 0.541             | 0.481  | 0.541   |
| <b>175.00</b> | 6,286.17             | 6,286.17  | 544.84                  | 381.07   | 10,624.43               | 9,266.77  | 0.219                             | 0.219  | 0.688             | 0.624  | 0.688   |
| <b>200.00</b> | 7,353.10             | 7,353.10  | 669.64                  | 450.16   | 12,227.41               | 10,701.65 | 0.256                             | 0.256  | 0.797             | 0.724  | 0.797   |
| <b>225.00</b> | 8,466.38             | 8,466.38  | 808.93                  | 528.18   | 13,933.62               | 12,296.11 | 0.294                             | 0.294  | 0.914             | 0.833  | 0.914   |
| <b>250.00</b> | 9,631.31             | 9,631.31  | 972.42                  | 622.93   | 15,842.10               | 14,062.77 | 0.335                             | 0.335  | 1.041             | 0.952  | 1.041   |
| <b>275.00</b> | 10,963.03            | 10,963.03 | 1,217.31                | 769.35   | 18,386.18               | 16,631.87 | 0.381                             | 0.381  | 1.205             | 1.112  | 1.205   |
| <b>300.00</b> | 12,903.67            | 12,903.67 | 1,885.46                | 1,149.63 | 22,825.11               | 21,118.40 | 0.449                             | 0.449  | 1.487             | 1.384  | 1.487   |
| <b>302.06</b> | 13,467.44            | 13,467.44 | 2,004.54                | 1,310.60 | 23,936.22               | 22,333.73 | 0.468                             | 0.468  | 1.558             | 1.462  | 1.558   |

\*φP<sub>nx</sub> = 28,768.4 lb    \*φM<sub>ny</sub> = 21,156.9 lb-in    \*φM<sub>nz</sub> = 21,156.9 lb-in

**Figure B.48** presents the applied load-interaction index plot of beam element 62 for the b-RD 090 3D structure. In this graph, the vertical axis corresponds to the applied load history expressed in percentage while the horizontal axis shows the interaction index of the beam element as the load is applied. The applied load-interaction index graph displays a non-linear response under initial loading which indicates the movement/closing of the jointing systems' gaps. After initial loading, the applied load-interaction index plot of beam element 62 shows a linear response up to 150% of the applied load. Subsequently, a non-linear behavior of the element is observed until failure of the beam is reached at 241.92% of the applied load. The forces and moments at bar failure are:

- 1)  $P_{ux}$  is 9,254.69 lb.;
- 2)  $M_{uy}$  is 919.56 lb.-in; and
- 3)  $M_{uz}$  is 15,225.08 lb.-in.

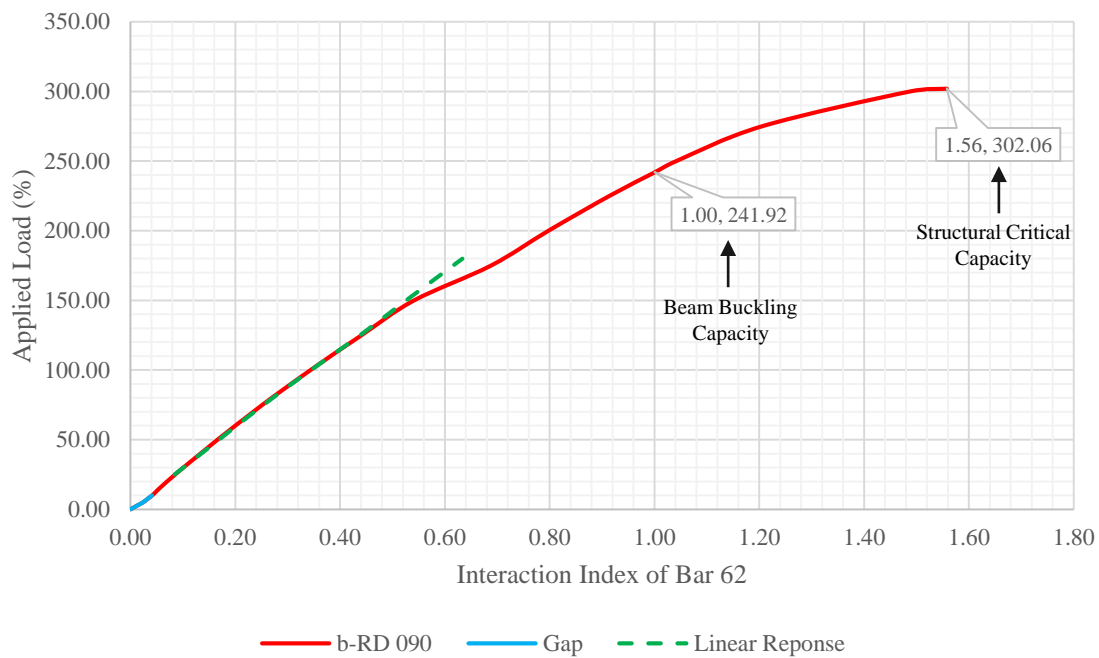


**Figure B.48** Applied Load-Interaction Index of Beam 62: b-RD 090 3D Structure

## **Curriculum Vitae**

Juan Salcido was born in El Paso, Texas on August 17, 1987; however, he was raised in Ciudad Juárez, Chihuahua, Mexico. At the age of 17, Juan moved to El Paso to pursue higher education studies and graduated with a BSc in Civil Engineering from The University of Texas at El Paso (UTEP) in spring 2012. Additionally, in the spring of 2012, Juan was awarded with a scholarship from the NSF allowing him to join the Ph.D. in Civil Engineering program at UTEP. After having accumulated enough credits, he earned a Master degree in Civil and Environmental Engineering (MECEE) in the summer of 2014.

As an undergraduate student, Juan collaborated as Research Assistant in the BIG Transportation Lab and in the Center for Transportation Infrastructure Systems. During his graduate studies, Juan collaborated as a Teaching Assistant and as a Research Assistant, allowing him to publish two journal articles related to the use of sustainable materials in construction and in the conservation of energy in office buildings, respectively.

In addition, he has attained different professional internships with local companies including: HKN Structural Engineers, Professional Service Industries (PSI), and Veliz Construction. Additionally, during the summer of 2015, Juan worked for the Federal Highway Administration (FHWA) as a Research Engineer Intern at the Turner Fairbank Highway Research Center in Mclean, Virginia.

Permanent address: 367 Aidan Gordon

El Paso, Texas, 79932

This dissertation was typed by Juan C. Salcido